Three-Dimensional Optical Coherence Tomography Imaging of the Optic Nerve Head

Thesis submitted for the degree of

Doctor of Philosophy at UCL

Nicholas Gabriel Strouthidis MBBS MD FRCOphth

Supervisors

Professor PT Khaw

Professor DF Garway-Heath

Institutions

Institute of Ophthalmology, UCL, London, UK

Devers Eye Institute, Portland, Oregon, USA

1. SECTION I:

OVERVIEW

1.1 Declaration

I, Nicholas Gabriel Strouthidis, confirm that the work presented in this thesis is my own. Where information has been derived from other sources, I confirm that this has been indicated in the thesis.

Nicholas Strouthidis 21/09/2011

1.2 Abstract

Background: the primary site of injury in glaucoma is likely to be at the lamina cribrosa (LC), deep within the optic nerve head (ONH). Optical coherence tomography (OCT) in glaucoma has, to date, focused on the detection of nerve fibre loss. Spectral domain OCT (SDOCT) has improved speed and axial resolution, allowing acquisition of three-dimensional ONH volumes and may capture targets deep within the ONH. This thesis explores the capabilities and potential of deep SDOCT imaging in the monkey ONH.

Plan of research: an investigation was conducted into the detection of key landmarks that would be necessary for future quantification strategies. In particular, detection of the neural canal opening (NCO) was assessed and how the NCO relates to what is clinically identified as the disc margin. The next phase involved clarifying the anatomical and histological basis of ONH structures observed within SDCOT volumes, by comparison with histological sections and disc photographs. Finally, quantification strategies for novel parameters based on deep targets were developed and used to detect chronic longitudinal changes in experimental glaucoma and acute changes following IOP manipulation.

Results: SDOCT reliably detects the NCO, which can be used as an anchoring structure for reference planes. Usually the NCO equates to the disc margin but disc margin architecture can be complex and highly variable. SDOCT captures the prelaminar tissue and anterior LC surface. Prelaminar thinning and posterior LC displacement were both detected longitudinally in experimental glaucoma. Prelaminar thinning was observed with acute IOP elevation; posterior LC movement was rare.

Significance: deep ONH structures, including the LC, are realistic targets for clinical imaging. These imaging targets may be useful in the detection of glaucoma progression and in the verification of ex-vivo models of ONH biomechanical behaviour.

1.3 Table of Contents

1.4 List of Figures

1.5 List of Tables

1.6 List of Abbreviations

2D	Two-dimensional
3D	Three-dimensional
ALCS	Anterior lamina cribrosa surface
ARVO	Association for Research in Vision and Ophthalmology
BL	Baseline
BM	Bruch's membrane
BMO	Bruch's membrane opening
CCD	Couple charged device
CCT	Central corneal thickness
CNTGS	Collaborative Normal Tension Glaucoma Study Group
CSLO	Confocal scanning laser ophthalmoscope
DCM	Department of comparative medicine
DEI	Devers Eye Institute
EDI	Enhanced depth imaging
EG	Experimental glaucoma
EGPS	European Glaucoma Prevention Study
GCC	Ganglion cell complex
GPS	Glaucoma probability score
HE	Haematoxylin and Eosin

FDOCT	Fourier domain optical coherence tomography
FU	Follow-up
GFAP	Glial fibrillary acidic protein
GON	Glaucomatous optic neuropathy
HRT	Heidelberg Retina Tomograph
ILM	Internal limiting membrane
IOP	Intraocular pressure
IR	Infrared
IV	Intravenous
LC	Lamina cribrosa
LFB	Luxol fast blue
MAP	Mean arterial pressure
MPD	Mean position of the disc
MPHSD	Mean pixel height standard deviation
MRA	Moorfields regression analysis
MT	Masson Trichrome
NCO	Neural canal opening
NICE	National Institute for Clinical Excellence
NTG	Normal tension glaucoma
OBL	Ocular Biomechanics Laboratory

OCT	Optical coherence tomography
OHSU	Oregon Health and Sciences University
OHTS	Ocular Hypertension Treatment Study
ONH	Optic nerve head
ONHRL	Optic Nerve Head Research Laboratory
PAC	Primary angle closure
PACG	Primary angle closure glaucoma
PLTT	Prelaminar tissue thickness
POAG	Primary open angle glaucoma
RC	Repeatability coefficient
RGC	Retinal ganglion cell
RM-ANOVA	Repeated measures analysis of variance
RNFL	Retinal nerve fibre layer
RNFLT	Retinal nerve fibre layer thickness
RNFLV	Retinal nerve fibre layer volume
RPE	Retinal pigment epithelium
SDOCT	Spectral domain optical coherence tomography
SLO	Scanning laser ophthalmoscope
SSOCT	Swept-source optical coherence tomography
TDOCT	Time domain optical coherence tomography

1.7 Supporting Publications

1. Detection of optic nerve head neural canal opening within histomorphometric and spectral domain optical coherence tomography data sets. Strouthidis NG, Yang H, Fortune B, Downs JC, Burgoyne CF. *Invest Ophthalmol Vis Sci* 2009;50(1):214-23

2. Comparison of clinical and three-dimensional histomorphometric optic disc margin anatomy. Strouthidis NG, Yang H, Downs JC, Burgoyne CF. *Invest Ophthalmol Vis Sci* 2009;50(5):2165-74

3. Comparison of clinical and spectral domain optical coherence tomography optic disc margin anatomy. Strouthidis NG, Yang H, Reynaud J, Grimm J, Gardiner S, Fortune B, Burgoyne CF. *Invest Ophthalmol Vis Sci* 2009;50(10):4709-18

4. A comparison of optic nerve head morphology viewed by spectral domain optical coherence tomography and by serial histology. Strouthidis NG, Grimm J, Williams G, Cull GA, Wilson DJ, CF Burgoyne. *Invest Ophthalmol Vis Sci* 2010;51(3):1464-74

5. Longitudinal change detected by spectral domain optical coherence tomography in the optic nerve head and peripapillary retina in experimental glaucoma. Strouthidis NG, Fortune B, Yang H, Sigal IA, Burgoyne CF. *Invest Ophthalmol Vis Sci* 2011;52(3):1206-19 (Cover image)

6. The effect of acute intraocular pressure elevation on the monkey optic nerve head as detected by spectral domain optical coherence tomography. Strouthidis NG, Fortune B, Yang H, Sigal IA, Burgoyne CF. *Invest Ophthalmol Vis Sci* 2011 Nov 4. [Epub ahead of print]

1.8 Acknowledgements

I would like to thank all of the staff at Devers Eye Institute for their help and assistance during (and beyond) my period of study. Professor Burgoyne has built an admirable team within the ONHRL. Much of the foundation for what I wished to achieve was already established through the far-sightedness and hard work of Professor Burgoyne and his team. Furthermore, all of the scientists at Devers conduct themselves in a highly collegial manner, which allowed me to optimise my time there.

The group has a well-established timetable of animal testing and post mortem 3D histomorphometric ONH reconstruction achieved by a roster of highly able full time technicians, led by Galen Williams and including Christy Hardin and Erica Dyrud. I was very grateful for the programming abilities of both Juan Reynaud and Jonathan Grimm. Jonathan developed the Multiview visualisation and delineation software used in all but one of the experiments; he also developed the method for generating interpolated B-scans at any orientation within an SDOCT volume (section 4.5). Juan developed a program called 'clickermaster' that was used for the delineation of the disc margin onto co-localised images (sections 4.3 and 4.4). Juan's contribution to all of the work undertaken at Devers cannot be underestimated. He built most of the hardware used within the lab, maintains all of the servers, leads the programmers and can solve any problem with ingenuity, brilliance and good humour.

I worked closely with Hongli Yang during my time at Devers. Hongli had developed most of the structural parameters used in 3D histomorphometry during her PhD and so was able to help me modify these concepts for SDOCT imaging. Specifically, Hongli assisted me in all computations that required the use of Matlab (quantifications performed in sections 4.2, 4.6 and 4.7). My good friend, Dr Brad Fortune, was immensely helpful in enabling me to conceptualise the importance of each of my projects and to instill a sense of scientific rigour and confidence in all that I undertook. He also provided me statistical support, where needed, along with Drs Stuart Gardiner and Shaban Demirel. Brad also served as one of the SDOCT delineators (sections 4.6 and 4.7) along with Christy Hardin and Karin Novitsky.

I am also very grateful for the input of my colleagues and friends at the Devers OBL - specifically Dr Crawford Downs and Dr Ian Sigal. Both helped me to understand ocular biomechanics and allowed me to interpret the results of my studies in those terms. I would also like to express my thanks to Dr Lin Wang who allowed some of his monkeys to be tested in my longitudinal study (section 4.6). Outside of Devers, I must thank Dorothea Burke from the pathology service at Casey Eye Institute who carried out serial sectioning and staining of the normal monkey ONH for comparison with SDOCT (section 4.5).

At UCL, I would like to thank my two supervisors, Professors Khaw and Garway-Heath. Both have proved to be inspirational figures throughout my training in ophthalmology and in my research career to date. They have provided me a steady hand in guiding me through this PhD and were able to provide objective criticisms from a perspective outside of the ONHRL. I would also like to thank Peggy Khaw who has been extremely helpful, kind and supportive in directing me through all of the administrative aspects of my PhD.

My final thanks go to Professor Claude Burgoyne, who although not one of my official UCL supervisors, inspired and led me throughout and beyond my period of study at Devers. I am grateful for the opportunity that he gave me to work within his laboratory and the experience has been a rich one. I have learned a great deal from Claude; I owe much of my development as a scientist and as a person thanks to his mentorship and friendship.

2. SECTION II:

INTRODUCTION

2.1 The Normal Optic Nerve

2.1.1 Gross Anatomy of the Optic Nerve

The optic nerve is the part of the eye that acts as a conduit, transmitting visual information from the light sensitive cells (photoreceptors) of the retina to the brain. The optic nerve has, by convention, been divided anatomically into four regions (Bron et al., 1997; Ritch et al., 1989). The first of these, the intraocular portion, is approximately 3 mm in length and is the focus for the work contained within this thesis. Once the optic nerve exits the eye, there is an intraorbital portion of approximately 25 mm in length. This is a greater distance than that between the posterior surface of the sclera from which the nerve exits the eye and the optic foramen, the opening in the bony orbit through which the optic nerve exits the orbit. The intraorbital optic nerve therefore follows a sigmoidal course, giving sufficient 'slack' so as not to compromise the nerve during extremes of ocular motility. The optic nerve then passes through the optic foramen into the optic canal; this intracanalicular portion of the nerve is approximately 10 mm in length. Upon exiting the optic canal, the nerve runs an intracranial course for approximately 16 mm, until it reaches the optic chiasm. The optic nerve is enclosed in meningeal sheaths (dura, arachnoid and pia mater) in its intraorbital and intracanalicular portions; these sheaths are continuous with those that line the brain (Hogan et al., 1971).

The intraocular portion of the optic nerve begins where 1.2 to 2.0 million ganglion cell axons converge and turn 90° to start their exit from the eye. The intraocular optic nerve may be divided into three regions - the retinal, the choroidal and the scleral (Anderson and Hoyt, 1969; Hogan et al., 1971), as the nerve passes through each of these structures. An alternative is to divide the intraocular optic nerve into a prelaminar zone (equivalent to the retinal and choroidal region), the laminar zone (equivalent to the scleral region wherein the sclera is continuous with the lamina cribrosa) and the postlaminar or retrolaminar zone (equivalent to the scleral region beyond the lamina and extending to the posterior scleral opening where the optic nerve exits the eye) (Bron et al., 1997; Ritch et al., 1989). The subdivision of the intraocular optic nerve is illustrated in Figure 2-1. The intraocular optic nerve usually has a conical conformation (thinnest superiorly) when viewed in a meridional section, as the 'neural canal' usually widens in the scleral portion of

the nerve, although it may also be cylindrical if the ocular coats are in parallel or diamond-shaped (Hogan et al., 1971).

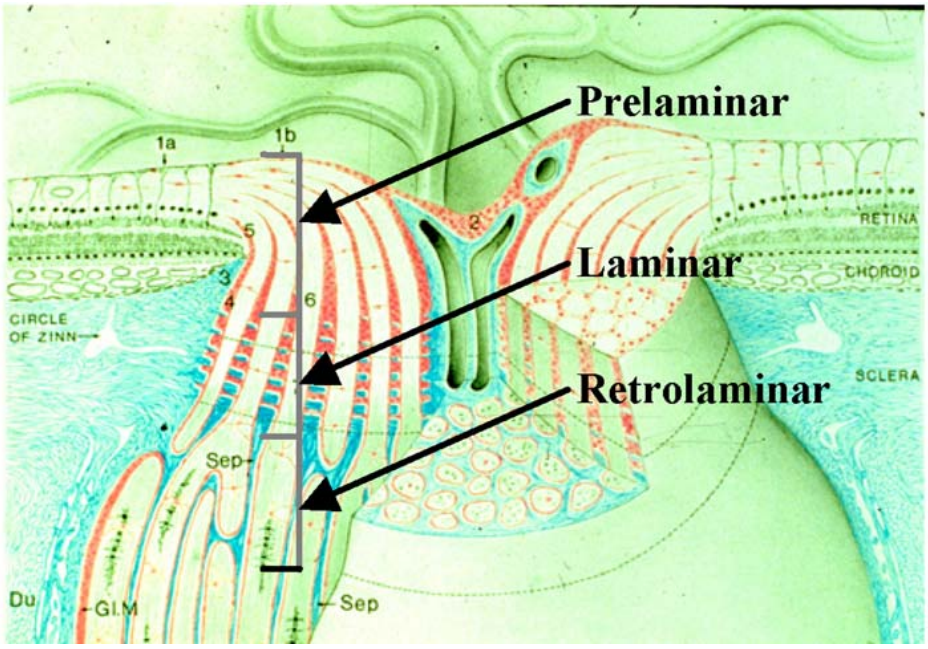

Figure 2-1. Subdivision of the intraocular optic nerve. Adapted from (Anderson and Hoyt, 1969)

Clinicians often use the terms optic nerve head (ONH) and optic disc *interchangeably* to refer to that part of the optic nerve that is visible by ophthalmoscopy. This refers to all tissues of the nerve that extend from the anterior surface of the disc to the lamina cribrosa; in other words the prelaminar zone or the retinal and choroidal portions of the nerve. The optic disc or ONH is a vertically oval structure containing a peripheral 'rim' composed primarily of neural tissue (as well as blood vessels and supporting cells) and, usually but not always, a more central depression known as the 'cup' that is devoid of neural tissue. The surface of the optic disc is in contact with the vitreous cavity. The outer-most limit of the optic disc is known as the disc margin, and clinicians identify this landmark ophthalmoscopically as a whitish, reflective 'halo' or crescent at the innermost periphery of the neuroretinal rim. Clinicians usually refer to this sign, and therefore to the disc margin, as 'Elschnig's ring'. Frequently, however, clinicians will use the term 'scleral

ring' to define the disc margin. As the anatomical basis of the clinical disc margin is not yet fully understood, this term is perhaps inaccurate. The disc margin represents an important landmark as it defines the extent to which neural tissue is confined to the ONH and as such is of central importance in defining the size of the ONH. It is also a key landmark in the quantification of structural parameters used in ONH imaging. A proportion of the experimental work contained within this thesis will explore the anatomy of the clinical disc margin.

2.1.2 Ultrastructure of the ONH

The inner limiting membrane of the retina, which is located on the vitreal surface of the retina, forms a continuum with the inner limiting membrane of Elschnig, which begins at the disc margin and is the glial layer covering the surface of the optic disc. The inner limiting membrane of Elschnig is derived from astrocytes and is also continuous with the perivascular glia surrounding the central retinal vessels as they emerge onto the disc surface. Where there is a deep physiological cup, the inner limiting membrane of Elschnig and the perivascular glia and connective tissues may be thickened to form the meniscus of Kuhnt (Hogan et al., 1971).

The principal structural support for nerve fibres as they turn 90° into the retinal and choroidal portions of the intraocular nerve is supplied by specialised astrocytes known as spider cells. The collagenous border tissue of Elschnig separates the choroid from neural tissue. This is an extension of scleral connective tissue from the pial-scleral junction; it is not uniform throughout the circumference of the disc, frequently being thickest at the temporal margin of the disc. Inferior to this, the scleral portion of the nerve is lined by a layer of astrocytes known as the border tissue of Jacoby. Occasionally, this layer can extend forward beyond the choroid to separate the intraocular nerve from the inner retinal layers whereby it is known as the intermediary tissue of Kuhnt. The proportion of glial tissue in the prelaminar optic nerve increases from 5% at the surface of the disc to 23% just anterior to the lamina cribrosa, with a corresponding decrease in axonal area (Minckler et al., 1976).

As the optic nerve axons approach the disc margin, they become separated into fascicles (bundles) by neuroglial cells at right angles to the fascicles. These neuroglial cells are part of a

three-dimensional (3D) network of astrocytes surrounding the fascicles that begins at the retinal edge and extends through the lamina cribrosa (Hogan et al., 1971).

2.1.3 Lamina Cribrosa

The lamina cribrosa (LC) is effectively a connective tissue 'scaffold' that anchors the bundles of optic nerve axons to each other and to the walls of the scleral canal. Along with the peripapillary sclera that surrounds the intraocular optic nerve, the LC represents the chief load-bearing tissue of the ONH (Burgoyne et al., 2005).

The LC is formed by an extension of collagen bundles and elastic fibres commencing from the inner two thirds of the sclera and spanning across the optic nerve canal. These bundles of collagen and elastic fibres intersect at various angles to form a 'sieve' (Hogan et al., 1971). The openings in this sieve-like structure are traversed by the optic nerve fascicles. Some of these collagen and elastic fibers will not completely span the optic nerve, instead joining the connective tissue surrounding the central retinal vessels. The connective tissue bundles, as they traverse the optic nerve canal, form a series of 10 or so horizontal cribriform plates (Anderson, 1969; Emery et al., 1974; Radius and Gonzales, 1981). The laminar beams that make up the cribriform plates are made up of collagens type I, II, IV, V, VI, as well as elastic fibres, laminin and fibronectin (Hernandez et al., 1990; Hernandez et al., 1987).

The openings in the cribriform plate, through which the optic nerve fascicles pass, are called laminar 'pores'. There are 500 to 600 such pores in human optic nerves (Ogden et al., 1988). The number of pores increases from the anterior to the posterior LC and as a result the pores are not vertically aligned in successive cribriform plates (Emery et al., 1974; Ogden et al., 1988). The conventional view has been that axon bundles follow a relatively direct course through the lamina, passing through successive pores, alongside their neighbours to maintain a retinotopic arrangement in the retrolaminar region (Hoyt and Luis, 1962; Quigley and Addicks, 1981). The complex 3D microstructure of the LC has been recently examined using digital reconstructions of cadaveric monkey optic nerves (Roberts et al., 2009). A comparison between such a 3D digital

reconstruction of the LC with an electron micrograph of the LC following trypsin digest of a cadaveric ONH is illustrated in Figure 2-2.

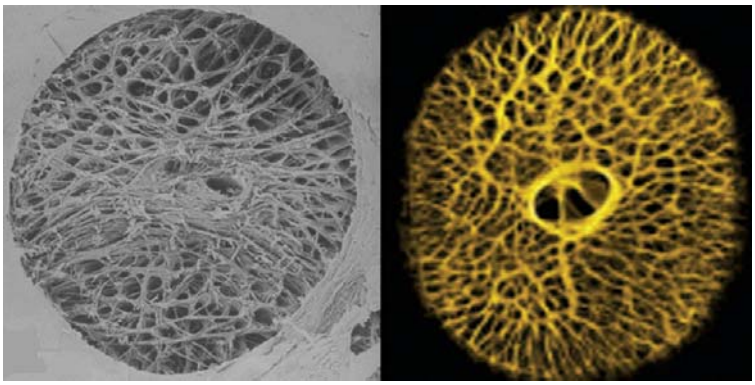

Figure 2-2. The complex 3D architecture of the connective tissue LC. On the left, an electron micrograph shows the arrangement of interconnecting laminar beams enclosing the laminar pores, following trypsin digest of a normal human cadaveric ONH. On the right, architecture of the LC is shown following a 3D digital reconstruction of a cadaveric normal monkey ONH. Adapted from (Quigley et al., 1990; Roberts et al., 2009)

Whilst a great deal of anterior to posterior 'directionality' was found in the neural spaces (i.e. the gaps between connective tissue beams), there was also substantial lateral interconnectivity of the neural tissue pore space. In other words, the lamina should not be regarded necessarily as a stack of perforated cribriform plates but more like a sponge through which pores channel from anterior to posterior with openings and connectivity existing between adjacent pores. Branching and subdivision of adjacent laminar pores has been also noted in human cadaveric eyes (Ogden et al., 1988; Quigley and Addicks, 1981). In an examination of two normal human cadaveric eyes, the majority of axons were seen to pass directly through the LC, although approximately 10% deviated to pass through adjacent spaces (Morgan et al., 1998), supporting the concept of neural space interconnectivity.

An 'hourglass' shaped distribution of pore size and connective tissue density has been described in both humans and monkeys whereby there are larger pore spaces (and thereby reduced

connective tissue density) at the superior and inferior quadrants as compared to the nasal and temporal quadrants (Dandona et al., 1990; Jonas et al., 1991; Ogden et al., 1988; Quigley and Addicks, 1981; Radius, 1981; Radius and Gonzales, 1981).

Astrocytes in the LC form a thin mantle that separates the nerve bundles from the laminar connective tissue and from the connective tissues around the central retinal vessels (Hogan et al., 1971). The astrocytes also separate the nerve from scleral collagen at the edge of the scleral canal. Capillaries, resembling those found in the sclera, course through the connective tissue of the lamina where they have thin adventitial connective tissue (Figure 2-3). Axonal nutrition and oxygenation within the LC are not fully understood and have not been measured directly; however they are presumably dependent upon the movement of oxygen and nutrients from laminar capillaries, through the laminar beam extracellular matrix, across the astrocyte basement membrane into the astrocyte, finally reaching the peripheral and central axons of each bundle via astrocyte processes.

The LC is not a ‘discrete’ connective tissue structure within the optic nerve, rather it happens to be the most prominent part of a continuous 3D cytoskeletal structure spanning the prelaminar, laminar and retrolaminar zones. An exhaustive light microscopic and scanning electron microscopic examination of the connective tissues of the human optic nerve has recently been undertaken, which was augmented by glial fibrillary acidic protein (GFAP) immunohistochemical staining to detect glial structures (Oyama et al., 2006). In this study, GFAP-positive cells were found to form columns (glial columns), which were located in the fibrous sheaths of collagen fibrils and elastic fibres. In the laminar region, these collagen fibrils and elastic fibres run transversely across the optic nerve canal to form the LC. A 3D glial architecture was found to extend into both the prelaminar and retrolaminar zones. In the prelaminar zone the GFAP-positive cells form vertical glial columns that serve to partition nerve fibres into small bundles. In the retrolaminar zone, where the GFAP-positive cells closely resembled fibrocytic astrocytes, the connective tissues of the LC connected with fibrous sheaths that accommodate nerve bundles as they enter the extraocular nerve. It has been suggested that the 3D glial network synthesises the additional connective tissue components within the scleral canal (thereby forming the LC) in order to

withstand the higher forces (due to intraocular pressure) experienced by the nerve in this region (Oyama et al., 2006; Roberts et al., 2009). The way connective tissues respond to stress is a key component of biomechanics and this will be discussed in more detail in a later section (section 2.4).

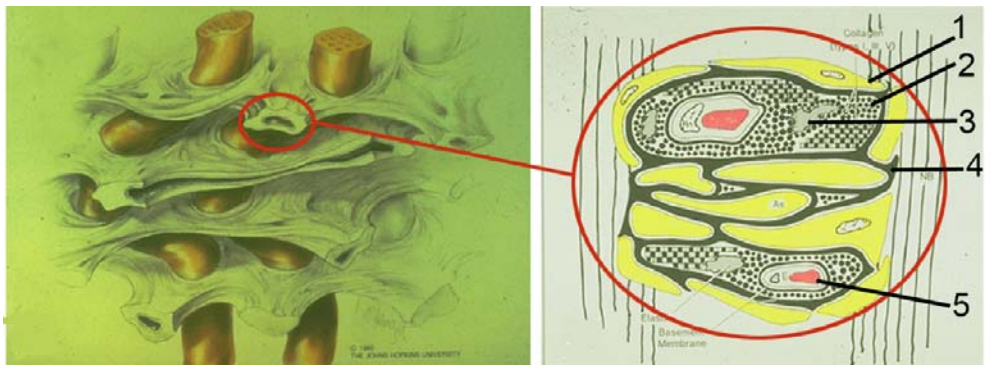

Figure 2-3. The arrangement of connective tissues, capillaries and astrocytes within the LC. On the left, the passage of nerve fibre bundles through a section of the lamina is shown. On the right, an area of the laminar beam has been magnified and its ultrastructure shown in cartoon form. The yellow cells (1) represent the astrocytes, the basement membranes (4) of which surround the laminar beams. Contained within each laminar beam are collagen (2) and elastin (3) fibrils and a capillary (5). Adapted from (Morrison et al., 1989b; Quigley, 1995)

2.1.4 Vascular Supply

The laminar zone receives its blood supply either directly from short posterior ciliary arteries or indirectly via the circle of Haller and Zinn (Hayreh, 2001). This circle is formed by anastamoses between posterior ciliary arteries and is located in the peripapillary sclera. It is present in approximately three quarters (Olver et al., 1990) of human eyes and gives off branches to the LC, to the peripapillary choroid and to the retrolaminar region (Olver et al., 1994). In vivo fluorescein angiographic studies have indicated that the blood supply to the prelaminar zone is derived from centripetal branches from the peripapillary choroid (Hayreh, 1975), and this observation has also

been made in histological studies of human and primate optic nerves (Anderson and Braverman, 1976). A number of post-mortem morphometric studies, however, appear to be in disagreement with this observation, suggesting that the anterior optic nerve receives minimal contribution from choriocapillaris and that the principal supply is derived from scleral short posterior ciliary arteries (Lieberman et al., 1976; Onda et al., 1995). At the anterior-most part of the ONH, at the surface nerve fibre layer, the blood supply is from retinal arterioles, although the posterior ciliary artery from the deeper prelaminar zone may also supply the temporal region (Hayreh, 1978).

2.1.5 Variability in Normal ONH Morphology

There is considerable variability in optic disc size within white populations, with disc area ranging from approximately 0.80 mm^2 to approximately 6.00 mm^2 (Bengtsson, 1976; Britton et al., 1987; Franceschetti and Bock, 1950; Jonas et al., 1988b). Optic disc size has been observed to follow a near Gaussian distribution and in the non-highly myopic white population the mean optic disc area is 2.5 mm^2 (Chihara and Chihara, 1994; Jonas et al., 2003; Ramrattan et al., 1999). Men have larger optic discs than women (Quigley et al., 1990; Varma et al., 1994). Optic discs are generally larger in black subjects, with average disc area being approximately 12% larger (Varma et al., 1994).

Refractive error has an important relationship with optic disc size, with significantly smaller discs occurring with greater than + 5.0 dioptres of hyperopic correction and significantly larger discs with greater than - 8.0 dioptres of myopic correction as compared to emmetropic eyes (Britton et al., 1987; Jonas et al., 1988d, e). There is a positive correlation between optic disc size and optic disc cups and neuroretinal rims (Jonas et al., 1988d; Xu et al., 2007). Large discs will have large cups and large rims, as well as a larger vertical 'cup to disc' ratio than smaller discs (Caprioli and Miller, 1987; Garway-Heath et al., 1998a; Jonas et al., 1988d). Cup to disc ratio varies from 0.0 to 0.9 in a normal white population (Jonas et al., 1988d). The degree of 'cupping' tends to be symmetrical between pairs of normal eyes, with a vertical cup to disc ratio difference of less than 0.2 being found in over 96% of normal subjects (Carpel and Engstrom, 1981; Jonas et al., 1988d). The depth of the cup tends to vary according to disc size, with larger discs having deeper

cups (Jonas and Budde, 2000). The neuroretinal rim follows a characteristic distribution in most discs, whereby it is thickest in the inferior region, followed by the superior, then the nasal and finally the temporal region where it is thinnest (Jonas et al., 1988c).

A common finding in the general population is the tilted disc, whereby the disc appears rotated and tilted along its axes. This is a form of developmental anomaly in which the optic nerve exits the eye at an oblique angle while being rotated along its antero-posterior axis. The orientation of the tilt is most commonly inferotemporal, with the superonasal portion of the disc appearing elevated and the inferotemporal portion appearing flat. The direction of the tilt may also be horizontal, vertical or along an oblique axis. Tilted optic discs may also demonstrate 'torsion' whereby the disc has rotated about the sagittal axis of the nerve. The normal optic disc is slightly longer in the vertical axis, with the longest diameter falling within 15° of the vertical meridian; an axis beyond 15° indicates that the disc is torted. Tilted discs can appear to be excessively rotated about the sagittal axis, resulting in the longest diameter falling beyond 30° of the vertical meridian (How et al., 2009; Vongphanit et al., 2002).

Titled discs occur in 0.4 - 3.5% of populations (How et al., 2009; Vongphanit et al., 2002; You et al., 2008). These figures may be confounded by whether or not highly myopic eyes (greater than -8 dioptres) were excluded. In the Singapore Study of Myopia, 44.9 % of 316 randomly selected schoolchildren were found to have tilted discs (Tong et al., 2007). In the Tanjong Pagar Study, there was a significant association between tilted discs and myopia as compared to normals (How et al., 2009). Tilted disc morphology is assumed to be non-progressive as the prevalence and severity of tilt does not increase with age (How et al., 2009; Vongphanit et al., 2002) although good longitudinal studies have yet to be published in this area.

Beyond the disc margin, regions of peripapillary atrophy are a common finding. This atrophy can be divided into a central beta zone and a peripheral alpha zone (Jonas, 2005). The alpha zone is characterised by irregular hypo and hyperpigmentation and thinning of the chorioretinal tissue layer. It is in contact with the retina at its outer limit and at its inner limit it is either in contact with a zone containing visible choroidal vessels and sclera (the beta zone) or if this is absent, the peripapillary scleral ring itself. Within the beta zone there is marked atrophy of the retinal pigment

epithelium (RPE) and choriocapillaris such that the large choroidal vessels and the sclera become visible. In normal eyes, both zones are most frequently found temporally, followed by inferotemporally and then superotemporally and most rarely nasally. Alpha zone atrophy is fairly ubiquitous in normal eyes whereas beta zone atrophy is only found in 15 - 20% of normal eyes (Jonas, 2005).

2.1.6 Ageing Changes

The existence of a clinically detectable (morphometric or ophthalmoscopic) age-related decline in neuroretinal rim thickness (or conversely, an increase in cupping) is controversial. Two longitudinal studies failed to identify a loss of rim area over time which exceeded the rim area variability gleaned from repeated optic disc stereophotographs (Airaksinen et al., 1992; Caprioli, 1994) and a further study, using optic disc photographs from the Framingham study, found that measurement imprecision prevented the detection of an appreciable rate of rim loss (Moya et al., 1999). In a population-based study, an increase in cup diameter of 0.002 mm/year was reported in a series of monoscopic disc photographs from 2274 eyes (Bengtsson, 1980). By contrast, digital photogrammetric analysis of simultaneous stereoscopic pairs taken from 6378 eyes failed to identify a relationship between any optic disc variable and age (Varma et al., 1994). Using an early commercial confocal scanning laser ophthalmoscope (CSLO), neuroretinal rim area was found to be significantly smaller in elderly compared to younger subjects although there was a preponderance of small discs in the elderly group which may have confounded the results of that study (Tsai et al., 1992). Another study, also using the same device, failed to detect a relationship between age and rim area (Funk et al., 1989). An age-related neuroretinal rim area decline of 0.28 - 0.39% per year has been reported using computer assisted planimetry of optic disc photographs and CSLO images (Garway-Heath et al., 1997). These results concur with a more recent study in which a neuroretinal rim loss rate of 0.36% per year was detected after 10 years of follow-up in 42 control eyes assessed by digital planimetry of optic disc photographs (Laemmer et al., 2007). Most recently, a longitudinal study conducted using CSLO identified a global median rim loss of -0.07% per year in 54 control subjects followed for 7 years as compared to -0.42% per

year in 94 open angle glaucoma patients followed for 9 years (See et al., 2009). Interestingly, in that study a similar pattern of sectoral rim loss was identified between control and glaucoma eyes with highest rates of rim loss being noted in the inferotemporal sector.

There is a histopathological basis by which one might expect to detect a loss of neuroretinal rim clinically. A number of studies have documented a significant age-related loss of optic nerve fibres in normal human optic nerves (Balazsi et al., 1984; Jonas et al., 1992b; Mikelberg et al., 1989); in one further study that loss was not statistically significant (Repka and Quigley, 1989). In human eyes, the mean axon diameter increases with age, suggesting that there is a preferential loss of smaller axons with age (Mikelberg et al., 1989). An age-related decline in axon counts has also been found in normal monkey eyes (Morrison et al., 1990a; Sandell and Peters, 2001). Characteristic cytoplasmic inclusions develop in the astrocytes, oligodendrocytes and microglia with ageing of the normal monkey optic nerve (Sandell and Peters, 2002). The astrocytes hypertrophy to fill the spaces left by degenerated nerve fibers and they develop numerous glial filaments in their processes. Oligodendrocytes and microglia become more numerous with age, with the microglia being engorged with phagocytic debris; with greater loss of axons, the more active the microglia appear (Sandell and Peters, 2002).

Connective tissue changes are also apparent in the ageing normal human ONH, particularly within the LC. In a post mortem comparison between three premature infants and 6 adult eyes, interstitial collagen types I and III were found to be heavily distributed within laminar beams in the adult eyes, along with discrete heavy bands of elastin (Morrison et al., 1989a). In the neonates, there was far less interstitial collagen and the elastin bands within the beams tended to be less numerous and discrete. An age-related increase in laminar collagen types I, III and elastin has been observed by other researchers who additionally reported that collagen type IV coated the cribriform plates and this formed a fine filamentous network which increased in density with age as the cribriform plates expand (Hernandez et al., 1989).

The total LC collagen content increases from 24% in the first decade of life to 45% in the eighth decade, with the percentage of elastin increasing from 7% to 28% (Albon et al., 2000a). Such connective tissue changes associated with ageing will undoubtedly alter the biomechanical

behaviour of the ONH and may help to explain why the risk of glaucoma increases with ageing (section 2.4.2).

2.1.7 Comparison Between the Human and Monkey ONH

With the exception of a single highly myopic human eye, all of the work conducted in this PhD has been undertaken using monkey eyes, most commonly the rhesus macaque *(Macaca mulatta).* As it is hoped that this body of work should have translational impact into human clinical practice, in particular the diagnosis and monitoring of glaucoma, it is important to understand the similarities between the normal human and normal monkey ONH. The strengths and weaknesses of the non-human primate model of experimental glaucoma will be discussed in a later section (section 2.2.6).

From my experience working at the Devers Eye Institute (DEI) Optic Nerve Head Research Laboratory (ONHRL), it was my impression that, ophthalmoscopically, the optic disc of the normal rhesus macaque was very similar to that of the human. Anecdotally, at least, the exceptions to this observation were that the central retinal vessel trunk was frequently centrally sited, as opposed to nasally as in humans; optic disc tilt and peripapillary atrophy were not common findings; heavy pigmentation in the peripapillary region, at the disc margin and on the cup surface was common; the retinal nerve fiber layer (RNFL) tended to be very thick at the superior and inferior poles; there appeared to be a preponderence of Bergmeister's papillae in younger animals.

Jonas and Hayreh have formally conducted a review of the ophthalmoscopic appearance of 17 normal rhesus monkey optic discs (Jonas and Hayreh, 2000). In this study, they identified that the pattern of neuroretinal rim distribution followed the same broad pattern as in humans, with the thickest rim being in the inferior region, successively thinning through the superior, nasal and then the temporal rim. The monkey optic discs examined were generally more vertically oval than those of humans. An alpha (peripheral) zone of peripapillary atrophy was found in 14 of 17 eyes and this was largest in the temporal region, as with humans. A more central beta zone of

peripapillary atrophy was an infrequent finding, occurring in only 2 of 17 eyes, with a predilection for the temporal region.

One of the key reasons for using monkey eyes in this PhD, other than the aforementioned morphometric similarities between the human and monkey ONH, is the presence of a substantial connective tissue LC. In the mouse, which represents a popular animal glaucoma model, there is a complete absence of the LC (May and Lutjen-Drecoll, 2002), although a glial network does span the optic canal and may serve the same supportive role as the connective tissue lamina seen in primates.

Much of our understanding of the ultrastructure of the intraocular optic nerve and the LC has been made through the detailed examination of both human and monkey optic nerves examined in parallel (Anderson, 1969; Anderson and Hoyt, 1969). In his canonical work, Anderson reported the only distinct differences in the monkey ONH as being the presence of pigment cells in the laminar connective tissue sheets, the lack of a connective tissue border tissue of Elschnig and the fact that the connective tissue septae separating the nerve bundles were more delicate and narrower as compared to human optic nerves.

2.2 Glaucoma

2.2.1 Definition and Clinical Context

The term ‘glaucoma’ refers to a group of conditions in which the common clinical feature is the development of glaucomatous optic neuropathy (GON). In 2002, an international consensus panel published definitions of glaucoma, which specify that glaucoma requires at least one eye to have typical structural and functional deficits, in other words glaucomatous optic disc damage and visual field loss (Foster et al., 2002; Quigley and Broman, 2006). The development of GON is the result of the loss of the retinal ganglion cells (RGCs) and their neurons. The pathognomic signs of glaucoma - a loss of neuroretinal tissue at the optic disc rim (resulting in a focal or generalised increase in ‘cupping’) and thinning of the RNFL (resulting in focal or diffuse RNFL defects) result in visual field loss. If visual field loss is allowed to progress, it may impact upon the patient’s ability to function and quality of life.

The effect of glaucoma on visual function is the principal rationale why substantial research effort, including that described within this PhD, is directed towards the early detection of GON and to the understanding of the pathogenesis of GON. Glaucoma is the second most common cause of blindness worldwide. An estimated 79.6 million people worldwide are expected to have glaucoma by 2020 and among these 11.2 million will be bilaterally blind (Quigley and Broman, 2006). The prevalence of glaucoma in white subjects over 40 years of age in Europe varies from 1.1 - 2.5% (Anton et al., 2004; Bonomi et al., 1998; Coffey et al., 1993; Dielemans et al., 1994), with a much higher prevalence of 2.7 - 3.1% in black subjects over 40 in Africa (Buhrmann et al., 2000; Rotchford and Johnson, 2002; Rotchford et al., 2003). A peak prevalence of 7.0% has been reported for black subjects aged 40 - 84 years in Barbados (Leske et al., 1994). The prevalence of glaucoma is low before the age of 40 and increases exponentially with age (Leske, 2007).

The estimated direct cost of treating glaucoma (principally pharmacologically but also by surgery or laser) was estimated at £3.6 billion annually in the UK, with an additional indirect cost of £34.5 billion (Grainger and Hutchinson, 2003). Glaucoma is a major public health concern and its burden will reach increased levels as life expectancy in the UK continues to increase, as glaucoma is primarily a disease of the elderly. This concern is shared amongst all developed

countries although the burden is perhaps even greater in the developing world where access to healthcare is limited.

In the past, the definitions of glaucoma would usually include elevated intraocular pressure (IOP), as a causal relationship between high IOP and GON has been espoused, correctly, as far back as 1857 (von Graefe, 1857). Epidemiological surveys have established a mean population IOP of approximately 15 -16 mmHg (Armaly, 1965a; Bankes et al., 1968; Kahn et al., 1977; Klein et al., 1992); from this an upper limit of normal of 21 mmHg has been established, derived from this mean + 2 standard deviations. Such a 'cut-off' is not strictly valid as IOP is, in fact, not normally distributed, with an increasing right skew with age (Colton and Ederer, 1980). Indeed, more than 30% of subjects with GON and visual field loss have been found to have an IOP less than 21 mmHg (Sponsel, 1989). This has given rise to a clinical distinction between 'normal tension glaucoma' (NTG), where the untreated IOP is less than 21 mmHg, and 'high tension glaucoma' where the IOP is greater than 21 mmHg. Much debate exists as to whether these are separate clinical entities or are within the spectrum of the same disorder. There are some features, such as a history of vasospasm (Raynaud's phenomenon, migraine), increased frequency of optic disc haemorrhages and a more focal distribution of nerve loss (focal rim loss and focal RNFL defects) which indicate that the development of GON in NTG may be influenced by ONH vascular insufficiency. Given that reducing IOP remains the only proven method for retarding glaucomatous progression in both high tension glaucoma and NTG (CNTGS, 1998; Heijl et al., 2002), it seems likely that IOP plays a central role in the development of GON, regardless of magnitude.

The classification of the glaucoma is based on the presence or absence of an obstruction to aqueous outflow at the trabecular meshwork within the iridocorneal angle. Open angle glaucoma refers to the presence of glaucoma in the absence of significant iridotrabecular contact. Open angle glaucoma may be further subdivided into primary open angle glaucoma (POAG), which is by far the commonest form of glaucoma in white populations of European descent, and secondary open angle glaucoma. In the latter, an underlying cause for elevated IOP in the presence of an open iridocorneal angle is identifiable; the most important causes include

pseudoexfoliation, pigment dispersion syndrome, uveitis and steroid response. POAG refers to the presence of glaucoma in the context of an open iridocorneal angle (with or without elevated IOP) and no underlying secondary cause and is, therefore, a diagnosis of exclusion. Angle closure refers to situations where there is greater than 180° degrees of iridotrabecular contact; the iris can therefore block aqueous outflow leading to elevated IOP. In primary angle closure (PAC), the iridotrabecular contact is a consequence of a combination of anatomical features; peripheral iris thickness and conformation, anterior placement of the lens-iris diaphragm and pupil block. When GON is associated with PAC it is referred to as primary angle closure glaucoma (PACG) and this form of glaucoma has a much higher prevalence in South East Asia than in Europe. Secondary angle closure (and by extension, secondary angle closure glaucoma) is either caused by something in the posterior segment pushing the lens-iris diaphragm forward (most commonly the expansile intraocular gases used in vitreoretinal surgery) or by pathological changes in the iridocorneal angle causing closure of the angle (principal causes include fibrovascular closure as seen in rubeotic glaucoma and peripheral anterior synechial closure, usually seen following uveitis).

It is important to note that the optic disc and visual field changes are similar between both open angle and angle closure glaucoma, although there is perhaps a greater preponderance of diffuse visual field loss in PACG (Boland et al., 2008). In circumstances where patients suffer a very sudden acute attack of elevated IOP (acute PAC), it is possible for a much more diffuse optic atrophy to develop with a pale, non-excavated disc with visual loss. Such a neuropathy has more in keeping with an ischaemic aetiology (Douglas et al., 1975). In order for the work contained within this PhD to be broadly applicable to most forms of human glaucoma, it was important to identify an experimental model whereby chronic sustained IOP elevation was sufficient to result in the classic form of ‘excavated’ GON common to all forms of glaucoma whilst avoiding sudden extreme elevations of IOP which could result in the sort of ‘ischaemic’ neuropathy occasionally seen in acute PAC. The rationale for selecting the monkey model of experimental glaucoma (EG) is discussed in detail in a later section (section 2.2.6).

An exhaustive review of the clinical management of glaucoma is beyond the scope of this thesis, as the work contained herein pertains to the early detection and pathogenesis of glaucoma. In summary, though, the only recognised treatment for glaucoma - whether high tension or normal tension - is to lower the IOP. Furthermore, there is evidence to suggest that IOP-lowering reduces the risk of developing glaucoma in subjects with ocular hypertension, in whom there is high IOP but no evidence of glaucoma at presentation (Kass et al., 2002). The key importance of IOP in the management of glaucoma further strengthens the supposition that IOP plays a role in the development of GON, regardless of its magnitude. Two broad mechanisms - increasing the outflow of aqueous and reducing the production of aqueous - can achieve IOP lowering. Pharmacological agents (both eye drops and tablets) work by one, or in some cases, both of these mechanisms. Surgery for glaucoma invariably aims to increase aqueous outflow either by creating an artificial bypass to the trabecular drainage system (trabeculectomy or shunt devices) or by modifying the configuration of the iridocorneal angle (lens extraction surgery as performed in angle closure subjects). Laser treatments either increase outflow or, in the case of ciliary body ablation, reduce the production of aqueous.

2.2.2 Major Risk Factors

A description of the risk factors that predispose to the development of glaucoma is relevant to the work described in this thesis as these risk factors may, either directly or indirectly, give some indication as to the pathogenesis of glaucoma.

IOP - the role of raised IOP has already been mentioned in the previous section (section 2.2.1). In the Baltimore survey, 10.3% of individuals with an IOP of greater than 22 mmHg were found to have glaucoma (Sommer et al., 1991). The equivalent percentage for individuals with an IOP less than 21 mmHg was 1.2%. This equates to a relative risk of developing glaucoma 8.6 times higher in ocular hypertensive as compared to normotensive subjects. Furthermore, the magnitude of IOP is positively correlated with risk of glaucoma (Sommer et al., 1991) and the magnitude of IOP is associated with more severe visual field loss at presentation (Jay and Murdoch, 1993). Although it is well established that a significant proportion of glaucoma subjects, indeed over half in some

cross-sectional studies, have a normotensive IOP (less than 21 mmHg) at presentation (Dielemans et al., 1994; Leske et al., 2001; Sommer et al., 1991), the eye with the higher IOP in NTG subjects will have the more severe field loss (Cartwright and Anderson, 1988) and the magnitude of IOP is a risk factor for disease progression (Crichton et al., 1989; Orgul and Flammer, 1994).

Ageing - is a major risk factor for the development of glaucoma. The mean age of onset is typically after the age of 60 years and the frequency of occurrence increases with age (Leske et al., 2001; Mukesh et al., 2002). There is a potential confound to this observation, as some studies have identified a positive relationship between age and mean level of IOP (Bonomi et al., 1998; Carel et al., 1984; Klein et al., 1992; Mason et al., 1989; Wu and Leske, 1997). The Blue Mountains Eye Study, however, identified an exponential increase in the prevalence of glaucoma with increasing age but no significant age related increase in ocular hypertension (Mitchell et al., 1996). There is strong evidence from recent longitudinal studies that age is a significant baseline risk factor for glaucomatous progression (Gordon et al., 2002; Leske et al., 2003). In a study carried out using data from the Beaver Dam Eye Study, an increase in optic disc cupping with high IOP was more likely to be found in subjects over 75 years of age as compared to younger subjects with high IOP or subjects over 75 with lower IOP (Klein et al., 2006). The mechanism by which ageing might influence the development of GON has been intimated in a previous section (2.1.6), where there is a description of the connective tissue changes occurring at the LC with ageing. It is possible that these connective tissue changes (specifically an increase in collagen deposition) will affect the way the ONH responds to an IOP-mediated insult (Albon et al., 1995). A discussion centred on ONH biomechanics is included in a later section (section 2.4).

Myopia - an association between high myopia and glaucoma is also evident. POAG occurred two to three times more frequently in myopic eyes examined in the Blue Mountains Eye Study (Mitchell et al., 1999). A 60% increased likelihood of developing glaucoma was found in myopic subjects at baseline, after correcting for age and gender, in the Beaver Dam Eye Study (Wong et al., 2003). A number of clinic-based studies have also reported an association between high myopia and POAG (Mastropasqua et al., 1992; Perkins and Phelps, 1982; Wilson et al., 1987),

NTG (Leighton and Tomlinson, 1973; Perkins and Phelps, 1982) and ocular hypertension (David et al., 1985; Seddon et al., 1983). The Ocular Hypertension Treatment Study (OHTS), however, failed to identify a significant relationship between myopia at baseline and the development of POAG in ocular hypertensive subjects (Gordon et al., 2002).

One potential confounding influence is the fact that myopic eyes tend to have larger optic discs, and as such will have larger cup to disc ratios. It is possible that, at least in some population-based studies, there is some detection-bias with myopic eyes being more likely to be flagged as glaucomatous because they have increased cupping. Furthermore, it is perhaps easier to detect glaucomatous changes in a larger myopic disc where the cup is large as opposed to a small disc in which the cup is usually much smaller (or perhaps absent) in which circumstance the signs of glaucomatous damage may be subtler. In myopia, the axial length of the eye is increased and it is likely that, as with ageing, there are connective tissue changes at the ONH and peripapillary sclera that may influence how the nerve responds to IOP. This may, in part, explain the predisposition of myopic ONHs to develop glaucoma damage.

Central corneal thickness (CCT) - it has long been understood that CCT influences measurement of IOP, whether using non-contact tonometry (the 'air-puff' technique used in the majority of UK optometric practices) or Goldmann applanation tonometry (as used in hospital eye clinics). In both circumstances, measurement of IOP requires flattening of the cornea; with a thicker central cornea the force required to do so is greater, predisposing to an over-reading of IOP, whereas less force is required to flatten a thin central cornea resulting in an under-reading of IOP (Ehlers, 1970; Li et al., 2004; Shimmyo et al., 2003). The results of OHTS have indicated that a thin CCT is one of the strongest risk factors for conversion to glaucoma in ocular hypertensive subjects; furthermore, this risk is over and above what might be expected through measurement error alone (Gordon et al., 2002). This finding was confirmed independently in the European Glaucoma Prevention Study (EGPS) and the combined OHTS/EGPS risk model features CCT as a major component of glaucoma risk (Gordon et al., 2007; Miglior et al., 2007; Pfeiffer et al., 2007). Numerous investigators have now explored the role of CCT in patients with existing glaucoma

and in general have found that CCT has a significant impact in these patients (Congdon et al., 2006; Herndon et al., 2004; Hong et al., 2007; Jonas et al., 2005).

Randomised controlled trials have yet to confirm the role of CCT in established glaucoma as convincingly as in ocular hypertension. EMGT initially found no relationship between CCT and either incident glaucoma or disease progression although with longer follow-up a modest relationship was found between CCT and progression but only in subjects with high IOPs (Leske et al., 2007).

One explanation for a relationship between thin CCT and glaucoma is the possibility that patients with higher IOPs are perhaps treated more aggressively with IOP-lowering treatment than those with lower IOPs and thinner corneas. As such, progression may be more likely to occur in those with thinner corneas. An indication, though, that CCT exerts an influence over glaucomatous progression that is not just tonometry-related is the fact that a relationship, albeit modest, was found in the EMGT, a study in which tonometry played no part in recruitment or treatment (Brandt, 2007; Leske et al., 2007).

A tantalising explanation is the possibility that CCT may in some way be a surrogate marker for the connective tissue behaviour of the peripapillary sclera and LC. After all, the cornea contains the same biological building block (collagen), encoded by the same genes, as found in the connective tissues in and around the ONH. The cornea, sclera and LC effectively form a continuous coat around the globe. It should be noted, however, that CCT alone cannot be used to determine the biomechanical behaviour of the cornea (see section 2.4.1 for a description of the relationships between structural stiffness, 3D geometry and material properties) and so any potential link to the biomechanical behaviour of the remote connective tissues of the ONH remains speculative. Studies that have tried to link CCT with movement of the ONH surface (assumed to be a proxy for LC movement) following IOP-lowering have met with equivocal results (Lesk et al., 2006; Nicolela et al., 2006).

Family history - heredity has a role in both the occurrence and the severity of open angle glaucoma, with the likelihood of developing the disorder 10 times higher in people with an affected first degree relative (Wolfs et al., 1998). Mutations in multiple genes and genomic

regions contribute to open angle glaucoma (Wiggs, 2007), or may be associated with the development of pseudoexfoliation, a condition with a high risk of developing secondary open angle glaucoma (Grodum et al., 2005; Thorleifsson et al., 2007). The higher prevalence and severity of glaucoma in people of African origin as compared with European or Asian people is perhaps further evidence of the hereditability of glaucoma (Racette et al., 2003; Tielsch et al., 1991). It should be noted that limited access to healthcare may influence the severity of glaucoma in both black populations in the developing world and also, for socio-economic reasons, in the developed world. A detailed account of the genetics of glaucoma and the influence of ethnicity is beyond the scope of this thesis.

2.2.3 Ophthalmoscopic and Morphometric Features

Careful planimetric examination of optic disc stereophotographs has established a widely accepted sequence of sectoral rim loss in glaucoma (whether focal or diffuse loss) - specifically the inferotemporal, followed by the superotemporal, then the temporal, inferonasal, and superonasal sectors (Airaksinen et al., 1992; Jonas et al., 1993; Tuulonen and Airaksinen, 1991). The nasal sector is regarded as the final neuroretinal remnant in advanced glaucoma, corresponding to the preservation of a temporal island of vision, although it is possible that rim loss in the nasal region may be underestimated clinically because of the higher proportion of blood vessels as compared to the temporal sectors (Strouthidis et al., 2009a).

A number of characteristic glaucomatous optic disc appearances have been categorized and are illustrated in figure 2-4 (Nicolela and Drance, 1996; Nicolela et al., 2003; Spaeth, 1994; Spaeth et al., 1976).

In the Type 1 disc (focal glaucomatous disc) localised neuroretinal rim loss occurs preferentially at the superior and inferior poles (Caprioli and Spaeth, 1985; Hitchings and Spaeth, 1976; Kirsch and Anderson, 1973). It is possible that focal rim loss is easier to detect in these regions as this is where the rim is broadest and generally there is an absence of blood vessels. Where a focal notch extends to the edge of the disc, a ‘sharpening’ of the rim is observed. A deep notch, extending to the edge of the disc may acquire a grey colour in its depth and is described as an

‘acquired disc pit.’ This is distinct from congenital disc pits that are usually located temporally and are associated with accumulation of subretinal fluid. Focal rim loss progresses by notch area enlargement, deepening and sharpening of the polar edge and eventually leading to narrowing and loss of neuroretinal rim.

Type 2 (myopic glaucomatous) optic discs are characteristically tilted, shallow and have a myopic temporal crescent of peripapillary atrophy. These discs typically demonstrate glaucoma damage in the form of superior and inferior rim narrowing (Nicolela et al., 1996b).

Type 3 (senile sclerotic or atrophic glaucomatous) optic discs are characterised by diffuse rim loss resulting in rim narrowing and a ‘moth-eaten’ pattern of rim loss (Geijssen and Greve, 1987). A complete ring of peripapillary atrophy is usually present in such discs. Rim loss is characterised by a gentle sloping, shallow cupping leading to a central pale area of the cup, a process known as ‘saucerisation’ of the disc.

The final category of glaucomatous disc is Type 4, which is typified by generalised enlargement of the optic disc cup. These discs possess enlarged round cups without focal rim loss and healthy-looking residual rim tissue; this has been reported as the most frequently encountered glaucomatous disc appearance (Pederson and Anderson, 1980), although anectdotally this has not been my experience in clinical practice. Concentric atrophy of the neuroretinal rim occurs whereby the rim narrows in a concentric, circular fashion with the cup enlarging in an inferotemporal, superotemporal or horizontal direction (Portney, 1976; Spaeth et al., 1976).

Deepening of the cup occurs in most forms of glaucoma and is due to a combination of neuroretinal rim loss and a remodeling of the connective tissue architecture, resulting in a posterior movement of the LC. Loss of the prelaminar neural tissue in advanced glaucoma results in the laminar pores becoming visible (Read and Spaeth, 1974). The characteristic ‘bean pot cupping’ of end stage glaucoma occurs when the cup enlarges to form a bowl behind the scleral opening of the ONH (Hitchings and Spaeth, 1976; Spaeth et al., 1976).

A number of vascular changes may be observed which is invariably a consequence of the loss of surrounding neuroretinal tissue or of connective tissue remodelling. As the cup progressively enlarges, the main trunk of central retinal vessels may migrate towards the nasal edge of the

disc, although nasal location of these vessels is frequently a finding in physiologically cupped discs. Loss of rim tissue may cause a vessel to appear exposed or ‘bared’ or to ‘bayonette’ as it courses up a steep cup slope or undermined rim.

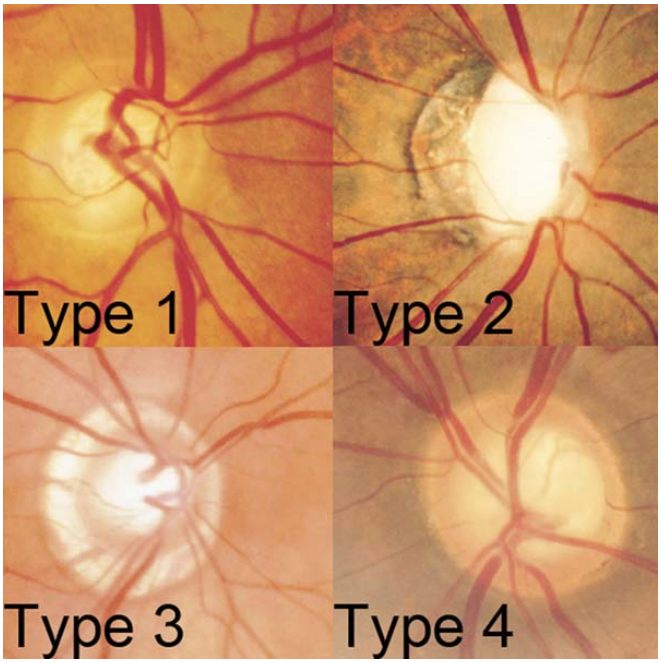

Figure 2-4. Ophthalmoscopic appearances of the four patterns of glaucomatous optic disc damage. In type 1, focal thinning is seen in the superotemporal and inferotemporal neuroretinal rim; in type 2, the disc is tilted and has a large temporal crescent of peripapillary atrophy with thinning of the superior and inferior rim; in type 3, the disc has a shallow cup with gently sloping sides and a concentric ring of peripapillary atrophy; in type 4, the cup is uniformally enlarged and there is no localised rim loss. Adapted from (Broadway et al., 1999)

Alpha and beta zones of peripapillary atrophy are both significantly larger in eyes with glaucomatous optic nerve damage than in normal eyes and beta zone atrophy occurs more frequently in glaucomatous eyes than normal eyes. The location of peripapillary atrophy is spatially related to neuroretinal rim loss being larger in the sector with the more marked neuroretinal rim loss (Jonas et al., 1992a; Jonas and Naumann, 1989). Some studies have

suggested that increasing peripapillary atrophy may be indicative, or predictive, of progressive glaucoma (Rockwood and Anderson, 1988; Tezel et al., 1997a; Tezel et al., 1997b; Uchida et al., 1998). A large beta zone and small neuroretinal rim have been identified as significant risk factors for progression of visual loss in ocular hypertensive and POAG patients (Jonas et al., 2004). When optic disc variables are ranked for their utility in detecting GON, peripapillary atrophy is a second order variable, being less useful than parameters based on the neuroretinal rim (Jonas, 2005). Peripapillary atrophy is perhaps useful in distinguishing glaucoma from other forms of optic atrophy (particularly arteritic anterior ischaemic optic neuropathy) where regions of peripapillary atrophy do not enlarge.

Optic disc haemorrhages have long been known to be associated with glaucoma (Bjerrum, 1889) but their significance in terms of risk of glaucoma progression was not appreciated until more recently (Drance et al., 1977). Disc haemorrhages occurring in POAG are usually located on or close to the disc and are most frequently seen at the poles (Sonnsjo et al., 2002). They usually occur in the prelaminar region of the ONH and in the superficial nerve fibre layer, appearing thin and radially ‘stretched’ when located at the disc margin (splinter haemorrhage) and round when occurring more centrally on the disc. With extensive extravasation of haemorrhage, a flame- or fan-shaped appearance may be noted. Although up to 70% of disc haemorrhages may occur in subjects with no evidence of glaucoma (Healey et al., 1998), the presence of a disc haemorrhage has been found to be a significant prognostic factor in glaucoma (Ishida et al., 2000), being associated with notching of rim tissue (Ahn and Park, 2002; Airaksinen and Tuulonen, 1984; Jonas and Xu, 1994) focal nerve fibre loss (Airaksinen et al., 1981; Sugiyama et al., 1997; Sugiyama et al., 1999) and progression of visual field loss (De Moraes et al., 2011; Rasker et al., 1997; Siegner and Netland, 1996). There is some evidence to suggest, however, that disc haemorrhages may be a consequence of an ongoing degenerative process at the ONH with disc haemorrhages being reported to occur in regions with pre-existent spatially consistent visual field loss (De Moraes et al., 2009).

Changes in the appearance of the RNFL occur in glaucoma subjects and their detection (either ophthalmoscopically or using photographs) may be enhanced using a red-free filter. These RNFL

changes include slit- and wedge-shaped defects (focal atrophy) as well as diffuse loss (Hoyt, 1976; Hoyt et al., 1973; Hoyt and Newman, 1972). RNFL loss has been detected up to five years before visual field loss in glaucoma patients and has been found to be at least as predictive of future damage as changes within the optic disc itself (Quigley et al., 1982; Sommer et al., 1977; Sommer et al., 1979a, b). RNFL loss is usually detected first in the superotemporal or inferotemporal arcuate regions, with a loss of the characteristic striate pattern and increased visibility of the retinal vessels (Quigley, 1986; Quigley and Sommer, 1987). Localised wedge-shaped defects commence at the disc margin and then fan out towards the retinal periphery and may be associated with rim notches in the adjacent region of the disc. With disease progression, localized wedge defects will increase in size and become more diffuse. To date, the application of optical coherence tomography (OCT) in glaucoma has been centred on the measurement of RNFL thickness (section 2.3.5).

2.2.4 Histopathological Changes

Gross post-mortem changes at the LC in glaucoma eyes (Figure 2-5) include a posterior bowing and vertical compression of the laminar sheets (Emery et al., 1974; Quigley et al., 1983). The laminar pores lose their round shape, becoming more elongated as glaucoma progresses (Emery et al., 1974). Histopathological studies of the glaucomatous ONH have demonstrated persistent glial activation, which is accompanied by increased synthesis of extracellular matrix (Hernandez et al., 1990; Morrison et al., 1990b; Quigley et al., 1991b; Varela and Hernandez, 1997). Astrocytes located within the cribriform plate have been found to migrate towards the laminar pores in glaucoma and this migration appears to be activated by elevated IOP in vitro (Tezel et al., 2001). These changes highlight the important role astrocyte activation has upon the remodelling of the ONH and the development of GON.

Axons of larger diameter have been identified as being more susceptible to glaucomatous damage, both in humans and in animal models (Quigley, 1998; Quigley et al., 1987), although there is the possibility that axonal shrinkage, preceding cell death, may account for the observed pattern of loss, rather than a selective process per se (Morgan et al., 2000). Although axons are

lost throughout the optic disc, they are preferentially (or rather, predominantly) lost in the superior and inferior sectors of the nerve (Figure 2-5) (Quigley et al., 1982; Quigley et al., 1983).

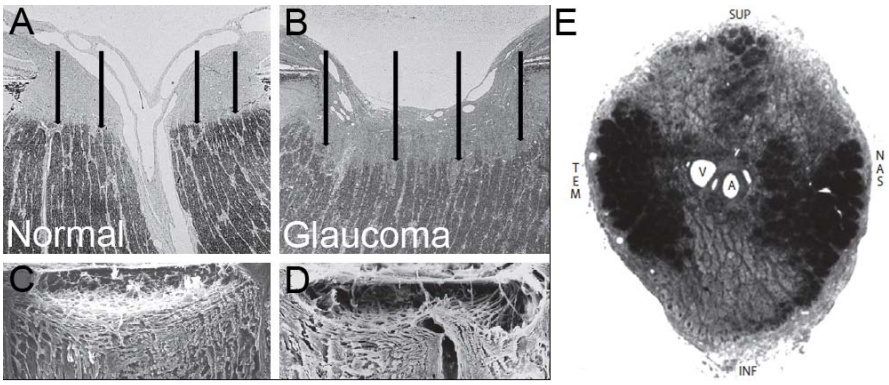

Figure 2-5. Pathological changes at the glaucomatous ONH. Panels A and B compare histological sections through a normal and glaucomatous ONH. The arrows highlight the position of the anterior LC surface; in the glaucomatous nerve there is a posterior displacement of the lamina, accompanied by a loss of the overlying neural tissue and an increase in the size of the cup. In panels C and D, the connective tissues of the ONH following trypsin digest are compared between normal and glaucoma. A fixed deformation, with compression and deep excavation can be seen in the glaucomatous lamina. In panel E, a section through an ONH demonstrates the selective loss of nerve fibres in glaucoma, with atrophy (light areas) occurring predominantly at the superior and inferior poles. Adapted from (Quigley, 2011)

Researchers at the ONHRL, where the experimental work for this PhD was undertaken, have pioneered a technique for digitally reconstructing ONH histological sections in 3D. This technique, known as 3D digital histomorphometry will be described in detail in the Materials and Methods section (section 3.8). 3D histomorphometry has been designed to map the complex 3D architecture of connective tissues (in particular the LC) within the ONH. Using this technique, my colleagues at the ONHRL have been able to identify connective tissue alterations in the ONH at

the earliest stages of a monkey model of EG (Burgoyne et al., 2004; Downs et al., 2007; Yang et al., 2007a; Yang et al., 2009a; Yang et al., 2007b; Yang et al., 2011).

The onset of what is perceived clinically as 'cupping' following modest to moderate chronic IOP elevation appears to be defined by posterior laminar deformation and neural canal expansion. These phenomena are maximal within the superotemporal and/or inferonasal quadrants and are accompanied by laminar thickening, axial elongation and outward peripapillary scleral bowing in the majority of eyes (Figure 2-6). Cupping in this early experimental model occurred in the context of an initial *thickening* of the prelaminar tissue, suggesting that early-onset cupping is due to laminar and not pre-laminar changes (Yang et al., 2007a; Yang et al., 2007b). Interestingly, there is some evidence to indicate that existing laminar beams become thicker and there is effective recruitment of retrolaminar septae into the load bearing LC structure (Roberts et al., 2009). Separate from this, the lamina appears to effectively migrate beyond its scleral insertion and into the pia in more severely affected eyes, with complete 'pialisation' of the laminar insertion occurring in some eyes. Laminar insertion into the pia has also been observed in normal human cadaver eyes (Sigal et al., 2010).

Given that such important connective tissue changes occur within the ONH, even at the earliest stages of glaucoma, it would be worthwhile to see whether such changes could be detectable in vivo using modern ONH imaging techniques. An ability to detect these changes in living human subjects may have important implications for the early detection and monitoring of glaucoma in clinical practice and also could assist in our ability to understand why an individual may be susceptible to glaucoma damage. These broad aspirations have driven much of the research undertaken for this PhD.

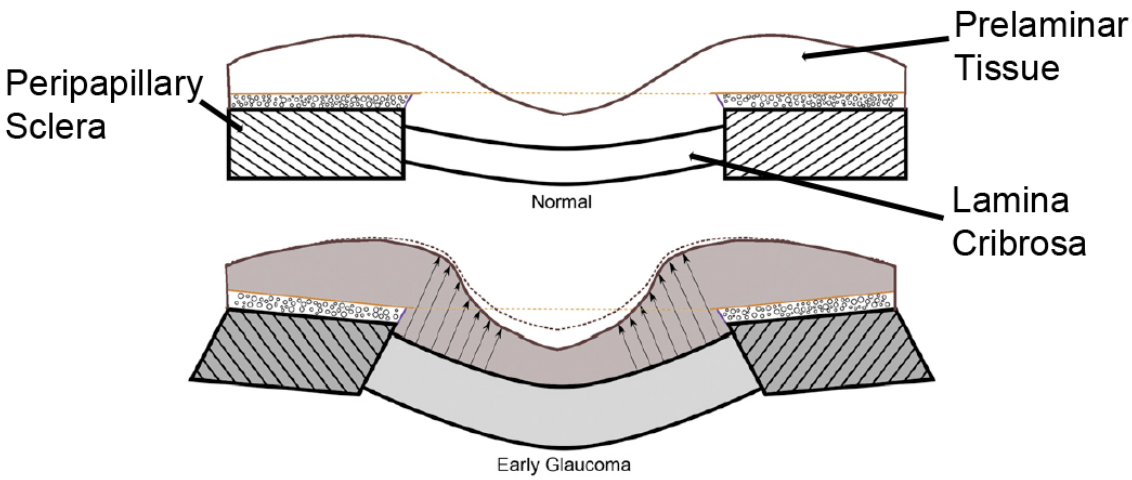

Figure 2-6. ONH changes seen in early EG in the monkey eye, as demonstrated by 3D histomorphometric reconstruction. Changes include expansion of the scleral canal opening, posterior displacement of the lamina and thickening of the prelaminar tissue and LC. Adapted from (Yang et al., 2007a)

2.2.5 Pathogenesis

The precise site of injury in glaucoma is not known, with pathophysiological changes having been found to occur in the bodies of RGCs (Garcia-Valenzuela et al., 1995; Quigley et al., 2000; Quigley et al., 1995; Weber et al., 1998), photoreceptors (Janssen et al., 1996; Nork et al., 2000; Panda and Jonas, 1992), the lateral geniculate body (Yucel et al., 2000; Yucel et al., 2001, 2003) and the visual cortex itself (Yucel et al., 2003). There is strong evidence to suggest, however, that the central pathophysiology is damage to the RGC axons at the LC (Bellezza et al., 2003b; Burgoyne et al., 2004; Gaasterland et al., 1978; Minckler et al., 1977; Quigley et al., 1981; Quigley and Green, 1979).

There are a number of observations that support the hypothesis that the changes driving RGC death are IOP-mediated and occur at the level of the LC. Axonal transport is known to be compromised at the level of the LC at normal levels of IOP (Ernest and Potts, 1968; Minckler, 1986) and is further compromised with acute and chronic elevation of IOP (Quigley and Anderson, 1976; Quigley and Anderson, 1977). Various detrimental effects lead to axonal injury

at the ONH and both anterograde and retrograde blockade of axonal transport occurs (Anderson and Hendrickson, 1974). Responses mediated by axonal injury likely transmit to the ganglion cell body in the retina and to the brain, explaining the observed changes in distal areas to the ONH as RGCs depend on neurotrophic support provided by the target neurons in the brain and by retinal interactions (Quigley, 2011). Interruption of axonal transport causes a reduction in trophic molecules. Apoptosis of RGCs commences after an abortive attempt at regeneration, with early axonal loss by Wallerian degeneration followed by somal death (Buckingham et al., 2008). Degeneration of RGCs may result in a toxic environment in which glutamate excitotoxicity (Hare et al., 2001), free radical generation (Ko et al., 2000) and immune responses (Bakalash et al., 2005) lead to secondary RGC damage.

Astrocytic glia that support ganglion cells and their axons are important in both protecting and damaging neurons with evidence that tumour necrosis factor alpha derived from astrocytes may by pathogenic (Nakazawa et al., 2006).

A number of researchers believe that vascular factors play a significant role in the development of GON. The vascular theory considers GON to be a consequence of insufficient blood supply to the ONH (and by extension, a reduction of oxidative and nutrient supply to the ganglion cell) either as a consequence of increased IOP or due to other risk factors that might reduce ocular blood flow. An example of this may be the clinically observed relationship between nocturnal 'dipping' of arterial blood pressure and disease progression in NTG (Graham and Drance, 1999; Graham et al., 1995; Hayreh et al., 1999; Hayreh et al., 1994). Further evidence is provided by several studies that have found an association between reduced ocular blood flow (measured indirectly) and glaucoma (Fontana et al., 1998b; Hitchings and Spaeth, 1977; Kerr et al., 1998, 2003; Michelson et al., 1996; Nicolela et al., 1996a; Rankin et al., 1995; Schmidt et al., 1998; Schwartz et al., 1977; Silver et al., 1989; Trew and Smith, 1991; Yamazaki et al., 1996). There is a suggestion that GON may be a consequence of vascular dysregulation/vasospasm (note the link between migraine and Raynaud's phenomenon with NTG), causing fluctuations in ocular blood flow that damage the ONH through reperfusion injury (Flammer et al., 2001).

In all likelihood, the conceptual separation of mechanical (IOP-related) and vascular pathophysiologies is artificial. The biomechanical theory hypothesises that glaucoma damage is a consequence of the interplay between IOP-mediated connective tissue damage, axonal compromise (which is both mechanical and vascular) and the physiological age of the tissues. The biomechanical theory of glaucoma will be discussed in detail in a later section (section 2.4.2).

2.2.6 Animal Models

The study of animals with experimental ocular hypertension and glaucoma is advantageous as the visual system, and indeed other body systems (the immune system, vascular function) are intact. As a result, physiological responses involving multiple cell types are more likely to resemble what occurs in the eye of a glaucoma patient than the responses seen in cell or tissue cultures. In other words, the responses to chronically elevated IOP in an animal model will more closely mimic those of a human, as they will include the responses of the trabecular meshwork cells, ciliary muscle cells, RGCs, the ONH glia and vasculature, optic nerve axons and retino-recipient brain neurons in several brain regions including the lateral geniculate nucleus and the superior colliculus (Kaufman and Barany, 1976; Weinreb et al., 2002; Yucel et al., 1999).
The general limitation of animal models is that animals are uncooperative and anaesthesia must be used to counter the discomfort (or indeed, pain) associated with experimental treatments. Choice of animal model should consider the size of the eye, the similarity of the studied ocular system to that of the human as well as practical considerations such as cost and availability.
The non-human primate (monkey) model of glaucoma has several advantages related to the fact that the eye has the closest general similarity to that of the human. There are similar aqueous humour dynamics and ONH cupping and axon loss are observed with elevated IOP. Disadvantages are that it is very expensive, animals are difficult to obtain, testing is difficult, and the animals are difficult to maintain and handle. There are also major concerns over this model on ethical and emotive grounds. Stringent administrative hurdles need to be overcome in order to obtain a license to undertake monkey experimentation in the UK.

The rodent eye may have less similar anatomy to that of the human eye but aqueous humour dynamics are similar and they will develop ONH cupping and axon loss with raised IOP. Rodents are also readily available at low cost and are easy to maintain and handle compared to non-human primates. Rodent models of glaucoma may either be genetic or secondary to experimental induction of ocular hypertension. Perhaps one of the best-characterised genetic models of glaucoma is the DBA/2J mouse strain, with features of pigment dispersion, iris transillumination, iris atrophy and anterior synechiae (Anderson et al., 2002). This results in aqueous outflow obstruction leading to ocular hypertension by the age of 9 months, accompanied by death of RGCs, optic nerve atrophy and cupping. Even though mice lack a connective tissue lamina (instead possessing a 'glial' network spanning the optic nerve canal), the fact that axon loss at the ONH appears to be a primary lesion in this model supports the previously discussed theories regarding the pathophysiology of human glaucoma (Jakobs et al., 2005). The DBA/2J strain is a glaucoma model that was discovered retrospectively; there are also transgenic and knockout models, which have been developed prospectively. Examples include the development of strains that express either mutated mouse or human myocilin, leading to a moderate elevation in IOP (Senatorov et al., 2006; Zhou et al., 2008) and a model that expresses a mutated version of the collagen type-I alpha 1 subunit, resulting in 5 mmHg IOP elevation as compared to controls at 36 weeks and progressive optic nerve axon loss (Mabuchi et al., 2004).

Elevated IOP can be experimentally induced (most commonly in rat models) in a number of ways. Lasering of the episcleral and limbal blood vessels and lasering of the trabecular meshwork (augmented by injected India Ink particles) has been used to reduce aqueous outflow and thereby elevate IOP (Gross et al., 2003; Ueda et al., 1998). Alternatively one may sclerose the trabecular meshwork by injecting hypertonic saline into the episcleral veins (Morrison et al., 1997). A more chronic IOP elevation may be induced by cauterising the episcleral veins (Shareef et al., 1995). Finally, one may elevate the IOP by injection of substances into the anterior chamber such as hyaluronic acid (Moreno et al., 2005) and latex microspheres (Urcola et al., 2006) that can block aqueous outflow.

The very close similarity between the human ONH and the monkey ONH has been discussed previously (section 2.1.7). The experimental optic neuropathy that develops in the monkey model of glaucoma is largely clinically indistinguishable from that seen in human glaucoma. In particular, the presence of a robust connective tissue LC, almost identical to that of a human, has influenced the adoption of the monkey model of EG at the ONHRL. Unlike the mouse, there is no spontaneous ocular hypertensive monkey model, at least not one that has been fully characterised. There are, anecdotally, two isolated colonies with spontaneous ocular hypertension but these are yet to be phenotyped or reported. EG in monkeys can be induced, as with rats, by intracameral injection of latex microspheres (Weber and Zelenak, 2001), gels (Kaufman et al., 1994), enzymes (Lessell and Kuwabara, 1969; Rauhut and Rohen, 1972; Zimmerman et al., 1967) and using topical steroids (Armaly, 1964, 1965b; Becker, 1965; Fingert et al., 2001). A far more consistent method, however, is by laser photocoagulation of the trabecular meshwork (Gaasterland and Kupfer, 1974; Wang et al., 1998); this is the experimental model used in this PhD. A full description of our method for inducing this model is included in Materials and Methods (section 3.6).

Another advantage of the monkey model, albeit not one that is available at the ONHRL, is the ability to train monkeys to perform standard automated perimetry. Visual field defects have been demonstrated in such trained glaucomatous monkeys (Harwerth et al., 1997) and these defects are similar to those in seen in humans with glaucoma (Harwerth et al., 1999; Harwerth et al., 2002). Functional testing can also be undertaken using electrodiagnostics (also in the rat); in particular multifocal electroretinogram, flash electroretinogram and visual evoked potential amplitude changes occur in monkey EG and components of each correlate highly with histological measures of glaucoma damage (Frishman et al., 2000; Frishman et al., 1996; Hare et al., 1999; Hood et al., 1999; Johnson et al., 1989; Viswanathan et al., 2000; Viswanathan et al., 1999). Functional testing using electrodiagnostic methods is available at the ONHRL but was not required for any of the experiments described in this thesis.

2.3 ONH Imaging In Glaucoma

2.3.1 Clinical Importance of Optic Disc Imaging

As glaucoma is, by definition, a progressive optic neuropathy, it is logical that an ability to document the appearance of the optic disc will be important in clinical glaucoma practice. Generally an ophthalmologist should examine the optic discs by stereoscopic indirect ophthalmoscopy, taking particular note of the optic disc dimensions, the spatial distribution of neuroretinal rim (looking for both focal and diffuse rim loss), the presence or absence of optic disc haemorrhages, the slope of the neuroretinal rim and the presence of RNFL thinning either as a diffuse loss or as a focal defect. The ophthalmologist should then document their findings in the case notes as a carefully annotated diagram, highlighting all of the relevant features (including disc size) as well as the type of condensing lens used for the examination, as this will affect the magnification of the image. The problem with this approach is that, as a system of documentation, it is highly subjective and prone to errors when different clinicians examine the patient longitudinally.

One method that can assist in the documentation of optic disc appearance is to augment the clinician's diagram with a photograph of the optic disc (either monoscopic or stereoscopic). Stereoscopic photographs may be acquired using a simultaneous system whereby two images of the disc are acquired at the same time, with a slight offset so as to generate a 3D effect when the two images are viewed using a stereoviewing lens system. An alternative approach is to acquire the two images consecutively, offsetting the camera between the two consecutive images. In either case, stereophotograph acquisition is technically quite challenging. This is the main method for documenting monkey optic disc appearance at the ONHRL. Red-free photography is a good method of picking up the RNFL pattern and this is a particularly important part of patient assessment and follow-up in certain parts of the world, particularly in Scandinavia. Once again, acquisition of RNFL photographs is technically challenging.

Interpreting optic disc photographs, either when trying to detect glaucomatous optic neuropathy, or when trying to detect progressive change in longitudinal photographs, is highly variable and error-prone, even amongst experienced 'expert' observers (Altangerel et al., 2005; Azuara-Blanco

et al., 2003; Jampel et al., 2009; Reus et al., 2010). Disc photographs have been used to define end-points in clinical trials, whereby an independent reading centre is used (Parrish et al., 2005; Zeyen et al., 2003). Optic disc photographs are not, however, a true diagnostic 'gold standard'. A reference standard means that all other tests (whether for glaucoma diagnosis, or for detection of progression) should be validated against it in order to assess their performance. Subjective interpretation of disc photographs is too variable for this to be the case. The absence of a gold standard test for either glaucoma diagnosis or detection of glaucomatous change remains a weakness in the assessment of all clinical tests in glaucoma.

Over the past twenty years, semi-automated quantitative ONH and RNFL imaging devices have been introduced into clinical practice. The role of these devices in the care of the glaucoma patient has yet to be fully finalised. Most experts agree that they have potential in two main areas. Firstly they can be used to assist the clinician in discriminating between a normal and a glaucomatous optic disc. Imaging devices contain normative databases from which classification algorithms are derived. The term 'classification' rather than 'diagnostic' is used as the latter could imply that the device was in possession of a degree of clinician-independent infallibility. Of course this can never be the case, as no 'diagnosis' should be made without the clinician weighing up the results of the imaging test, along with other tests (such as visual fields and CCT), family history, age and other features in the history. The second area in which imaging devices have great potential is in the monitoring of disease progression. In order for an imaging test to be useful for detecting glaucomatous progression it should firstly measure a parameter that is clinically meaningful in glaucoma. For example, we know that neuroretinal rim is lost in glaucoma, and that the RNFL thins. Secondly there needs be a good signal to noise ratio for that parameter; in other words the images acquired should be highly repeatable so that any change in the parameter of interest can be distinguished from measurement noise.

In this discussion, I will focus on two imaging modalities; confocal scanning laser ophthalmoscopy (CSLO) and optical coherence tomography (OCT). The reason for doing this is two-fold. Firstly CSLO and OCT are the two imaging techniques used in the experiments described in this thesis. Secondly, these two technologies are now the pre-eminent imaging techniques in glaucoma. In

the case of CSLO, as performed using the Heidelberg Retina Tomograph (HRT, Heidelberg Engineering, Heidelberg, Germany) and its derivatives, this pre-eminent position is largely by default rather than through any perceived technical or practical superiority over its competitors. The HRT has been available longer than any other device and has undergone only minimal hardware changes, along with incremental software improvements. Thus, the HRT has the largest body of scientific evidence to support its use, particularly for longitudinal analysis. There remain a large number of these devices in use in clinical practice. OCT technology, on the other hand, continues to develop at a rapid pace, undoubtedly fuelled by its central importance in the management of macular diseases. By contrast, its role in glaucoma imaging is a secondary concern to the developers of OCT imaging devices. However, as OCT imaging technology continues to improve it is likely that its glaucoma capabilities will become increasingly recognised and its utility in glaucoma clinical care will gain traction. A third technology - scanning laser polarimetry - has been shown to be useful in detecting RNFL loss in glaucoma and is popular amongst some clinicians. Monkeys at the ONHRL also undergo imaging by scanning laser polarimetry but this was not used in any of the experiments described in this thesis. Furthermore, scanning laser polarimetry as currently available (GDx and its derivatives, Carl Zeiss Meditec, Dublin, CA) risks becoming an underinvested and, eventually, obsolete technology as the manufacturer has also invested in OCT technology. 'Polarisation-sensitive' OCT is also on the horizon (section 2.3.6), which is likely to outperform and supersede the older technology. Despite their promise and availability, semi-automated quantitative imaging devices have yet to find a defined role in the care of the glaucoma patient. This can be demonstrated by the recent UK National Institute for Clinical Excellence (NICE) guidance for the management of ocular hypertension and glaucoma (NICE, 2009). The only identified role for imaging is in the documentation of disc appearance at baseline and whenever a subsequent change has been identified either ophthalmoscopically or by visual fields. In preparing the NICE guidance, there was felt to be insufficient evidence to justify a role for imaging technology either in the diagnosis or in the monitoring of progression. In terms of 'documentation' of disc appearance, the NICE guidance allowed disc photographs, HRT, OCT and GDx to be used with equal merit. Politically

speaking, a clearer case for the use of these devices could be defined if funding bodies were prepared to recognise their use in the definition of end-points in longitudinal glaucoma trials. From a clinical perspective, there might be a stronger argument for the adoption of novel imaging technology if research can demonstrate that it can be used to identify features in an individual eye that will predispose to future functional deficit. It was with this long-term 'translational' aim in mind that the experimentation contained within this PhD was undertaken.

2.3.2 CSLO - Basic Principles

The first landmark in the genesis of CSLO was the development of 'TV ophthalmoscopy', over fifty years ago (Ridley, 1950). This used the principle of indirect ophthalmoscopy to transfer an image of the fundus onto a television monitor. This was subsequently adapted to use low-powered laser light, instead of direct illumination, in a device called 'the flying spot TV ophthalmoscope' (Webb et al., 1980). The same group described the operating principle of scanning laser ophthalmoscopy, wherein a single point on the fundus is illuminated at any one time by a beam of laser light sweeping the fundus in a raster fashion (Mainster et al., 1982; Webb and Hughes, 1981). The scanning of fundal sections enables cumulative construction of a retinal image that can be viewed on a television monitor. The use of a focused laser enabled acquisition of high quality fundus images using less than 1/1000 of the light necessary to illuminate the fundus with conventional light ophthalmoscopy; scanning laser ophthalmoscopy requires irradiance of less than 70 $\mu W/cm^2$ compared with 100,000 $\mu W/cm^2$ for conventional indirect ophthalmoscopy (Webb and Hughes, 1981).

The confocal principle refers to the fact that light reflected from the fundus is received at a photodetector via an aperture (pinhole) that is confocal (having the same focal length) with the light source. Light from the region of interest (in this case, the ONH) is reflected back to the imaging device through the subject's pupil and directed to a photodetector, using a beam splitter. Prior to reaching the photodetector, the reflected light passes through the confocal pinhole, which allows only light reflected from the illuminated focal plane to pass to the detector. Light reflected from structures anterior and posterior to the focal plane are not focused through the pinhole; a

minimal amount of light from these structures reaches the detector. The signal to noise ratio is increased by the aperture, or pinhole, by excluding reflected light which is not from the point (and plane) of interest on the fundus.

HRT-II/3 uses a 675 nm diode laser as a light source. The emitted beam is scanned in a flat plane (plane of focus) in a horizontal (x-axis) and vertical direction (y-axis) roughly parallel to the optic disc surface. Multiple 'optical sections' of the optic disc at different depths can be collected by varying the location of the focal plane in depth (z-axis) by adjusting the focus and moving the confocal aperture (Girkin, 2005; Zinser, 2005). This generates a 3D image of the disc; a process called confocal scanning laser tomography. The field of view for the acquisition of these two-dimensional (2D) sections is set at 15° x 15° when using the HRT-II/3 (Heidelberg Engineering, 2006).

The HRT-II/3 acquires optical sections at 16 to 64 planes up to a scan depth of 4 mm. In terms of the practical aspects of image acquisition, the manufacturers suggest that pupil dilation is not required as a 1 mm pupil diameter is sufficient to acquire high quality images (Heidelberg Engineering, 2006). However, it is accepted that pupil dilation may allow a small improvement in image quality, particularly in patients with cataracts and small pupils (Zangwill et al., 1997). The manufacturers do not recommend using the HRT II/3 beyond ±6 diopters of spherical refractive error (Heidelberg Engineering, 2006). Each optical section is digitised with a transverse resolution of 384 x 384 pixels. The optical sections are aligned for horizontal and vertical shift, to compensate for any head or eye movements or blinking that may occur during image acquisition. A 'reflectivity profile' is generated for each aligned pixel by plotting light reflectivity as a function of distance along the z-axis. The position of the 'centre of gravity' for the reflectivity profile at each pixel - approximating to the peak reflectance - determines the relative topographical height value for the pixel. At this stage, pixel height is given relative to the focal plane of the eye (Chauhan et al., 2000). Each image acquisition generates over 147,000 pixel height measures, resulting in a 'topographic image' (single topography). A minimum of 3 single topographies is obtained in each imaging test (Weinreb et al., 1993); a mean topography and reflectance image is generated from these single topographies. In order to achieve this, horizontal, vertical and rotational alignment

are achieved using a correlation function performed on the reflectance images; depth and tilt alignment are made using the topography images (Chauhan et al., 2000).

The variability of pixel heights, across the 3 single topographies used to generate the mean topography, is calculated as the mean pixel height standard deviation (MPHSD); this value may be used as a proxy measure of image quality (Dreher et al., 1991). As the light source used by the HRT-II/3 is monochromatic, the reflectance image is also monochromatic. A colour coding according to signal intensity is applied by post-hoc image processing. Similarly, the topography image is colour-coded according to topographic height, with darker colours being more anterior.

In order to generate the quantification parameters for an individual optic disc image, the operator needs to draw a contour line onto the mean topography image. This is placed at the edge of the optic disc, at the disc margin. Visual cues observed in the mean reflectance image (more highly-reflective ring around the disc) and the mean topography image (an artifactual topographic dip) are useful in defining the limits of the disc, as the innermost margin of the reflective halo at the edge of the disc. Contour lines may be drawn freehand, or by using disc photographs or clinical examination to assist definition. Very little difference in inter-observer variability was detected In a study comparing contour lines drawn freehand and with the assistance of disc photographs (Watkins and Broadway, 2005). It may therefore be sufficient, in most circumstances, to base contour line placement on the HRT-generated images alone. However, use of photographic assistance may be of benefit in large or tilted discs where the true size of the optic disc may be underestimated using the HRT.

In addition to the placement of a contour line at the disc margin, a reference plane is required to generate stereometric parameters. A reference plane refers to an imaginary plane, below and parallel to the retinal surface, above which all structures within the contour line are referred to as ‘rim’ and below which are referred to as ‘cup’. The default reference plane available on the HRT Explorer platform is the ‘standard’ reference plane, which is located 50 µm posterior to the temporal disc margin. As the ‘anchoring’ landmark for this reference plane is liable to move posteriorly with progressive glaucoma it might be advantageous to use a reference plane anchored to a site in the retinal periphery whose height is liable to be less affected by worsening

glaucoma. An alternative reference plane, located 320 µm posterior to a reference ring located in the periphery of the HRT image, is also available on the HRT software. This has been shown to generate less variable stereometric parameters (in particular rim area) than the standard reference plane and therefore may be more appropriate for the monitoring of longitudinal change in such parameters (Strouthidis et al., 2006; Strouthidis et al., 2005a; Strouthidis et al., 2005b; Tan et al., 2003a).

2.3.3 CSLO - Clinical Applications in Glaucoma

Classification Algorithms - the current HRT 3 Explorer software features two classification algorithms, the Moorfields Regression Analysis (MRA) and the Glaucoma Probability Score (GPS), both of which are designed to assist the clinician in discriminating between a normal (healthy) ONH and an outside normal limits (presumed glaucomatous) ONH.

The MRA algorithm is based on the understanding that rim area varies with disc size, may decline with advancing age and may narrow in any sector of the disc in glaucoma. It was originally derived from measurements acquired from 112 healthy caucasian eyes. The normative database of the HRT has subsequently been expanded to include 733 healthy eyes of white subjects as well as some ethnic-specific databases. A logarithmic transformation of rim area, performed to normalise the variability distribution, is plotted against optic disc area to define the normal ranges. 95%, 99% and 99.9% prediction limits are generated from a linear regression analysis. A disc is defined as 'within normal limits' if rim area values are greater than the 95% prediction interval (represented by green ticks in the MRA printout). A disc is defined as 'borderline' if the rim area value lies between the 95% and 99.9% prediction interval (represented as yellow exclamation marks in the printout). Finally, a disc is defined as 'outside normal limits' if the rim area value falls below the 99.9% prediction interval (represented as red crosses in the printout).

When MRA was first described, a sensitivity of 84.3% and specificity of 96.3% were reported for discriminating normal subjects from early glaucoma cases (Wollstein et al., 1998). A subsequent study reported MRA sensitivity and specificity at 78% and 81%, respectively, when 'borderline' outcomes were regarded as test-positives (Ford et al., 2003). When 'borderline' outcomes were

classified as test negatives, MRA sensitivity was 58% with a specificity of 96%. Sensitivity of 74% and specificity of 94% have been reported by another group (Miglior et al., 2003). Very large and very small optic discs confound the MRA (Coops et al., 2006; Zangwill et al., 2007), with a greater proportion of false-positive 'outside normal limits' classifications in large discs. One should therefore interpret MRA in the context of disc size. One should also look out for atypical ONH morphology (eg tilting) as such nerves may fall outside the MRA normative range without necessarily being glaucomatous.

The GPS is based on an approach that discriminates normal and glaucomatous eyes using a mathematical model of ONH shape (Swindale et al., 2000). The model includes ten parameters that describe the morphology of the ONH; a least squares fitting-technique is used to approximate the model's morphological parameters to those of the nerve under examination. Discrimination between normal and glaucomatous discs is achieved by applying a linear discriminant function to seven of the aforementioned parameters.

The method has an advantage in that it is operator independent, not requiring contour line placement and being independent of reference plane position. The GPS does not, however, confer any advantage over the MRA in terms of sensitivity and specificity (Coops et al., 2006; Ferreras et al., 2007). There is a dependency on disc size for both MRA and GPS classification, with more false-positives identified in large discs and poorer sensitivity to identify glaucoma in small discs; this tendency is more pronounced for the GPS (Coops et al., 2006). As with MRA, GPS uses a system of green ticks, yellow exclamation marks and red crosses to denote within normal limits, borderline and outside normal limits, respectively.

Progression Algorithms - the HRT3 software features two progression algorithms, trend analysis and topographical change analysis (TCA). The latter is used at the ONHRL for longitudinal assessment of HRT images and in defining structural end-points in monkey EG.

Briefly, the trend analysis utilises graphs of change from baseline of a parameter over time. The parameter values are normalised against mean values in a normal eye and an eye with advanced glaucoma. The trend is then scaled between -1 (maximum deterioration) and +1 (maximum improvement). A major criticism of this technique is that interpretation of the trend is empirical and

a ‘rate’ of change cannot be generated. A recent comparison has been made between ‘subjective’ detection of progression using TCA, trend analysis, stereophotographs and by change in MRA classification, using images from the Diagnostic Innovations in Glaucoma Study (Vizzeri et al., 2009b). A moderate to good agreement was found between the 3 different HRT-based techniques, however a poor level of agreement was found between the HRT techniques and stereophotograph assessment. This suggests that HRT may be identifying different markers for change than stereophotographs.

TCA assesses progression by measuring changes in the topographical height of 4 x 4 groups of pixels (superpixels) within the HRT image. There are 96 x 96 superpixels in an HRT3 topography image. The key determinant in TCA is the variability in topographical height values within the superpixel over the two sets of three (single topography) images taken at baseline and at follow-up. The statistical method estimates the probability that an observed height difference at a superpixel between baseline and follow-up images occurred by chance alone. Where $p < 0.05$, the probability is low and the change is therefore unlikely to be due to chance. Where the variability is high between images, which typically occurs at the edge of the cup and along blood vessels, a much greater difference in height values is required to reach significance. TCA generates a ‘change probability map’ (Figure 2-7) - the reflectivity map is overlaid with colour-coded pixels, with red pixels representing significant height depression and green pixels representing significant elevation, compared to baseline (Chauhan et al., 2000).

In the current software, for two follow-up images, superpixels will be flagged as significant in the second follow-up if the change occurs in both images. For three follow-up images, superpixels are flagged as significant if the change occurs in all three follow-ups. Finally, for more than three follow-ups, the change needs to be observed in at least three of the last four images. For the current TCA algorithm, progression is defined as a cluster of 20 or more significantly depressed superpixels within the disc margin.

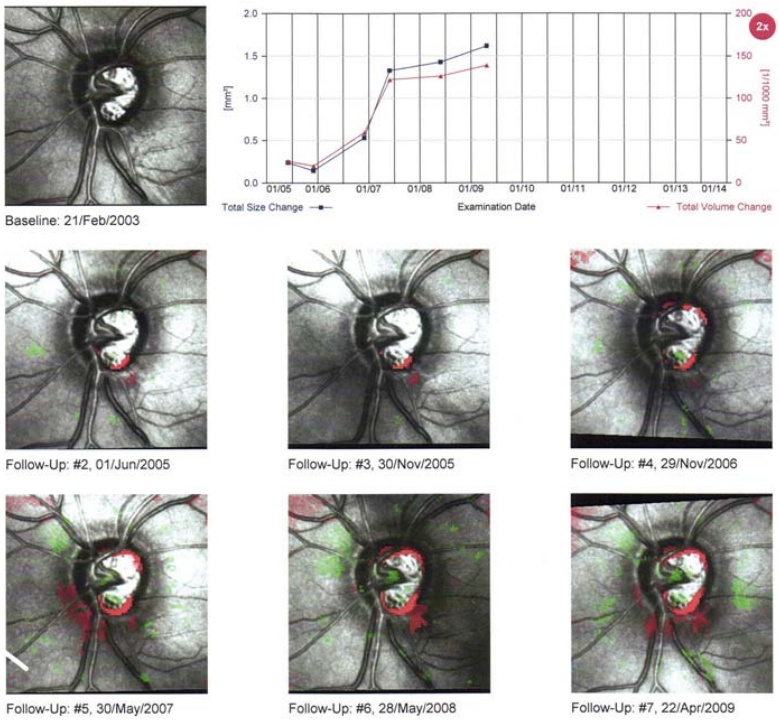

Figure 2-7. TCA demonstrating progression. In this representative example, inferotemporal surface height depression (red pixels within the disc margin) is seen at the first follow-up. This expands circumferentially and increases in depth over successive follow-up images. A similar pattern is seen at the superior pole, commencing at the third follow-up image. Surface height depression in the inferotemporal region outside of the disc corresponds to an enlarging nerve fibre layer defect. The graph in the top right shows the increase in size and volume of the defect over time

TCA is highly dependent on the quality of the baseline image; large changes may be observed if the baseline is of poorer quality than the follow-up images. It may therefore be advisable to acquire more than one set of topographies at the first visit, to ensure that more than one baseline mean topography is available for longitudinal analysis. It is also important to ensure that all images in the series are inspected for adequate alignment; a manual alignment facility is included in the software to correct for misalignments. If satisfactory alignment is not possible for an

individual mean topography, it may be preferable to exclude the image from the longitudinal analysis rather than risk generating misleading data.

TCA tends to identify more subjects as progressing than stereophotographic assessment (Kourkoutas et al., 2007). As previously mentioned, it is likely that TCA may be picking up structural changes that may not be detectable by stereophotographic examination. At the time of writing it is unclear whether TCA-detected surface height depression represents loss/thinning of prelaminar neural tissue or posterior displacement of the LC, or indeed a combination of both. The clinical significance of positive height changes (ie green superpixels) in areas of an otherwise progressing disc is also yet to be fully understood.

2.3.4 OCT - Basic Principles

OCT is often described as the optical corollary of ultrasound, given that the images generated (cross sectional or 3D) are formed by measuring the echo-time delay and magnitude of back-scattered or reflected light, as opposed to sound in the case of ultrasound. Interestingly, the key conceptual element in OCT is the use of interferometry - a method first described by Michelson and Morley in one of science's most famous 'failed' experiments (Michelson and Morley, 1887). In the late 19th century, there was a theory that light travelled through a medium, known as the 'luminiferous ether', just as sound passes through air or water. As the speed of light is so great, it was technically very difficult to demonstrate the presence or properties of this ether. Given that the Earth rotates at a certain speed, it was postulated that the flow of ether across the Earth should generate an ether wind. By analysing the return speed of light in different directions and at various different times, it was expected that the motion of the Earth relative to the ether could be measured. In the Michelson-Morley experiment, a single source of white light was split into two right-angled beams by being passed through a half-silvered mirror. The two beams then travelled down long arms, to be reflected back by small mirrors. The reflected beams then recombined on the far side of the splitter in an eyepiece, where interference patterns (or fringes) were generated based on the transit time of the light in the arms. If, as was expected, the Earth was travelling through ether, a beam reflected back and forth parallel to the ether flow would take longer than a

beam reflected perpendicular to the ether. This delay would cause a shift in the generated interference fringes when the beams recombined. In their experiment, Michelson and Morley were able to measure a small velocity but this was far too small to be considered as evidence of speed relative to the ether and indeed the measured speed was within the range of experimental error so could effectively be considered zero. Although the results of this experiment resulted in disproving the existence of the ether (thereby consigning the concept to the history books), the basic apparatus used in the experiment - the Michelson interferometer - is central to the set-up of all OCT devices.

The earliest measurements of one-dimensional axial information (effectively the optical equivalents of ultrasound A-scans) were demonstrated in the 80s (Fercher et al., 1988; Fujimoto et al., 1986) but it was not until the generation of cross sectional or 2D images (optical equivalents of ultrasound B-scans) that the potential for OCT in medical, in particular ophthalmic, imaging became realised (Huang et al., 1991). The original commercially available time domain OCT (TDOCT) devices (OCT versions 1, 2 and Stratus$_{OCT}$; all Carl Zeiss Meditec, Dublin, CA) each contained a fibre optic Michelson interferometer and used a near-infra red, low-coherence super-luminescent diode centred at a wavelength of 820 nm with a bandwidth of 25 nm as the light source. In TDOCT, the time of light delays reflected from the sample of interest (most usually the retina) are compared with time of light delays of the same beam reflected from a reference mirror at an adjustable distance (Figure 2-8). Interference occurs when the interferometer combines the reflected light from the sample arm and from the reference arm; the interference is detected and measured by a photodetector using low coherence interferometry. By altering the distance of the reference mirror, the distance travelled by each ‘echo’ (A-scan) reflected from the sample can be varied. In doing so, the delay information can be used to determine the longitudinal location of each reflection site. The light source is sweeped across the retina, generating a 2D map of reflection signals from within the microstructure of the tissue of interest. A series of post-hoc processing techniques, including alignment of A-scans to correct for eye movement and digital smoothing help to improve the signal to noise ratio (Jaffe and Caprioli, 2004).

TDOCT has an axial resolution of approximately 10 µm and acquires 2D optical B-scans at a speed of 400 Hz (400 A-scans/second); the scanning speed is, of course, limited by the speed at which the reference mirror can move (Drexler and Fujimoto, 2008; Gabriele et al., 2011). A significant advance, particularly in terms of acquisition speed, has been the adoption of Fourier domain OCT (FDOCT). In this technique, the entire optical echo signal is measured simultaneously rather than sequentially. The backscattered depth information is collected without the need to move a reference mirror (Figure 2-8).

This can be achieved in one of two ways. In the first method, which is usually referred to as spectral domain OCT (SDOCT), a broad bandwidth light source is used, the mirror is stationary and the interference pattern is split by a grating into its frequency components; all of these components are simultaneously detected using a spectrometer and a high speed couple charged device (CCD) camera system (de Boer et al., 2003; Leitgeb et al., 2000; Nassif et al., 2004; Wojtkowski et al., 2002; Wojtkowski et al., 2005). The depth information (intensity data) for each frequency component is obtained following a Fourier transformation. This method is employed by all of the current generation of commercially available high-resolution OCT devices. SDOCT has effectively replaced the older time domain system in the commercial setting.

The second method, usually referred to as swept-source OCT (SSOCT), uses a narrow bandwidth light source that is swept through a broad range of frequencies (using a ‘tunable’ laser) and then detected using a photodetector (Choma et al., 2005; Zhang et al., 2005a). As with SDOCT, the frequency data are converted to intensity data following a Fourier transform.

The upshot of these advances is that impressive acquisition speeds can be achieved; up to 300,000 A-scans/second for SDOCT (Potsaid et al., 2008) and 250,000 A-scans/second for SSOCT (Srinivasan et al., 2008). In practical terms, the fastest commercial SDOCT systems achieve a speed of 55,000 A-scans/second, with most systems achieving 27,000 A-scans/second. The speed of the system is governed by the read out rate of the CCD camera or the ‘sweep speed’ of the light source. The reason for the sharp decline in acquisition speed when comparing current clinical SDOCT devices with what can be achieved in research systems is largely down to limitations and costs of the CCD cameras used in those systems. Indeed, the

concept of Fourier domain detection has been known for a long time but development was held back by over a decade because of limitations in CCD technology (Fercher et al., 1995).

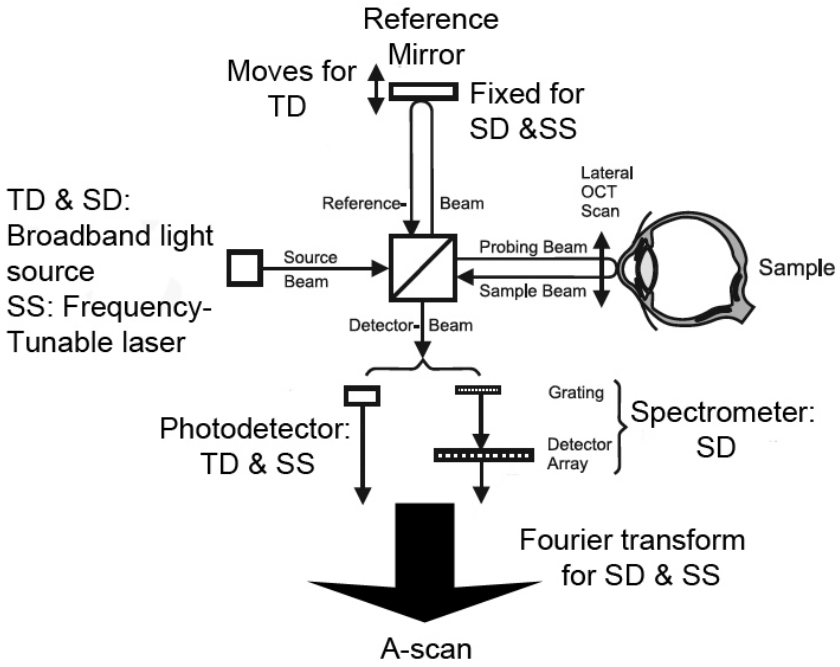

Figure 2-8. Schematic representation of the Michelson interferometer configurations used in TD, SD and SSOCT systems. Adapted from (Fercher, 2010)

Axial resolution, which is particularly important when trying to discriminate layered structures (as in the retina), is dependent upon the coherent length of the light source which is inversely proportional to the bandwidth of the light source (Drexler et al., 2001). In commercial SDOCT systems, axial (depth) resolution can be improved to 5 - 6 µm by employing a broad bandwidth light source with resultant improvement in structural definition. A drawback of camera-based SDOCT systems is that there is a drop-off in signal with increasing depth of scanning due to the finite pixel size of the CCD camera (Leitgeb et al., 2003; Yaqoob et al., 2005). Furthermore the Fourier transform effectively reduces the number of axial pixels by a factor of 2. One can improve the balance between axial resolution and depth measurement range (i.e. improve sensitivity and dynamic range as a function of depth) by reducing the camera pixel size but this is results in

increasing complexity, and thereby the cost, of the CCD array (Gabriele et al., 2011). Other factors that affect the balance between axial resolution and depth of scanning include limitations in spectrometer resolution, imperfect scaling and imperfect post-processing of the interference signal (Drexler and Fujimoto, 2008). One method that can improve structural definition is scan-averaging (either of multiple B-scans or at the level of A-scans for greater speed) to remove speckle noise and to improve the signal to noise ratio (Sakamoto et al., 2008).

Perhaps the most important advance associated with the higher acquisition speeds of SDOCT, particularly for the purposes of this PhD, is that it enables in vivo capture of high-resolution images in 3D. Higher speed acquisition allows dense raster scans consisting of multiple closely spaced B-scans to cover a volume of the retina, or indeed, the ONH. The effect is similar to the volumetric scanning possible with computerised tomography or magnetic resonance imaging, but with resolution at a microscopic scale. Through post-processing of these volume or 'cube' scans it is possible to generate a sequential run-through movie of adjacent B-scans through the volume and to generate tomograms at different cuts from which the scans were acquired. It is this latter feature that allows the generation of en face tomograms (sometimes referred to as C-mode scans). An OCT fundus image can directly be generated from 3D SDOCT data by summing the dataset along the axial direction, thereby generating a pixel brightness value for each axial scan position (Drexler and Fujimoto, 2008). An important advantage of this OCT fundus image is that it can be used to register individual OCT scans precisely and reproducibly with fundal features such as blood vessel position.

2.3.5 OCT - Clinical Applications in Glaucoma

Scanning protocols - in the last commercially available iteration of TDOCT, $STRATUS_{OCT}$, there were two basic glaucoma scanning protocols.

Firstly, one could acquire a radial scanning protocol, whereby a 6 radial B-scan pattern is centred either on the optic disc (4 mm) or at the macula (6 mm). For the disc scans, the edge of the disc is automatically detected as the termination of the RPE/choriocapillaris on each side of the scan and the disc contour is extrapolated from the resulting 12 edge points (Iliev et al., 2006). There is

a facility to manually adjust the placement of the disc edge. In a study of 49 eyes, 53% needed manual adjustment (Iliev et al., 2006). This is particularly problematic in regions of peripapillary atrophy so needs to be considered when examining glaucoma subjects longitudinally as the area of peripapillary atrophy may increase. The optic nerve scan is used to obtain cup area, disc area, cup diameter, disc diameter, rim area as well as cup to disc area ratio, horizontal and vertical cup to disc diameter ratios.

Secondly, a circumpapillary scan pattern, located at 3.4 mm around the centre of the optic disc, can be used to measure RNFL thickness. An automated segmentation algorithm detects the anterior and posterior margins of the band of reflectance representing the RNFL (Budenz et al., 2005; Budenz et al., 2008; Chauhan and Marshall, 1999; Hee et al., 1995). RNFL thickness around the disc is quantified and can be compared against a normative database.

Using the macular radial scan pattern, macular thickness is automatically segmented as the distance between the reflectance patterns representing the internal limiting membrane and the photoreceptor inner and outer segment junction.

Reproducibility - generally very good reproducibility has been reported for the $STRATUS_{OCT}$ in terms of RNFL thickness measurements (Budenz et al., 2005; Budenz et al., 2008; DeLeon Ortega et al., 2007; Paunescu et al., 2004). In 51 stable glaucoma patients, intra- and inter-visit mean RNFL thickness measurements achieved an intraclass correlation coefficient of 0.98 and 0.96, respectively, with a range of coefficients of variation of 3.8 to 5.2% and a test-retest value of 6.7 µm (Budenz et al., 2008). Furthermore, the repeatability of TDOCT RNFL measurements has been shown to be stable throughout all stages of glaucomatous visual field loss (Deleon-Ortega et al., 2006). In the same study, however, TDOCT ONH parameters were shown to have reduced repeatability with increasing severity of glaucomatous damage. This coupled to the fact that, in general, TDOCT ONH parameters are less reproducible than RNFL measurements (Carpineto et al., 2005; Paunescu et al., 2004), would indicate that caution is required if using these parameters to detect glaucoma progression.

RNFL thickness as measured by TDOCT may be influenced by a number of factors. Older age and increased axial length are both associated with thinner RNFL (Budenz et al., 2007; Hougaard

et al., 2006; Parikh et al., 2007; Savini et al., 2007). Larger discs are associated with thicker RNFL measurements (Budenz et al., 2007; Savini et al., 2007). This observation is most likely secondary to the fact that, in larger discs, the fixed (3.4 mm) diameter scan is effectively at a shorter distance from the edge of the disc, where RNFL is relatively thicker.

Good RNFL measurement reproducibility has been reported for each of the different commercial SDOCT devices. RNFL reproducibilities are either better or at least comparable to those of TDOCT (Leung et al., 2009; Schuman, 2008; Vizzeri et al., 2009a). The measurement variability of sectoral RNFL thickness is significantly lower for SDOCT (Leung et al., 2009; Schuman, 2008). RNFL measurements are also more reproducible when generated from a 3.4 mm 'virtual' circumpapillary scan interpolated from volumetric data as compared to those acquired using the standard TDOCT circular pattern scan (Kim et al., 2009). The Cirrus SDOCT (Carl Zeiss Meditec, Dublin, CA) provides higher intra-visit and inter-visit reproducibility than TDOCT in both normal and glaucoma eyes (Leung et al., 2009); furthermore there is no influence of pupil dilation upon these measurements (Savini et al., 2010). The improved repeatability most likely reflects the fact that the Cirrus RNFL protocol extracts data for the 3.4 mm circular scan once the centre of the disc is automatically identified. This removes the measurement variability that occurs in TDOCT through improper location of the scan circle (Gabriele et al., 2008). The Cirrus SDOCT also demonstrates high repeatability and inter-visit reproducibility in established glaucomatous eyes for both RNFL thickness measurements and also ONH parameters (Mwanza et al., 2010). Similar results have been observed with other devices (Garas et al., 2010; Gonzalez-Garcia et al., 2009). In general though, RNFL measurement reproducibility is lower (equivalent to that of time domain) where RNFL measurements are just acquired from the circular sweep scan and not following extraction from the 3D volumetric data (Nakatani et al., 2011). The observation that SDOCT has improved sectoral RNFL reproducibility is encouraging for early glaucoma detection as glaucoma may present with localised RNFL defects.

Diagnosis/Classification - several studies have demonstrated the performance of TDOCT in discriminating between normal and glaucomatous eyes (Bowd et al., 2000; Deleon-Ortega et al., 2006; Greaney et al., 2002; Jaffe and Caprioli, 2004; Medeiros et al., 2005; Schuman et al., 1995;

Williams et al., 2002; Zangwill et al., 2001). Comparisons between TDOCT, CSLO and scanning laser polarimetry have failed to identify a significant advantage of one device over another in terms of differentiating normal from glaucoma eyes within the same populations (Deleon-Ortega et al., 2006; Medeiros et al., 2004; Zangwill et al., 2001). In another study, a comparison was made between the RNFL, ONH and macular thickness parameters of the $STRATUS_{OCT}$; this found that RNFL thickness and ONH parameters had similar performance in differentiating between healthy and glaucomatous eyes and both outperformed the macular thickness parameters (Medeiros et al., 2005).

It is essential to appreciate that in all of these studies, performance was assessed using well-defined case controls with established repeatable glaucomatous visual field defects. Almost certainly, all imaging devices will perform far better in this setting than in a real clinic where phenotypes are less well defined and many patients are 'glaucoma suspect' or have pre-perimetric changes. The problem, of course, of assessing performance in these latter subjects is the lack of any gold standard reference against which glaucoma may be diagnosed.

A large number of studies have now assessed the 'diagnostic' capability of the currently available SDOCT devices, and most of these have made a comparison with the performance of TDOCT (Chang et al., 2009; Cho et al., 2011; Jeoung and Park, 2010; Leung et al., 2009; Moreno-Montanes et al., 2010; Park et al., 2009; Sehi et al., 2009; Sung et al., 2009). In all cases, SDOCT has been found to have a good diagnostic capability but in a large number, no statistically significant advantage over TDOCT was identified (Cho et al., 2011; Jeoung and Park, 2010; Leung et al., 2009; Moreno-Montanes et al., 2010; Park et al., 2009; Sehi et al., 2009). In an exception to this, SDOCT was found to have a higher sensitivity to detect 'outside normal limits' classifications in eyes with an established glaucomatous visual field defect (Sung et al., 2009). The authors speculated that this was due to higher scan resolution, more accurate data registration and also the fact that the constitution of the normative database differed between the SDOCT and TDOCT devices, with 20% Asian eyes included in the Cirrus database as compared to 3% in the $Stratus_{OCT}$.

The ability of the best-performing TDOCT and SDOCT parameters to detect localised defects in subjects with pre-perimetric glaucoma has been found to be equivalent (Jeoung and Park, 2010). One reason why SDOCT may fail to 'outperform' the diagnostic capabilities of TDOCT is because the subjects used in these studies already have advanced structural damage that ought to be detectable by either device. Discriminatory performance is likely to be improved using parameters obtained from 3D volumes.

It has long been theorised that macular thickness may serve as a surrogate marker for glaucoma diagnosis (Zeimer et al., 1998; Zeimer et al., 1996). This is because RGCs are multilayered (up to seven layers) and densest in the region of the macula; the macula contains approximately 50% of all RGCs (Curcio and Allen, 1990). The RTVue device (Optovue, Fremont, CA) contains software that can automatically segment the RNFL, the ganglion cell layer and the inner plexiform layer at the macula. These three layers make up the parameter known as the ganglion cell complex (GCC). In the RTVue device, GCC data are displayed as a thickness map with percentage loss analysed as a comparison to a normative database of 300 healthy eyes. GCC has been shown to have significantly higher diagnostic power than macular thickness as measured by SDOCT or TDOCT and the best performing GCC parameters have been found to be equivalent to mean RNFL thickness as measured by TDOCT (Tan et al., 2009). There is evidence to suggest that GCC thickness assessed by SDOCT has a comparable diagnostic capability with that of peripapillary RNFL thickness (Seong et al., 2010; Tan et al., 2009), although the role of macular GCC measurements in clinical glaucoma practice has yet to be elucidated.

Progression - There is very little evidence to highlight the usefulness (or otherwise) of longitudinal OCT imaging to detect progressive structural changes in glaucoma. To date there are only three reports, all of which utilised TDOCT technology. In each case, longitudinal thinning of RNFL was detectable and this was found to be a more useful measure of progression than ONH or macular parameters (Leung et al., 2010; Medeiros et al., 2009; Wollstein et al., 2005). Of course, the paucity of longitudinal studies reflects the rapidity by which OCT technology is advancing. As a consequence, technology is leaping forward before substantial longitudinal data can be accrued and analysed. One approach to overcome this obstacle might be to perform longitudinal imaging

in an experimental model of glaucoma where structural changes may occur more rapidly than in clinical practice.

A number of studies have demonstrated that, although there is good correlation between measurements made using TDOCT and SDOCT, there are systematic and significant differences between measurements (Cho et al., 2011; Gonzalez-Garcia et al., 2009; Knight et al., 2009; Sung et al., 2009; Vizzeri et al., 2009a). For example, the Cirrus generates thinner RNFL measurements (Knight et al., 2009; Sung et al., 2009; Vizzeri et al., 2009a), whereas the RTVue generates thicker measurements (Gonzalez-Garcia et al., 2009). As the precise RNFL measurements differ between the two iterations of the device, the two cannot be used interchangeably. As a result, one cannot directly analyse a longitudinal OCT data series commencing with TDOCT and then latterly switching to SDOCT. One approach that might compensate for this and allow for compatibility between devices is to resample the 3D OCT dataset for every possible 3.4 mm circular scan location within the boundaries of the volume (Kim et al., 2010). One can then cross-correlate these 'virtual' circular scans with the TDOCT 3.4 circular sweep scans to automatically match the TDOCT scan circle location within the volume.

Anterior segment - As an aside, TDOCT technology has also been adapted for anterior segment imaging, providing imaging of the cornea and of the iridocorneal angle without contacting the eye. It has considerable advantages over ultrasound biomicroscopy, being non-contact and having higher axial resolution although it cannot capture deeper structures such as the ciliary body, unlike ultrasound biomicroscopy. Anterior segment OCT is increasingly finding a role in the assessment and management of patients with angle closure; this is, however, beyond the scope of this thesis.

2.3.6 OCT - Future Directions

Given the improved axial resolution and increased depth penetration of the newer SDOCT devices, it is possible that targets 'deep' within the ONH, specifically the prelaminar region, LC and the peripapillary sclera, may be detectable. If this hypothesis is correct, then it is possible that these structures might become legitimate targets for both diagnostic and longitudinal imaging of

patients with, or at risk of, glaucoma. To date, this aspect of SDOCT imaging has yet to be exploited clinically. A major rationale for undertaking this PhD was to explore the potential of SDOCT to capture and longitudinally image these targets.

Beyond what is currently commercially available, there are a number of laboratory developments that may enhance clinical OCT imaging in the future. SSOCT has already been discussed as an alternative to SDOCT (2.3.4). Although essentially slightly slower than SDOCT, SSOCT has the advantage that a noticeable drop-off in signal with depth does not occur due to the narrow bandwidth of the light source (Choma et al., 2003; Yaqoob et al., 2005). One disadvantage is that most swept source systems use long wavelengths (1 - 1.3 µm), with very few studies demonstrating the technique at 800 nm (Lim et al., 2006; Srinivasan et al., 2007). The reason why this is important is that water absorption limits the usable bandwidth at 1.0 and 1.3 µm thereby limiting the axial resolution whereas the water absorption window is larger at 850 nm, allowing greater axial resolution. Although axial resolution may be diminished, there are some advantages to using the longer wavelength. Posterior segment imaging using 1040 - 1060 nm wavelengths can achieve deeper penetration into the retina, ONH and choroid (de Bruin et al., 2008; Lee et al., 2006; Yasuno et al., 2007). This wavelength may therefore be beneficial in capturing choroidal vessels and LC.

The main reason why such swept source devices are not yet commercially available is the cost of the light source. By the same token, longer wavelength systems employing SDOCT technology are hampered by the availability and cost of the CCD cameras required.

Adaptive optics is a technique first adopted in astronomy where deformable mirrors are used to correct distortions of light passing through the atmosphere. In OCT imaging, a transverse 1mm OCT beam has a transverse resolution of 15 to 20 µm. In order to improve our ability to distinguish between adjacent cellular structures (for example, photoreceptors), it would be helpful to ameliorate this transverse resolution. This can be achieved by increasing the OCT beam diameter, in theory decreasing the size of the spot on the retina, but the theoretical resolution is hampered by ocular aberrations (Artal et al., 2001; Donnelly and Roorda, 2003; Fernandez and Drexler, 2005). Adaptive optics OCT works by measuring and correcting for these aberrations

using wavefront sensing and deformable mirrors; as a consequence spot size is minimised and transverse resolution is improved (Miller et al., 2003).

Ultrahigh resolution adaptive optics OCT can improve transverse resolution to 5 - 10 µm (Hermann et al., 2004). It has been shown to enhance the photoreceptor outer segment/inner segment in vivo (Zhang et al., 2005b). Furthermore, when C-mode sectioning of a 3D volume is used, it is possible to visualise RNFL axon bundles (Zawadzki et al., 2007).

Disadvantages of adaptive optics OCT include a narrow depth of focus, meaning that structures at different depths cannot be imaged in focus simultaneously. Also, the field of view is limited to 1° - 3°. Both of these limitations may be overcome either by 'stitching' together volumes or using eye-tracking software to build together series of adjacent scans into a larger volume (Burns et al., 2007; Zawadzki et al., 2009). In addition to improving image quality in eyes prone to ocular aberrations, adaptive optics represents an exciting development as the enhanced lateral resolution may lead to improved performance of automated segmentation algorithms, which will help to improve disease diagnosis and follow-up.

Polarisation-sensitive OCT may be considered an OCT-based corollary to scanning laser polarimetry being that it detects polarisation changes in circularly polarised light (de Boer et al., 1997). RNFL birefringence has been measured in humans using polarisation-sensitive OCT and it has been found to not vary as a function of increasing radius from the ONH, unlike RNFL thickness (Cense et al., 2004a). It does, however, vary by region around the ONH being higher in areas where RNFL is thicker (Cense et al., 2004b). Given this observation, it is likely that birefringence will increase in certain areas as glaucoma develops. Birefringence as measured by polarisation-sensitive OCT therefore has the potential to be an indicator of glaucomatous change. The sclera and LC have been successfully imaged using a polarisation-sensitive SSOCT system centred at a wavelength of 1 µm (Yamanari et al., 2009).

2.3.7 Capturing the LC

The advent of semi-automated ONH imaging devices has heralded the prospect of being able to capture the morphometry of LC in vivo, with obvious implications for glaucoma diagnosis and management. An ability to capture laminar pores using a prototype confocal scanning laser tomography device was demonstrated as far back as 1993 (Fitzke and Masters, 1993). Further development involved the adoption of image processing techniques to create a binary image from the CSLO image at the level of the lamina in which the pores could be more easily, and reproducibly, differentiated (Bhandari et al., 1997). The same group went on to examine 60 eyes of glaucoma subjects and 15 eyes of normal controls and found that the pores became increasingly elongated/less circular with increasing severity of glaucomatous field loss (Fontana et al., 1998a). One shortcoming of these initial studies is that patients were selected on the basis of laminar pores being visible by ophthalmoscopy. This suggests that the prelaminar tissue may have been thin to allow clinical detection of the pores by direct observation. In subsequent work, an imaging processing system using a fast Fourier transform algorithm enabled the analysis of surface CSLO images (not selected on the basis of ophthalmoscopic pore visibility) to quantify pore morphology. Using this technique, average pore size was found to increase with neuroretinal rim loss (A Kotecha, PhD thesis, UCL, 2003).

Further studies involving CSLO images have suggested that the dimensions of the LC may be quantified using the dark peripheral annulus and bright central reflectance seen as surface landmarks within en face CSLO images (Miglior et al., 1998), or that LC morphology may be extrapolated from measurements of the variation in depth of the cup floor (Morgan-Davies et al., 2004). In both cases, the fundamental assumption has been made that whatever the CSLO captures at the base of the cup represents the LC. This is almost certainly not the case in all but the most advanced glaucoma cases as there will be a layer of prelaminar tissue, containing neural tissue and supporting structures, between the surface of the cup and the anterior surface of the LC.

Our ability to truly capture the LC requires the use of a technology that is capable of resolving different structures at varying depth. This has been shown to be achievable using experimental

OCT systems (Kagemann et al., 2008; Srinivasan et al., 2008; Yamanari et al., 2009). Two such examples of experimental LC imaging are shown in Figure 2-9. This PhD aims to further explore the deep ONH imaging capabilities of SDOCT using a commercially available device.

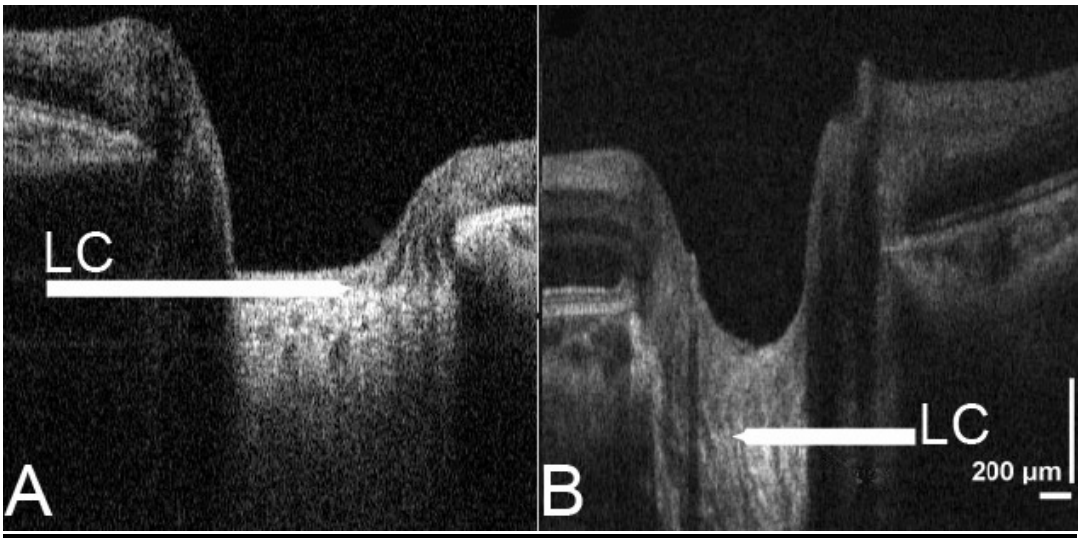

Figure 2-9. Capturing the LC using experimental OCT systems. A shows an ONH B-scan acquired using polarisation-sensitive SSOCT. In B, a swept-source system was used. Both systems used a 1 µm light source. The presumed position of the anterior LC surface is marked in both images. Adapted from (Srinivasan et al., 2008; Yamanari et al., 2009)

2.4 ONH Biomechanics

2.4.1 Basic Principles

Biomechanics refers to the application of mechanical principles to biological systems. The ONH is of particular interest from a biomechanical perspective as it represents a relative weak spot in the otherwise strong corneoscleral coat of the globe. Furthermore, the ONH (in particular the LC) is assumed to be the principal site of injury to RGC axons in glaucoma (Anderson and Hendrickson, 1974; Quigley et al., 1981) and IOP, essentially a mechanical entity, is the primary risk factor for the development of glaucoma. Given these observations, it is reasonable to suggest that biomechanics of the ONH might play a role in the development of GON. Before discussing the biomechanical theory of glaucoma (2.4.2), the engineering terminology and concepts used in the field of biomechanics will be explained.

Stress is a measure of the load applied to, transmitted through or carried by a tissue (Downs et al., 2008; Sigal and Ethier, 2009). It can be defined as the force applied to a tissue divided by the surface area over which the force is applied. When used in a biomechanical context, where it is a mathematical description of mechanical load bearing, it is distinct from the use of the word 'stress' in other physiological situations (such as ichaemic or oxidative stress). The stress within a biological tissue can vary regionally as a result of spatial variations in shape, cross sectional area and non-uniform distribution of the points at which forces are applied. Stresses can be compressive, tensile (pulling) or shearing (forces in tangentially opposite directions).

Strain is a measure of local deformation induced by stress (Downs et al., 2008; Sigal and Ethier, 2009). It is usually expressed as a percentage change in the length of the original shape. As with stress, it can comprise normal (compressive or tensile) and shear (distortional) components. As strain is a measure of local tissue deformation it is possible for part of a tissue to displace substantially whilst the local deformation (and consequently the strains) in that part remain low; likewise it is possible for a structure to displace minimally in one direction yet experience large strains in another direction. Unlike stress, strain can be observed and measured. Strain is therefore a measurable indicator of the level of micro-deformation experienced by a tissue and

this is important in biomechanics as it is strain, not stress, that damages tissues (Sigal et al., 2007).

Stress and strain in a tissue therefore represent different quantities and so should not be used interchangeably. They are, however, related to each other through the material properties of the tissue in question (Downs et al., 2008; Sigal and Ethier, 2009). Material properties may be classified according to the nature of the relationship between load and deformation (linear or non-linear), the time-dependent response to loading (elastic or viscoelastic) and the level of material symmetry (isotropy or anisotropy).

In linear materials, the stress is directly proportional to the strain by a constant (Young's modulus). In non-linear materials, there is a variable relationship between stress and strain and there is no unique or constant Young's modulus for that material. Viscoelastic materials exhibit higher resistance when loaded quickly; by contrast the stiffness of elastic materials is not dependent on the rate of load application. Isotropic materials exhibit identical resistance to loading in all directions whereas anisotropic materials vary in stiffness in different directions. Structural stiffness is a concept that incorporates both material properties and geometry of a load bearing structure to create a composite measure of a structure's resistance to deformation.

In the ONH, the geometry and material properties of the sclera and LC contribute to the stiffness of the ONH, thereby determining its ability to withstand strain when exposed to IOP. The biomechanics of an individual ONH will therefore be determined by tissue geometry (including such features as scleral canal size and shape, scleral thickness, laminar beam density and orientation) and the material properties (stiffnesses) of the LC and sclera.

Using these definitions, the simplest description of a material property would be that of an isotropic, linearly elastic material, such as steel. Unfortunately, this isn't usually applicable when trying to measure and understand the biomechanics of the ONH. Biological soft tissues such as sclera and lamina are usually non-linear, anisotropic and have viscoelastic properties. It is therefore extremely challenging to measure the material properties of such tissues. However, once known, they can be used in conjunction with descriptions of the 3D geometry of the

structure (highly complex in the case of the LC) and loading conditions (IOP) to model the stress and strain fields experienced by the ONH.

When a tissue is strained beyond its elastic limit, mechanical yield will occur. Once a tissue has 'yielded' it has permanent damage, is deformed and is normally less resistant to further loading (hypercompliant). At even higher strains, mechanical failure may occur after yield. This results in the rupture or pulling apart of soft tissues. In any ONH, it is likely that there is a specific IOP that induces yield in laminar beams but no visible failure; at higher IOPs it is possible that failure may be seen in individual beams. Yield and failure in the ONH probably result in a chronic cellular remodeling response that results in restructuring of the ONH, altering its future response to loads. Early connective tissue damage leads to astrocyte remodeling which may make the remaining connective tissues more susceptible to future damage at all levels of IOP (Hernandez, 2000; Hernandez et al., 1990; Morrison, 2006; Quigley et al., 1991a; Quigley et al., 1991b). This concept is central to the theory of how chronic IOP elevation leads to glaucoma and also how ageing changes may also predispose to GON.

2.4.2 The Biomechanical Theory of Glaucoma

The biomechanical theory of glaucoma proposes that ONH biomechanics may explain how IOP-related stress and strain within the load bearing tissues of the ONH influence the physiology and pathophysiology of the connective tissues (peripapillary sclera, scleral canal wall and LC), the supporting tissues (astrocytes, glia, endothelial cells, vascular pericytes and their basement membranes) and the RGC axons (Burgoyne et al., 2005; Burgoyne and Morrison, 2001; Fechtner and Weinreb, 1994).

ONH biomechanics is the 'link' by which such apparently non-IOP factors such as ischaemia, inflammation, autoimmunity, astrocytic and glial cell biology are influenced by or interact with the effects of IOP (Figure 2-10). The interaction of these factors with laminar and peripapillary scleral connective tissue geometry and material properties may be used to explain the physiology of ageing in the normal ONH, the susceptibility of the ONH to IOP and the clinical phenotype of GON at any level of IOP (Burgoyne et al., 2005).

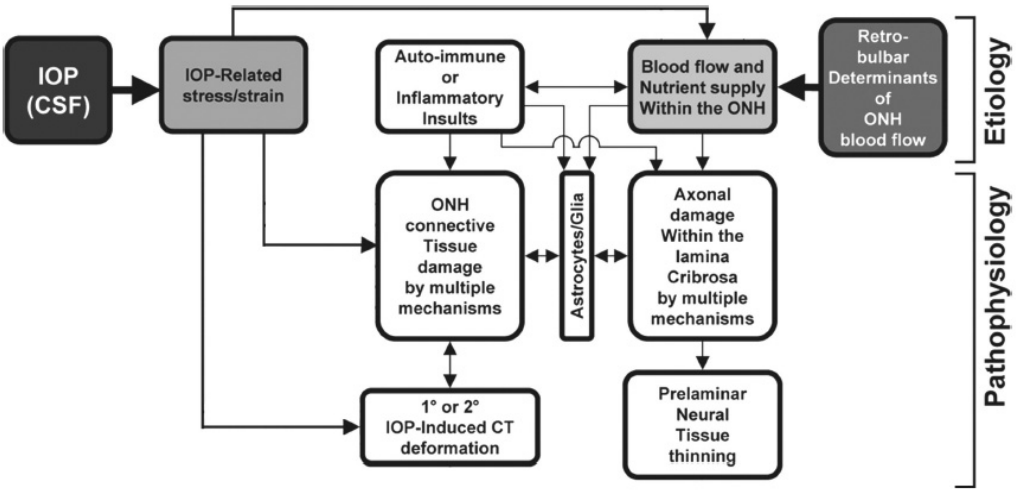

Figure 2-10. The biomechanical paradigm in glaucoma. Adapted from (Downs et al., 2008)

The likely factors that will influence an individual ONH's susceptibility will include the magnitude (and perhaps variation) of IOP and the geometry and material properties of the ONH and peripapillary scleral tissues. Furthermore the volume flow and perfusion pressure of blood within the laminar capillaries will influence the diffusion of nutrients to astrocytes. The way astrocytes and glia respond either to strain and/or changes in localised nutrient diffusion (the two being linked within the biomechanical theory) will also play a role. Finally there may be features within the RGC itself that will result in an increased susceptibility to apoptosis in response to localised distress (Burgoyne and Downs, 2008).

From an engineering perspective, the eye may be considered a vessel with inflow and outflow facilities that regulate IOP. IOP exerts a load normal to the surface of the wall of the eye, generating an in-wall circumferential stress known as 'hoop stress' that is primarily taken up by the relatively stiff sclera. The burden of IOP at the ONH is taken by the connective tissues of the LC and it is this in-wall hoop stress transferred from the peripapillary sclera that dominates laminar biomechanics. Hoop stress is up to 15 times greater than the stress generated by the translaminar pressure gradient, which is the differential of the compressive stress of IOP at the ONH counteracted by the compressive stress caused by retrolaminar CSF pressure (Bellezza et al., 2000).

Our ability to study the biomechanics of the ONH is complicated by a number of factors. Firstly the 3D geometry of the connective tissues is highly complex and difficult to measure, with the thickness of the monkey sclera varying up to four times from the equator to the peripapillary region (Downs et al., 2002; Downs et al., 2001) and the microarchitecture of the lamina being regionally complex and individual (Dandona et al., 1990; Quigley and Addicks, 1981; Radius, 1981). The connective tissues of the cornea, sclera and lamina have highly anisotropic collagen and elastin fibril orientations, meaning that experimental characterisation and mathematical description of their constituent material properties is both complex and difficult to achieve. IOP-related stress generates strain patterns in the ONH and peripapillary sclera that are also influenced by complex loading patterns. These are influenced by the alignment and density of collagen fibrils in each tissue (i.e. stiffness and anisotropy), the rate of change in IOP (relating to the viscoelastic properties of the tissue) and the level of IOP-related strain at the time of a change in load (relating to the non-linearity of the tissue). Theoretically, ONH connective tissues should be stiffer (more resistant) when there is already considerable strain present and/or the load is applied quickly. By the same token, the ONH should be less stiff and more compliant at lower levels of strain or if the IOP changes slowly (Downs et al., 2008).

2.4.3 Compliance Testing

The compliance of the normal ONH in response to an acute elevation of IOP has been studied by a series of investigators using a number of techniques. These include: X-ray photography of cadaveric non-human primate eyes with fine platinum wires inserted into the peripapillary sclera and optic disc (Levy and Crapps, 1984), laser doppler velocimetry of normal human autopsy eyes (Zeimer and Ogura, 1989), conventional histology of human eyes (Yan et al., 1994), 2D (Bellezza et al., 2003b, a), and 3D histomorphometric reconstructions of post mortem normal monkey eyes (Yang et al., 2009b). Various imaging modalities have been used in vivo in normal monkey eyes (Coleman et al., 1991; Quigley and Pease, 1996). Numerical models have also been used (Roberts et al., 2010; Sigal et al., 2011). These reports were all consistent (to a greater or lesser

degree) in finding a posterior movement of the optic disc surface in response to an acute elevation of IOP.

Over a series of experiments, the method of in vivo surface compliance testing has been refined. Initially the effect of acute IOP elevation in a group of normal monkey eyes was reported following analysis of digitised photographic images (Burgoyne et al., 1995b). In this study, small (mean, -28 μm), reversible (i.e. elastic) posterior deformations of the optic disc surface occurred following acute IOP elevation in the normal monkey eye. In a companion article, surface compliance testing was conducted using the same technique but in monkey eyes with chronic EG (Burgoyne et al., 1995a). In that study, the degree of compliance increased, a phenomenon that was referred to as 'hypercompliance', within 2 to 4 weeks from the onset of EG. This returned to a level of compliance statistically indistinguishable from normal within 13 to 18 weeks from the onset of EG. Strictly speaking, from an engineering perspective, the use of the word hypercompliance is incorrect as this, by definition, occurs following mechanical yield so should not be a reversible phenomenon. However, it is possible that the phenomenon was not 'reversible' per se and that the changes might be explained by connective tissue damage and axonal loss stimulating connective tissue synthesis, thereby resulting in an eventual stiffening. Subsequently, the group investigated ONH surface compliance in normal monkey eyes using CSLO and found that the ONH surface deforms rapidly in response to increased IOP but that the degree of deformation varies between subjects and between eyes of the same subject (Heickell et al., 2001). This phenomenon was not detected in the preceding compliance studies (Burgoyne et al., 1995b, a) but has been identified in 3D morphometric studies (Sigal et al., 2010; Sigal et al., 2011).

Throughout these in vivo compliance experiments in monkey eyes, the ongoing hypothesis has been that changes in the surface of the optic disc will reflect changes to deeper load bearing structures - chiefly the LC and peripapillary sclera. Post mortem studies, performed both in human and monkey eyes, have indicated that the LC and scleral canal wall deform after acute IOP elevation (Albon et al., 2000b; Bellezza et al., 2003b, a; Yan et al., 1994). The effect of acute IOP elevation upon monkey ONH connective tissues was initially explored using 2D histomorphometry by comparing a series of eyes perfusion fixed at IOP 10 mmHg with eyes that

had been immersion fixed at IOP 0 mmHg (Bellezza et al., 2003a). In that study, the lamina was found to be thinner and more anterior, and the scleral canal diameter larger in the IOP 10 mmHg eyes. These observations suggested that, with acute IOP elevations at a low native IOP, the scleral canal expands resulting in a tauter, thinner, more anteriorly placed lamina. Subsequently, 2D histomorphometry was performed in normal young adult monkeys perfusion fixed at 10 mmHg in one eye and 30 or 45 mmHg in the fellow eye (Bellezza et al., 2003b). In that study, a posterior laminar deformation of 10 - 23 µm in the high IOP eyes compared to their contralateral fellow eyes was demonstrated. Most recently, ONH connective tissue deformation has been characterised in 3D histomorphometric ONH reconstructions of eyes perfusion fixed after acute IOP elevation to 30 or 45 mmHg compared to 10 mmHg in their fellow eyes (Yang et al., 2009b). Minimal to modest regional laminar thinning, posterior bowing of the peripapillary sclera, thinning and expansion of the scleral canal was observed in most of the high IOP eyes.

These studies all highlight the importance of being able to directly measure the acute deformations of the tissues within the ONH. In order to really be certain of the changes being observed, one needs to capture them in vivo, preferably in a non-invasive manner. Although surface compliance testing can point the way, it is uncertain whether surface compliance truly reflects what is occurring within the deeper connective tissues. Recent advances such as second harmonic imaging, albeit in cadaveric eyes (Brown et al., 2007), and more crucially in vivo SDOCT imaging (Srinivasan et al., 2008) can be applied to ONH compliance measurements and might help to clarify the relationship between surface and deeper tissue deformations. As this approach is still being developed - indeed it is one of the areas of investigation within this PhD - mathematical modelling is the current mainstay in the study of ONH biomechanics.

2.4.4 Modelling Biomechanics

A detailed description of the modelling techniques used in biomechanics is beyond the scope of this thesis. A brief description is warranted; if SDOCT imaging can be used to successfully measure ‘deep’ ONH compliance then it will become a crucial tool for the in vivo verification of these mathematical models of ONH biomechanics.

Briefly, modelling approaches can be divided into the analytic and numerical, with numerical models being subdivided into those that are generic and those that are eye-specific (Sigal and Ethier, 2009). Analytical models have a 'closed form solution' whereby the relevant stresses and strains can be written in terms of known mathematical expressions. The simplest models are based on Laplace's law, which relates tension on the wall of a spherical vessel to the magnitude of the pressure, the radius and the thickness of the wall. Another approach is to derive the coefficient of ocular rigidity (Ethier et al., 2004); refinements of both of these methods have been used to estimate whole globe mechanics (Greene, 1985; Silver and Geyer, 2000). Unfortunately these analytic models can't provide any information about biomechanics of the ONH as the ONH is composed of tissues with differing mechanical properties and complex geometries. Analytical models require these factors to be homogenous. Although analytical models are elegant, and can be refined so that they can be laminar specific (Dongqi and Zeqin, 1999; Edwards and Good, 2001; Sander et al., 2006), generally they work best for simplified geometries, tissue properties and loading conditions. As this is clearly not the case in the ONH, most researchers in this field have turned to numerical models.

The most common numerical approach is finite element modelling, which can be used to determine the mechanical response of a complex structure. It allows the deformation of all parts of an object to be computed if the loading, material properties and geometry of the tissue in question are known. Generic numerical models derive their informative data from general, perhaps population-based, dimensions and material properties (Bellezza et al., 2000; Sigal et al., 2005a; Sigal et al., 2004). An advantage of this approach is that the model can be parameterised so that aspects of shape, material properties and loading can be varied. This means that models can differ only in a parameter of specific interest (i.e. one can create models where the only aspect that changes is globe size or axial length).

A disadvantage of generic numerical models is that they cannot be used to make predictions for a specific eye. In order to address this, eye specific models have been developed that incorporate more details that are individual to a specific eye. Eye specific models have been developed based on 3D reconstructions of human (Sigal et al., 2005b, 2009a, b) and monkey eyes (Downs

et al., 2009). As one would expect, such models are more complex than generic models and require a great deal of effort in terms of computation and analysis.

Ultimately, it is hoped that SDOCT imaging of specific targets within the ONH may lead to both refinement and validation of eye specific models. Specifically, one may speculate that in vivo measurements following acute IOP elevations (at multiple IOP levels and multiple time points) of scleral canal enlargement, laminar deformation, peripapillary scleral deformation and peripapillary scleral thickness will be of major benefit, if such measurements are achievable with non-invasive imaging technology.

3. SECTION III:

MATERIALS AND METHODS

3.1 ONHRL

The ONHRL, led by Professor Burgoyne, was set up at the Devers Eye Institute in 2005/2006 following the move of key personnel from Professor Burgoyne's group at Louisiana State University and Tulane University (both in New Orleans). Over the past decade, the group has worked with the monkey model of glaucoma, which Burgoyne learned whilst working in Professor Quigley's lab at Johns Hopkins. Burgoyne and co-workers have developed and refined their testing protocols for in vivo imaging of the monkey eye. Furthermore, the group has developed and refined a sophisticated method for digitally reconstructing histological sections of the ONH to render 3D volumes - a process known as 3D histomorphometric reconstruction. This method allows for the visualisation of ONH connective tissue changes following compliance testing and following the onset of EG. The ONHRL works in very close collaboration with the ocular biomechanics laboratory (OBL) led by Dr Downs, also at the Devers Eye Institute. The collaboration between Professor Burgoyne and Dr Downs is fully engaged with developing an understanding of the pathophysiology of glaucoma through furthering our knowledge of the morphometry and biomechanics of the ONH.

What follows in this Materials and Methods section is an overview of the standard experimental techniques developed and used by the group over the past decade. The one area in which my research was a major departure for the group was the adoption of in vivo SDOCT imaging. An overview of SDOCT imaging as conducted during animal testing is included in here (section 3.4). Specific SDOCT imaging algorithms for individual experiments will be outlined in the methods section for that experiment (Section 4). Furthermore, any novel methodology that has been developed for a specific experiment that does not form part of routine ONHRL protocol will also be discussed in the methods section for that experiment (Section 4).

3.2 Animals

All animals used in this research were rhesus macaques *(Macaca mulatta),* unless stated otherwise in the methods section for a specific experiment (Section 4). All animals were treated in accordance with the Association for Research in Vision and Ophthalmology (ARVO) Statement for the Use of Animals in Ophthalmic and Vision Research. The local Institutional Animal Care and Use Committee (Legacy Health) approved all of the studies included in this thesis.

All animals used in this research were purchased from either the Oregon National Primate Research Center at Oregon Health and Sciences University (OHSU) or the Wisconsin National Primate Research Center at the University of Wisconsin at Madison.

Animals were housed in stainless steel cages. There were two arrangements of cages. The 1/1 arrangement comprises two individual cages, one on top of the other, with dimensions for each cage of 39” x 30” x 30” (8.1 Sq ft). The other arrangement was for quad cages (a unit of four individual cages). There were two different quad units - one had dimensions of 31” x 30” x 32” (6.4 Sq ft) per cage and the other had dimensions of 27” x 24” x 32” (4.5 Sq ft) per cage. Paired animals were housed in a minimum of two individual cages that were joined together (i.e. one half of a quad system). Depending on the number of animals at the Legacy facility, individual animals may be housed in 2, 3 or 4 cages joined together.

Monkeys were fed twice per day with 10 - 25 biscuits of monkey chow (lab Fiber-Balanced monkey jumbo, PMI Nutrition International LLC, Brentwood, MO). In addition, monkeys received a fruit or vegetable each day and monkey ‘morsels’ and other treats as enrichment. They had access to water ad libitum via lixit waterers.

The monkeys did not leave the cages for anything other than testing, although they were rotated through an enrichment cage, which was 4 individual cages with the doors open between them. On one side of the enrichment cage were toys, food in a bin for foraging, a basin of water and objects for climbing and swinging. On the other side of the enrichment cage was their typical cage. Rotation through the enrichment cage was dependent on the total number of animals at the facility, but each animal would spend a week at a time in the enrichment cage.

While not all animals were in the enrichment cage every week, the Department of Comparative Medicine (DCM) would provide some sort of enrichment twice a week whilst they were in standard cages, such as the provision of toys and treats.

The veterinary technician staff from the DCM cared for all monkeys at the facility. The ONHRL funded the provision of a certified veterinary technician dedicated to testing and anaesthesia within the ONHRL. There was also an attending veterinarian who oversaw the DCM where the group's monkeys were housed.

ONHRL animals were tested no more than once per working week, with tests/knockdowns (any anaesthetic induction) needing to be at least five days apart. This scheme applied except where there was some form of medical emergency such as an injury or infection to the animal that required the animal to be anaesthetised for treatment. Animals might have been tested twice in the same week, with special permission from the attending veterinarian, if the second test was non-recovery (i.e. sacrifice immediately following the second testing session).

3.3 Testing Procedure - Short and Long Compliance Tests

The testing protocol began with induction of general anaesthesia by veterinary staff (Legacy Health) using ketamine (15 mg/kg, by intramuscular injection) and midazolam (0.2 mg/kg, by intramuscular injection). A single subcutaneous injection of atropine sulphate (0.05 mg/kg) was also administered. Animals were then intubated with an endotracheal tube. An intravenous (IV) line (24 gauge, 0.75 inch BD Insyte Autoguard IV Catheter) was then placed into the saphenous vein in order to administer fluids (Lactated Ringer's Solution, 10 ml/kg/hr and/or 6% HetaStarch) for maintenance of hydration and normal blood pressure. The endotracheal tube was connected to an anaesthesia machine and animals began breathing a mixture of 100% oxygen and isoflurane gas (1-2%, typically 1.25%) to maintain anaesthesia for the duration of the imaging session. Heart rate and arterial oxyhaemoglobin saturation were monitored continuously throughout each session (Propaq Encore model 206EL, Protocol Systems, Inc., Beaverton, OR) and maintained above 75 per min and 95%, respectively. Body temperature was maintained at 37°C with a pair of warm-water heating pads (TP500 T/Pump, Gaymar Industries, Orchard Park,

NY, USA) placed above and below the animal. Blood pressure was measured approximately every 10 minutes (NIBP system 7100, Advanced Medical Instruments, Inc., Broken Arrow, OK) and maintained above a mean arterial pressure (MAP) of 75 mmHg. If MAP decreased below 70 mmHg, an IV bolus of lactated Ringer's (10 ml/kg/hour) was administered. If MAP did not elevate above 75 mmHg, despite the administration of IV fluid, the experiment was discontinued immediately and the subject recovered.

One drop of topical corneal anesthetic was placed in each eye (0.5% proparacaine), and a lid speculum was inserted to keep eyelids open. Intraocular pressure (IOP) was measured by applanation tonometry (Tonopen XL, Reichert, Depew, NY) and reported as the average of three or more measurements at each session.

The anterior chambers of both eyes of each subject were cannulated via the temporal peripheral corneas using a single 27-gauge needle for each eye. Each needle was connected to an adjustable height reservoir of sterile balanced salt solution (BSS; Alcon Laboratories, Inc., Forth Worth, Tx) via polyurethane tubing. In order to adjust the IOP during the testing protocol, the height of the reservoir could be adjusted in 5 mmHg increments. These increments had been pre-calibrated using a pressure transducer (MX860; Medex, Inc., Carlsbad, CA).

Short compliance tests - these were the routine imaging testing sessions within the ONHRL. Following measurement of 'native' IOP using the Tonopen, as outlined above, IOP was manometrically adjusted to 10 mmHg. Imaging commenced after thirty minutes of acclimatisation (stabilisation) at an IOP of 10 mmHg. All imaging in the short compliance test was performed with the IOP controlled at 10 mmHg. This adjustment was made to ensure that all structural changes in the ONH were due to chronic connective tissue remodelling and not due to an acute effect of an elevated native IOP at the time of testing.

Long compliance tests - these sessions began as per the standard procedure, with measurement of native IOP by tonopen, then imaging following thirty minutes of IOP-stabilisation at 10 mmHg. In these longer tests, however, imaging was also repeated with IOP further elevated manometrically for a sustained period of time. The magnitude and duration of IOP elevation was varied according to the specific protocol for an individual experiment and as such will be detailed

in the methods section for the single experiment within this PhD in which long compliance testing was undertaken (section 4.7.3).

Prior to imaging (for both short and long tests), pupillary dilation was induced topically with one drop each of tropicamide (0.5%) and phenylephrine (2.5%) in each eye. A clear, plano-powered rigid gas permeable contact lens was placed on each eye with topical lubricant (0.5% carboxymethylcellulose sodium, Refresh, Allergan, Irvine, CA, USA). At the end of each testing session, the intracameral needles were removed and a broad spectrum topical antibiotic ointment was applied.

3.4 Imaging

For the purposes of the experiments described in this thesis, three types of ONH image were acquired during testing.

The first of these were optic disc stereophotographs, which were taken regularly although not at every testing session. Stereophotographic pairs were acquired using a Topcon TRC-WT Retinal Camera (Topcon, Paramus, NJ). Latterly, this system was replaced with a Nidek 3-D_X fundus camera system (Nidek, Fremont, CA). All images were captured onto 35 mm slide film, which was developed and processed into color slides.

The second type of ONH imaging was by CSLO using the commercial HRT II/3 system (Heidelberg Engineering, Heidelberg, Germany). The technical specifications and standard imaging method for this device have been discussed in detail earlier (section 2.3.2 and 2.3.3). At each testing session, three or more single topographies were acquired (automatically during one acquisition) to generate a mean topography. The specifics as regards HRT-defined structural end-points will be discussed in the methods section pertaining to the longitudinal assessment of EG (section 4.6.3).

The third imaging modality was SDOCT, as performed using a commercially available Spectralis device (Heidelberg Engineering, Heidelberg, Germany). The technical specifications of the Spectralis device are covered in detail elsewhere (Heidelberg Engineering, 2007). The Spectralis is a dual laser system, using an 870 nm semi-luminescent diode light source to acquire OCT

scans (40,000 A-scans per second) and a near infrared 820 nm wave-source to simultaneously acquire SLO images. The SDOCT optical resolution is approximately 7 μm in depth and 14 μm transversely. The depth of each A-scan is 1.8 mm and consists of 512 pixels providing a digital depth sampling of 3.5 μm per pixel. Each B-scan spans 15 degrees (unless stated otherwise) and consists of 768 A-scans providing a digital transverse sampling of 5 μm per pixel (in an emmetropic human eye with average axial length).

The Spectralis incorporates a real-time eye tracking system that measures eye movements and provides feedback to the SDOCT scanning system in order to stabilise the retinal position of the B-scan. This therefore allows sweep averaging at each B-scan location in order to reduce speckle noise. In every experiment, the eye tracking facility was turned on and nine sweeps were averaged for every B-scan. This is the optimal number of sweeps identified by the manufacturer to acquire B-scans at high speed but without significant diminution in overall image quality. Improved image quality may be achieved by increasing the number of scans averaged, but this may lead to unacceptably long scanning times.

Details regarding the specific ONH test patterns (radial, peripapillary, raster) and any other modifications adopted for an individual experiment will be discussed in the methods section for each experiment.

3.5 Induction of EG

Certain animals would undergo laser to the trabecular meshwork in order to induce ocular hypertension, leading on to EG with the development of irreversible signs of glaucomatous optic nerve damage. In each case, lasering would be undertaken in one eye (the EG eye), leaving the other eye untreated (the control eye).

Laser treatments were performed under ketamine anaesthesia, either on its own or with xylazine or dexmedetomidine anaesthesia. Initially laser was performed at two separate treatment sessions, treating 180° of the trabecular meshwork on each occasion, separated by a two week interval. Laser treatments were subsequently repeated approximately every two weeks, but

limited to a 90° sector, until an IOP elevation was first noted; laser treatments were continued if the post-laser IOP returned to pre-treatment levels.

Argon laser energy was delivered to the trabecular meshwork using a slit lamp mounted HGM PC-EDO Ophthalmic laser (Lumenis, Yokneam, Israel) with the trabecular meshwork visualised using an Ocular Kaufman Single Mirror Gonio Laser Lens (OKSMA, Ocular Instruments, Bellevue, WA). Laser spot size was 50 microns with a power of 600 to 850 mW applied for a duration of 1000 msecs, titrated to achieve blanching or fine bubbles in the trabecular meshwork, as opposed to a frank 'pop'. Sixty to one hundred burns were applied during each of the two initial 180° treatments. In the subsequent 90° treatments, thirty to fifty burns were applied. The goal of each treatment was to create confluent blanching, bubbles and/or pigment change in the region of treatment of the trabecular meshwork. During laser treatment an ointment mixture of neomycin, polymyxin B and dexamethasone was used in both eyes to prevent ocular surface drying before the animal woke up. At the end of the laser procedure, 0.5 - 1.0 ml of 10 mg/ml dexamethasone was injected into subtenons space. Animals also received a three day course of meloxicam (0.2 mg/kg each day given intramuscularly, subcutaneously or orally) to reduce post-operative inflammation and pain.

3.6 Animal Sacrifice and Perfusion Fixation

Any animals sacrificed were done so during perfusion fixation with IOP set to 10 mmHg in both eyes. This procedure allowed the IOP at the time of death to be controlled. Each procedure was undertaken under deep pentobarbitone anaesthesia with the anterior chambers of both eyes cannulated with 27-gauge needles and the IOP set to 10 mmHg using an adjustable height saline reservoir, as per short compliance testing.

The surgeon opened the mediastinum and pericardium to expose the beating heart, using large toothed forceps to hold the heart. A single 8 to 14 gauge bevelled trocar was inserted into the right ventricle to reduce flow and to maximise perfusion pressure (of the fixative). The left ventricle was cut to allow outward flow. Pressurised flow of fixative via the descending aorta commenced after at least 30 minutes of IOP-stabilisation at 10 mmHg. Initially one litre of 4%

buffered hypertonic paraformaldehyde solution was passed through the pressurised perfusion system, followed by six litres of 5% buffered hypertonic glutaraldehyde solution. Both paraformaldehyde and gluteraldehyde were buffered in 1 M Sorenson's solution (0.15 M KH_2PO_4 and 0.85 M Na_2HPO_4). Osmolarity of each solution was approximately 0.4 osm/L. During perfusion fixation, the pressure in the perfusion system was adjusted to maintain an MAP of 50-60 mmHg. Once the six litres of glutaraldehyde had perfused, the flow to the cannula was stopped using a stopcock. After perfusion fixation, IOP was maintained for 1 hour after which both eyes were enucleated (including a 0.5 - 1.5 cm section of the intraorbital optic nerve), and all orbital contents were exenterated via a lateral orbitotomy. The anterior chamber was removed by opening the globe at the ora (2 - 3 mm behind the limbus). The posterior scleral shells with intact ONH, choroid and retina were placed in 5% glutaraldehyde solution for storage.

3.7 3D Histomorphometric ONH Reconstruction

This methodology has been described in detail elsewhere (Burgoyne et al., 2004; Downs et al., 2007). Following enucleation, each ONH and surrounding peripapillary sclera were trephined (6 mm diameter) and pierced with four to seven 10-0 polypropylene alignment sutures (Prolene, Ethicon, Somerville, NJ). The trephine was then photographed to document the position of the alignment sutures in relation to the optic disc surface. The tissue was degraded through a graded series of ethanols, cleared in chloroform and infiltrated with paraffin (TissuePrep 2, Fisher Scientific, Pittsburgh, PA) using an automatic tissue processor (Tissue-Tek II, Ames Division, Miles Laboratories Inc., Elkhart, IN). The specimen was oriented in the desired position, embedded in paraffin and mounted on a microtome (RM2165, Leica, Wetzlar, Germany), with the vitreous surface of the ONH visible in the block.

A 1080 x 1520 pixel chip camera (Spot RT, Diagnostic Instruments, Sterling Heights, MI) was positioned so that an image of the centred embedded tissue block surface could be acquired at a resolution of 2.5 x 2.5 µm per pixel. The block was then sectioned without imaging until the cutting plane was just superficial to the internal limiting membrane of the retina. At that point, a 1:1 (vol/vol) mixture of Ponceau S and acid fuchsin stains (which stains only the exposed

connective tissues) was manually applied to the surface of the block, the excess stain was blotted away and the stained surface of the embedded tissue block was imaged. Successively, a 3.0 µm section was cut away, the stain would be applied and the imaging process repeated.

Therefore, for each ONH, imaging began at the vitreo-retinal interface and continued through the LC, extending approximately 200 µm into the orbital optic nerve. Depending on the degree of tilt of the embedded issue, the number of sections obtained per eye ranged from 222 to 411. Each section image was aligned in the z-axis (anterior to posterior) using custom software to register the cut ends of the embedded prolene sutures that were visible in each section.

For each ONH, these aligned serial section digital images were stacked at 3.0 µm intervals, which was the section thickness and therefore the distance between images. Stacking of these aligned 2D images generated a 3D reconstruction of the ONH and peripapillary connective tissues consisting of 1080 x 1520 x 411 voxels, each 2.5 x 2.5 x 3.0 µm. A 3D ONH reconstruction can occupy up to 2.25 GB of memory, so it was necessary to reduce its memory footprint to facilitate responsive interaction with the digital data. Custom software was therefore used to reduce the colour map of each reconstruction from 16 million to 256 colours while maintaining full volumetric resolution, thereby allowing the entire 3D volume to be loaded into memory and manipulated on a Windows-based (subsequently Mac-based) graphics workstation.

A second generation, higher resolution protocol was latterly instituted in which cuts were made at a depth of 1.5 µm and the surface imaged at a resolution of 1.5 x 1.5 µm per pixel. Image alignment in the higher resolution protocol was achieved using laser displacement sensors rather than using the fiducial sutures as in the earlier protocol.

The method by which pertinent structures within each 3D ONH reconstruction were identified and delineated will be detailed in the methods sections of the relevant experiments (sections 4.2.3 and 4.3.3).

4. SECTION IV:

EXPERIMENTS

4.1 Aims and Plan of Research

The aims of the research are as follows:

1. In the first three experiments (4.2 - 4.4), the intention is to explore the ability of SDOCT to capture key ONH landmarks that will be useful for the parametric quantification of SDOCT ONH volumes. In order to reliably detect 'deep' structural changes in the ONH, one first needs to identify 'anchoring' landmarks by which one may apply a reference plane and by which one may define the limits of the ONH. In the first experiment (4.2), I explore the detection of the neural canal opening (NCO), which is used to define the reference plane in 3D histomorphometric volumes. In the following two experiments (4.3 and 4.4) I explore the anatomical basis of what is clinically detected as the optic disc margin. I first establish the anatomical underpinnings of the disc margin using 3D histomorphometric reconstructions and then explore this anatomy in vivo using SDOCT.

2. The fourth experiment (4.5) represents a crucial step in the application of SDOCT to detect deep targets within the ONH. In this experiment, I attempt to match B-scans acquired from a normal monkey ONH in vivo with histological sections acquired from the same ONH post mortem. In doing so, the aim is to definitively identify which structures can be defensibly identified within SDOCT ONH volumes. In particular, I am interested in establishing whether LC anatomy can be delineated.

3. In the final two experiments (4.6 and 4.7), I develop parameters based on the structures identifiable within SDOCT ONH volumes (having been demonstrated in the preceding experiments 4.2 - 4.5). These structural parameters are then measured in two scenarios. The first (4.6) is in the context of a longitudinal series of SDOCT ONH volumes in a group of monkeys with unilateral EG. The aim of this experiment is to establish whether deep ONH targets may be used to detect experimental glaucomatous progression. The second (4.7) is in the context of a long compliance test, where IOP is elevated for a sustained period of time. The aim of this experiment is to identify whether SDOCT is capable of ascertaining the anatomical basis for acute surface compliance changes.

4.2 Detection of the Neural Canal Opening

4.2.1 Background

The commercial introduction of high speed, high resolution 3D SDOCT creates the potential for ONH surface and subsurface change detection. These changes may precede either the onset of peripapillary RNFL thickness changes or visual field loss. However, to date, there has been no rigorous investigation of this technology's ability to image the deep ONH structures and to generate volumetric parameters based on Bruch's membrane (BM), BM opening (BMO), the anterior LC surface and the anterior scleral surface.

A central requirement for ONH surface and subsurface change detection is a longitudinally stable zero reference plane, from which all structural measurements are defined (Burk et al., 2000; Chen et al., 2001; Leung et al., 2005; Strouthidis et al., 2005a; Strouthidis et al., 2005b; Tan et al., 2003b; Tan and Hitchings, 2003). Ideally, the SDOCT reference plane should be located at, or linked to, a biologically continuous structure (a 'reference plane source structure') that is both clinically recognisable and easily identifiable in all SDOCT B-scan images. However a reference plane source structure does not necessarily need to be planar or clinically visible as long as it may be segmented reproducibly within SDOCT images. Also its position relative to the ONH target structures should be relatively stable over time and through the pathophysiology of glaucomatous damage.

BMO has previously been used as a reference plane within quantitative 3D histomorphometric reconstructions of the monkey ONH (Downs et al., 2007; Yang et al., 2007a; Yang et al., 2007b). The choice of BMO as a reference plane in histomorphometric reconstructions was predicated upon the observations that it was obviously continuous, delineated reproducibly and altered minimally in the pathophysiology of early EG damage (Downs et al., 2007; Yang et al., 2007a; Yang et al., 2007b).

The ONHRL group has previously proposed the term *neural canal* for the axonal pathway through the eye wall (Burgoyne et al., 2004; Downs et al., 2007), which includes a pre-scleral region as well as the scleral canal (Figure 4-1). The neural canal extends from its ophthalmoscopically visible internal opening, the optic disc margin, to its external opening (the posterior scleral canal

opening), which is not detectable ophthalmoscopically. Defining the neural canal in this manner is clinically significant, because at present the relationship between the most anterior (or inner-most) portion of the canal and the disc margin within 3D histomorphometry, confocal scanning laser tomography imaging, OCT imaging and disc photographs is controversial (Barkana et al., 2006; Correnti et al., 2003; Downs et al., 2007; Iester et al., 1997; Leung et al., 2007; Neubauer et al., 2006; Schuman et al., 2003).

The neural canal opening (NCO) is defined as the anatomical entrance to the neural canal at the level of the RPE and BM. Within all monkey ONH 3D histomorphometric reconstructions which have been completed to date, BMO is both the NCO and it co-localises to the disc margin in color photos that are registered to that reconstruction (Downs et al., 2007). However, the anatomy of the NCO in human eyes, and within OCT images of human eyes, is more complicated than the monkey. Furthermore, the ability of OCT to discriminate BM as distinct from the RPE is not yet resolved (Drexler and Fujimoto, 2008). At present, most clinical OCT systems suggest that the end of the RPE is being delineated as the zero-order reference plane (Drexler and Fujimoto, 2008).

This experiment proposes that in all SDOCT sagittal ONH sections, there is a discernible NCO that can be manually (and eventually automatically) delineated. While the underlying histological and clinical relationships are important, this study further proposes that the NCO detected by SDOCT (regardless of its histological and clinical underpinnings) will serve as a stable anchor for a longitudinal reference plane for SDOCT imaging of the ONH.

4.2.2 Purpose

The purpose of this experiment is to assess the ability to delineate the NCO within 3D histomorphometric and SDOCT reconstructions of the normal monkey ONH and to characterise its planarity as a structure.

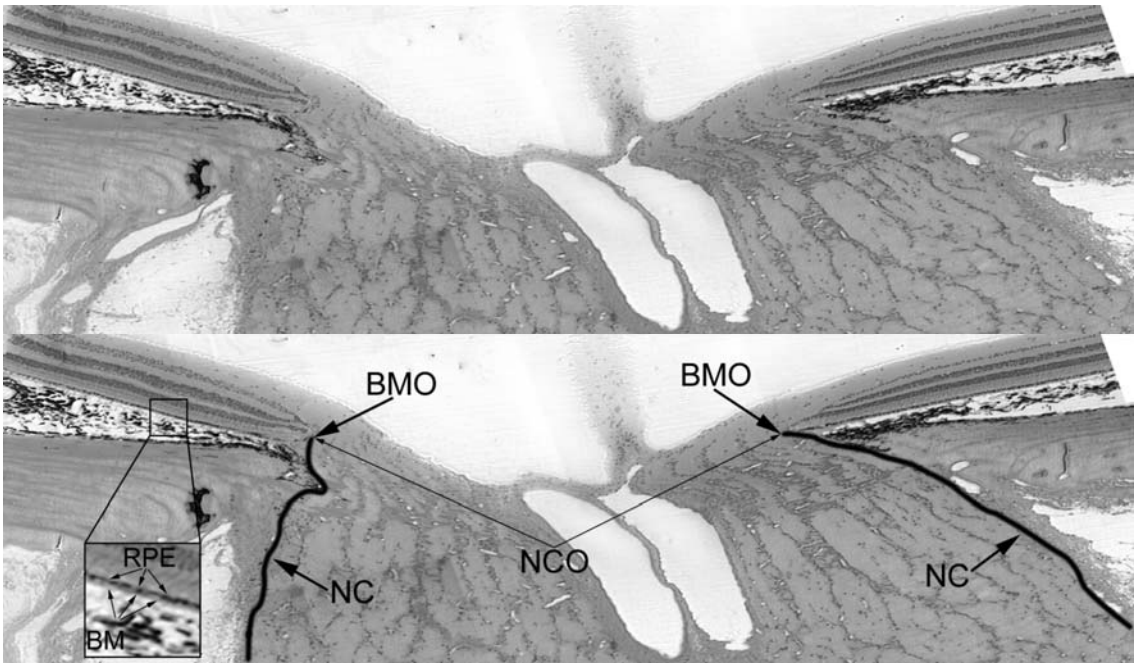

Figure 4-1. Histological section of the ONH of a rhesus macaque. NC = neural canal

4.2.3 Methods

All eyes were either SDOCT imaged in vivo or histomorphometrically reconstructed post mortem as part of other ongoing research studies. 44 normal eyes of 38 monkeys (32 rhesus macaque and 6 cynomolgus) were histomorphometrically reconstructed. A separate group of 33 normal eyes from 24 rhesus macaque monkeys were imaged in vivo using SDOCT. The characteristics of the monkeys included in the study are summarised in Table 4-1.

Histomorphometry Group (44 eyes):

These study eyes were perfusion fixed at 10 mmHg during sacrifice, as per the description in section 3.6. The generation of aligned serial sections to develop 3D histomorphometric reconstructions of the ONH has been described in section 3.7. In 14 eyes, the older lower resolution protocol was adopted in which cuts were performed at 3.0 µm depth and imaging of each cut was performed at a resolution of 2.5 x 2.5 µm per pixel. In the remaining 30 eyes, the newer higher resolution protocol was adopted in which cuts were made at a depth of 1.5 µm and the surface imaged at a resolution of 1.5 x 1.5 µm per pixel.

SDOCT Group (33 eyes):

The technical specifications of the Spectralis device have been discussed in section 3.4. All imaging was performed at 10 mmHg, using the 'short' compliance test protocol (section 3.3). For this study, 290 individual horizontal B-scans were acquired over a 15º retinal window (768 A-scans per B-scan, each B-scan was acquired 9 times and averaged for speckle noise reduction). The 290 horizontal B-scans for each OCT data set were then exported from the native Spectralis Explorer software using a 'raw' export function into custom-built, Multiview 3D visualisation and delineation software based on the Visualization Toolkit (VTK, Clifton Park, NY) (Downs et al., 2007; Yang et al., 2007a; Yang et al., 2007b) that has been modified for Spectralis SDOCT data sets. Within the Multiview software, the horizontal B-scans were interpolated into a 3D SD-OCT volume.

	HISTOMORPHOMETRY	**SDOCT**
Number of Subjects	38	24
Sex (Male : Female)	25 : 13	6 : 18
Number of Eyes	44	33
Laterality (Right : Left)	18 : 26	11 : 22
Age / Years (Median, Range)	10 (2 - 32)	10 (1 - 19)
Condition	Normal	Normal
IOP / mmHg	10	10

Table 4-1. Summary of the characteristics of the monkeys included in the NCO detection experiment. IOP shown is the IOP set at perfusion fixation in the histomorphometry eyes and the IOP at which imaging was performed in the SDOCT eyes

3D Delineation of NCO Points:

The ONHRL's 3D delineation technique within histomorphometric reconstructions has been described in detail elsewhere (Downs et al., 2007; Yang et al., 2007a; Yang et al., 2007b). The 3D ONH histomorphometric volume was loaded into memory on a remote Linux server using a suite of custom software based on the Visualization Toolkit (VTK, Clifton Park, NY). Viewing

serial digital transverse and/or radial sagittal sections of the volume, the delineator assigned the approximate centre of the neural canal to be the centre of rotation for 40, radial sagittal slices of the 3D reconstruction which were generated at 4.5° intervals.

Within each radial section, the delineator marked the NCO on either side of the neural canal (Figure 4-2, top image). Delineation of each point was 3D (3D delineation) in that each sagittal section pixel was linked to its location within a serial transverse (en face) section through the exact same location (simultaneously shown on a second monitor). Once the NCO points had been delineated for all 40 sections (80 points in total), the 3D Cartesian coordinates for each point were saved, allowing a 3D NCO point cloud to be generated (Figure 4-3).

Within each SDOCT volume, interpolated radial sagittal sections at 4.5° intervals (40 in total) were generated as per the histomorphometric reconstructions. In the case of the SDOCT volumes, the centre of rotation was taken as the centre of SDOCT image acquisition. As with the histomorphometric sagittal sections, within each section the delineator marked the location of the NCO (2 points per section; Figure 4-2, bottom) as the point at which the posterior surface of the RPE/BM complex reached the neural canal. Once the delineator had marked NCO points in all 40 radial sections (80 NCO points in total), the Cartesian coordinates for each delineated point were saved, allowing a 3D NCO point cloud to be generated (Figure 4-4).

NCO Ellipse Fitting and Quantification:

For each histomorphometric and SDOCT volume, a plane was fitted to the 80 NCO points satisfying a least mean square error restraint using Matlab (Mathworks, Natick, MA) (Figure 4-5). The shortest perpendicular distance (in 3D space) of each NCO point from the fitted plane was then calculated. Plane error for each histomorphometric and SDOCT volume was derived from the mean distance of NCO points from the fitted plane. Plane error may thus be regarded as a gauge of the planarity of the observed NCO points, with smaller magnitudes equating to higher planarity.

All NCO points were projected onto the level of the fitted plane and an ellipse was least squares fit (NCO fitted ellipse - Figure 4-5). The major and minor axes of the fitted ellipse (μm) and the area of the ellipse (μm^2) were then calculated. Within the histomorphometric volumes, the

dimensions of the fixed and embedded tissues (each with its own shrinkage artifact) were based on the voxel size dictated by the method. Within the SDOCT volumes, transverse voxel dimensions were corrected to compensate for the magnification error caused by the optical system of the monkey eye. The power change due to change in axial length (D_{axial}) was taken as $D_{axial} = (24.46 - L)/0.42$ (Wakitani et al., 2003) where L is the axial length, which was not measured in these eyes, but an estimate of 19 mm was used (Heickell et al., 2001; Qiao-Grider et al., 2007b, a) giving a D_{axial} of 13 dioptres. Lateral magnification correction (D_M) was taken as $D_M = 0.018D_{axial} + 0.002D_{refraction}$ (Wakitani et al., 2003) where $D_{refraction}$ is the power change due to the change in refractive error. As change in axial length has a 9 times greater impact on the magnification error than refractive error, it was assumed that the influence of refractive error was negligible and therefore not included in the estimation. D_M was therefore estimated as

$D_M = 0.018 * 13$

$= 0.234$

Thus NCO lateral magnitudes were divided by 1.234, while depth magnitudes (z-axis coordinates) were not affected by the optical system and were therefore not adjusted.

The relationship between monkey age and plane error was assessed using linear regression ($p < 0.05$). All statistical analyses were performed using R (R Foundation for Statistical Computing, Vienna, Austria).

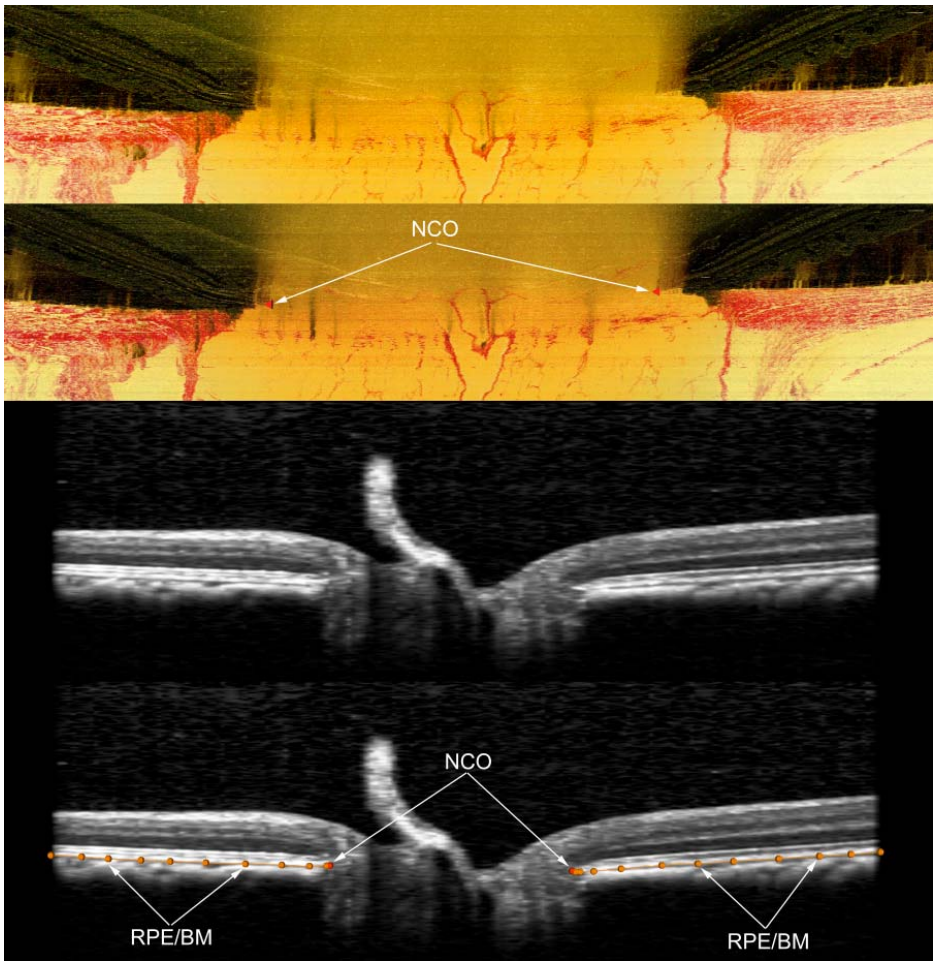

Figure 4-2. Delineation of the NCO within histomorphometric and SDOCT reconstructions. These images are Multiview software screen captures. *Top image:* digital, radial sagittal section of a histomorphometric reconstruction section (90° or horizontal in location), taken from the right eye of monkey 23540, a 9 year old female rhesus macaque. *Middle-Top image:* red triangles demarcate the location of the NCO, which in this eye is coincident with BMO. *Middle-Bottom image:* sagittal view of a radial interpolated SDOCT section (90° location), taken from the left eye of monkey 23511, a 12 year old male rhesus macaque. *Bottom image:* as per middle image, but with NCO points marked (red glyphs). The posterior surface of the RPE/BM complex is also marked (orange lines and glyphs); the NCO points are at the innermost aspect of this surface

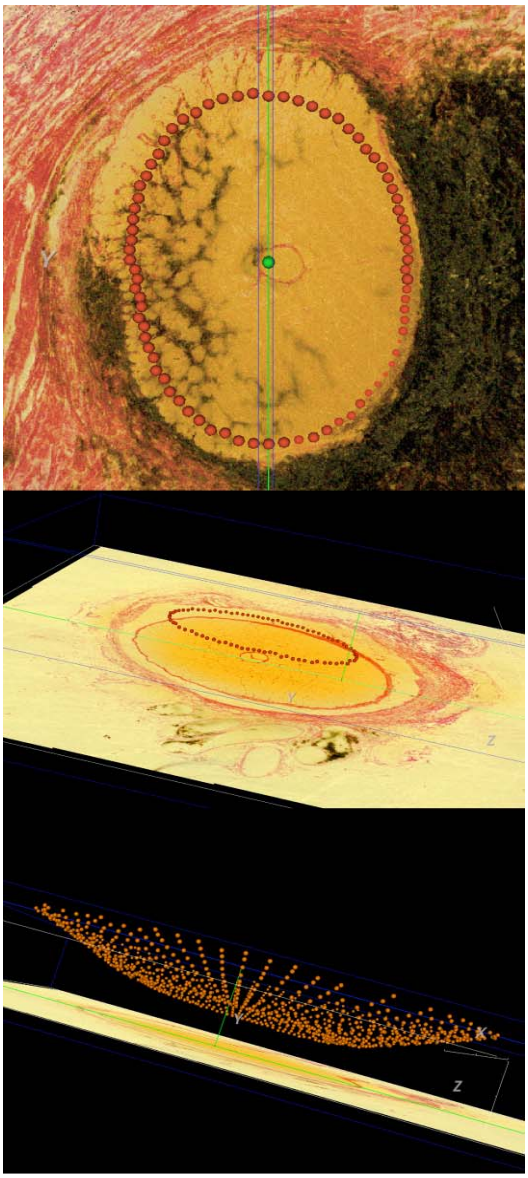

Figure 4-3. Generation of histomorphometric NCO point cloud for monkey 23540. ***Top image:*** **en face (transverse) view of histomorphometric reconstruction. All 80 NCO points (red glyphs) are shown, having been delineated in all of the 40 radial sections at 4.5° intervals. The centre of rotation is marked by a green glyph.** ***Middle image:*** **the en face view has been rotated in space, so as to demonstrate the appearance of the NCO point cloud in 3D space.** ***Bottom image:*** **an alternative view of the NCO point cloud in 3D space; the delineated BM points (orange glyphs) are also shown**

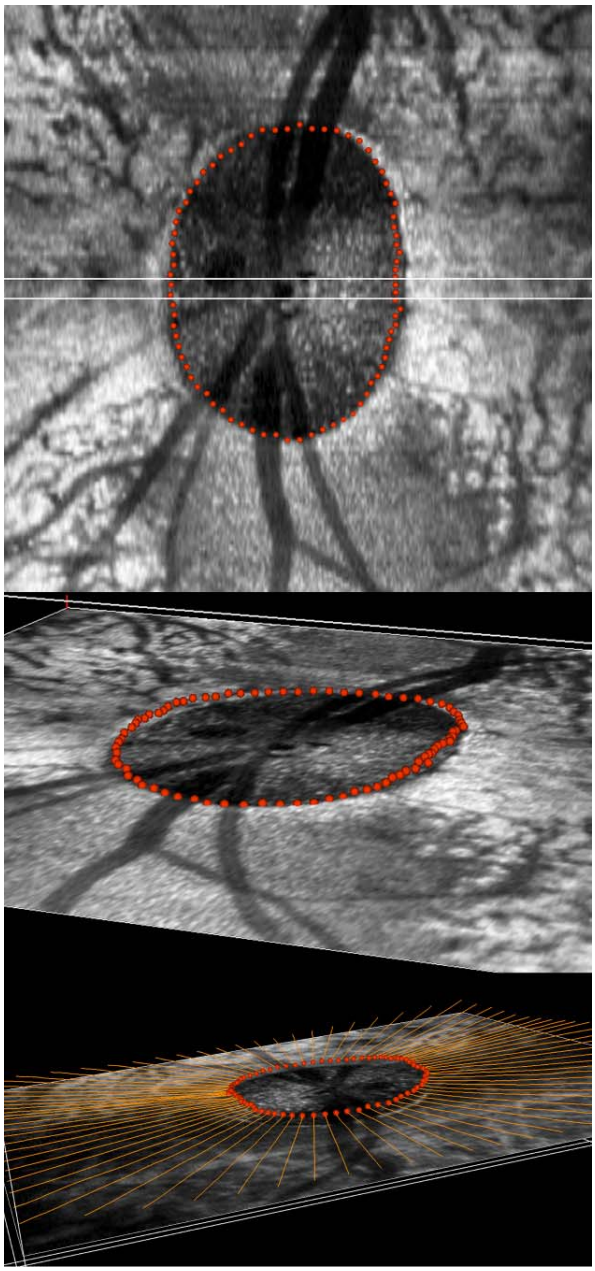

Figure 4-4. Generation of the SDOCT NCO point cloud for monkey 23511. *Top image:* en face (transverse) view of SDOCT volume. All 80 NCO points (red glyphs) are shown, having been delineated in all of the 40 radial sections at 4.5° intervals. *Middle image:* the en face view has been rotated in space, so as to demonstrate the appearance of the NCO point cloud in 3D space. *Bottom image:* an alternative view of the NCO point cloud in 3D space; the delineated BM points (orange lines) are also shown

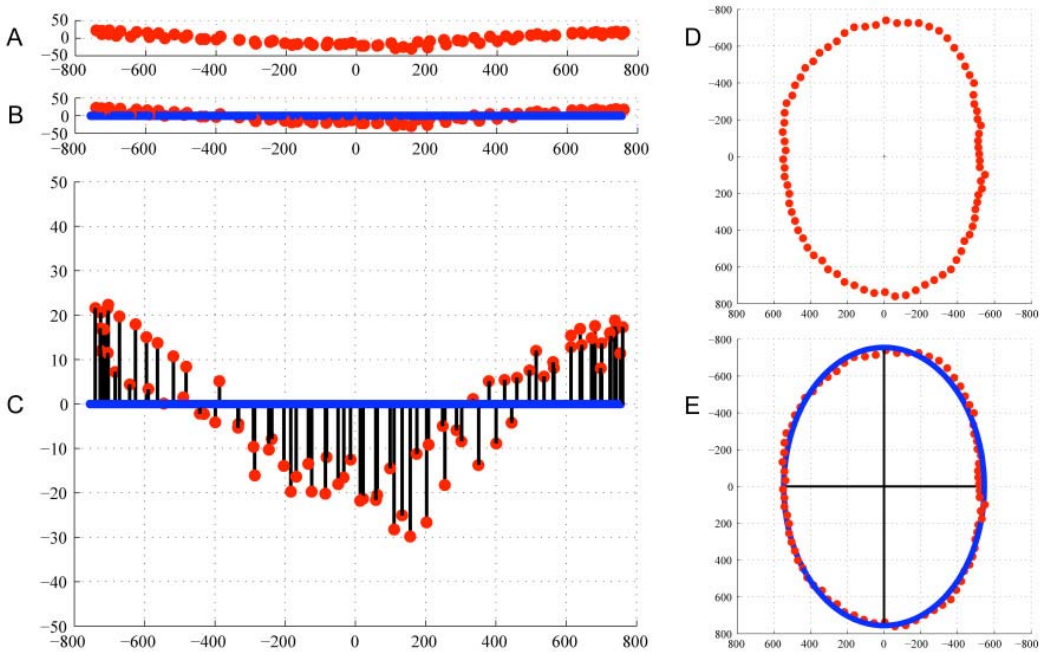

Figure 4-5. Fitted NCO plane and ellipse within an SDOCT volume from the left eye of monkey 23511. *A:* the NCO points are shown in space. *B:* a plane has been least-squares fit to the NCO points. *C:* the y-axis scale has been magnified to exaggerate the distance of the NCO points from the fitted plane (shown by the black lines). Plane error for each eye is calculated from the mean of these distances. *D:* the NCO points have been projected onto the level of the fitted plane; these 'planar' NCO points are viewed in the en face orientation. *E:* an ellipse has been least-squares fit to the 'planar' NCO points. Two black axes are shown within the ellipse, demonstrating the major (longer) and minor (shorter) axes. Eccentricity is derived from the ratio of the major ellipse axis to the minor ellipse axis

4.2.4 Results

NCO was detectable and could be manually delineated in all radial sections in both the 3D histomorphometric reconstructions and the 3D SDOCT volumes examined in this experiment. The plane errors and fitted NCO ellipse dimensions for both histomorphometric reconstructions and for 3D SDOCT volumes are summarised in Table 4-2. The magnitude of plane error in both

categories is small relative to the dimensions of the NCO ellipse, with a median plane error of 8 µm and 10 µm for histomorphometric reconstructions and SDOCT volumes, respectively. Two examples of data sets with a larger magnitude of plane error have been included for histomorphometry (Figure 4-6) and for SDOCT (Figure 4-7). It should be noted that the plane errors generated in these two examples (15 µm for monkey 675D OD and 18 µm for monkey 25904 OS) are small relative to the dimensions of their fitted NCO ellipses (1507 µm, major ellipse axis and 1193 µm, minor ellipse axis for 675D OD; 1582 µm, major ellipse axis and 1174 µm, minor ellipse axis for 25904 OS).

	Histomorphometry	**SDOCT**
Number of eyes	44	33
Major axis of ellipse (µm)	1453 (1218 - 1737)	1512 (1191 - 1865)
Minor axis of ellipse (µm)	1066 (808 - 1263)	1060 (772 - 1248)
Eccentricity (major/minor)	1.38 (1.26 - 1.56)	1.43 (1.29 - 1.67)
Area of ellipse (μm^2)	1216567 (801287 - 1722124)	1305342 (741410 - 1828049)
Plane error (µm)	8 (4 - 19)	10 (4 - 26)

Table 4-2. NCO fitted plane and fitted ellipse characteristics within the 3D histomorphometric reconstructions and SDOCT volumes. Values are median (range)

A significant association between plane error magnitude and age was observed in the histomorphometric eyes (p = 0.001, linear regression of plane error/age). However, when the two oldest monkeys, a 32 year old with a plane error of 18 µm and a 31 year old with a plane error of 15 µm, were removed from the linear regression, the association was no longer significant (p = 0.243, linear regression of plane error/age). There was no significant association between plane error and age in the SDOCT group (p = 0.565, linear regression of plane error/age).

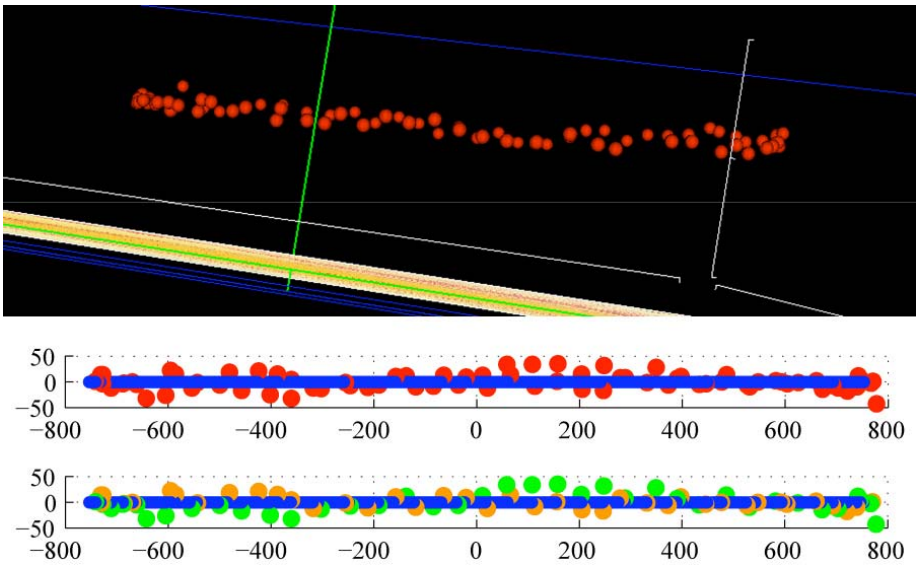

Figure 4-6. NCO point cloud *(upper image)* generated from the histomorphometric reconstruction of the right eye of monkey 675D, a 31 year old male rhesus macaque. *Middle image:* the NCO points relative to their fitted plane viewed from temporal to the disc (OD configuration, superior left and inferior right) are depicted. NCO plane error (defined as the average of the shortest distance to the plane for each NCO point) is 15 µm. *Bottom image:* when the nasal and temporal points are displayed with different colors (temporal points are green, nasal points are orange) their distribution can be seen to continuously follow a structure that is slightly twisted. This finding is easily seen when the points are visualised in 3D, but difficult to demonstrate in 2D. While method error contributes to plane error, so too does physiological non-planarity. Physiological non-planarity that is delineated reproducibly over time will still provide a stable fitted plane for a zero reference

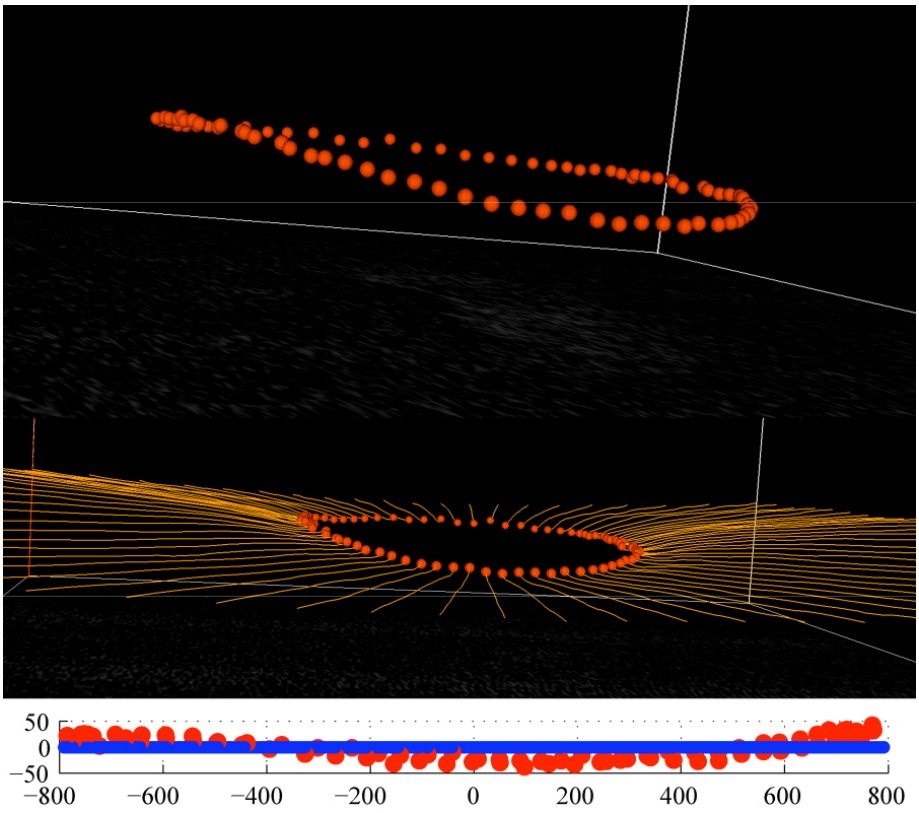

Figure 4-7. NCO point cloud *(upper image)* generated from the SDOCT volume of the left eye of monkey 25904, a 1 year old female rhesus macaque. *Middle image:* RPE/BM complex has also been delineated (orange lines). *Bottom image:* the NCO points relative to their fitted plane viewed from temporal to the disc (OD configuration, superior left and inferior right) are depicted. NCO plane error (defined as the average of the shortest distance to the plane for each NCO point) is 18 µm. Unlike in Figure 4-6, in this eye the NCO points are clearly continuous suggesting a gently bowed structure that is symmetrical about the vertical axis. While method error still contributes to plane error in this eye, physiological non-planarity is most likely the principal component

4.2.5 Discussion

The Burgoyne group has previously delineated BMO as the NCO and used it as a reference plane within quantitative 3D histomorphometric reconstructions of the ONH from both eyes of three monkeys with early EG in one eye (Downs et al., 2007; Yang et al., 2007a; Yang et al., 2007b). The purposes of this experiment were to examine the ability to detect and delineate manually the NCO within 3D histomorphometric reconstructions of a larger group of normal monkey ONHs and secondly, to perform the first rigorous assessment of NCO detection within interpolated SDOCT ONH volumes, in a separate group of normal eyes. An additional aim of this study was to characterise the structure of the NCO in both 3D histomorphometric reconstructions and in interpolated SDOCT ONH volumes, with particular reference to planarity.

The principal findings of this experiment are summarised as follows. Firstly, NCO points can be delineated within all digital, radial sagittal section images from interpolated SDOCT volumes. Secondly, NCO plane error appears to be of a similar magnitude in both histomorphometric reconstructions and SDOCT volumes of normal monkey ONHs. The NCO plane error is similarly small relative to the size of the NCO fitted ellipse. Thirdly, the NCO point clouds of both histomorphometric reconstructions and SDOCT volumes indicate that the NCO appeared to be a physiologically ‘continuous’ structure.

This experiment is the first to report 3D visualisation and delineation of SDOCT interpolated ONH volumes. As such, this study establishes the NCO to be clearly discernable and physiologically continuous within single SDOCT volumes of 33 normal monkey eyes. The depth resolution of the 870 nm Spectralis imaging system within the 40 serial radial interpolated SDOCT sections has been shown to be consistently capable of imaging the NCO, as well as the RPE/BM complex in all 33 eyes. These observations support the concept of applying SDOCT technology to image the ONH in a volumetric and quantifiable fashion using the NCO as a reference plane.

The fact that NCO plane error was low in both histomorphometric and SDOCT data sets is important for several reasons. The histomorphometric data in a much larger number of eyes strengthen the use of an NCO reference plane for quantification within 3D histomorphometric reconstructions (Downs et al., 2007; Yang et al., 2007a; Yang et al., 2007b). Likewise, the

SDOCT data provide support for an identical application of the NCO within 3D SDOCT volumes. Indirectly, one may also extrapolate that, as their magnitude of planarity is similar, in vivo SDOCT imaging may be capable of capturing the 3D architecture of the NCO in a clinically meaningful manner that is similar to its post-fixed, post-embedded, post-stained and post-reconstructed architecture. This latter statement is made with the important caveat that this experiment has not directly compared in vivo SDOCT imaging to post mortem 3D histomorphometry in the same eyes. However, in making this point, one should also note that even if the same ONH had been SDOCT imaged, then 3D histomorphometrically reconstructed post mortem, the measurements obtained would still not be directly comparable. This is because, although 3D histomorphometry is capable of measuring the dimension of structures after they have been processed (in summary, following perfusion fixation, embedding, staining, sectioning, alignment, 3D visualisation and delineation), these measurements are influenced by tissue shrinkage and measurement error. Likewise, the image acquisition and alignment software, individual eye magnification correction algorithms, as well as the 3D visualisation and 3D delineation methods affect the accuracy of in vivo measurements obtained by SDOCT. Given their respective sources of measurement error, the comparison of the SDOCT data to the 3D histomorphometric data in this experiment, and its application to human imaging must remain qualitative and preliminary in nature.

Although a correction for SDOCT magnification error has been included to compensate for the optical system of the monkey eye, this is at present imprecise. A number of methods have been published to correct for eye-camera (Bengtsson and Krakau, 1977, 1992) and eye (Littmann, 1982, 1988) magnification, all of which make assumptions regarding the optics of the eye. In the method used in this experiment, the error is based on axial length; methods using this technique have been shown to result in smaller errors and to be more accurate than those using ametropia and keratometry (Garway-Heath et al., 1998b). The magnification error only affects x- and y-axis coordinates, not those within the z-axis. The SDOCT ellipse dimensions, which are entirely based on x-and y- coordinates, are likely to be greatly influenced by any measurement error. One should therefore regard the SDOCT NCO dimensions (namely major ellipse axis, minor ellipse

axis and ellipse area) as being a best available estimate only and not infer importance from the observed similarity with histomorphometrically-derived ellipse dimensions.

Eccentricity, however, which is the ratio of the major to minor ellipse axes, is independent of magnification error in either imaging system. Eccentricity is very similar between histomorphometric reconstructions and SDOCT volumes (median values of 1.38 and 1.43, respectively), suggesting that the scale of measurements is likely to be similar, regardless of differences in magnification error. Amongst SDOCT NCO metrics, plane error is likely to be the least influenced by magnification issues as a significant component of the normal distance between observed NCO points and the fitted plane will be in the z-axis. Plane error appears to be low relative to ellipse magnitude in both imaging systems, suggesting that NCO is a relatively planar structure in both 3D histomorphometric reconstructions and in SDOCT volumes.

The resolution of the 3D histomorphometric technique improved from a 3.0 μm to a 1.5 μm voxel dimension within the group of histomorphometric reconstructions in this experiment. Despite this, neither the ability to detect the NCO in the 3D histomorphometric reconstructions nor its plane error (once detected) appeared to be influenced by this improvement. The increase in 3D resolution achieved by the newer protocol theoretically achieves a greater 'bio-fidelity' to smaller structures such as individual laminar beams and the extension of unpigmented BM beyond the end of the RPE (Downs et al., 2007).

These data suggest a relationship between the magnitude of plane error and advancing age in the histomorphometric but not the SDOCT data sets. However the maximum age of the monkeys imaged by SDOCT was only 19 years whereas there were two monkeys over 30 years of age in the histomorphometric data set. The relationship between age and NCO plane error should be studied in larger data sets as volumetric SDOCT imaging of the human ONH begins to be reported.

SDOCT NCO delineation was performed using interpolated B-scans generated from 290 x 768 horizontal 'grid' B-scan acquisitions. It is likely that the SDOCT delineation technique will be improved both by using interpolated sections generated from higher density acquisitions (for example 768 A-scans per each of 768 B-scans) or by using actual radial B-scan acquisitions,

which will have a better image quality than the current interpolated scans. Despite this, the ability to delineate NCO points in this study is encouraging, with a manageable detrimental influence from motion artifact and/or shadowing from blood vessels.

The 290 horizontal B-scan acquisition protocol takes 70 seconds in an anaesthetised monkey. It is likely that the same scan will take considerably longer in an awake human subject, and longer still for a test of higher B-scan density. Acquiring 40 or 80 radial B-scans will likely be of shorter duration and will have the advantage that one will be able to delineate structures within the acquired B-scan, rather than an interpolated SDOCT section. A disadvantage to this approach is that interpolated 3D volumes cannot, at present, be generated from radial B-scan acquisition patterns. As a consequence, true 3D delineation of the NCO points (in which the delineator can cross-reference demarcated points between the location in the transverse and sagittal view prior to actual delineation), which powerfully aided this experiment, will not be possible using radial B-scan acquisitions in isolation.

NCO visualisation with volumetric (or serial B-scan) SDOCT images may be enhanced with clinical application of a higher wavelength source. In an in vivo study of high resolution OCT imaging of the human retina, a 1050 nm wavelength source was found to achieve greater depth resolution than an 870 nm source (Povazay et al., 2007a). Visualisation beyond the RPE and into the choroidal vasculature was achieved and this depth resolution was maintained even in the presence of significant cataract. It will therefore be necessary in the future to investigate the effect of a 1050 nm light source on the ability to delineate NCO and deep ONH structures in the monkey eye.

Whilst the results show that SDOCT is capable of reliably discerning the NCO in the monkey eye, this may not necessarily be consistent in the human eye. The reason for potential discrepancy is due to differences in the amount of pigment at the level of the RPE/BM. In normal monkey eyes, RPE and choroidal atrophy are uncommon whereas they are relatively common in humans, particularly in the aged eye. It will not be apparent whether the NCO is detectable in this context until this experimental methodology can be applied to human eyes.

The location of the reference plane - effectively the landmark from which all structural quantification is measured - is critical in longitudinal imaging of the ONH. The topographical height of the reference plane has been shown to be the major contributor to parameter variability using the HRT. The default reference plane used in the HRT operational software is the standard reference plane, which is located 50 μm posterior to the temporal disc margin. The choice of the temporal disc margin was based on the assumption that its height would be stable until the latest stages of glaucoma when papillomacular bundle thinning would be expected to take place (Burk et al., 2000). However, OCT evidence suggests that RNFL thinning occurs at a much earlier time frame in the disease process (Park and Caprioli, 2002). Given this caveat, any measurements generated using a reference plane anchored to the retinal surface height at the disc margin are likely to fluctuate longitudinally as the topographical surface shifts posteriorly as glaucoma progresses.

Studies have shown that HRT reference planes anchored to the retinal surface height at a reference ring located in the image periphery generate less variable stereometric parameters, particularly rim area, and this most likely reflects the more stable topographical surface height at locations distal to the optic disc (Poli et al., 2008; Strouthidis et al., 2005a; Tan et al., 2003b; Tan and Hitchings, 2003). However, the peripheral surface-anchored reference planes have the shortcoming that they generate erroneous measurements when applied to atypical disc morphology, particularly those with gross tilt or advanced peripapillary atrophy. Indeed, defining the reference plane relative to the topographic surface is always likely to be problematic, as the height of the internal limiting membrane will alter as the nerve fiber layer thins in progressing glaucoma.

A reference plane source structure deep within the ONH, such as the NCO, is a more logical option if it is reasonable to assume that this structure will be more stable than the internal limiting membrane through the onset and progression of glaucomatous damage. It is likely that the position of the NCO will remain relatively stable throughout the course of the neuropathy relative to the ONH neural and connective tissues, the primary sites of glaucomatous damage that are known to be damaged early in the neuropathy (Bellezza et al., 2003b; Burgoyne et al., 2004;

Gaasterland et al., 1978; Minckler et al., 1977; Quigley et al., 1981; Quigley and Green, 1979). If this is true, alterations in the anterior laminar surface and prelaminar neural tissue internal limiting membrane should be more sensitively detected relative to the NCO during periods in which retinal surface based reference planes are themselves being altered by the neuropathy. However, the position of the NCO and the same ONH target tissues may change relative to the peripapillary sclera due to glaucomatous (outward) bowing of the peripapillary sclera (Yang et al., 2007b). Since this bowing, when it is present, is believed to be part of the neuropathy, it may be advisable to use the NCO as a source structure for a secondary (peripheral) reference plane that is located at a fixed distance from the NCO on the RPE/BM complex. The advantage of such a peripheral zero reference plane would be the detection of both glaucomatous scleral deformation and ONH neural and connective tissue alterations at all stages of the neuropathy.

This experiment is the first to visualise and delineate deep ONH structures within SDOCT 3D volumes acquired in vivo. In doing so, the NCO has been shown to be continuous and reasonably planar which supports its adoption as the SDOCT reference plane source structure within the monkey and human ONH.

4.3 Assessment of Disc Margin Anatomy Using 3D Histomorphometry

4.3.1 Background

An appreciation of the optic disc margin is centrally important in the examination of all glaucoma patients as it defines the clinically visible boundary of neural tissue within the ONH. With the advent of semi-automated ONH imaging devices, the ability to clearly identify and delineate the optic disc margin has assumed increasing importance. The disc margin serves both as a basis for cross-sectional neural tissue quantification and perhaps as a structural anchor for a reference plane for longitudinal change detection.

Understanding the anatomical basis of the clinical disc margin remains a significant challenge for all clinicians (Manassakorn et al., 2008). Although the optic disc is usually examined in a stereoscopic fashion - either by slit lamp biomicroscopy, or by stereophotograph examination - it remains difficult to appreciate the location of the disc margin within the ONH's complex 3D architecture. The conventional view is that the clinical disc margin is defined by the scleral ring of Elschnig which is the anterior-most extension of the border tissue of Elschnig (Jonas et al., 1988a). The border tissue of Elschnig refers to densely compacted connective tissues that rise up from the sclera to join BM and thereby enclose the choroid. Previous work by the ONHRL has proposed, however, that in monkey eyes, the clinically visible disc margin is the BMO, which in this species often extends beyond the border tissue (Downs et al., 2007).

4.3.2 Purpose

In this experiment, the histological basis of the monkey optic disc margin is explored by co-localising post mortem 3D ONH reconstructions to their clinical (in vivo) optic disc photographs in 28 normal monkey eyes.

4.3.3 Methods

All eyes were histomorphometrically reconstructed post mortem as part of other ongoing research studies. 28 normal eyes of 21 rhesus macaques and one cynomolgus monkey were reconstructed.

All animals included in the study had regular optic disc stereophotographs acquired as part of imaging protocols developed for other ongoing research studies, as per the description in section 3.4. Stereophotographs were acquired after 30 minutes of IOP stabilisation at IOP 10 mmHg, as per the 'short' compliance test protocol (section 3.3). Stereophotographic pairs in 15 eyes were acquired using a Topcon TRC-WT Retinal Camera (Topcon, Paramus, NJ). Latterly, this system was replaced with a Nidek 3-D_X fundus camera system (Nidek, Fremont, CA) that was used to acquire stereophotographs in the remaining 13 eyes. Images were captured onto 35 mm slide film, which was developed and processed into color slides.

For the purposes of the current study, a stereophotograph pair was selected from the day on which the animal was killed. If stereophotographs were not acquired on this date then images acquired on the closest date were selected. Images had to be of sufficient quality to allow co-localisation to the histomorphometric 3D vessel reconstruction, meaning that at least one photograph in the pair should have had clearly discernible central retinal vessels. A good stereo-effect and a clear focus at the disc margin were desirable secondary considerations but were not grounds for exclusion of a stereophotograph pair. Selected stereophotograph slides were digitised at a resolution of 4800 dpi using a colour-calibrated Microtek ArtixScan M1 slide scanner (Microtek Lab, Inc., Fontana, CA).

All eyes underwent perfusion fixation at 10 mmHg during sacrifice, as described in section 3.6. The method for generating 3D histomorphometric ONH reconstructions has been described in section 3.7. In this experiment, 3 eyes were reconstructed using the older, low resolution technique (3.0 x 2.5 x 2.5 μm voxels) and the remaining 25 eyes were reconstructed using the second generation high resolution technique (1.5 x 1.5 x 1.5 μm voxels).

The method for delineating the BMO points in the 28 3D histomorphometric reconstructions in order to generate a 3D BMO point cloud is as described in the previous experiment (section 4.2.3).

Overlay and Alignment of Histomorphometric Reconstructions Onto Disc Photographs:

In order to establish the clinical orientation of each 3D histomorphometric reconstruction, a high resolution 3D reconstruction of the central retinal vessels and BMO points was generated for each eye. The 3D vessel reconstruction was then overlaid onto a digitised clinical photograph (the best focused photo from the stereophotograph pair) using Paraview (Kitware, Inc., Clifton Park, New York) parallel viewing software. A single operator (myself) performed all of these co-localisations. Paraview enabled the operator to move the clinical photograph in 3D space in terms of x-axis, y-axis and z-axis shifts as well as allowing rotation about the z-axis, z-axis tilt and magnification change.

The 3D co-localisation protocol is depicted in Figure 4-8. Z-axis adjustments were made with the photograph viewed on its side, along the coronal plane, with the BMO point cloud visualised; this allowed the disc photograph to be tilted in the same orientation as the BMO point cloud. The BMO points were excluded from view for x- and y-axis manipulations, as well as z-axis rotation and magnification changes so that the final co-localisation was based on the alignment of the central retinal vessels rather than by the alignment of the BMO points to the clinically visible disc margin.

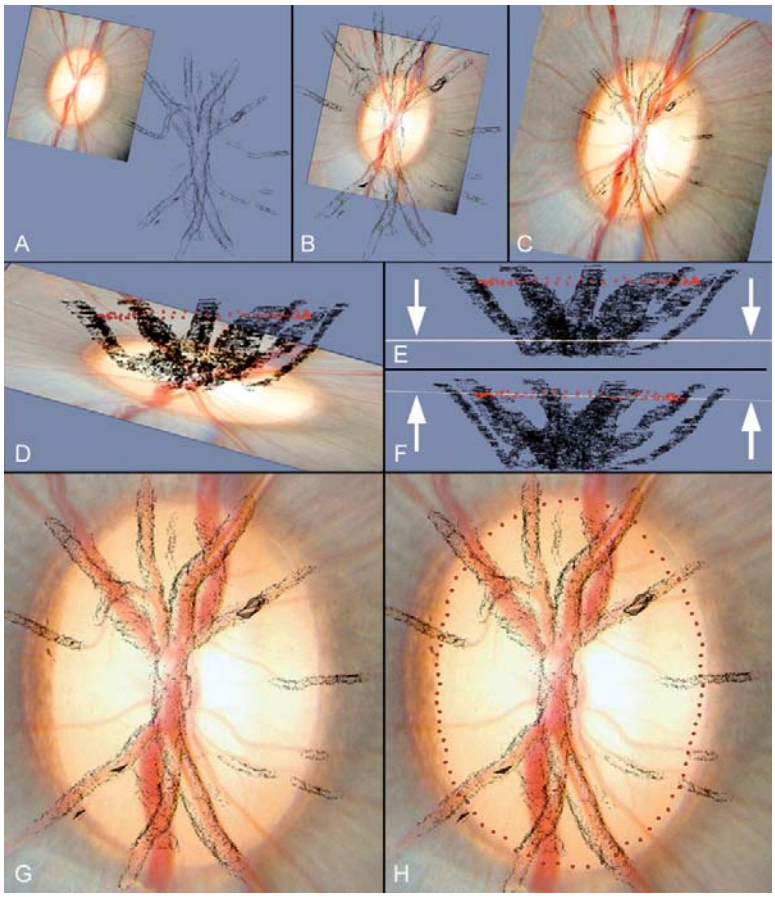

Figure 4-8. Method for co-localising the disc photograph to the 3D vessel reconstruction. *A:* the photograph and vessel reconstruction are viewed prior to co-localisation. *B:* x- and y-axis shifts allow approximate co-localisation in the horizontal plane. *C:* magnification of the disc image has been increased to match dimensions of the vessel reconstruction. *D:* the photograph and vessel reconstruction are viewed in the coronal plane, with BMO point cloud visible (red glyphs). *E:* z-axis tilt has been adjusted so that the disc image (highlighted by arrows) is orientated in the same plane as the BMO point cloud. *F:* the disc image has been moved vertically so that the image profile coincides with the BMO point cloud. Once completed, the BMO points are switched off. *G:* the disc image is viewed in the en face orientation following z-axis adjustment. A rotation about the image centroid has been performed to align the photographic vessel outline to the vessel reconstruction. *H:* the final location of the BMO points in relation to the disc photograph is displayed

Systematic Review of Stereophotographs and Delineation of the Disc Margin:

Once I had achieved a satisfactory co-localisation of the clinical vessels to the 3D vessel reconstruction, screen captures were saved of the disc photographs with and without the co-localised BMO points. The two photographs were then overlaid using Adobe Photoshop CS3 (Adobe Systems, Inc., San Jose, CA) and saved as a two-layer image file.

An experienced clinical observer (Professor Burgoyne) viewed each eye's digitised stereophotograph pair on a computer monitor using a Screen-Vu stereoscope (PS Mfg., Portland, OR). Where the disc margin structures were not clearly discernible, the observer also had access to the original stereophotograph slides which could be viewed either using a hand-held stereo viewer (Asahi-Pentax Co., Englewood, CO) if the stereophotographs were acquired using the Nidek system or using a light box and mounted stereo viewer (Luminos Photo Corp, Yonkers, NY) if the stereophotographs were acquired using the Topcon system.

For each eye, the observer marked out the disc margin on the clinical photograph using a custom Java-script application. The clinical photograph used for this purpose was the co-localised image layer with the BMO excluded from view. The observer could make two categories of marks - blue marks for where the observer was 'certain' of the disc margin and green marks for where the observer was 'uncertain' and made a 'forced' choice.

For this study the operator marked the innermost visible disc margin structure that was usually the internal edge of an unpigmented, whitish halo or crescent. Where this unpigmented structure was not visible, the termination of the variably mottled disc margin pigment was delineated. In some eyes, the observer could stereoscopically discern two different levels of pigment, an outer superficial layer and an inner deeper layer, with a portion or 'lip' of unpigmented tissue variably present at the termination of either pigmented tissue. In these circumstances two rows of marks were made - an outer row of single marks to demarcate the internal edge of the superficial tissue (either pigmented or unpigmented) and an inner row of double marks (a green mark touching a blue mark) to demarcate the termination of the deeper tissue (either pigmented or unpigmented).

Once the observer completed the demarcation of the clinically visible disc margin, the coordinates of the marked points were saved and the points transferred onto the image layer in which the

BMO points were also shown. An image of the disc photograph incorporating the co-localised BMO points and the clinical disc margin demarcations was then saved for each eye.

Systematic Review of Histomorphometric Reconstructions:

Prior to assessing the alignment of the BMO to the disc margin, the 3D histomorphometric volumes of all 28 eyes were reviewed by two observers (myself and Professor Burgoyne). For each eye, we documented the quality of the connective tissue staining, the degree of pigment in the reconstruction and the presence or absence of artifacts such as choroidal or retinal detachments. Choroidal and retinal detachments were assumed to be post mortem artifacts as they were not present in optic disc images/disc photographs acquired on the day of sacrifice. The perfusion fixation process is assumed to provide sufficient hydrostatic pressure to cause expansion of the choroidal space in a majority of eyes. Sections at 0°, 45°, 90° and 135° were loaded, enabling the histology in the superior-inferior, superotemporal-inferonasal, temporal-nasal and inferotemporal-superonasal regions to be inspected. In order to establish the histological underpinnings of the clinical disc margin, we carefully reviewed the configuration of BM, BMO and the border tissue of Elschnig in each sector of the disc. We noted how far BM extended beyond the termination of the border tissue, the presence or absence of an unpigmented portion of BM, the configuration of the border tissue in relation to where it met BM and whether or not the histomorphometric BMO delineation was felt to be accurate.

Comparison of the Histomorphometrically-Defined BMO with the Clinical Disc Margin:

Once delineation of the disc photos was completed, two observers (myself and Professor Burgoyne) qualitatively reviewed the images incorporating the histomorphometric BMO marks and disc margin marks. This was performed to assess how well the co-localised histomorphometric BMO marks aligned with the disc margin delineations. An eye was classified as being well aligned if there was less than a glyph's diameter separation between adjacent BMO and disc margin glyphs in all disc sectors, with disc sectors being defined as per the systematic histomorphometric review. In eyes with misalignment between the histomorphometric BMO and disc margin marks by the above definition, the following investigations were performed to identify causes for the observed discrepancies. First, the co-localisation process was repeated, leading to

a ‘second pass’ review of the co-localised BMO and disc margin marks. In eyes where the alignment between BMO and disc margin marks could not be improved by repeated co-localisation, a second, systematic review of the relevant sterephotographs and 3D histomorphometric reconstructions was carried out so as to identify the salient clinical and/or histologic features that might explain the misalignment.

4.3.4 Results

Systematic Review of 3D Histomorphometric Reconstructions:

In most eyes, an extension of BM with mottled pigment on its surface, which was defined as ‘pigmented’ BM, was usually present beyond the histomorphometric termination of the border tissue of Elschnig and choroid. A further extension of BM without surface pigment (‘unpigmented’ BM) could be detected internal to pigmented BM in most high resolution 3D histomorphometric reconstructions. Figure 4-9 illustrates the distinction between unpigmented and pigmented BM in a histomorphometric section. An extension of BM was visible in at least one disc region of every eye examined in this study. A substantial extension of BM was observed most frequently in the superior and nasal sectors (both 43% of eyes), followed by the inferonasal (39%), superonasal (36%), temporal (29%), inferotemporal (25%) and superotemporal (21%) sectors. Unpigmented BM was usually visualised despite the presence of darker tissues or poor tissue staining. However, its detection in the three low resolution volumes was less consistent as this resolution was perhaps insufficient to allow reconstruction of unpigmented BM.

Accurate delineation of BMO was made difficult where pigment was present on the laminar or scleral surface, as the ‘shadow’ cast by this pigment could obscure the termination of BM (Figure 4-10). Rarely, the border tissue met the termination of BM and no extension was present. Artifactual choroidal or retinal detachments were present in three eyes (Figure 4-10), but these did not involve the BM/border tissue junction and so did not affect the configuration of the disc margin anatomy.

Border Tissue of Elschnig Configuration:

Four principal border tissue configurations were recognised. In the most common form, the superior edge of the border tissue extended internal to the border tissue/scleral junction. I defined this configuration to be ‘internally oblique’ (Figures 4-11A and 4-12A). Less commonly, the superior edge of the border tissue was external to the border tissue/scleral junction. I defined this configuration to be ‘externally oblique’ (Figures 4-11B and 4-12B). The border tissue also manifested vertical (no obliqueness) and horizontal (an extreme form of internal obliqueness) configurations (Figure 4-11C and 4-11D, respectively). These configurations could vary regionally within an individual eye. In rare instances the border tissue was regionally not discernible. As noted above, regardless of border tissue configuration, a pigmented or unpigmented extension of BM beyond its termination was commonly present.

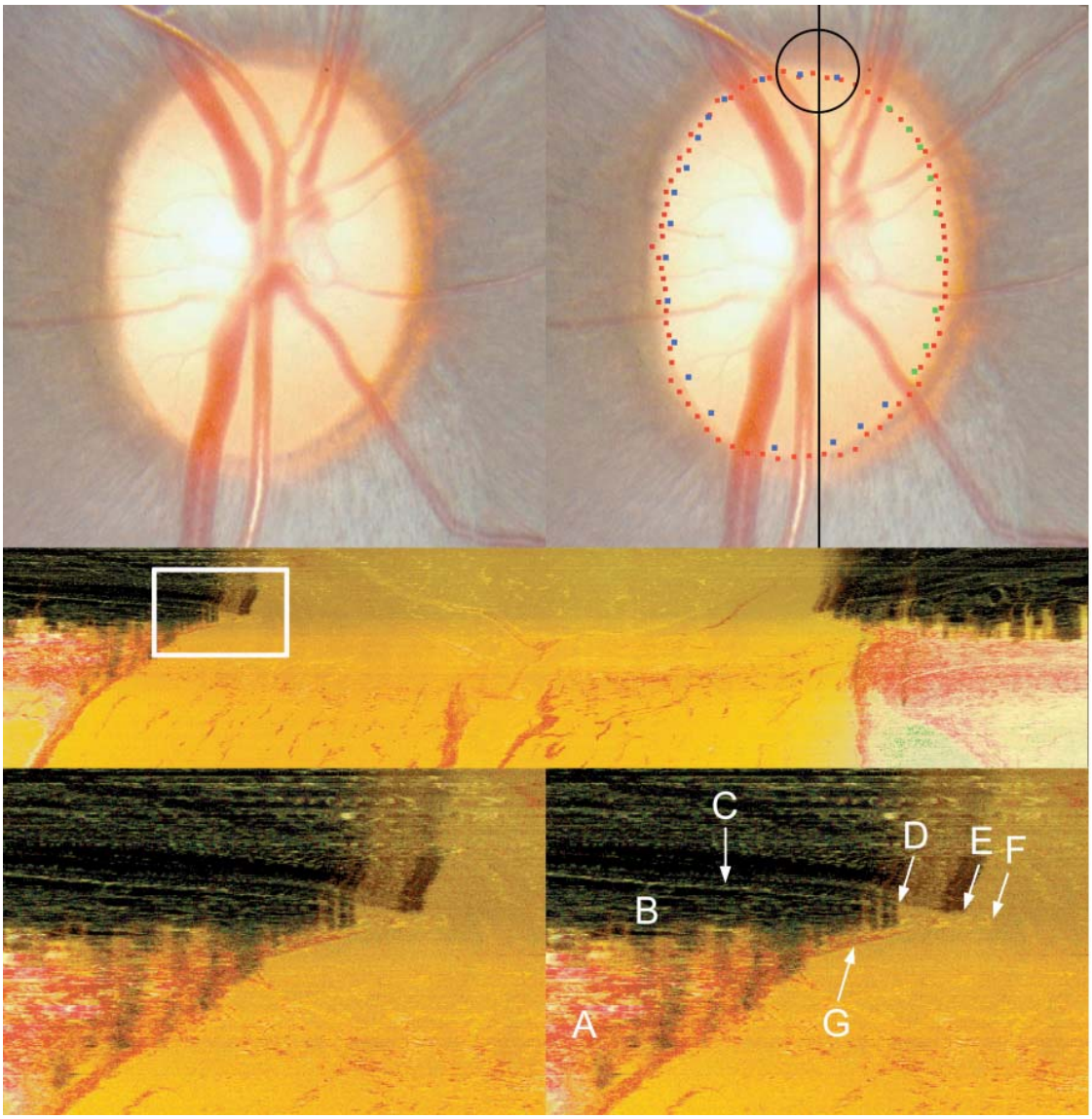

Figure 4-9. The identification of BM and BMO in a histomorphometric section. *Top left panel*: the disc photograph (OD) prior to disc margin delineation. *Top right panel:* the disc photograph displaying both the co-localised histomorphometric BMO points (red glyphs) and the disc margin points (blue and green glyphs). The black line is the approximate location of the vertical histomorphometric section shown in the middle panel. The area circled in black is the approximate location of the histomorphometric region (white box in the middle panel) magnified in the two bottom panels. *Middle panel:* central vertical histomorphometric section shown as a black line in the top right panel. Superior is left and inferior is right. The area within the white box is magnified in the bottom panels. Note that

because the tissues are sectioned from the vitreous (top) to the orbital optic nerve (bottom) a dark shadow is present until the serial sectioning plane passes through the dense pigment of the RPE, choroid and BM. *Bottom left panel:* magnified view of the highlighted white box in the middle panel which demonstrates the superior disc margin anatomy. Bottom right panel: The same region, labelled as follows:

A = sclera

B = choroid

C = BM

D = commencement of pigmented BM, which in this section appears to co-localise to the termination of the choroid (B)

E = termination of pigmented BM and the commencement of unpigmented BM. Note the presence of pigment 'shadows' of variable density cast vertically along the course of the pigmented BM, which are absent in the regions where BM is unpigmented

F = termination of unpigmented BM, which would be delineated as BMO in this section

G = border tissue of Elschnig. In this eye, BM fuses with the superior edge of the border tissue and extends slightly beyond its termination

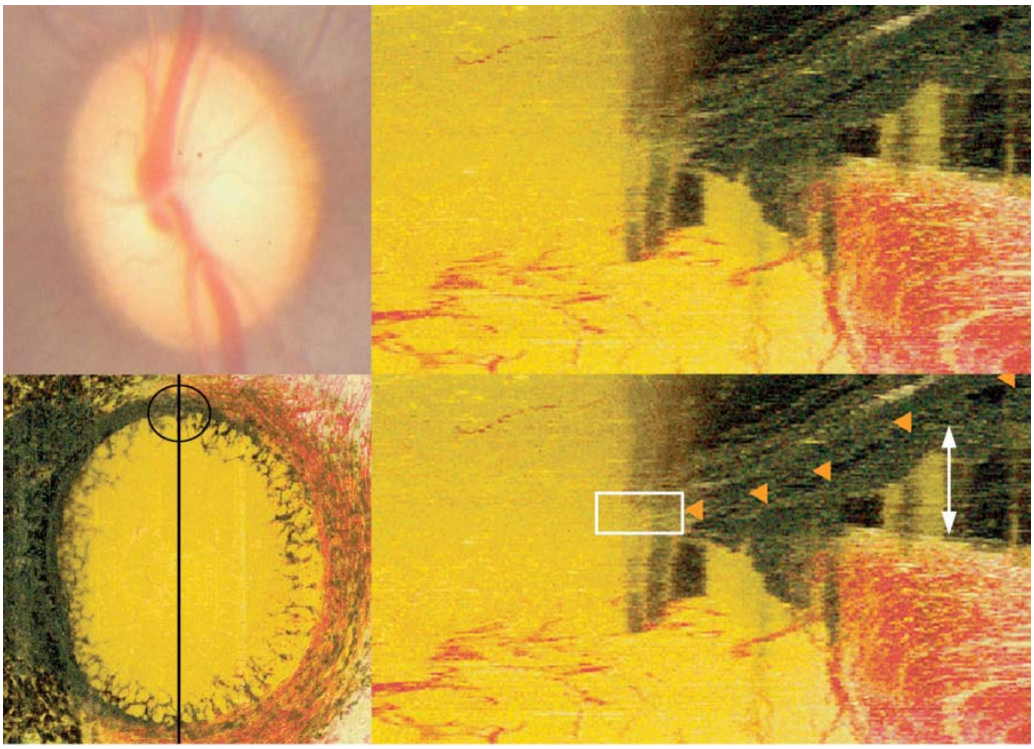

Figure 4-10. Pigment on the laminar surface causing obfuscation of BMO. ***Top left panel*****: disc photograph (OS).** ***Bottom left panel:*** **en face view of the histomorphometric reconstruction of the same eye. Black line shows the orientation of a histomorphometric section image, a portion of which (the superior disc margin) is magnified in the right panels. The black circle highlights the region viewed in the right panels; note the presence of pigment on the laminar surface.** ***Top right panel*****: histomorphometric view of the superior part of the neural canal.** ***Bottom right panel:*** **BM is delineated (orange glyphs). The white rectangle highlights an area where the view of BM is obscured by a dark shadow cast from the laminar pigment below. In this circumstance, accurate delineation of BMO can be difficult. The white arrowheads highlight the extent of an artifactual choroidal detachment, most likely caused by the perfusion fixation process**

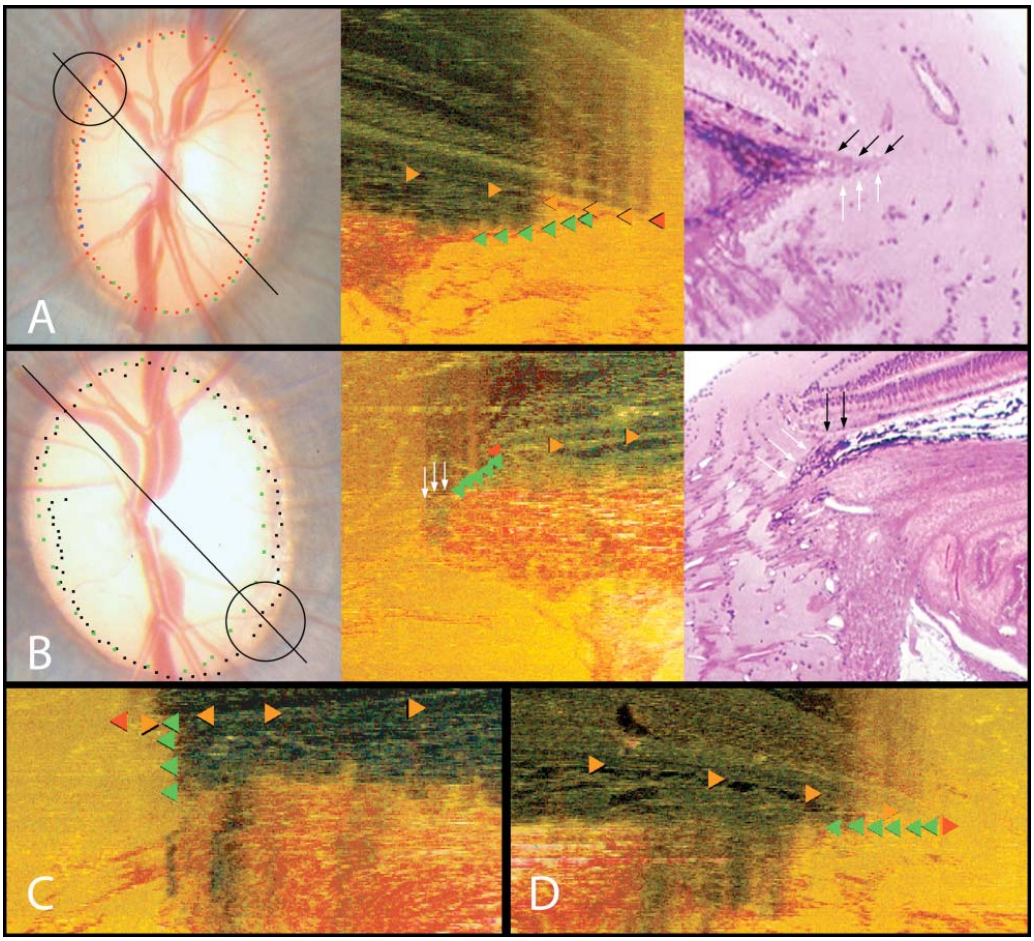

Figure 4-11. Two principal border tissue configurations with variations.

***A* illustrates the internally oblique configuration. *Left panel:* disc photograph (OS) showing the co-localised BMO (red glyphs) and disc margin delineations (blue and green glyphs). The black line shows the approximate orientation of the histomorphometric section from which the circular region is the adjacent panel. *Middle panel:* histomorphometric disc margin region showing the delineations for BM (orange glyphs), BMO (red glyph) and border tissue (green glyphs). The inferior edge of border tissue communicates with sclera and the superior edge extends into the neural canal fusing with BM, which extends beyond this point and includes an unpigmented portion. *Right panel:* representative histological section taken from a different, normal monkey eye (perfusion fixed at IOP 10 mmHg, haematoxylin and eosin stain) demonstrating an internally oblique configuration. White**

arrows highlight border tissue, black arrows highlight an extension of unpigmented BM. In this case there is no clear extension of BM beyond the termination of the border tissue

B **illustrates the externally oblique configuration.** ***Left panel:*** **disc photograph (OD), demarcated as in A. Note that within and around the circled region the clinical disc margin has been marked internal to the BMO points.** ***Middle panel*****: histomorphometric section showing the border tissue configuration, demarcated as in panel A. Note that the inferior edge of the border tissue is internal to its termination at BM. BM does not extend beyond the border tissue's termination. In this instance, dense pigment within the sclera immediately adjacent to the neural canal casts a shadow upwards that probably explains the lack of a highly reflective "scleral lip" (white arrows) within this region of the clinical photograph.** ***Right panel:*** **representative histological section taken from a different, normal monkey eye (perfusion fixed at IOP 10 mmHg, haematoxylin and eosin stain) demonstrating the externally oblique configuration. White arrows highlight the border tissue, black arrows highlight BM (pigmented)**

C **illustrates the vertical configuration. Border tissue extends vertically from the sclera to meet BM. BM extends beyond this point with both pigmented (outer) and unpigmented (inner) portions**

D **illustrates the horizontal configuration. Border tissue extends horizontally to meet BMO. This configuration is an extreme form of an internally oblique border tissue configuration**

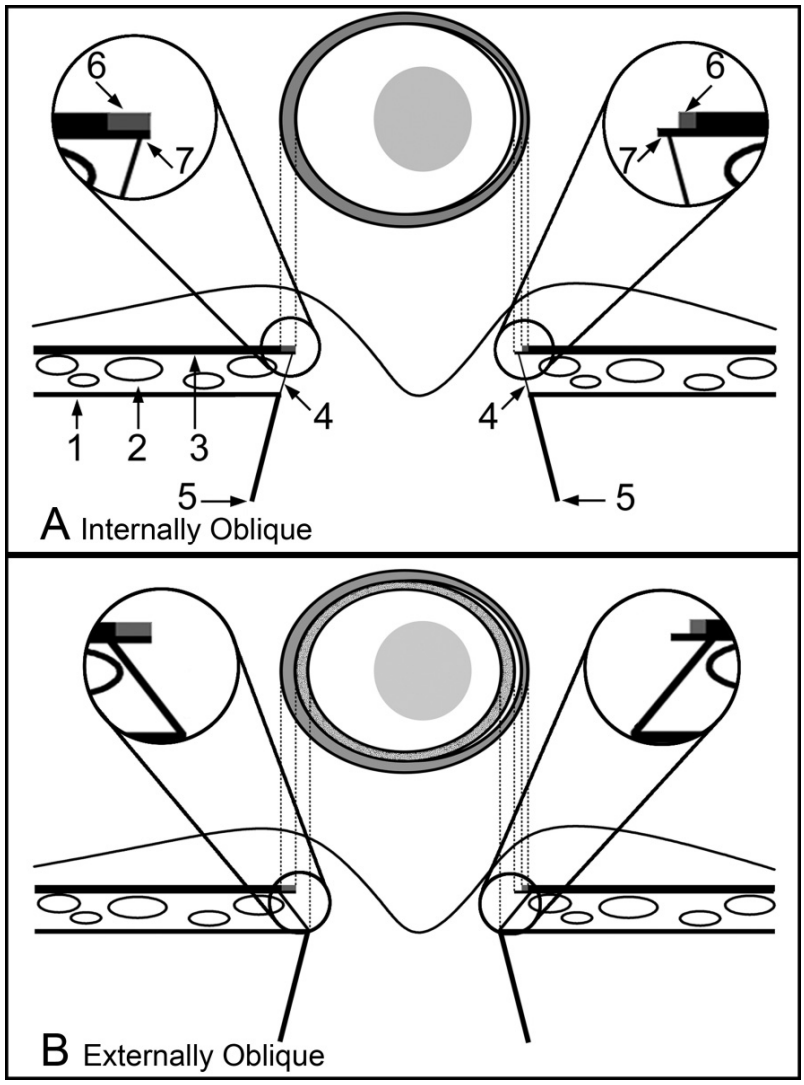

Figure 4-12. Two principal border tissue configurations, their relationship to a pigmented or unpigmented extension of BM and the resultant disc margin anatomy. ***A*** **illustrates the internally oblique configuration. The diagram shows the optic disc appearance (above) and a cross section of the ONH (below). 1 = sclera, 2 = choriocapillaris, 3 = RPE with BM, 4 = border tissue, 5 = neural canal boundary, 6 = pigment on the surface of BM, 7 = BM.** ***Magnified inset left:*** **pigmented BM corresponds to the halo of pigment on the left side of the disc margin.** ***Magnified inset right:*** **a region of unpigmented BM is shown; this corresponds to a white crescent internal to the pigment halo at the disc margin (which corresponds to a portion of pigmented BM)**

***B* illustrates the externally oblique configuration. Labelling is as per the schematic in panel A. *Magnified inset left:* BM is pigmented to its end and extends beyond the termination of the border tissue. This BM extension corresponds to an external crescent of pigment at the disc margin that is internal to the termination of the RPE. The portion of the border tissue that is internal to BMO may be recognisable as an inner reflective or a pigmented crescent (if there is pigment on the border tissue surface) that is posterior to the plane of the RPE. An inner pigmented halo (lighter grey and stippled) is shown on both sides of the disc diagram. *Magnified inset right:* unpigmented BM extends internally to the border tissue termination, corresponding to a reflective crescent internal to the pigment crescent. Again, pigmented border tissue (lighter grey and stippled) extends internal to the reflective crescent. In both the left and right insets the border tissue/scleral junction is depicted without a true scleral lip which when present and visible, appears internal and deep to the other structures**

Comparison of Clinical Disc Margin and BMO Alignment:

20 eyes demonstrated good alignment between histomorphometric BMO marks and clinical disc margin marks (examples shown in Figure 4-13) within all sectors of the disc. Of these 20 eyes, 16 had the disc margin marked where an innermost unpigmented region was present at the disc margin (Figure 4-13C). In these eyes, the termination of unpigmented BM corresponded to the delineated disc margin and the clinically visible mottled pigment external to it corresponded to pigmented BM.

Of the 4 remaining eyes with good agreement between the clinical markings and histomorphometric BMO, 2 did not have a clinically visible ‘unpigmented’ disc margin structure, so the termination of mottled pigment was marked instead, which coincided with the histomorphometric BMO. In 2 eyes, the observer felt that there was pigment at two different planes, with an internal unpigmented ‘stripe’ present at the internal border of the superficial outer pigment. In these eyes, the inner edge of both the unpigmented stripe and the termination of the ‘deeper’ pigment were marked. Following co-localisation, however, the BMO aligned with the

innermost clinical markings. Systematic review of the relevant histomorphometric sections confirmed that BM was the innermost disc margin structure, and not the border tissue, within these areas of the disc. There was, however, no histomorphometric correlate that could explain the pale stripe seen within the pigment, nor the clinically perceived different levels of pigment. It is possible that the pale stripe could represent an area of vitreous attachment to the optic disc, but this could not be confirmed in the absence of in vivo examination of these eyes.

Sources of Misalignment:

In 8 eyes there were substantial regions in which the disc margin and histomorphometric BMO points were poorly matched. Alignment improved considerably in 4 of these eyes following repeat co-localisation.

4 eyes did not achieve a good match between disc margin marks and BMO marks, despite satisfactory co-localisation at the second attempt. In each of these 4 eyes, however, the discrepancy between marks was confined to 2 or fewer sectors. In the first of these eyes, the disc margin marks were internal to the histomorphometric BMO marks in the superonasal and nasal sectors. Careful review of the histomorphometric sections within the poorly matched regions revealed that a substantial portion of unpigmented BM was present, extending internally into the neural canal, beyond where the BMO had been originally delineated. Thus, in this eye, the disc margin and histomorphometric BMO marks would have been more closely matched if the full extension of unpigmented BM had been histomorphometrically delineated.

In the second eye, the disc margin marks were again internal to the histomorphometric BMO marks in the temporal sector only. Histomorphometric review confirmed that an extension of unpigmented BM was not histomorphometrically detectable in this region of the disc. When a review of the disc photographs again confirmed the presence of a reflective inner halo within this region, it was assumed that the histomorphometric technique had failed to reconstruct unpigmented BM within this region. As this was one of the low resolution histomorphometric reconstructions, this finding may confirm a relative inability to resolve unpigmented BM.

In the third eye, the disc margin marks were external to the histomorphometric BMO marks in the nasal and superonasal sectors. In this eye, histomorphometric review revealed that, similar to the

first eye, a narrow extension of unpigmented BM had been missed in the original delineation. However, in this instance, correcting the histomorphometric BMO points would have left them even more internal to the disc margin points, enhancing rather than resolving the discrepancy. It should be noted, however, that the fundus photograph used for this co-localisation (taken from the only available stereophotograph pair for this eye) was of poor quality, making accurate co-localisation difficult.

In the remaining eye, there was a marked misalignment in the temporal and inferotemporal sectors, with the disc margin marks coinciding with an internal pigment border and the histomorphometric BMO marks coinciding with a more external pale stripe (defined by crescents of mottled pigment on either side). Histomorphometric review confirmed an externally oblique border tissue configuration within this region accompanied by no extension of BM beyond the border tissue's termination (Figure 4-11B). Here, because the border tissue was externally oblique to its junction with the sclera, and because there was no extension of BM beyond its termination, pigment on the surface of the border tissue was clinically visible beyond the termination of BM but in a plane that was clearly deeper to it. In this instance, the disc margin was the border tissue/scleral junction and the lack of a true unpigmented 'scleral lip' on subsequent repeat stereophotograph examination could be explained as the result of a shadow cast by dense pigment present on the surface of the border tissue and within the scleral canal wall tissues (Figure 4-11B).

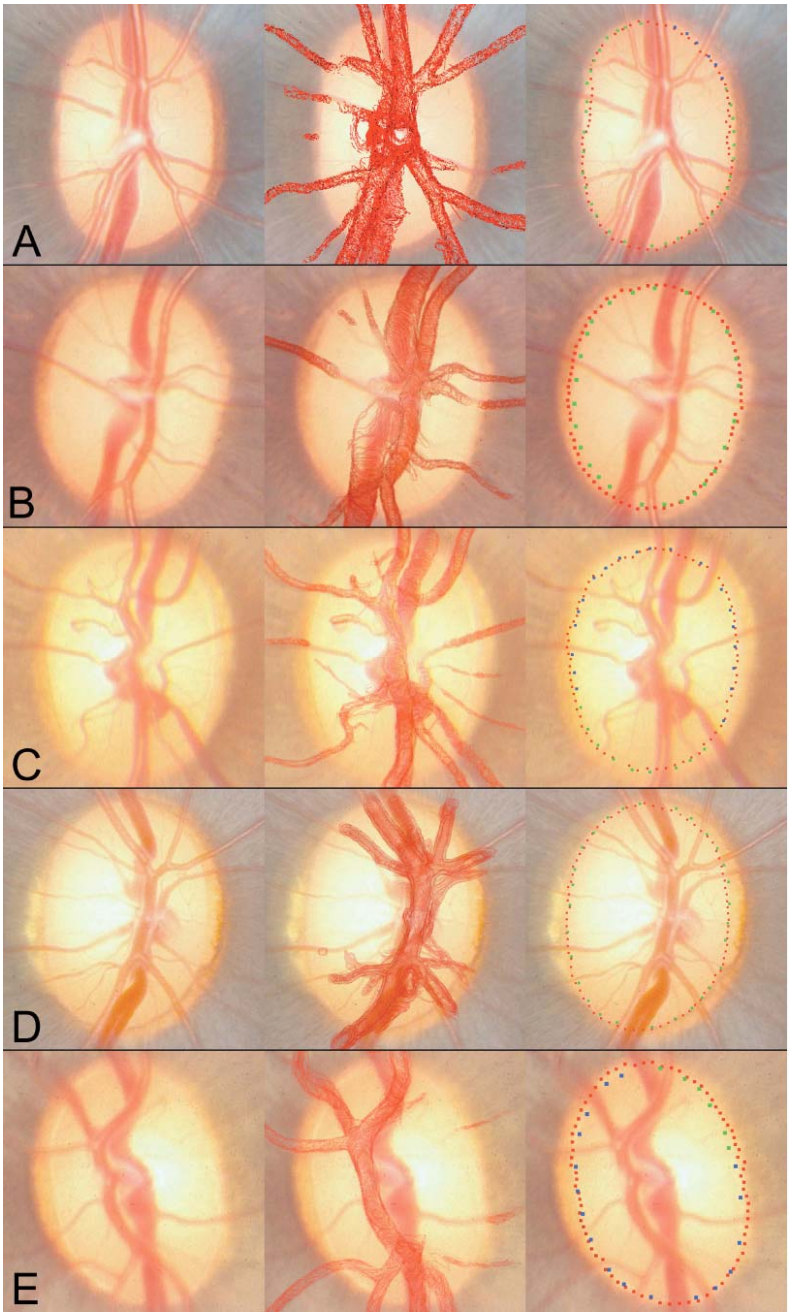

Figure 4-13. Five examples (A-E) of good alignment between BMO points and the disc margin, following 'first pass' co-localisation. Clinical images are shown in the left panels. The co-localisations of the vessel reconstructions to the clinical images are shown in the middle panels. The co-localised BMO points (red glyphs) and the disc margin delineations (blue and green glyphs) are shown in the right panels

4.3.5 Discussion

In this experiment I co-localised post mortem 3D ONH reconstructions to the clinical (in vivo) optic disc photographs of 28 normal monkey eyes. The principal findings of this experiment are as follows. First, in the majority of eyes, the histomorphometrically delineated BMO aligned with the clinically defined innermost disc margin structure. Thus the innermost termination of BM (BMO) is a clinically discernible structure in the normal monkey eye. Second, two core components of optic disc margin architecture can be histomorphometrically identified and their multiple combinations invoked to explain disc margin anatomy in the majority of normal monkey eyes. The first component is border tissue of Elschnig obliqueness and pigmentation relative to the sclera. The second component is BM extension and pigmentation beyond the border tissue termination.

In most eyes, a narrow halo (if present for 360°) or crescent (if present in a region less than 360°) of unpigmented BM was visible as a pale discrete structure internal to, concentric with, and in the same plane as the termination of pigment at the disc margin. In regions where unpigmented BM was not clinically visible, histomorphometrically delineated BMO usually coincided with the termination of the pigmented tissues at the disc margin.

The disc margin pigmented tissues themselves assumed two principal regions, an inner halo or crescent of mottled pigment followed by an outer, dense and dark grey pigment which is traditionally thought to correspond to the termination of the viable RPE and underlying choroid. It is important to again emphasise that in the overwhelming majority of eyes, the pale halo, mottled pigment and dense pigment border were all in the same plane by stereoscopic examination and co-localised (respectively) to histomorphometrically delineated unpigmented BM, pigmented BM and the shadow associated with the termination of the choroid (and presumed overlying RPE). The fact that these structures appear stereoscopically to be on the same plane is especially important because it is the presence of pigmented structures deeper to the plane of the RPE/BM complex that underlies the clinical recognition of an externally oblique border tissue.

The conventional view is that the ophthalmoscopically visible optic nerve margin begins at the termination of the RPE. Where the edge of the choroid and the edge of the RPE align, an extension of densely packed collagenous tissue arising from the sclera is usually interposed

between the choroid and the ONH (Fantes and Anderson, 1989). This structure, defined as the border tissue of Elschnig, is visible ophthalmoscopically as a white halo bounding the disc, terminating as a ‘scleral lip’.

The clinical appearance of the scleral ring has been referred to as the ‘scleral ring of Elschnig’ and has been the traditional clinical (Jonas et al., 1988a) and stereophotographic definition of the disc margin (Airaksinen et al., 1992; Britton et al., 1987; Garway-Heath et al., 1997; Laemmer et al., 2007; Moya et al., 1999; Sommer et al., 1979a). Although BM has been observed to extend beyond the termination of the RPE and to cover the border tissue, this has not been described as a phenomenon detectable by ophthalmoscopic examination (Fantes and Anderson, 1989).

The results of this experiment suggest that in those normal monkey eyes in which the border tissue had an internally oblique configuration and BM extended beyond the border tissue termination (by far the most common orientation), it was the termination of BM (BMO) that was the clinically visible disc boundary. In these eyes, the white crescent observed at the disc margin was due to a rim of unpigmented BM rather than a manifestation of a ‘scleral’ ring that, in fact, was shielded from clinical view (Figure 4-12A). Figure 4-14 further illustrates this point. The scleral ring of Elschnig (white glyphs in 4-14C and E) does not co-localise to the innermost white reflective disc margin structure (indeed it is at a considerable distance external to it). The termination of unpigmented BM (red glyphs in 4-14C and E) does in fact co-localise to the white crescent, indicating that in this region of the disc, BMO is the disc margin. The ONHRL group has previously demonstrated that the termination of ‘lightly’ pigmented BM co-localises to the disc margin (Downs et al., 2007). In Figure 4-14, however, I clearly demonstrate that unpigmented BM, effectively a transparent structure, is an ophthalmoscopically visible structure that co-localises to the disc margin.

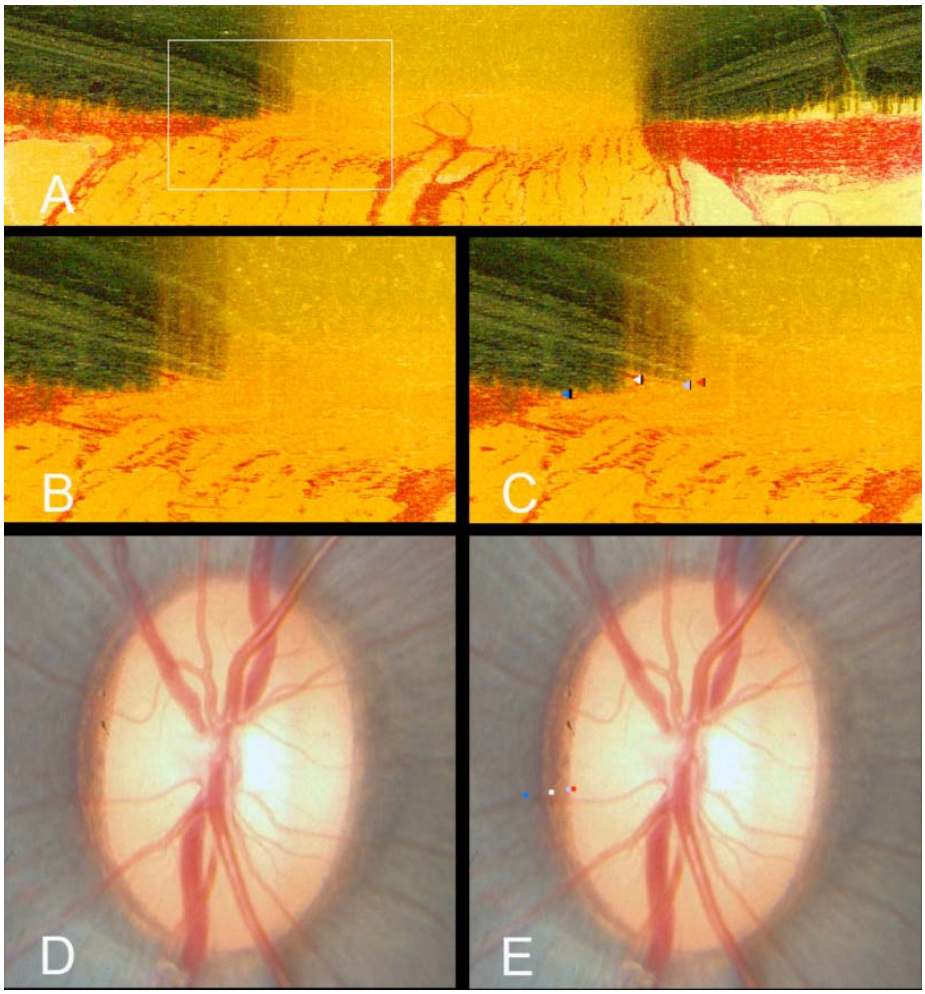

Figure 4-14. The termination of unpigmented BM aligns to the disc margin. ***A:*** **histomorphometric section with white box highlighting the area magnified in B and C.** ***B:*** **the nasal disc margin. There is overhang of BM (both pigmented and unpigmented) beyond the termination of border tissue.** ***C:*** **disc margin structures have been delineated; termination of unpigmented BM (BMO - red glyph), termination of pigmented BM (light blue glyph), junction of border tissue with BM (ring of Elschnig - white glyph) and the anterior scleral canal opening (dark blue glyph).** ***D:*** **disc photograph of the same eye.** ***E:*** **following co-localisation, BMO coincides with the innermost white reflective halo. The termination of pigmented BM coincides with the inner edge of the pigment at the disc margin. Elschnig's ring coincides with a white reflective stripe within the mottled disc margin pigment; anterior scleral canal opening is external to this**

Where the border tissue had an externally oblique configuration and BM terminated before the edge of the border tissue, the disc margin was indeed the edge of the border tissue. Unfortunately, in the one example where this was apparent, the histomorphometric presence of pigment in the underlying sclera combined with poorly focused stereophotographs did not allow for a true 'scleral lip' to be detected in the stereophotograph. In this circumstance, the pigment observed clinically was therefore composed of two zones. The first was a superficial external pigment rim that was within the plane of the RPE and histomorphometrically co-localised to pigmented BM. The second was an internal pigment rim that was deep to the plane of the RPE and histomorphometrically co-localised to pigment on the surface of the border tissue. This latter pigment may be seen stereoscopically to slope downwards and inwards, following the angle of incidence of the border tissue as it slopes down from BM to the sclera.

There have been two clinical reports of 'grey' optic disc crescents in human eyes (Higginbotham et al., 2007; Shields, 1980). A grey crescent is defined as 'a crescent-shaped, slate grey pigmentation in the periphery of the neuroretinal rim that is completely inside of the scleral crescent'. In these reports, the authors used the existing 'scleral lip' definition of the disc margin to define the crescent and were uncertain of its histological derivation. They did not specifically comment on whether the grey crescent appeared posterior to (and sloping away from) the RPE/BM plane. I propose that the grey crescent is likely to be pigment on the surface of an externally oblique border tissue of Elschnig. Clinical awareness of the plane in which the crescent occurs, perhaps clarified by SDOCT ONH imaging may provide further insight into this form of pigmentary crescent.

The co-localisation method used in this study was prone to several inherent sources of error. The calibre and size of the photographed retinal vessels and the 3D reconstructed vessels may differ because of tissue shrinkage during processing, cardiac pulse and distention during the perfusion fixation process. Co-localisation is unlikely to be 100% accurate because the process required the 2D photographic plane to be aligned to a 3D structure. It was therefore felt reasonable to explore co-localisation error as a source of misalignment, and therefore to repeat the co-localisation process in those eyes in which a poor alignment between the BMO and the disc

margin marks was observed. It should also be noted that ‘quantification’ of the accuracy of alignment would be rendered largely meaningless due to the difference in size between the in vivo imaged eye and the post perfusion fixed histomorphometrically reconstructed eye. It is for these reasons that a qualitative approach to assessing alignment was adopted.

This work in monkeys is pertinent to humans for two important reasons. Firstly, I believe that the anatomical relationships I have described will contribute to the histological explanation of most forms of human disc margin anatomy, as its variation comes to be recognised within in vivo disc stereophotographs and SDOCT volumes as well as post mortem histological and histomorphometric sections. Secondly, by applying these concepts at the slit lamp and when interpreting SDOCT ONH images, clinicians who have previously understood the disc margin to be the ring of Elschnig, will recognise the histological origin of the disc margin to be the termination of BM in at the very least the nasal region of most human optic discs. The principal explanation for this is that the nasal disc margin in both monkeys and humans is prone to an internally oblique border tissue configuration in order to enable the optic nerve to pass obliquely through the sclera to reach the more midline optic chiasm.

The results of this experiment have additional clinical implications. Recognition of the disc margin plays an important role in examining the neuroretinal rim (or indeed assigning a focal cup-to-disc ratio). The ability to recognise a, perhaps subtle, rim of unpigmented BM as the disc margin may yield a more accurate assessment of the neuroretinal rim. Likewise, ONH imaging modalities, such as HRT, require the placement of a contour line around the disc margin. As disc margin anatomy is more clearly defined, this may be applied to imaging modalities enabling the reliability of contour line placement to be improved.

The BMO has previously been proposed as a source structure for a reference plane for quantification of 3D histomorphometric volumes (Downs et al., 2007). An expert consensus group has also proposed this concept (Jonas et al., 1988a). I have subsequently confirmed, in the previous experiment (section 4.2) that the BMO is a biologically continuous, relatively planar structure both in 3D histomorphometric volumes and in 3D SDOCT volumes (Strouthidis et al., 2009c). The results of this experiment further support the adoption of the BMO as a reference

plane in clinical ONH imaging. The fact that the BMO is usually the innermost disc margin structure in the monkey eye suggests that it will be easily and reliably delineated by automated segmentation. It is necessary, however, to first confirm that the SDOCT defined NCO aligns with the clinical disc margin (Manassakorn et al., 2008). This will be explored in the next experiment (section 4.4).

In summary, the innermost edge of BM (BMO) is a clinically visible structure in the monkey eye. It is usually the innermost disc margin structure and so constitutes the disc margin boundary in the majority of monkey eyes. The border tissue may be clinically visible in regions where it demonstrates an externally oblique configuration and the border tissue/scleral junction is internal to the termination of BM.

4.4 Assessment of Disc Margin Anatomy Using SDOCT

4.4.1 Background

In a series of recent publications, the ONHRL group has proposed three important concepts that are necessary to understand optic disc margin anatomy within 3D histomorphometric and SDOCT reconstructions of the monkey ONH (section 4.2) (Burgoyne et al., 2004; Downs et al., 2007; Strouthidis et al., 2009b). The first concept is that of an NCO (Figure 4-15A - arrows), which is the anatomic opening in BM (also referred to as BMO) through which RGC axons must pass to enter the choroidal and scleral portions of the neural canal (Downs et al., 2007; Strouthidis et al., 2009b; Strouthidis et al., 2009c). The second concept is that of a 'neural canal' which is the axonal pathway through the eye wall (Burgoyne et al., 2004). The neural canal begins at the NCO, and then extends through a choroidal component, bound on either side by the border tissue (Figure 4-15A - arrowheads). Beyond the choroidal component, the neural canal has a scleral component, bound on either side by the internal wall of the sclera. The neural canal terminates at the point at which the optic nerve leaves the globe. The third concept is that what the clinician perceives to be the disc margin is not a single anatomic structure but is instead variable with some portions being the NCO, and others the border tissue (Figure 4-15A - arrowheads) or the anterior scleral canal opening, depending upon the 3D architecture of these structures, as ascertained in the previous experiment (section 4.3) (Strouthidis et al., 2009b).

In the first experiment (section 4.2), I established that the NCO is an important anatomical landmark because it can be identified within SDOCT images and proposed it as the basis for a reference plane for SDOCT imaging (Strouthidis et al., 2009c). Within 3D histomorphometric reconstructions, the NCO is defined as the termination of BM (BMO) because BM is within the resolution of that technique (Downs et al., 2007). Within SDOCT reconstructions I have defined the NCO as the termination of the RPE/BM complex because it is uncertain whether BM in isolation can be resolved by SDOCT (Drexler and Fujimoto, 2008).

In the previous experiment (section 4.3) I co-localised post mortem 3D ONH histomorphometric reconstructions to stereophotographs acquired in vivo in 28 normal monkey eyes (Strouthidis et

al., 2009b). I now propose that the anatomical basis of the disc margin can also be identified and delineated within SDOCT volumes.

4.4.2 Purpose

The purpose of experiment was to examine whether the NCO and border tissue identified in SDOCT volumes define the optic disc margin in the normal monkey eye.

4.4.3 Methods

All eyes were SDOCT imaged in vivo as part of other ongoing research studies. Data from 33 normal eyes of 24 rhesus macaque monkeys were included.

All image acquisitions were performed after IOP had been stabilised at 10 mmHg, as per the 'short' compliance test protocol (section 3.3). The details as regards optic disc stereophotograph acquisitions have been described in section 3.4 and in the previous experiment (section 4.3). In terms of SDOCT image acquisition, 290 individual horizontal B-scans were acquired over a 15º retinal window (768 A-scans per B-scan, each B-scan was acquired 9 times and averaged for speckle noise reduction). In this scan pattern, the Spectralis software automatically registers all acquired B-scans relative to each other in the z-axis. All image acquisitions were well centered on the ONH and this scan location was consistent in all images used in this study.

Delineation of Disc Margin Structures Within SDOCT Volumes:

My delineation method within SDOCT images has been described in section 4.2.3 and has been published elsewhere (Strouthidis et al., 2009c). A single experienced operator (myself) manually delineated all of the volumes. No contour smoothing filtering techniques were applied to the interpolated data.

Figure 4-15 compares a horizontal B-scan with a comparable sagittal serial histological section taken from the same normal monkey ONH. This eye has not been included in the current study and is used for illustrative purposes only; a detailed account of the comparison between serial histology and SDOCT B-scans in this eye will be the subject of the following experiment (section 4.5). Figure 4-15B illustrates that SDOCT is capable of identifying both the termination of the

RPE/BM complex (NCO, marked with arrows) and the border tissue (marked with arrowheads). The anterior scleral canal opening, which is defined as the internal boundary of the anterior scleral surface, is not detectable in this particular representative B-scan. For each SDOCT volume, I identified and delineated the NCO (defined as the innermost extent of the posterior surface of the RPE/BM complex) within each interpolated radial SDOCT section (Figure 4-15B, arrows). There are therefore two NCO points within each single radial SDOCT section, one on either side of the neural canal, yielding 80 NCO points per volume. In sections where the innermost (most axial) extent of an externally oblique border tissue was observed to extend further into the neural canal than the NCO point on that side, the innermost termination of the border tissue was also delineated. Within the SDOCT radial sections, border tissue was defined as the transition from high to low intensity signal at the junction of the choroid and the neural canal, visible inferior to the RPE/BM complex (Figure 4-15B, arrowheads). Figure 4-16 demonstrates the distinction between internally and externally oblique border tissue within an SDOCT B-scan and serial en face (transverse) SDOCT C-scans relative to their respective features within a disc photograph.

Once manual delineation was completed, the Cartesian coordinates for each delineated point (both NCO and border tissue) were saved, allowing a 3D point cloud to be generated (Downs et al., 2007).

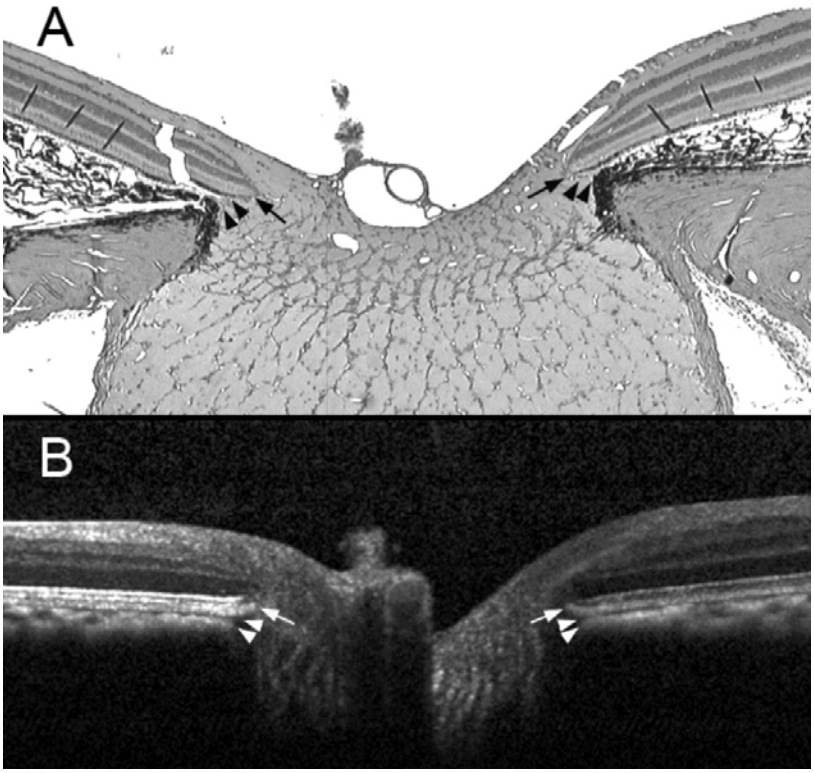

Figure 4-15. Neural canal architecture, demonstrating the NCO and border tissue within a histological section *(A)* and a co-localised SDOCT B-scan *(B)*. Arrows identify the NCO in both images, arrowheads identify border tissue. The neural canal extends from the NCO until the point where the optic nerve exits the globe, passing through a choroidal component (bound by the border tissue) followed by a scleral component

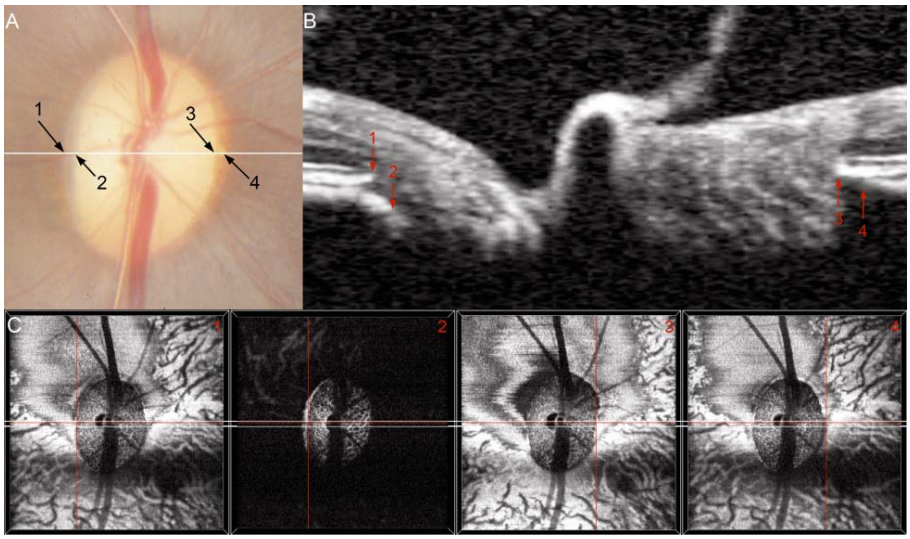

Figure 4-16. The disc photograph (panel A) and SDOCT (panels B and C) appearance of internally and externally oblique border tissue in the normal monkey eye.

Externally oblique: **in panel A, 1 marks a thin pale crescent. Internal to this is a pigment crescent; the end of this pigment is the temporal disc margin (arrow 2). In a co-localised B-scan (panel B, location of B-scan shown by a white line in panel A), an externally oblique border tissue configuration is seen temporally. 1 marks the location of the NCO and 2 marks border tissue. In the disc photograph (panel A), 1 is a stripe of unpigmented BM - external to this is pigmented BM continuous with RPE. The pigment crescent internal to 1 is caused by pigment on the surface of an externally oblique border tissue. Panels C1 and 2 show the location of these structures (at the centre of the red cross-hairs) within en face SDOCT images**

Internally oblique: **in panel A, 3 highlights the disc margin location, at the termination of a mottled pigment crescent. Within the B-scan (Panel B), internally oblique border tissue can be seen at the nasal side of the neural canal. 3 shows the NCO. The internally oblique border tissue can be seen to meet the RPE/BM signal external to NCO (4) and to extend away from the neural canal. The pigment crescent at the nasal disc margin represents a region of pigmented BM. The region of BM 'overhang', beyond the point where border tissue meets BM is visible as a dark crescent in the en face SDOCT image (panel C4), external to NCO (panel C3)**

Co-localisation of SDOCT Volumes to the Disc Photographs:

The selection of optic disc stereophotographs and their subsequent digitisation was performed as per the previous experiment (section 4.3.3).

Each SDOCT ONH volume was viewed in the en face orientation and the z-axis depth was adjusted until the outline of the central retinal vessels was clearly visible. Two en face SDOCT images were acquired; one showing the vessel outlines and the other showing all of the delineated glyphs (Figure 4-17A). The two images were overlaid using Adobe Photoshop CS3 (Adobe Systems, Inc., San Jose, CA) to create a perfectly aligned two-layer image file. The disc photographs were then overlaid onto their respective SDOCT images with the glyphs hidden from view (Figure 4-17B). The same operator (myself) performed the initial manual co-localisations. Co-localisation required the outline of the central retinal vessels and their bifurcations to be matched between the en face SDOCT image and the photograph. This was achieved by rotating the photograph image layer, moving it in the x- and y- orientation and by adjusting its magnification in a 1:1 ratio scale. The proximity of alignment between image layers was verified by reducing the opacity of the clinical image so as to view the two overlaid images simultaneously (Figure 4-17C). In order to not prejudice the co-localisation process, the SDOCT delineation glyphs were hidden throughout. At the completion of co-localisation, the co-ordinates of the SDOCT delineations were saved and the glyphs were transferred onto the clinical image.

Delineation of the Disc Margin:

An experienced clinical observer (Professor Burgoyne) viewed and marked the optic disc margin in each co-localised image (Figure 4-17D) using exactly the same method as described in the previous experiment (section 4.3.3). As with the previous experiment, the observer could classify the marks as ‘certain’ (blue) or ‘uncertain’ (green) in which case a ‘forced’ choice was made (Figure 4-17E). There were no constraints as to the number of points the observer needed to delineate in each photograph. The observer defined the disc margin as the innermost reflective structure that extended beyond the internal termination of pigment at the disc periphery; in doing so the observer delineated what clinicians interpret as Elschnig’s ring. Where a reflective structure was absent, the observer selected the termination of pigment as the disc margin. The

collected coordinates of the marked points were saved and the points were transferred onto the disc photograph image in which the SDOCT delineation glyphs were also shown. An image of the disc photograph incorporating both the co-localised SDOCT delineations and the disc margin demarcations was then saved for each eye (Figure 4-17F).

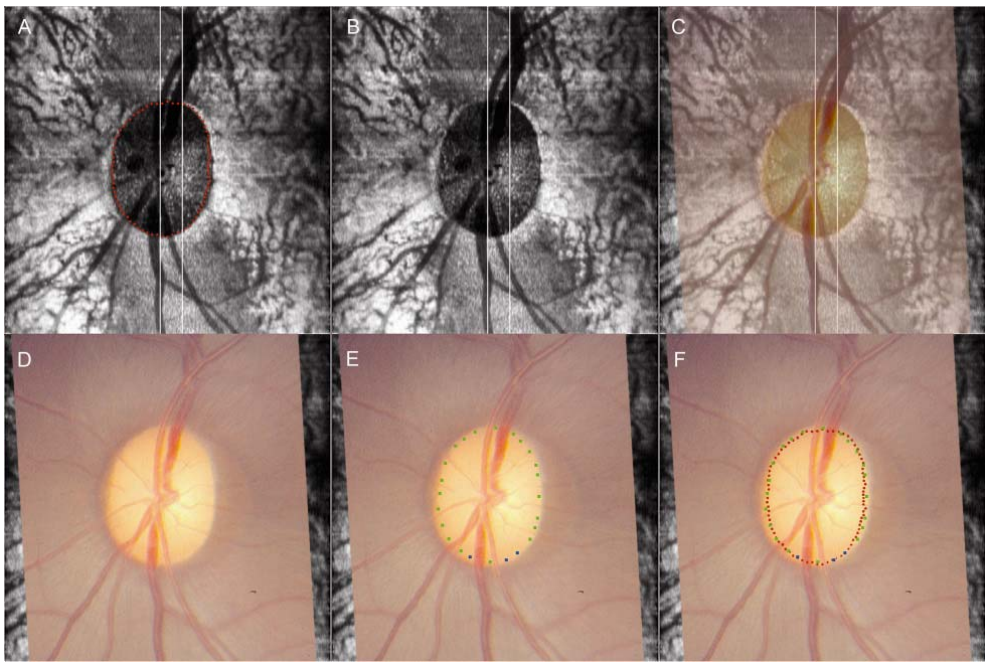

Figure 4-17. The SDOCT co-localisation and disc margin delineation process

Subjective Assessment of Alignment of SDOCT Delineations to the Disc Margin:

Two observers (myself and Professor Burgoyne) qualitatively reviewed the disc photographs incorporating the SDOCT delineations and the disc margin delineations. This was performed to assess how well the co-localised SDOCT NCO or border tissue delineations aligned to the disc margin. The observers classified good alignment as where there was less than a glyph's diameter separation between the SDOCT glyph (either NCO or border tissue) and the nearest adjacent disc margin glyph in all disc sectors. When the 2D SDOCT image was projected onto the disc photograph in the purpose-built disc margin delineation software, a universal 1:1 pixel ratio was applied. This was performed so as to negate any discrepancy in glyph diameter caused by SDOCT scaling issues related to differences in monkey axial lengths. The glyphs in this program

are 5 pixels in diameter, meaning that this is the minimum resolvable separation between adjacent glyphs. Disc sectors were defined according to 0° (vertical), 45°, 90° (horizontal) and 135° axes applied to the clinical photograph, generating superior, inferior, superotemporal, inferotemporal, temporal, nasal, superonasal and inferonasal disc sectors. Where the SDOCT NCO delineations aligned to the disc margin delineations, the NCO was defined as the anatomical basis for the disc margin in that region. Where both the NCO and the termination of an externally oblique border tissue had been marked, the landmark most closely aligned to the disc margin delineation was defined as the anatomical basis of the disc margin in that region. In eyes where good alignment was not observed for 360° of the disc margin, the number of sectors where there was a greater than one glyph diameter separation between SDOCT and disc margin glyphs was recorded. In order to identify causes for discrepancy in these regions of the disc, the relevant stereophotographs and B-scans were systematically re-examined, examples of which are discussed below.

Quantification of Alignment of SDOCT Delineations to the Disc Margin:

In addition to the subjective assessment described above, an attempt was made to quantify the degree of alignment between the clinician's disc margin and the SDOCT delineations. For the purposes of this analysis, all images were configured into right eye orientations. The 2D co-ordinates of all glyphs in x- and y-space were transferred to Matlab (Matlab Mathworks, Natick, MA). B-spline curves were fitted between glyphs so that three different continuous curves were generated for each co-localised image. In each image, a continuous disc margin curve and a continuous SDOCT NCO curve were generated. In those eyes in which externally oblique border tissue had been delineated, a third continuous curve was generated which incorporated the border tissue (where present) as well as the NCO in the remainder of the disc. The alignment 'error' was assessed along radial spokes generated at 4.5° intervals, from the centre of the clinician's disc margin to the disc margin curve, commencing at the temporal meridian (0°) and proceeding in a counter-clockwise fashion. Alignment error at each spoke was expressed as the distance between the disc margin curve and the SDOCT curve along the spoke, expressed as a percentage of the spoke length from the centre of the disc margin to the disc margin curve

(Figure 4-18). Percentage alignment error relative to disc margin radius was measured globally and regionally across all eyes (analyses performed using R, R Foundation for Statistical Computing, Vienna, Austria).

SDOCT Disc Margin Anatomy in A Myopic Human Eye:

To extend my findings to the human ONH and to better demonstrate their clinical implication, I delineated an SDOCT volume acquired from a myopic human eye (optical refraction, -9.00/-1.00 D x 90º, axial length 29.04 mm). The SDOCT volume was generated from 97 horizontal B-scans acquired over a 15º by 10º retinal window (768 A-scans per B-scan, each B-scan acquired 25 times and averaged). Human SDOCT imaging was performed at Dalhousie University, Halifax, Nova Scotia, Canada where there was regional Ethics Committee approval and the subject gave his informed consent.

In addition to the NCO, the full extent of the border tissue was delineated, regardless of whether it was internally or externally oblique or if it extended beyond the NCO. The anterior scleral canal opening (the innermost extent of the anterior scleral surface) was detectable in this eye so was also delineated within each radial SDOCT section (blue glyphs). These additional delineations were performed because of the complexity of the anatomy in this eye, compared to normal monkey eyes. Following delineation of these landmarks, the en face SDOCT image was co-localised to the disc photograph, and the clinician (Burgoyne) marked the disc margin, masked to the SDOCT landmarks, using exactly the same protocol as per the monkey eyes.

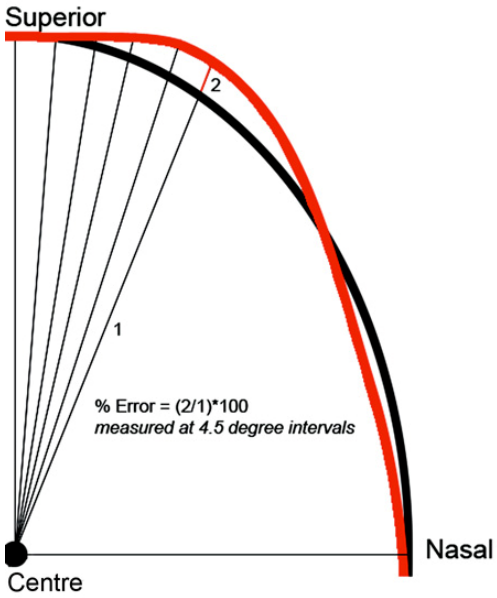

Figure 4-18. Schematic to illustrate the estimation of alignment error in the superonasal quadrant of a co-localised image. All images are in right eye orientation and all four quadrants are used in the analysis for each image (not shown in this figure). The clinician-ascribed disc margin is shown in black and the SDOCT delineated curve is shown in red. Radial spokes are generated from the centre of the disc margin at 4.5° intervals from the temporal meridian. Alignment error is the distance between the clinician's disc margin and the SDOCT curve (the red line labelled 2), expressed as a percentage of the disc radius (the black line labelled 1). The alignment errors are calculated for each radial spoke enabling an estimation of global and regional alignment error for each eye

4.4.4 Results

Assessment of Alignment Between SDOCT and Disc Margin Delineations In Monkey Eyes:

In 18 eyes, the delineated NCO was well aligned (within one glyph diameter) to 360º of the disc margin (6 examples are illustrated in Figure 4-19A). In 5 other eyes, NCO was misaligned from the disc margin in a single sector of the disc but was well aligned to the remaining circumference of the disc margin.

A region of externally oblique border tissue extending internal to the NCO was detectable by SDOCT in 10 eyes. In all cases, the region of externally oblique border tissue was located in the temporal half of the disc. Within these 10 eyes, where an externally oblique border tissue was delineated, the termination of border tissue rather than the NCO aligned to the disc margin. In 8 of these eyes, the NCO aligned well to the remainder of the disc where border tissue had not been delineated (Figure 4-19B). In one eye, the NCO and the disc margin were misaligned in a single sector. In the remaining eye, misalignment (greater than two glyphs' diameter separation) between the NCO and the disc margin was encountered in the nasal half of the disc.

The mean percentage alignment error (distance between the SDOCT delineations and the disc margin, expressed as a percentage of the center of the disc to the disc margin) was 3.8 % +/- 1.2 %. Figure 4-20 illustrates the regional alignment error for all of the eyes in the study. Absolute alignment error has been estimated using the moving average generated from each corresponding 4.5° location and the two locations either side of it (in other words a moving average based on 5 consecutive locations). In Figure 4-20 the median (middle lines), 95 % (upper lines) and 5 % (lower lines) quantiles for alignment error are shown. Median alignment error was less than 5%, with greatest misalignment of the NCO (solid lines) occurring in the temporal, inferotemporal and superotemporal regions. The misalignment in these regions was considerably reduced when the disc margin was compared to externally oblique border tissue (dotted lines).

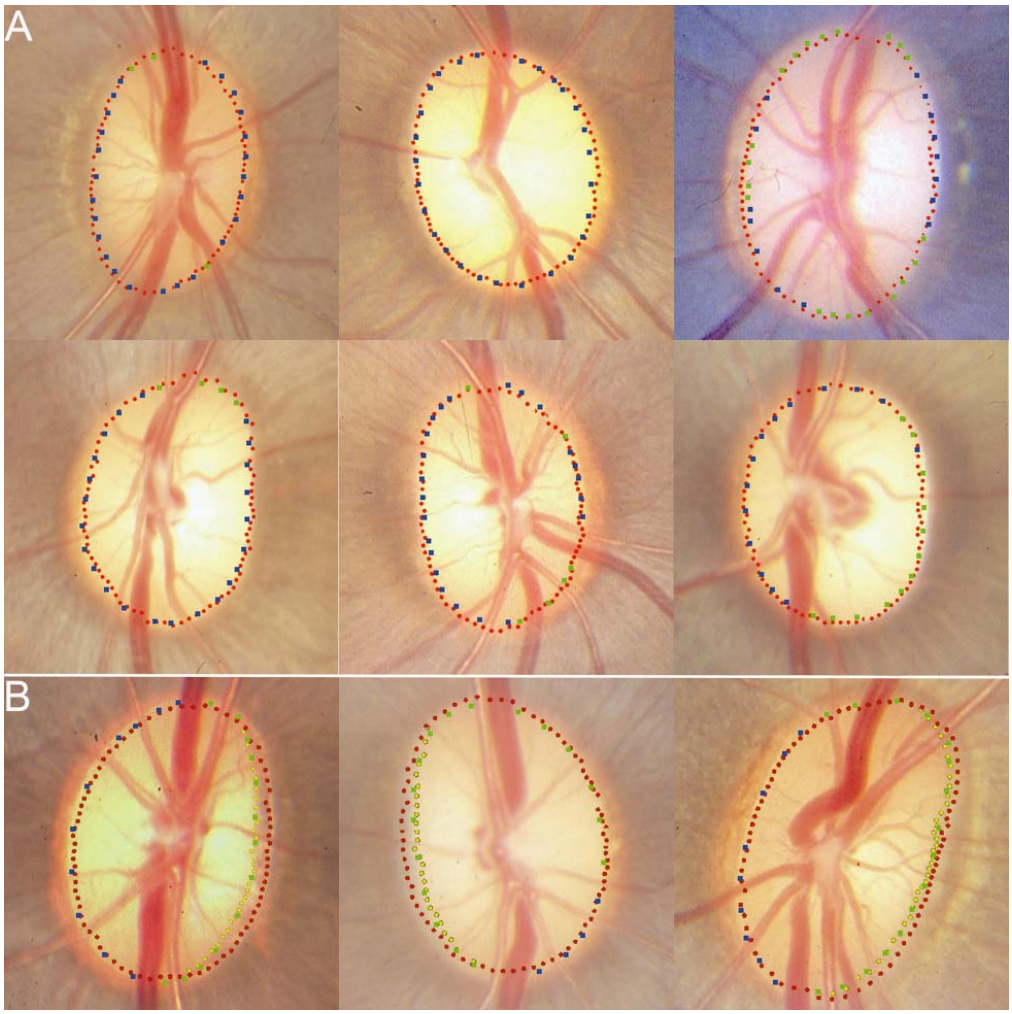

Figure 4-19. Examples of good alignment between disc margin delineations and SDOCT delineations. ***Panel A:*** **6 discs where the NCO (red glyphs) aligns to within one glyph's diameter for 360º of the disc margin.** ***Panel B:*** **3 examples where the termination of externally oblique border tissue (yellow glyphs) aligns to the temporal disc margin and the NCO aligns to the remainder of the disc margin**

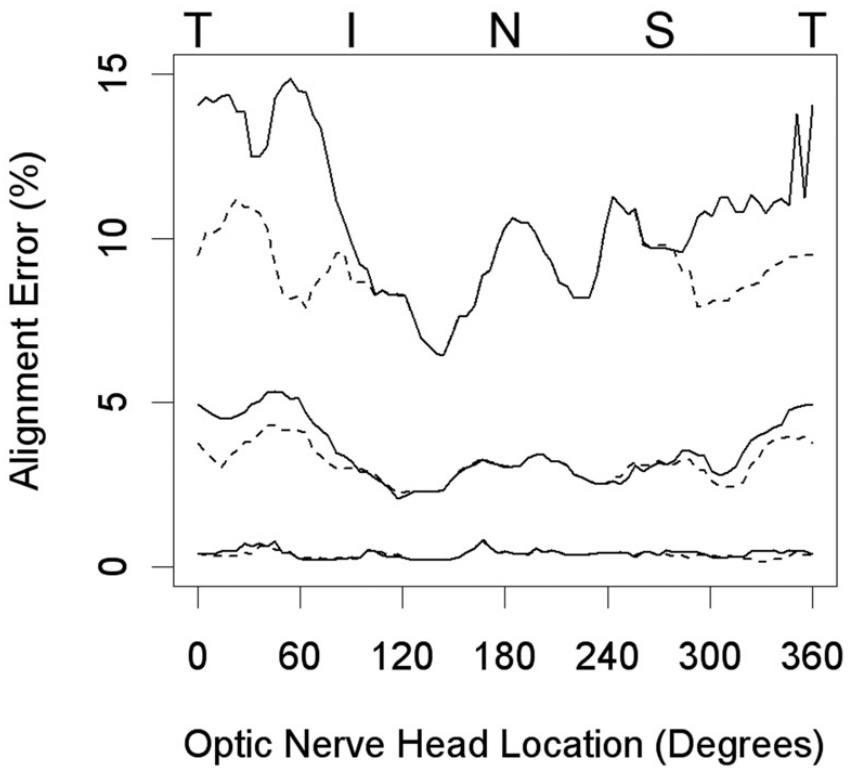

Figure 4-20. Regional alignment error for all 33 eyes analysed. The lines shown are for the median (middle lines), 95 % (upper lines) and 5 % quantiles of alignment error. Solid lines indicate the degree of misalignment from the disc margin of the curves generated by the NCO, whereas the dotted lines indicate the degree of misalignment from the disc margin of the curves generated by a combination of the NCO and the border tissue. (T = temporal, I = inferior, N = nasal, S = superior)

Sources of Misalignment:

In 5 of the 6 eyes where misalignment of the NCO to the disc margin was present in a single disc sector, the disc margin had been marked using green glyphs. This indicates that the clinical observer was not certain of the location of the disc margin in that region. These misalignments were all located in either the superior or inferior pole of the disc (two examples shown in Figure 4-

21A and B). In the normal monkey, the RNFL can be very thick where it enters the disc at the poles, making it difficult to clearly visualise the disc margin in stereophotographs. It is possible that this may explain the misalignment in these 5 cases. It should, however, be noted that the degree of misalignment is fairly minimal, amounting to less than two glyphs' diameter separation. In the remaining eye in which misalignment was confined to a single sector, the disc margin in the misaligned sector had been delineated using blue glyphs. This indicates that the clinical observer was 'certain' of the disc margin location (Figure 4-21D). Within the radial B-scans at that location, a substantial 'shadow' cast by a blood vessel made precise delineation of the NCO difficult (Figure 4-21E). This problem was not encountered in the remaining SDOCT ONH volumes examined in this study.

The reason for the misalignment between the SDOCT defined NCO and the nasal disc margin in one eye was less apparent (Figure 4-21C). The degree of misalignment was too large to be explained by either the small margin of error inherent in the co-localisation process or the potential differences in the size of vessels at the time of SDOCT imaging relative to their size at the time of stereophotography.

Assessment of Disc Margin Anatomy in A Myopic Human Eye:

The relationships between the photographic disc margin and the SDOCT NCO, border tissue and anterior scleral canal opening delineations are illustrated in Figure 4-21A - C. The 3D anatomy of this myopic human ONH was ascertained from the point cloud generated from the delineated NCO, border tissue and anterior scleral canal opening (Figure 4-21D - E). An exaggerated obliquity of the neural canal was clearly visible in the 3D point cloud.

As in 10 of the monkey eyes, externally oblique border tissue was present in the temporal half of the disc whereas an internally oblique border tissue was present in the nasal half of the disc. However, the extent and degree of obliquity of the border tissue far exceeded that seen in the normal monkey eyes.

In this eye, the temporal NCO coincided with the termination of retinal pigment (Figure 4-21B). The border tissue delineations in the temporal disc extended downward and internal to the NCO where they corresponded to a region of atrophy evident in the photograph. In this region, large

underlying choroidal vessels were visible. The temporal disc margin corresponded to the anterior scleral canal opening located at the innermost termination of the externally oblique border tissue. In the disc photograph, the anterior scleral canal opening was visible as a distinct white crescent internal to the variably pigmented border tissue. In this eye, this landmark represents a true 'scleral lip' or 'scleral crescent'.

In the nasal half of the disc, the internally oblique border tissue can be seen to sweep external to the NCO, terminating at the anterior scleral canal opening. Within these sectors the NCO corresponded to the disc margin.

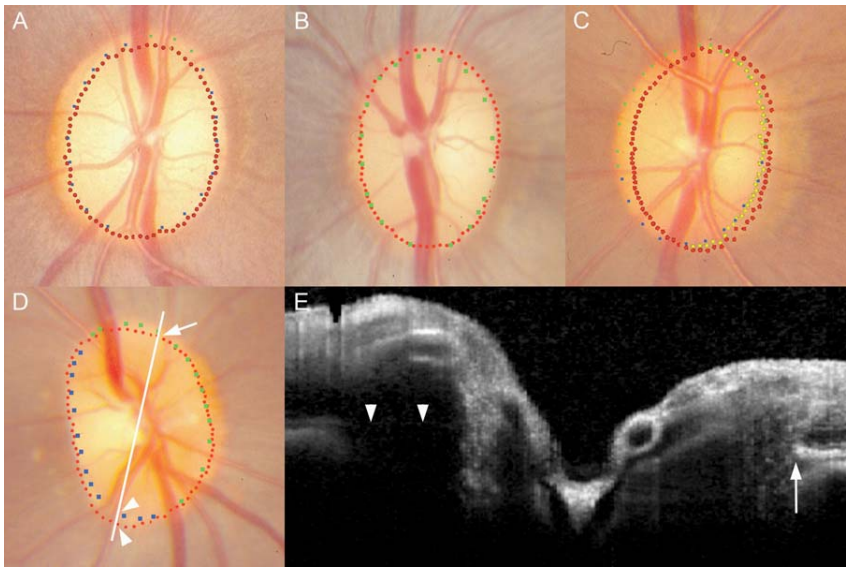

Figure 4-21. Examples of misalignment between the disc margin and SDOCT delineations. *A and B:* NCO is misaligned at the superior pole. *C:* the NCO is misaligned nasally. It is possible that a wide crescent of unpigmented BM was not visible at the nasal disc margin on the stereophotographs but was picked up by SDOCT. *D:* the NCO at the inferior pole is external to the disc margin. *E:* the B-scan acquired at the location highlighted by the white line in D. The inferior NCO and the RPE/BM complex are obscured by a shadow cast by a blood vessel (white arrowheads), causing difficulties in accurate delineation of the NCO

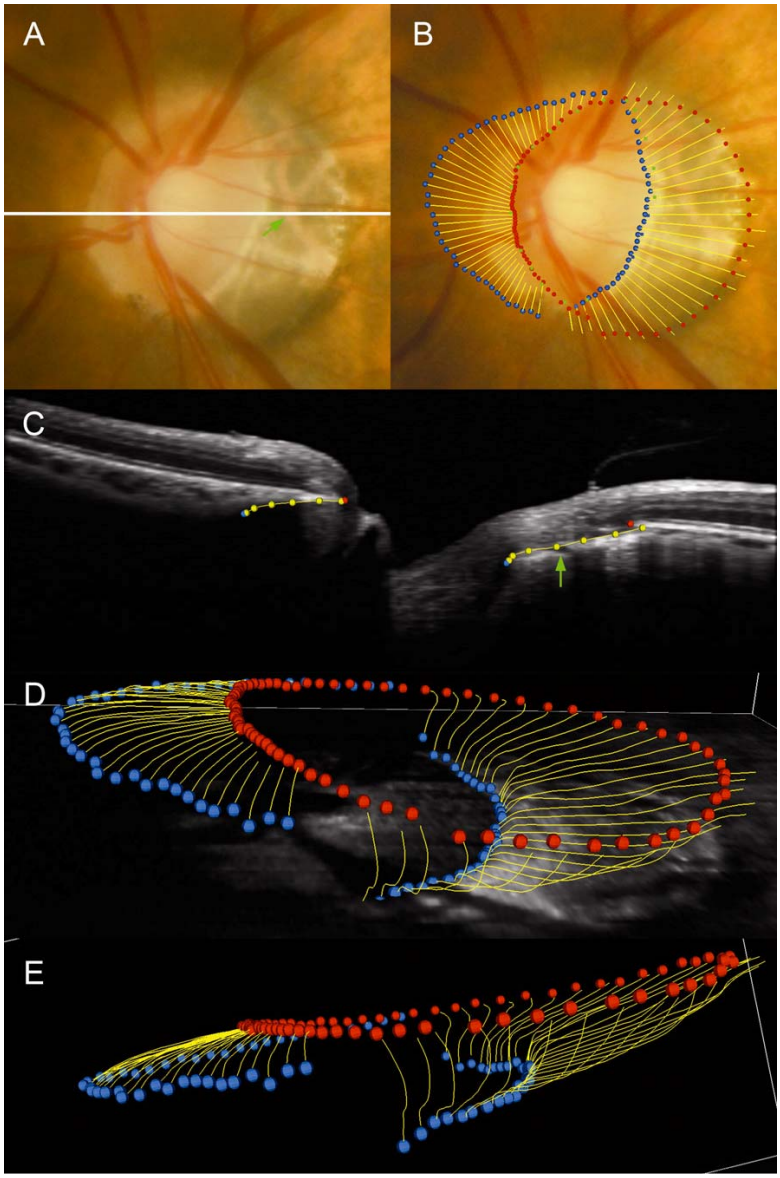

Figure 4-22. SDOCT disc margin anatomy in a myopic human left eye. *A:* disc photograph; a white line highlights the location of the B-scan (C). *B:* alignment of the disc margin (blue and green square glyphs) to the SDOCT delineations. Red glyphs are NCO, blue circular glyphs are anterior scleral canal opening and yellow lines represent border tissue. Anterior scleral canal opening can be seen to align to the temporal disc margin. NCO is aligned to the nasal disc margin. *C:* a green arrow highlights the location of a choroidal vessel within border tissue that is also shown within the disc photograph (A). *D and E:* 3D point clouds generated from the delineation of the SDOCT images

4.4.5 Discussion

The principal findings of this experiment may be summarised as follows. Border tissue and NCO anatomy was well visualised by volumetric SDOCT imaging in monkey eyes. The anatomical underpinnings of the disc margin were regionally variable depending upon border tissue obliquity as detected by SDOCT. Finally, these findings could be utilised to explain the much more complicated anatomy of a single myopic human eye.

The findings of this experiment are consistent with the results of the preceding assessments of disc margin anatomy using 3D histomorphometric reconstructions (section 4.3) (Downs et al., 2007; Strouthidis et al., 2009b). Chiefly, the NCO (equivalent to the histomorphometrically defined BMO in the monkey eye) corresponded to the disc margin in the majority of monkey eyes. Where an externally oblique border tissue extended into the neural canal internal to the NCO, the disc margin was comprised of the innermost termination of the border tissue and the anterior scleral canal opening (where visible). This orientation was observed in approximately one third of the monkey eyes examined in this study and was invariably located in the temporal half of the disc. An extreme form of this phenotype was also seen in the myopic human eye.

My findings suggest that disc margin anatomy is consistently detected within SDOCT volumes. SDOCT volumes therefore have the potential to inform the clinician of the true location of the disc margin in circumstances where defining the disc margin either by fundoscopy or within a disc photograph is difficult. This has important implications in the management of glaucoma patients as it will enable a precise identification of the peripheral boundary of neural tissue in the disc and will allow accurate placement of the contour line in optic disc images used in the quantitative assessment of glaucomatous progression.

In only one monkey eye did the SDOCT misalign to the clinician's ascribed disc margin in more than one sector. In this case, externally oblique border tissue co-localised to the temporal disc margin whereas the SDOCT-defined NCO was located at a considerable distance internal to the disc margin nasally. Given the overwhelming consistency regarding the relationship between the NCO, border tissue and the disc margin in the remaining SDOCT volumes as well as in 3D histomorphometric volumes (section 4.3) (Strouthidis et al., 2009b), it is unlikely that the disc

margin is the ring of Elschnig nasally. The most valid interpretation in this single exception is that a wide extension of unpigmented BM, beyond the termination of RPE, was detectable by SDOCT but was not visible within the stereophotograph. As such, the nasal disc margin may have been marked too externally in that disc photograph. Unfortunately the animal concerned was sacrificed on schedule for a separate study prior to the completion of this study, so I was unable to confirm the exact location of the nasal disc margin by stereoscopic ophthalmoscopy.

In the preceding experiment (section 4.3), I proposed that the reason for a tendency towards having an internally oblique neural canal orientation nasally and an externally oblique orientation temporally was likely due to an anatomical adaptation to facilitate passage of optic nerve axons to reach the chiasm (Strouthidis et al., 2009b). This explanation is supported by the results obtained from delineating a myopic human eye. In this case, the optic nerve axons may need to exit the eye in a more extreme oblique direction towards the midline because of the large size of the myopic globe.

When examining the 3D point cloud generated from the human SDOCT ONH volume, it is apparent that there are a number of potential ‘apertures’, through which the axons traverse as they pass through the neural canal and then exit the eye through the scleral canal. The first ‘aperture’ is the NCO; this represents the point at which retinal nerve fibre axons change direction to enter the ONH. The NCO is equivalent to the termination of BM in our histomorphometric volumes. Within SDOCT volumes, the innermost termination of the presumed RPE/BM signal was delineated as the NCO. In most cases, the NCO co-localised to a point on the disc photograph beyond the apparent termination of the visible retinal pigment. I interpret this to mean that portions of BM may be detectable by SDOCT, beyond the termination of the RPE.

These data suggest that in regions of the disc where the border tissue is externally oblique, the border tissue or anterior scleral canal opening will represent the disc margin. Where BM extends beyond the termination of border tissue (whether internally or externally oblique), the NCO will represent the disc margin. While both the NCO and the disc margin are clinically visible, it is important to recognise them as independent landmarks. Firstly, my work suggests that the NCO and not the disc margin will become the basis for an SDOCT reference plane for both ONH and

peripapillary RNFL quantification. Furthermore, I believe that clinical co-localisation of SDOCT-detected disc margin anatomy will inform the clinician's interpretation of the disc in eyes with tilted, highly myopic or glaucomatous ONHs.

It should be noted that it is possible for an experienced clinician to differentiate between the different anatomical components of a disc margin by judging the stereoscopic 'depth' of the disc margin relative to the retinal pigment. Where the NCO comprises the disc margin, the termination of BM will be located at the same depth as the retinal pigment. Where the disc margin is at a deeper level (more posterior) than the retinal pigment, it will comprise externally oblique border tissue or the scleral canal opening.

The neural canal extends posteriorly from the NCO to the anterior scleral canal opening, with neural tissue separated from the choroid by the border tissue. The scleral canal further extends from the anterior scleral canal opening to the posterior scleral canal, with the nerve passing through the full thickness of the sclera (Downs et al., 2007). The anterior scleral surface and the anterior scleral canal opening were not discernible in the monkey eyes examined in this study whereas they were detected in the myopic human eye. I cannot detect the posterior scleral surface and posterior scleral canal opening using 870 nm SDOCT. However, this may be possible using a 1050 nm light source, which has been reported to achieve increased axial depth penetration (Povazay et al., 2003; Povazay et al., 2007a; Srinivasan et al., 2008).

An ability to fully image the scleral canal (from anterior to posterior scleral canal openings) may be potentially useful in the detection of glaucoma progression as, using 3D histomorphometric reconstructions, scleral canal expansion has been identified as a feature of chronic IOP elevation in monkey eyes (Downs et al., 2007; Yang et al., 2009a).

Manassakorn and co-workers recently compared disc margins delineated in disc photographs of 17 normal human eyes with disc margins identified in scans acquired using a novel high speed, ultra-high resolution OCT device (Manassakorn et al., 2008). In that study, the termination of the RPE at either side of the ONH was manually delineated within the 180 consecutive horizontal raster frames within each scan volume. The x-axis co-ordinates of these delineations were used to transfer these locations onto the en face OCT image generated from the completed volume.

The en face OCT image was co-localised to the disc photograph without viewing any of the delineations, as in our study. In the 17 eyes studied, the disc area identified by the cross-sectional OCT images was significantly larger than that identified using the disc photographs, although the geometric centre of the disc margin was similar using both techniques. The authors suggested that the cross-sectional OCT disc margins might have larger dimensions than the photograph-defined disc margin because of difficulties delineating the termination of RPE under large vessel shadows and in areas of peripapillary atrophy.

Peripapillary atrophy was not a feature of any of the monkey eyes examined in this study and I encountered difficulty in identifying the NCO because of vessel shadowing in only a single region of one disc. In this experiment, the detection of NCO despite the presence of retinal vessel shadowing may be due to the density of the B-scans acquired, which exceeds what has been attempted to date in human subjects. It is also possible that the Bruch's membrane underlying the retinal vessels in the monkey eye is more reflective than in the human, rendering the signal detectable despite the presence of vessel shadowing.

My delineation of the 'disc margin' within B-scans also differed in that I not only delineated the NCO, but also regions where the border tissue extended further into the canal than the termination of the RPE/BM complex. It is possible that in some of the eyes examined in Manassakorn and co-workers' study, a portion of the disc margin circumference was comprised of externally oblique border tissue (Manassakorn et al., 2008). If only the termination of the RPE was marked in these regions, which would have been outside of the termination of the externally oblique border tissue, then it would result in an erroneously large disc area when compared to the photographic disc area.

More recently, the photographic disc margin has been compared with the SDOCT defined disc margin in 18 glaucomatous eyes (Kotera et al., 2008). In that study, a high concordance between the photographic disc margin and the SDOCT disc margin was found. The observers delineated either the termination of the RPE or the termination of the "highly reflective, curved line", which connected to the straight signal identified as the RPE. I believe that this highly reflective, curved line is the signal I have identified as border tissue in this experiment.

Furthermore, Kotera and colleagues additionally highlighted circumstances where the termination of the RPE identified by SDOCT coincided with the termination of visible retinal pigment at the edge of peripapillary atrophy (Kotera et al., 2008). I observed the same phenomenon in the myopic human eye, with the temporal NCO co-localising to the edge of the peripapillary atrophy. The appearance of this disc is in keeping with the concept of 'simple misalignment' of the scleral, choroidal and RPE layers caused by the oblique exit of the nerve in an axially myopic eye (Fantes and Anderson, 1989). I have identified this curved high intensity signal as border tissue, as opposed to choroid or sclera, as large choroidal vessels were visible posterior to this signal. These choroidal vessels co-localised to the correct location in the clinical photograph, highlighted by a green arrow in Figures 4-22A and C. This suggests that the signal was derived from tissue anterior to both the choroid and the sclera, most likely the compacted connective tissue comprising the border tissue.

There are a number of limitations to my methodology that should be considered. In particular, the co-localisations are subject to a degree of inherent variability in part because the calibre of the central retinal vessels is likely to differ between the time of SDOCT volume acquisition and the time of stereophotography. Also the width of the vessels imaged at the surface of the nerve (as in a photograph) may have differed from the width of vessels at the depth of the en face C-scan used for co-localisation. These differences may result in a discrepancy between the magnification of the en SDOCT image and the disc photograph. The co-localisation technique is 2D and so does not take into account the presence of ONH tilt. This was not a problem for the normal monkey eyes, in which tilt was not a feature. It could, however, lead to misalignment in human eyes with more pronounced tilt, although this was not observed in the single eye examined in this study. It may be necessary to further develop the co-localisation technique, perhaps using 3D viewing software, if this is found to be a problem in other human eyes. Finally, both co-localisation and disc margin delineation are limited by the quality of the acquired stereophotographs and SDOCT volumes.

In conclusion, border tissue and NCO anatomy are well visualised by volumetric SDOCT imaging. The anatomic underpinnings of the disc margin vary regionally, and depend upon border tissue

obliquity, which is detectable by SDOCT. These observations held true in the single myopic human eye examined in this study and served to enhance my understanding of its ONH architecture. These findings pave the way for a more detailed exploration of SDOCT-defined disc margin anatomy in normal, myopic and glaucomatous human eyes.

4.5 Comparison of ONH Morphology Viewed by SDOCT and by Serial Histology

4.5.1 Background

The ability of OCT to image retinal morphology has been validated by a number of seminal studies which have sought to compare OCT tomograms to conventional serial histology in humans (Blumenthal et al., 2007; Chen et al., 2006), monkey (Anger et al., 2004; Toth et al., 1997a; Toth et al., 1997b), tree shrew (Abbott et al., 2009), rodent (Ruggeri et al., 2007) and pig species (Gloesmann et al., 2003). Although not the principal aim, a number of these studies also included brief comments pertaining to ONH and peripapillary retinal morphology (Abbott et al., 2009; Anger et al., 2004; Gloesmann et al., 2003). Besides these commentaries, there have not been, to date, any formal, rigorous comparisons of ONH morphology as imaged by OCT and by light microscopy. An obvious reason for this is that the axial (depth) resolution of conventional TDOCT (approximately 10 µm) has not been sufficient for resolving structures deep to the surface of the optic disc cup. With the commercial introduction of SDOCT, which has both an improved axial resolution (approaching 5 µm) and vastly increased acquisition speed, the 3D detection of deep ONH targets has become tangible.

A number of recent reports suggest that SDOCT imaging of the human ONH can capture the LC (Inoue et al., 2009; Kagemann et al., 2008). Whilst these reports are encouraging, it is essential that SDOCT's ability to capture deep ONH targets be validated by comparison with conventional serial histology.

4.5.2 Purpose

The purpose of this study was to compare interpolated SDOCT B-scans generated from a volumetric SDOCT scan acquired in vivo from a normal monkey ONH with serial histological sections obtained post mortem from the same ONH. This study required the development of a novel method of generating 'tailor-made' interpolated B-scans in any orientation from the 3D SDOCT volume. This method is also fully described.

4.5.3 Methods

ONH Imaging and Sacrifice:

This study was performed on the left eye of a 6.8 year old, 4.5 kg female rhesus macaque (*Macaca mulatta*). All imaging took place immediately prior to sacrifice. Following 30 minutes of IOP stabilisation at IOP 10 mmHg, as per the 'short' compliance test protocol (section 3.3), a pair of left optic disc stereophotographs were acquired using a simultaneous stereo fundus camera (TRC-WT Retinal Camera, Topcon, Paramus, NJ). Following this, a horizontal raster SDOCT scan pattern was acquired with 290 individual horizontal B-scans, 768 A-scans per B-scan, and with each B-scan acquired 9 times and averaged for speckle noise reduction. The scan was centred on the ONH, using a 15º retinal window. The device's in-built eye tracking facility was turned on during acquisition. The device's native viewing software automatically registered all consecutive B-scans relative to each other in the z-axis.

At the conclusion of imaging, the animal was killed during perfusion fixation at an IOP of 10 mmHg and the posterior part of the globe prepared for storage as per the sacrifice protocol described in section 3.6.

Tissue Preparation:

The optic nerve was removed leaving a 3 mm stump attached to the globe. The ONH and peripapillary sclera were trephined (6 mm in diameter, passed from the vitreous surface through the sclera) and a triangular notch was cut into the superior peripapillary sclera. The trephine was photographed at x 2 magnification using an SLR camera (FM2, Nikon, Tokyo) attached to a dissecting microscope (Stereomaster, Thermo Fisher Scientific Inc, Waltham, MA).

Co-localisation of the SDOCT Infrared Image to the ONH Trephine Image:

In order to generate histological sections at approximately the same orientation as the acquired SDOCT B-scans, the location of the 15° SDOCT acquisition window was overlaid onto the digital ONH trephine image. Firstly, the 35 mm color slide image of the trephine was digitised at a resolution of 4800 dpi using a colour-calibrated scanner (ArtixScan M1 Slide Scanner, Microtek Lab, Inc., Fontana, CA). The SDOCT infrared (IR) image was then overlaid onto the digitised ONH trephine image using commercially available image processing software (Adobe Photoshop

CS3, Adobe Systems, Inc., San Jose, CA) by matching the central retinal vessels and their bifurcations. Figure 4-23A shows the co-localised IR image, including the SDOCT acquisition box, at 50% opacity, overlying the ONH trephine photograph. In Figure 4-23B, the co-ordinates of the SDOCT acquisition box have been burnt onto the ONH trephine image.

Tissue Embedding:

Three attempts were made to cut the inferior edge of the ONH trephine under the dissecting microscope parallel to the inferior boundary of the co-localised acquisition box. This was performed using a single edged number 12 industrial razor blade (VWR, West Chester, PA) whilst referencing the image shown in Figure 4-23B. After each cut the ONH trephine was re-photographed and the resultant digital image co-localised to Figure 4-23B so as to assess the accuracy of the cut relative to the inferior border of the overlaid acquisition box. After each inferior cut was found to be inaccurate, two additional cuts were made to the superior part of the trephine, the second of which best approximated the desired orientation (Figure 4-23C). The trephine was then embedded in paraffin using standard histological technique, with the superior cut surface facing downwards in the block.

Histological Sectioning and Staining:

The ONH specimen block was sectioned at 4 µm intervals using a microtome (RM 2155, Leica Biosystems, St Louis, MO). Sections were floated in a water bath (56º C) and picked up onto slides which were incubated overnight at 60º C. Prior to staining, slides were deparaffinised through two changes of xylene for 5 minutes. The slides were then hydrated through two changes each of absolute alcohol and 95% alcohol followed by one change of 70% alcohol and then rinsed in running tap water.

Every fourth section (16 µm intervals) was stained with haematoxylin and eosin (HE) by immersion for 4 minutes in Shandon's Instant Haematoxylin (Thermo-Fisher Scientific, Inc.) then rinsed in running tap water for 5 minutes, counterstained for 45 seconds in eosin, dehydrated, then mounted with a synthetic medium (Eukitt).

In addition to the HE stained slides, individual unstained slides from regions of interest within the ONH were selected for alternative staining (all stains acquired from Thermo-Fisher Scientific,

Inc.). For Masson Trichrome (MT) staining, the deparaffinised, hydrated slides were immersed in Weigert's Hematoxylin for 10 minutes then rinsed in running water for 10 minutes. The slides were then immersed in Biebrich Scarlet-Acid Fuchsin for 5 minutes, then rinsed in distilled water. Finally the slides were immersed in phosphomolybdic-phosphotungstic acid solution for 10 minutes and aniline blue solution for 3 minutes. The slides were rinsed in distilled water, immersed in 1% glacial acetic acid, dehydrated, cleared then mounted. Burke's modification for the combined staining of cells and fibres in the nervous system was used to achieve Luxol Fast Blue/Cresyl Violet Acetate (LFB) staining (Burke, 1968). Finally, staining with a 1:1 (vol/vol) mixture of ponceau-saffron and acid fuchsin was performed in a few selected slides as this is the connective tissue stain used in the 3D histomorphometric reconstruction technique (Burgoyne et al., 2004; Downs et al., 2007; Yang et al., 2007b).

Slides selected for comparison with SDOCT B-scans were imaged at 10 x magnification using an inverted microscope (Leica DM IRBE) and image capture software (Bioquant Life Science, Version 8.10.20, Bioquant Image Analysis Corporation, Nashville, TN).

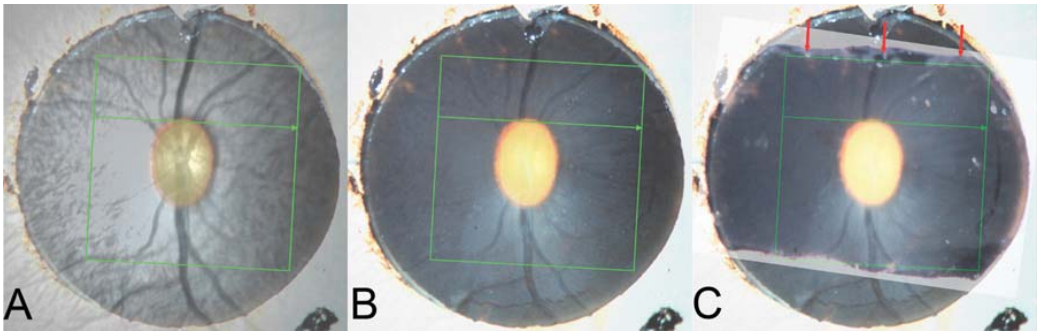

Figure 4-23. Cutting the ONH trephine in the orientation of the acquired B-scan. *A:* the SD-OCT IR image including the 15º-acquisition box, viewed at 50% opacity, aligned to an image of the ONH trephine. *B:* the coordinates of the acquisition box have been burnt onto the trephine image. *C:* cuts have been made in the trephine, in an attempt to get the closest approximation to the orientation of the acquired B-scans. The cut made in the superior part of the trephine (red arrows) most closely matches the acquired B-scan orientation

Orientation of Histological Sections Relative to The Optic Disc Photograph (Figure 4-24):

The 35 mm colour stereo slide pair was digitised as per for the trephine photo. The HE-stained sections (every fourth section) were then reviewed to identify in which slides the superior and inferior openings in the RPE and BM were present. These slides therefore served as 'cardinal' orientation slides, corresponding to the superior and inferior disc margin on the clinical disc photograph (Strouthidis et al., 2009b). The angle of rotation at which each section was acquired was ascertained by tracking the location of each major retinal vessel, its spacing relative to other vessels and relative to the boundaries of the optic nerve and then referencing to a location on the clinical photograph consistent with these anatomical relationships. The 'clinical' location of each histological section was then marked onto the disc photograph, which was then co-localised/aligned to the en face SDOCT image, using the method described above.

Generation of Interpolated B-Scans for Comparison with Serial Histology (Figure 4-25):

Having taken steps to ensure a close match between the histological sections and the acquired SDOCT B-scans, I then attempted to 'fine tune' the accuracy of the match by correcting for two sources of discrepancy. Firstly, I corrected for the degree by which the angle of rotation of the histological section differed from that of the acquired B-scan. Secondly, I corrected for the degree by which the angle of incidence of the microtome blade and the angle of incident light from the SDOCT device might differ. To do so, the ONHRL programmer (Jonathan Grimm) and I developed a method of extracting 'interpolated' B-scans, at any angle of rotation and incidence, from the data contained within the 3D ONH SDOCT volume (Figure 4-25).

Custom software, based on the Visualization Toolkit (VTK, Clifton Park, NY), was used to generate a B-scan plane (x-z plane) and to rotate it about the z-axis to reproduce the 'en face' angle of rotation. The B-scan plane was then rotated about the x-axis to reproduce the angle of incidence. These manipulations were translated to a specified point within the 3D SDOCT volume onto which a fine grid of 1 x 1 μm squares were overlaid. The application of this fine grid onto the B-scan plane was designed to overcome the distortion from the misalignment of the plane with the volume occurring at the sub-pixel level. The fine grid squares were used to sample the volume using a nearest neighbour technique, whereby the distance of the centroid of the

square in the plane to the centroids of the pixels in the volume was computed and the value from the pixel in the volume with the shortest centroid to centroid distance was selected. These data were saved as a floating point tiff image and the plane was shifted along its normal until a complete family of interpolated B-scans was generated. This software could alter the angle of rotation and incidence by 0.5º increments.

The method by which the interpolated B-scan angle of rotation was decided for each histological section is illustrated in Figure 4-26. The disc photograph, containing the topographical location of the HE-stained sections (Figure 4-26A) was co-localised to the en face SDOCT image, using the method described above. Using a fixed centre of rotation, the angle of rotation of each histological section was calculated with reference to the horizontal raster acquisition box, in which the vertical axis is 0º and the horizontal axis is 90º. Having identified the angle of rotation, the purpose-built software generated the complete series of interpolated B-scans for that angle, as though the acquisition window had shifted to the selected angle of orientation.

Once the optimum angles of rotation had been identified, the angle of incidence was estimated. The interpolated B-scans generated above, using an angle of incidence of 0º (perpendicular to the imaged surface), were compared to the histological sections from the same topographic locations. The angle of incidence was then varied by 0.5º increments until the interpolated B-scans best matched the histological section at each location. An example demonstrating the effect of varying the angle of incidence is shown in Figure 4-27.

Comparison of Histological Sections to Matched Interpolated B-scans:

Matched interpolated B-scans (defined to be best corrected for angle of rotation and incidence) and their histological sections were then qualitatively compared to identify which structures within the ONH could be identified by SDOCT. In order to facilitate this, an attempt was made to align ONH structures within each B-scan with their respective location within the matched histological section. Alignment was performed using image processing software (Adobe Photoshop CS3, Adobe Systems, Inc., San Jose, CA). Rotation and scaling in a 1:1 ratio were performed. I did not warp or morph images to correct for tissue processing artifacts in the histological sections such as differential horizontal or vertical shrinkage, choroidal expansion and retinal elevation.

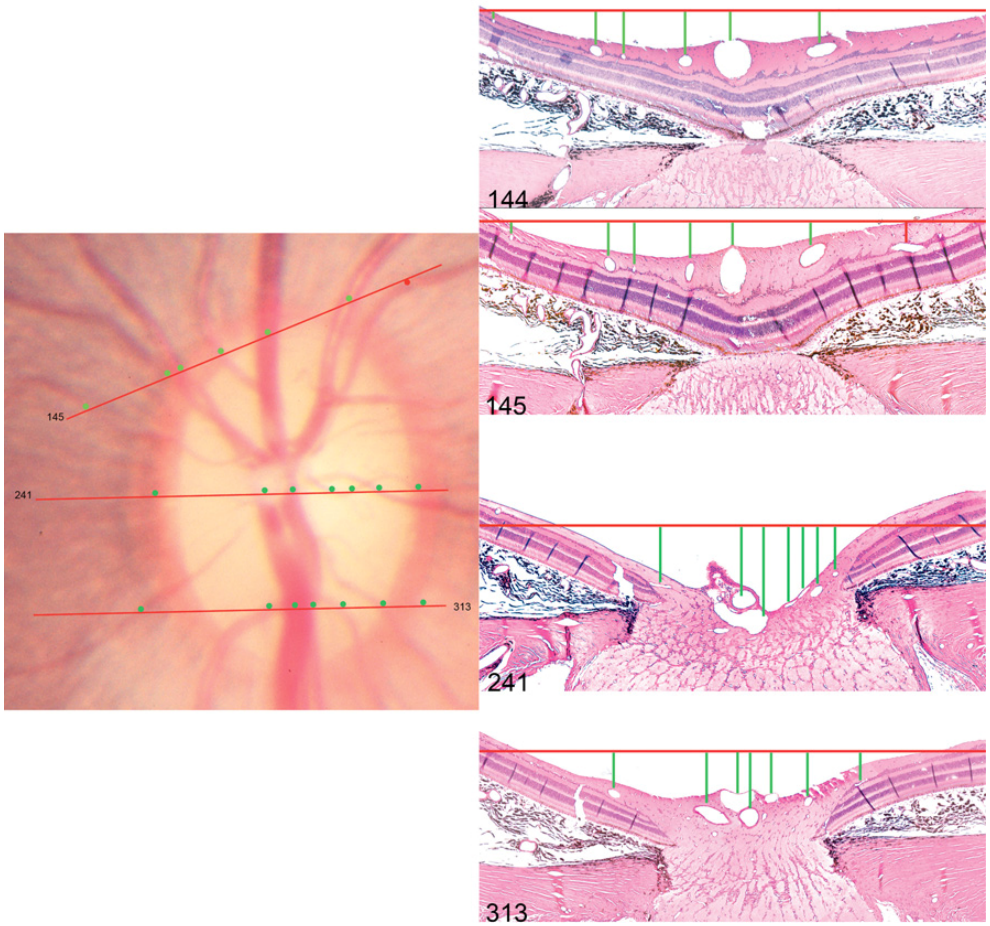

Figure 4-24. Method of orientating histological sections to the disc photograph. The topographical locations of histological sections 145, 241 and 313 (HE, x 10 magnification) are shown. The orientation of each section (red lines in the disc photograph) is judged by assessing the relative spacing of the retinal vessels, marked by circular glyphs in the disc photograph and by vertical lines in the histological sections. Note the temporal vessel highlighted by a red glyph is absent in section 144 but appears in the next section (145). The superior opening in BM (superior disc margin) was identified to be near section 145 (described in detail in Figure 4-27) and the inferior opening in BM was identified to be near to section 335 (not shown here but described in detail in Figure 4-28)

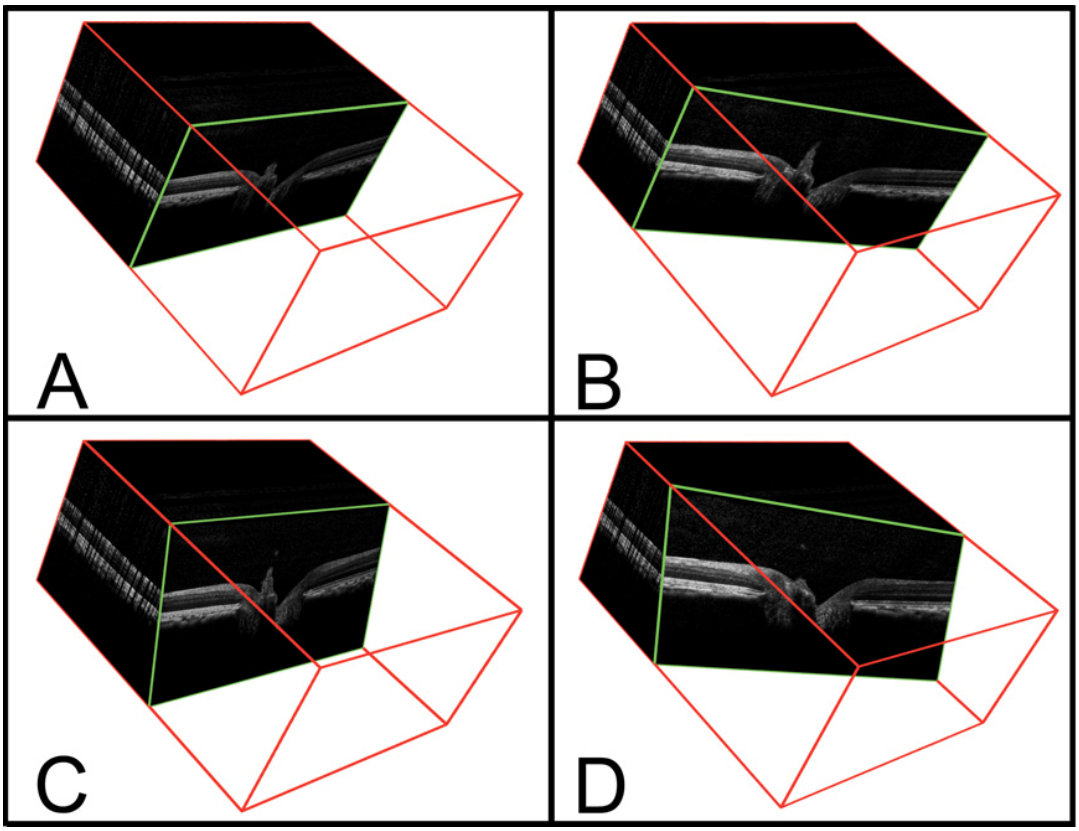

Figure 4-25. Method of identifying interpolated B-scans from the SDOCT volumetric reconstruction. *A:* a representative acquired B-scan is shown within the 3D volume (enclosed within a red cube) generated from a 290 x 768 horizontal raster scan. The angle of rotation of the B-scan is 90º and the angle of incidence is 0º. *B:* the interpolated B-scan shown has been generated following a 20º clockwise rotation (angle of rotation = 70º); the angle of incidence is unchanged. *C:* the interpolated B-scan shown has been generated following a -20º change in the angle of incidence. *D:* the interpolated B-scan shown has been generated using an angle of rotation of 70º and an angle of incidence of -20º

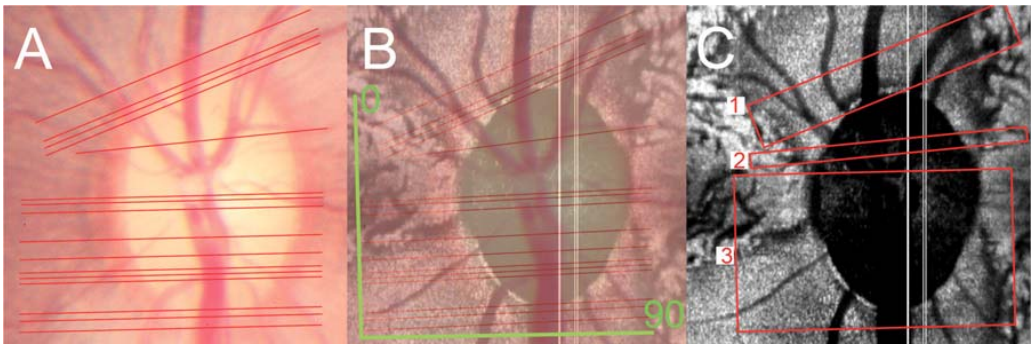

Figure 4-26. Method of identifying the B-scan angle of rotation. *A:* the topographical orientation of serial HE-stained sections is depicted as a series of red lines in the disc photograph. There is a minimum separation of 16 µm between sections. Sections that could not be orientated because of poorly preserved retina account for the variable width of gaps between the lines. *B:* the image shown in A (viewed at 50% opacity) has been co-localised to the en face SDOCT image (C-scan). The 0º and 90º orientations of the actual acquired horizontal raster B-scans are shown in green. *C:* the angle of rotation of the histological sections is assessed relative to that of the acquired B-scans and is found to vary within three regions; 73.5º in histological sections from region 1, 87º in histological sections from region 2 and 89º in histological sections from region 3

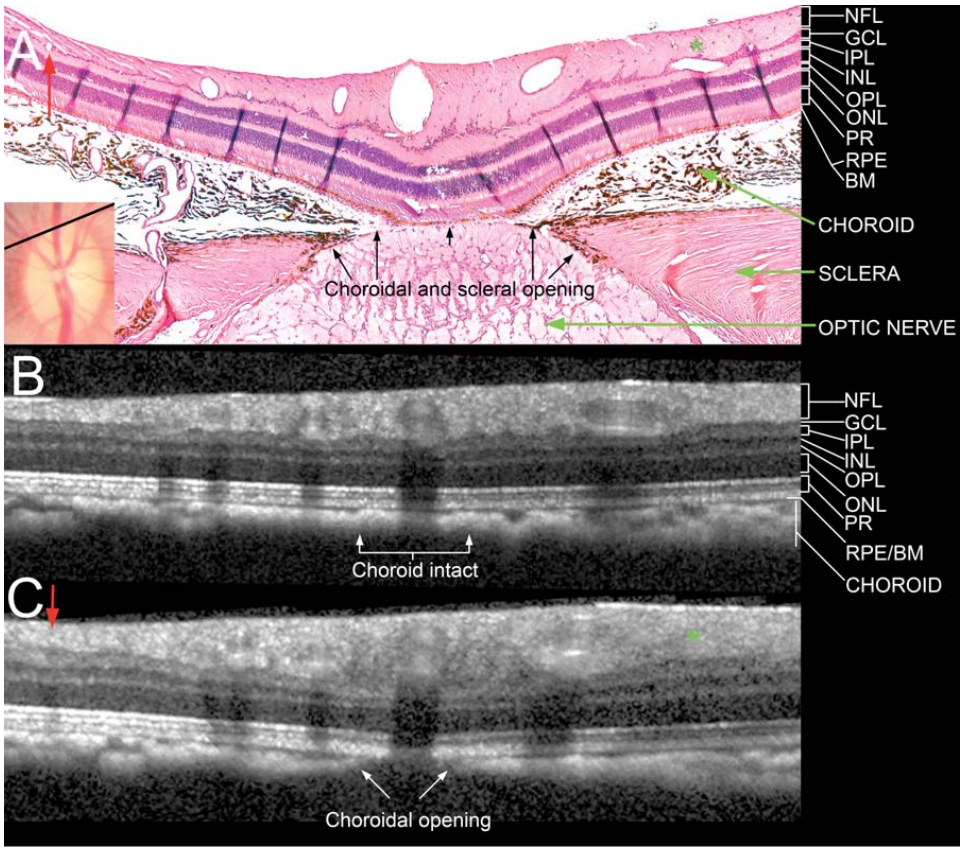

Figure 4-27. Comparison of a histological section located near the superior BMO (disc margin) with matched interpolated B-scans. *A:* section 145 (HE, x 10 magnification) is shown with its location in the disc photograph (inset) shown as a black line. Note the presence of a small vessel nasally (red arrow), and an oblique vessel temporally (green asterisk). There is an opening in the choroid and sclera but RPE and BM are intact over the optic nerve. *B:* an interpolated section generated from the same topographic location, at an angle of rotation of 73.5º, angle of incidence of 0º (perpendicular to the surface). Neither of the vessels highlighted in A are detected and the choroidal signal is continuous. *C:* an interpolated B-scan generated from the same location as B, an angle of incidence of -18º (angled towards the nerve). The two vessels are visible in the correct location (red arrow and green asterisk). An opening in the choroid is now visible, RPE/BM complex remains intact, but no signal from the deeper optic nerve and LC are detected. NFL = nerve fiber layer, GCL = ganglion cell layer, IPL = inner plexiform layer, INL = inner nuclear layer, OPL = outer plexiform layer, ONL = outer nuclear layer, PR = photoreceptor layer

4.5.4 Results

Topographic Location of Histological Sections:

525 histological sections, with a minimum separation of 4 µm between each section, were generated from the ONH trephine. Figure 4-26A illustrates the location of the initial HE-stained sections (every fourth section) throughout the full extent of the disc photograph. HE-stained sections in which the retina was insufficiently preserved to allow the accurate identification of retinal vessels were not used for comparison.

Generation of Matched Interpolated B-scans:

Histological sections in the superior part of the nerve (region 1 in Figure 4-26C) required interpolated SDOCT B-scans to be generated at an angle of rotation of 73.5º. Inferior to this, there was a small portion of the nerve (region 2 in Figure 4-26C) in which the matched angle of rotation was 87º. The remaining sections (region 3 in Figure 4-26C) required an angle of 89º, which was almost identical to the acquired B-scan angle of 90º.

The effect of altering the angle of incidence of the interpolated B-scan for a given histological section is illustrated in Figure 4-27 for section 145, which is located close to the superior disc margin. In this section the RPE and BM are still intact, although there is an opening in both the choroid and the sclera. An interpolated B-scan generated at an angle of incidence of 0º, perpendicular to the retinal surface, (Figure 4-27B) was not as accurate as an interpolated B-scan generated at an angle of incidence of -18º, which was angled towards the nerve (Figure 4-27C). Figure 4-28A shows histological section 335, which is located close to the inferior disc margin. In this section, an opening in the choroidal space is present below the intact RPE. A very small portion of the optic nerve is visible above a small intact portion of peripapillary sclera, suggesting that the section was acquired at a less oblique angle than section 145. Figure 4-28B shows the matched interpolated B-scan, generated at an angle of incidence of 0º. All of the major vessels seen in the histological section are detectable in this interpolated B-scan. Likewise the opening in the choroid is present, along with a faintly continuous RPE/BM complex signal. It should be noted that the shadow cast by the presence of two large retinal vessels above this region would have contributed to the ‘faintness’ of this latter signal. The sclera is not detected in this section,

although there is a faint signal below the choroidal opening suggesting that some reflected light from the underlying optic nerve has been captured.

An angle of incidence of -18º was found to achieve the best matches in the part of the nerve where sections were acquired at an angle of rotation of 73.5º (region 1 in Figure 4-26C). Where the angle of rotation was 87º (region 2 in Figure 4-26C), an angle of incidence of -10º achieved the best matches. In the remainder of the ONH, where the angle of rotation was 89º (region 3 in Figure 4-26C), the best matches were achieved with an angle of incidence of 0º.

Detection of Deep ONH Structures:

Two examiners (myself and Professor Burgoyne) qualitatively compared the matches between interpolated B-scans and their respective histological sections. The vitreal surface of the ONH was detectable by SDOCT throughout its full extent. However, SDOCT visualisation of structures deep to the surface was poor in regions where shadows were cast by the central retinal vessels. Interpolated B-scans matched to histological sections acquired from the central part of the disc (sections 256 - 260) were selected for the detailed assessment of deep ONH imaging, as they had the largest continuous 'shadow free' areas either side of the central retinal vessels (Figures 4-29, 4-30 and 4-31). For these comparisons, the same interpolated B-scan was matched to each section because the separation between adjacent B-scans was approximately 12 - 16 µm, which was comparable to the separation between the selected histological sections. Within these sections a prominent Bergmeister's papilla was clearly visualised within both the histological sections and the interpolated SDOCT B-scan.

Figure 4-29 reports the SDOCT correlates to the histological components of the NCO. Here the RPE/BM complex is defined to be the posterior signal from the hyper-reflective 'triple stripe' below the dark, hypo-reflective outer nuclear layer (Drexler and Fujimoto, 2008; Strouthidis et al., 2009c). I have defined the innermost termination of this signal at either side of the neural canal as the NCO (section 4.2) (Strouthidis et al., 2009c). In Figure 4-29A, section 257 (HE-stained) is shown, with the temporal canal opening magnified as an inset. The retinal layers can be seen to taper downwards towards a point between the outer nuclear and photoreceptor layers (marked by black arrows). In this section, the termination of the RPE is external to the termination of Bruch's

membrane and these same relationships are easily discerned within the matched interpolated B-scan (Figure 4-29B). Within section 260 (Figure 4-29C), Ponceau S stain better reveals the extension of unpigmented BM beyond the RPE.

In Figure 4-30A (histological section 258, stained with MT), the border tissue of Elschnig is seen at either side of the neural canal, between the sclera and BM. Within the matched interpolated B-scan (Figure 4-30B), the border tissue corresponds to the junction of the choroidal signal with the nerve and the heavy pigment located just below this, at the edge of the sclera. Within this matched interpolated B-scan, the anterior scleral surface is not visible.

The pre-laminar glial columns are most easily visualised in the HE-stained section (Section 257, Figure 4-31A, black arrows) where the glial nuclei are prominently stained; to a lesser extent, the connective tissue component of these columns is detectable with MT staining (Section 258, Figure 4-31B). These columns can be seen to commence within the neural canal at approximately the level of the NCO and the border tissue. The columns extend posteriorly as vertical struts until the point where they merge with the more horizontally orientated laminar beams. Vertically orientated striations within the matched interpolated B-scan (Figure 4-31A) appear to correspond to the prelaminar glial columns.

In Figure 4-31B, I define the anterior laminar surface in the histological section to be the innermost point at which horizontally/transversely orientated connective tissue can be identified. Within the matched interpolated B-scan there appears to be a distinction between the prelaminar glial columns (vertical striations) and the anterior laminar surface (transversely orientated signal), particularly in the nasal side of the scan. Although the precise peripheral scleral insertion of the lamina cannot be visualised in this B-scan, the anterior laminar surface signal can be seen to bend upwards towards a point below the border tissue on both sides of the neural canal. The posterior laminar surface (Figure 4-31C) was not detectable in the matched interpolated B-scan.

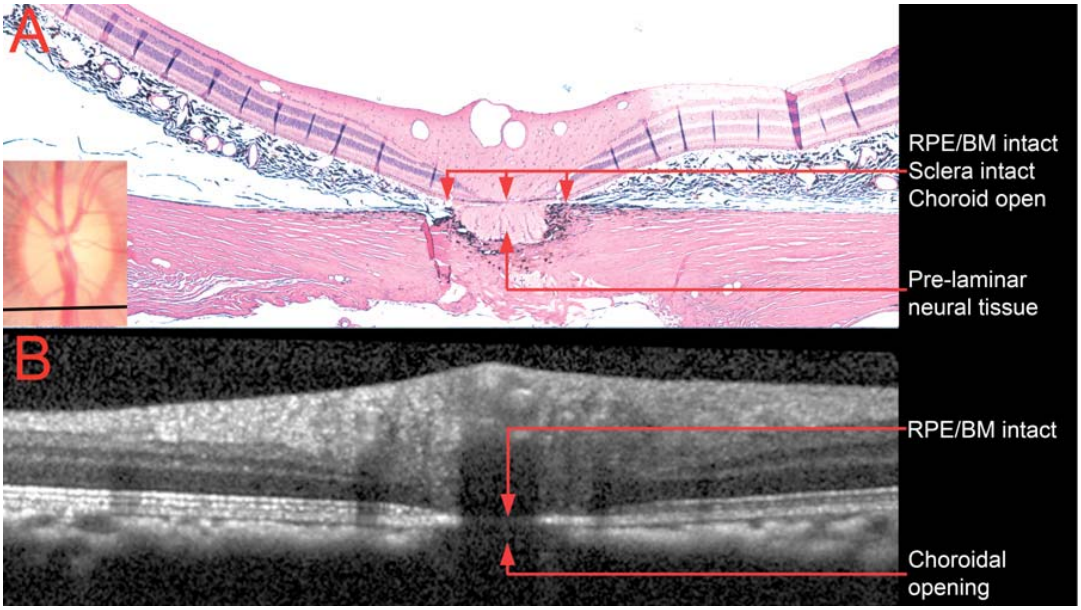

Figure 4-28. Comparison of a histological section located near the inferior BMO (disc margin) with its matched interpolated B-scan. *A:* section 335 (HE, x 10 magnification) is shown with its topographical location shown as a black line in the clinical photograph (inset). *B:* the matched interpolated B-scan has been acquired at an angle of rotation of 89º, but the angle of incidence was kept at 0º. Note that the RPE/BM complex is intact, but the opening in the choroid is present, as in the histological section. The prelaminar neural tissue and the intact sclera are most likely not detected because of shadowing from the central retinal vessels

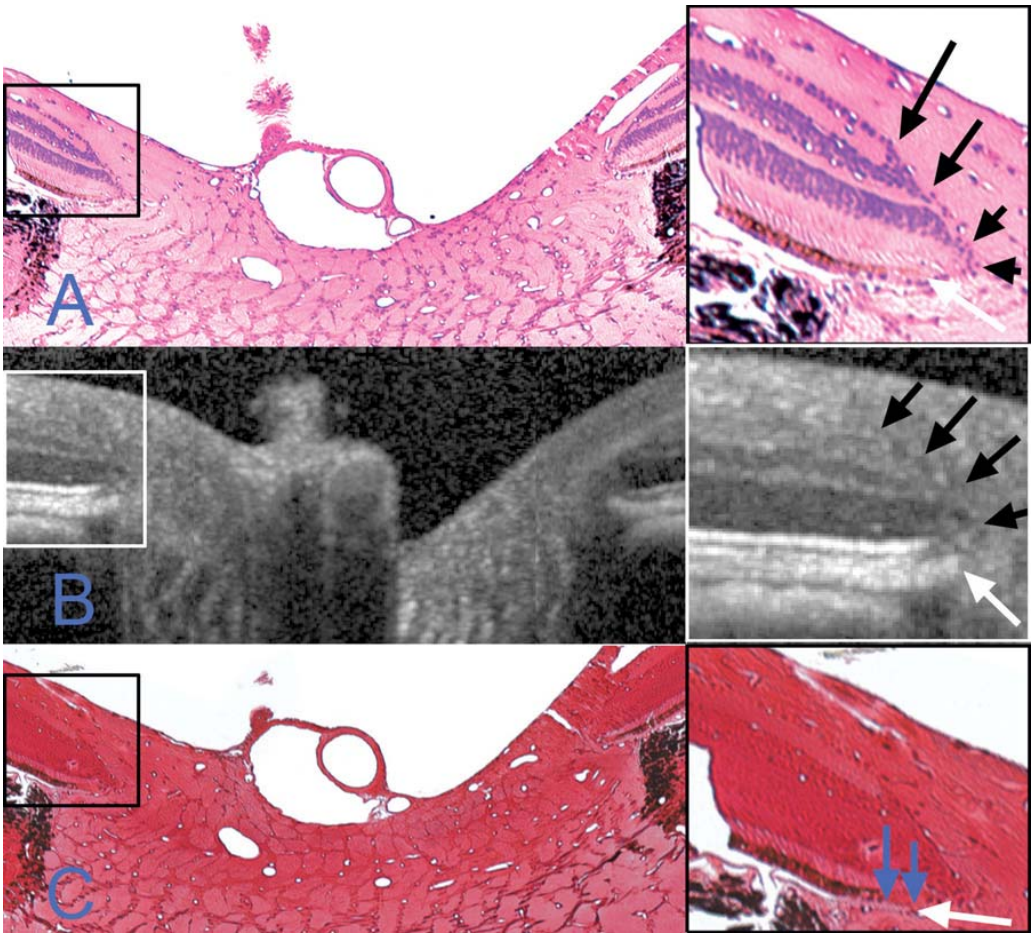

Figure 4-29. Identification of the NCO. Highlighted regions (boxes on left) are magnified on the right. Note that differences in anterior surface tilt between the B-scan and the histological sections can be explained by the presence of retinal elevation/detachment and of a 'rip' in the retina on the left hand side of the sections (both features cropped out of A and C). *A:* section 257 (HE, x 10 magnification) is shown. The NCO is highlighted with a white arrow in the magnified view. Note that at this location the retinal layers taper to a point (black arrows) at the photoreceptor layer, internal to the NCO. *B:* the matched interpolated B-scan. The same relationship between the retinal layers (black arrows) and the termination of the RPE/BM complex (white arrow) as was detected in A is seen in the magnified view. *C:* section 260 (Ponceau S, x 10 magnification). Using this stain, the distinction between the termination of the RPE and an extension of unpigmented BM (blue arrows) is clearly visible

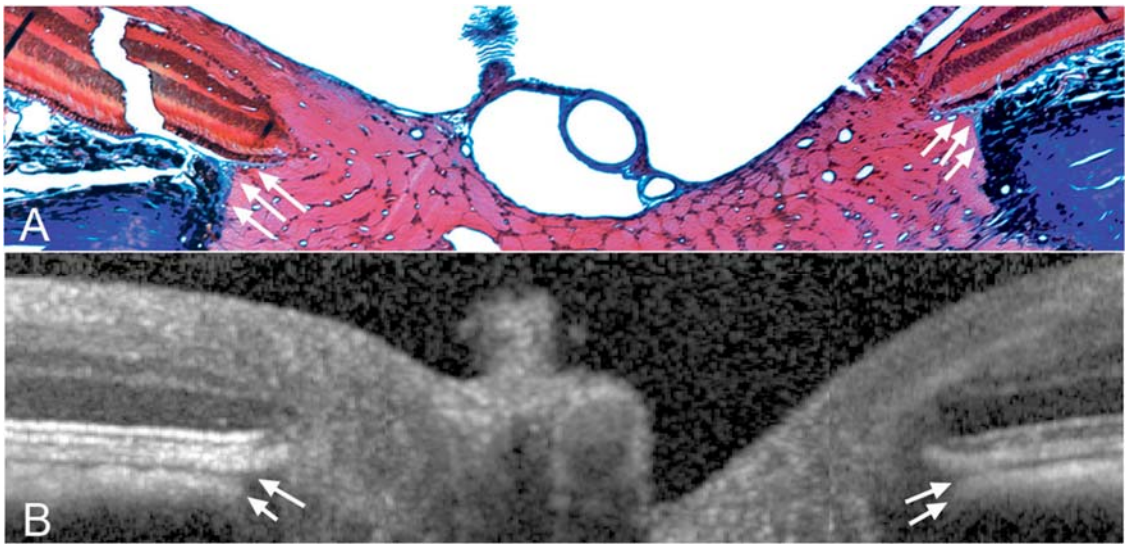

Figure 4-30. Detection of border tissue of Elschnig. *A:* section 258 (MT, x 10 magnification), with border tissue highlighted with white arrows. This histological section was located immediately adjacent to the section shown in Figure 4-29. Note that the border tissue is seen as a connective tissue strut (stained blue) connecting the anterior sclera to BM and enclosing the choroid. A more complete view of this section is shown in Figure 4-31. *B:* the border tissue signal in the matched interpolated B-scan is highlighted using white arrows. SDOCT appears to accurately capture the orientation of the border tissue with an internally oblique configuration seen nasally/left and an externally oblique configuration seen temporally/right (section 4.4) (Strouthidis et al., 2009b)

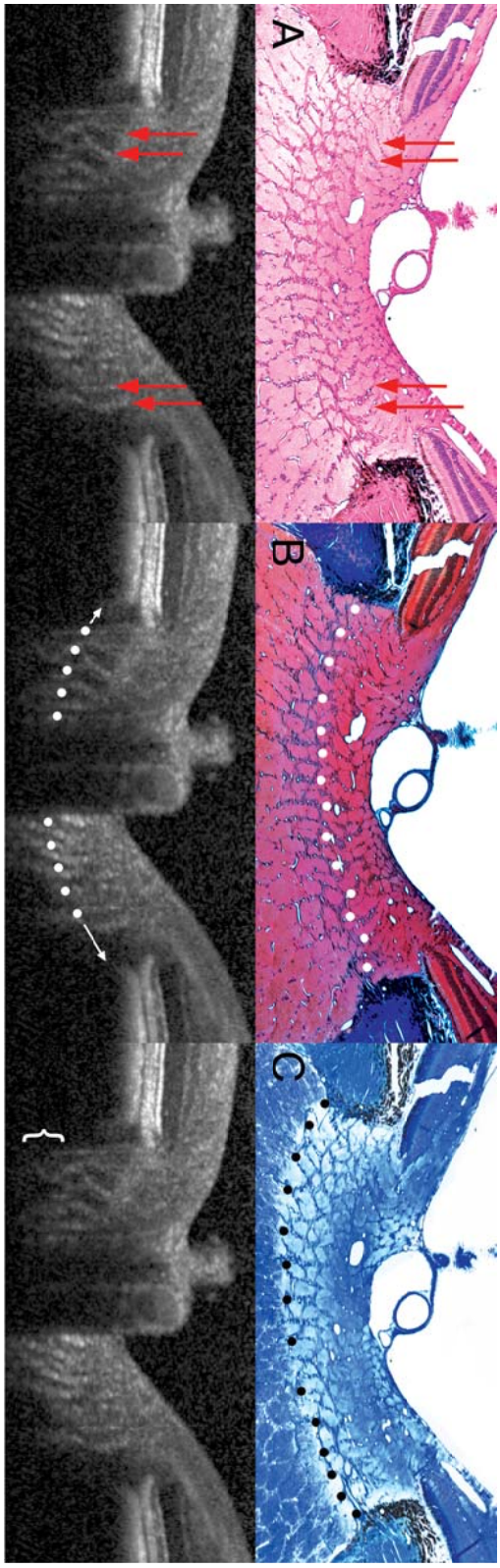

(Figure 4-31; figure legend overleaf)

Figure 4-31. Detection of the LC. *A:* section 257 (HE, x 10 magnification); prelaminar glial columns appear to correspond to vertical striations seen in the matched interpolated B-scan below (marked with red arrows). *B:* section 258 (MT, x 10 magnification); the anterior laminar surface is delineated with white glyphs. Note that the peripheral insertion of the lamina is not clearly visible in the interpolated B-scan, although the approximate level of insertion may be ascertained by following the contour of the anterior laminar signal to the periphery of the neural canal (white arrows). *C:* section 256 (LFB, x 10 magnification); the posterior laminar surface is delineated with black glyphs in the histological section. The posterior surface is not detectable in the matched interpolated B-scan, as the signal fades rather than comes to a discrete termination (region highlighted by a white bracket)

4.5.5 Discussion

This experiment represents an important step in verifying the deep ONH imaging capabilities of SDOCT. The following ONH targets could be identified by SDOCT: the vitreal surface of the ONH, prelaminar tissue, NCO, border tissue, choroid, prelaminar glial columns and the anterior laminar surface. The anterior and posterior scleral surfaces, the peripheral insertion of the lamina and the posterior laminar surface were not detectable within this SDOCT volume. I was unable to identify a distinct signal from BM separate from RPE. Interestingly, it would appear that the SDOCT defined NCO (magnified inset of Figure 4-29B) took into account a portion of unpigmented BM, extending beyond the termination of the RPE (magnified inset of Figure 4-29C). However, in this particular SDOCT volume, a transition point, such as an abrupt decrease in the width of the RPE/BM complex, was not detected.

The detection of an SDOCT signal attributable to the border tissue has clinical relevance in terms of defining the optic disc margin, as discussed in the preceding experiments (sections 4.3 and 4.4). In his classic description of the ultrastructure of the human and monkey ONH, Anderson was unable to detect border tissue of Elschnig in the monkey eye (Anderson and Hoyt, 1969). A connective tissue strut, emanating from the scleral surface, is clearly visible in the MT-stained

section (Figure 4-30A, white arrows). This structure almost certainly represents border tissue of Elschnig, although it is perhaps a less robust structure than in the human eye. This experiment confirms that, at least in this eye, SDOCT volumetric reconstruction appears to accurately capture the orientation of the border tissue relative to the sclera and Bruch's membrane.

A key finding of this experiment is the confirmation that SDOCT is capable of detecting the prelaminar glial columns and the anterior surface of the LC. This suggests that SDOCT might be useful for detecting morphological changes in the prelaminar glial columns as well as displacement of the anterior lamina. Inoue and co-workers recently identified the LC to be a highly reflective signal beneath the optic disc cup in horizontal SDOCT B-scans acquired from glaucomatous or ocular hypertensive human eyes (Inoue et al., 2009). Furthermore, the distance between the anterior and posterior borders of this signal was defined as the thickness of the LC. Laminar thickness measurements were found to have a high inter-observer reproducibility and to be significantly correlated with visual field mean deviation.

My comparisons between serial histology and SDOCT in this monkey eye suggest that the detection of the LC is not so straightforward. Within this SDOCT volume there was a distinction between the vertical striations, which likely represent the prelaminar glial columns, and the interconnecting horizontal signal, which likely represents the horizontal laminar beams between the vertical septae. The anterior laminar 'signal' is certainly more reflective in the SDOCT horizontal B-scans presented by Inoue and co-workers, than in the B-scans examined in the current study (Inoue et al., 2009). Likewise, in my experience, the reflectivity of the anterior laminar surface is higher in human eyes compared to monkey eyes. Laminar reflectivity appears to be further enhanced in highly myopic and glaucomatous eyes, which I assume is due to thinning of the prelaminar neural tissue. It is also important to note that, in humans, the central retinal trunk is located nasally whereas in the monkey the trunk tends to be central (as in this eye). If one assumes that laminar reflectivity is affected by the thickness of the prelaminar tissue, it follows that the most intense signal should be observed beneath the central, deepest, part of the cup. Unfortunately, in the eye examined in this study, the signal from the centre of the lamina was obfuscated by 'fringe-washout' from the main vessel trunk.

It is also important to recognise that the ocular tissues of monkeys tend to be more heavily pigmented than human eyes (Marshall et al., 1975). The heavy pigment on the surface of the anterior sclera (and indeed the peripheral lamina) of the eye examined in this study might absorb, rather than reflect, the incoming SDOCT illumination. This may, in part, explain why there was no signal from the anterior scleral surface or from the peripheral laminar insertion.

In this one eye, using a conventional 870 nm light source, the location of the posterior laminar surface was not apparent. In the B-scans examined, the laminar signal appears to 'fade' with increasing depth through the ONH volume. I cannot be certain whether this drop-off in reflectivity is due to the absence of horizontal laminar beams at the posterior laminar surface or because the posterior limit of tissue penetration has been reached. For this reason, I would exercise caution in trying to calculate in vivo laminar thickness using SDOCT. As Inoue and co-workers have reported that their measurements of laminar thickness were correlated to mean deviation in a cross-sectional cohort (Inoue et al., 2009), the inference is that SDOCT will detect progressive laminar thinning in glaucoma. Although this suggestion is supported by a body of literature reporting that compression of the lamina occurs at early, moderate and severe stages of glaucoma damage (Emery et al., 1974; Quigley et al., 1983; Yan et al., 1994), reports from the ONHRL have identified profound laminar thickening at the earliest stages of the neuropathy in a monkey model of glaucoma (Yang et al., 2007b). Longitudinal in vivo SDOCT ONH imaging should eventually assist in establishing the relationship between laminar morphology and stage of disease. My confidence in identifying the posterior laminar surface may be increased with the adoption of a 1060 nm light source, which has increased axial penetration as compared to the standard 870 nm light source as used in the Spectralis (Povazay et al., 2003; Povazay et al., 2007a; Wang et al., 2003). The deep ONH imaging capabilities of this alternative light source will be verified by repeating the current experiment using a Spectralis prototype equipped with the alternative wavelength light source.

By elucidating the topographic location of the HE-stained sections with well-preserved retina, as depicted in Figure 4-26A, I identified that there was a clear angular discrepancy between the histological sections and the acquired B-scans in the superior third of the ONH. It is very unlikely

that the microtome rotated through successive sections to such an extent as to account for the observed discrepancy. The most likely explanation is that the retina in that region was elevated and curled upwards within the block, resulting in a 'non-aligned' portion of the retina contacting the microtome blade. Histological sections in the lower two thirds of the nerve were fairly closely matched to the acquired B-scans, with only a 1º difference in the angle of rotation and the angle of incidence being perpendicular to the retinal surface. This suggests that the surface topography of the specimen was flatter and less variable in this region. The degree of retinal elevation in the ONH specimen may have been less pronounced were a larger diameter ONH trephine selected. It is also possible that the perfusion fixation process contributed to the retinal elevation by causing expansion of the choroidal space. The presence of retinal elevation in the histological sections explains the discrepancy observed in the tilt of the anterior retinal surface in the histological sections as compared to the interpolated B-scans, particularly in Figure 4-29. There is also a substantial rip in the peripapillary retina present in the nasal half of the histological sections shown in Figures 4-29 to 4-31, which was likely to have further affected the degree of anterior surface tilt.

The method of generating interpolated B-scans from the acquired SDOCT volume represents a potentially important development in the visualisation of ONH images. The matched interpolated B-scans in this experiment demonstrated minimal diminution in image quality compared to the acquired B-scans, despite the fairly wide variation in the angle of rotation and incidence. Greater diminution of image quality would have been observed if any of the interpolated B-scans approached a vertical orientation (perpendicular to the acquired B-scans). In the selected horizontal raster scan pattern, the x-axis contains 768 'samples' per 15º, whereas the y-axis contains 290 'samples' per 15º. The pixels generated are therefore not cubic but are 'stretched' in the y-axis, with less density of data compared to the x-axis. In order to minimise the diminution in image quality, regardless of the angle of rotation, a B-scan pattern with an equal sampling density in both axes would be required. Although it is theoretically possible to generate a 768 x 768, or indeed a 1536 x 1536, horizontal raster pattern scan using the Spectralis, achieving such a dense

pattern would be limited in practical terms by the test duration and by the memory constraints of the acquisition and viewing hardware and software.

In order to achieve the best approximate alignment between the interpolated B-scans and the serial histological B-scans, the magnitude of the B-scans was adjusted using a 1:1 scale. Although the approximate horizontal alignment appears defensible, the B-scans appear 'stretched' in the vertical direction, with the cup and the anterior laminar surface seemingly deeper in the B-scan as compared to the matched histological section. The SDOCT volumes are transferred to custom visualisation software in a 1:1 μm scale, rather than in a 1:1 pixel scale. Although the z-axis scaling is fixed, the lateral magnification (x- and y-axis orientation) of the Spectralis is based on the optics of the human and not the macaque eye. The purpose of this study was to establish the histological basis of SDOCT signals deep within the ONH, rather than to achieve precise structural quantification. While an algorithm for macaque-specific lateral magnitude scaling is currently being developed, that capability was beyond the scope of the current experiment. These scaling issues partly explain why the thicknesses of retinal layers (particularly the photoreceptor and the RPE/BM) appear much thicker in the interpolated B-scans than in the histological sections. Undoubtedly there is also an effect of differential tissue shrinkage, which has not been corrected in the rescaling of the interpolated B-scans. Finally, the thicknesses seen in the deep retinal layers by SDOCT are also likely to be influenced by the strength of reflected signal over distance, rather than just the thickness the tissue of interest.

A major limitation of this experiment is that it was performed on a single monkey eye, which might mean that the results are not be fully applicable to all human eyes. It is also important to recognise that the optic disc examined in this study had a very regular morphology, with a distinct clinical disc margin and no evidence of tilt or of peripapillary atrophy. Indeed these latter two features are far less prevalent in monkeys than in humans, and when present usually have a less exaggerated presentation than in the human eye. However, I believe that the merits of this experiment are such that the results are of relevance and interest. First, the morphology and histology of the monkey and human ONH are extremely similar and as such the characterisation by SDOCT is likely to be closely matched. By using a monkey eye, I was also able to perform

SDOCT imaging immediately prior to obtaining the tissue specimen by perfusion fixation. By using an anterior chamber manometer it was possible to establish the same level of IOP at the time of imaging and at the time of death. This kind of study cannot be replicated using a human eye.

This study provides histological evidence that volumetric SDOCT imaging of the ONH is capable of capturing ONH target structures, in particular the anterior laminar surface, which may prove useful in the detection of early changes in ocular hypertension and glaucoma (Yang et al., 2009a; Yang et al., 2007b). The novel method for generating interpolated SDOCT B-scans at any angle of rotation or incidence will expand the clinical application of this technology in normal and glaucomatous human eyes**.**

4.6 Longitudinal Change Detected by SDOCT in EG

4.6.1 Background

To date, most longitudinal imaging studies in glaucoma have utilised CSLO, in particular, the HRT (Heidelberg Engineering, Heidelberg, Germany), either by measuring changes in surface height (TCA) or changes in neuroretinal rim area (Artes and Chauhan, 2005; Chauhan et al., 2009a; Fayers et al., 2007). Progressive nerve fibre layer loss has also been reported in glaucoma subjects based on measurements by TDOCT (Medeiros et al., 2009; Wollstein et al., 2005), and more recently, longitudinal RNFL changes have been documented by scanning laser polarimetry (Alencar et al., 2010). It should be noted, however, that the preponderance of longitudinal imaging studies using the CSLO, as opposed to other imaging modalities, reflects the length of time CSLO has been available as compared to newer techniques. This remains a central problem, as development and improvement in imaging hardware and software tend to occur at a more rapid rate than the evaluation of their ability to detect longitudinal change.

One approach, which might help establish a new device's ability to detect longitudinal change, may be to use an EG model. In the case of the monkey model, the experimental neuropathy is largely clinically indistinguishable from that observed in human glaucoma and the changes observed develop over the course of months rather than years or decades, as in humans. The ONH of the rhesus macaque has a similar anatomy to that of the human, in particular the presence of a connective tissue LC. Post mortem studies suggest that the structural ONH abnormalities occurring at the earliest stages of the experimental neuropathy include posterior displacement of the LC, thickening of the LC, a widening of the scleral canal opening and a thickening of the prelaminar tissue (Downs et al., 2007; Yang et al., 2007a; Yang et al., 2007b). These changes may well represent the earliest signs of an ONH 'in distress' from an IOP related insult, which would make them an important target for detection by in vivo imaging. Such anatomical targets, deep to the surface of the cup, may be within the resolution of SDOCT as demonstrated in the previous experiment (section 4.5) (Strouthidis et al., 2010).

4.6.2 Purpose

The purpose of this experiment was to investigate whether longitudinal changes deep within the ONH, as well as RNFL and neuroretinal rim changes, are detectable by longitudinal SDOCT imaging in an experimental model of glaucoma. I also sought to determine whether deep ONH changes were detectable by SDOCT at the onset of ONH surface topography change as detected by CSLO.

4.6.3 Methods

Imaging:

Nine adult rhesus macaque monkeys (*Macaca mulatta*) were included in this study. All imaging was performed as per the 'short' compliance test protocol (section 3.3), following 30 minutes of IOP stabilisation at IOP 10 mmHg.

An 80 radial B-scan SDOCT (Spectralis, Heidelberg Engineering) pattern was acquired over a 15° area (768 A-scans per B-scan). All image acquisitions were centered on the ONH, and this scan location was consistent in all images used in this study. The device's eye tracking facility was turned on during image acquisition to enable B-scan acquisition repetition (n=9) and sweep averaging in real time to reduce speckle noise. For each eye, at each imaging session, the 80 B-scans were acquired relative to a single reference image. Therefore, for each eye, the location of each B-scan remained stable within all pre- and post-laser images.

Both eyes of each animal underwent 'baseline' imaging on three to four occasions prior to the commencement of argon laser treatment to the trabecular meshwork of one eye to induce unilateral, chronic, mild-to-moderate IOP elevation. Laser treatment was repeated approximately every two weeks to induce a sustained elevation in IOP. A full description of the EG induction method is included in section 3.6. The eye in which laser treatment was carried out will hereafter be referred to as the EG eye and the untreated, fellow eye as the 'control' eye. Imaging of both eyes of each animal continued every two to three weeks after the commencement of laser therapy.

In addition to SDOCT imaging using Spectralis, CSLO images were also acquired from both eyes at each imaging session using the HRT II. Two measures of HRT II-defined surface height depression (assumed to be posterior deformation) were used to identify the onset of experimental glaucomatous optic neuropathy. The first utilised the parameter mean position of the disc (MPD), which has been described in previous publications (Burgoyne et al., 2004; Burgoyne et al., 1994). Briefly, MPD refers to the height of the surface of the ONH (i.e. average of all pixels located within the contour line) relative to the height of a reference located on the peripapillary surface. $MPD_{Baseline}$ was calculated for each eye as the mean MPD from all pre-laser baseline images. 'MPD onset' was defined as the first post-laser session when MPD exceeded the 95% confidence limits of the $MPD_{Baseline}$ for that eye, if the change was confirmed in two subsequent follow-up imaging sessions. The second method used TCA, the native progression algorithm contained within the HRT II Explorer software platform (section 2.3.3). 'TCA onset' was defined as the first session when 20 or more significantly depressed superpixels were present within the disc margin, confirmed in two subsequent sessions.

For the purposes of this study, four time-points were selected for each animal, from which a single SDOCT volume from each eye at each time-point was analysed. Two baseline time-points, baseline 1 (BL1) and baseline 2 (BL2), were selected randomly from the series of three or four pre-laser imaging sessions. Two follow-up time points were selected from the sequence of sessions beginning after the onset of laser treatment. The first follow-up SDOCT volume, follow-up 1 (FU1), was chosen to be the time point when CSLO-defined surface height depression was first identified - either by MPD change or by TCA change, whichever occurred first. The second follow-up SDOCT volume, FU2 was chosen from the most recently available imaging session for each animal. This approach was taken to ensure that the EG eyes could be expected to be homogenous in terms of early experimental damage at FU1, but heterogeneous in terms of the stage of damage at FU2. Furthermore, it enabled me to determine whether any of the deep ONH changes identified at later stages of glaucomatous optic neuropathy would manifest at the onset of CSLO-detected ONH surface height depression.

Delineation and Parameterisation of SDOCT Volumes:

I have described the SDOCT delineation method within Multiview in previous experiments (sections 4.2.3 and 4.4.3).

In this experiment, 4 observers (including myself), masked to both eye status (whether EG or control) and time-point, manually delineated pertinent features within alternating B-scans in each SDOCT volume (i.e. 40 B-scans per 80 radial B-scan volume, with the first delineated B-scan being at the vertical, 0° location). The features delineated were: the internal limiting membrane (ILM), posterior surface of the RNFL, posterior surface of the RPE/BM, NCO (as defined in section 4.2.3), border tissue of Elschnig (as defined in section 4.4.3) and the anterior LC surface (ALCS). An example B-scan with these delineation categories is provided in Figure 4-32.

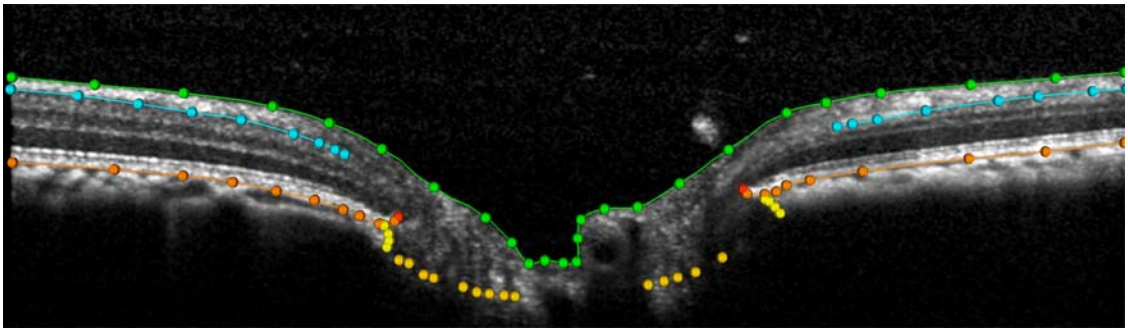

Figure 4-32. Delineation of landmarks within an ONH SDOCT B-scan.

Green = ILM

Blue = posterior surface of RNFL

Orange = posterior surface of RPE/M complex

Red = NCO, located at the innermost termination of the RPE/BM complex

Yellow = border tissue of Elschnig, located at innermost termination of choroidal signal

Gold = ALCS; refer to Figure 4-31 to see how this structure is identified in a B-scan

In the case of the ILM, RNFL, RPE/BM and border tissue categories, each surface was delineated using discrete points interconnected by a Bézier curve. The position of each point in each category was finely adjusted so that the fitted Bézier curve matched the feature of interest

as closely as possible. My strategy for identifying the ALCS was based on my findings from the preceding experiment (section 4.5) (Strouthidis et al., 2010). I therefore identified the ALCS as being the point where horizontal high intensity signal below the disc surface begins to intersect the high intensity vertical striations, which I have identified as the prelaminar glial columns (Figure 4-31). It is important to note that the signal from the ALCS may be discontinuous in regions where there is pronounced shadowing caused by overlying retinal vessels. It is for this reason that the ALCS was delineated using discrete marks, rather than using continuous Bézier curves. The observer could employ any number of marks, at their discretion, to delineate the ALCS.

All x,y dimensions in the SDOCT volumes were re-scaled from the linear units reported by the Spectralis (which assumes human eye optics and dimensions) to estimates optimised for the monkey eye using a scaling factor of 0.857, which was based on the average axial length of 20.6 mm obtained from measurements on 16 of the 18 eyes in this study. Structural parameters were based on these scaled delineations (MATLAB, MathWorks, Natick, MA).

Two reference planes were used for quantification purposes. The best-fitting ellipse through the 80 delineated NCO points in each volume defined the primary reference plane (section 4.2). A secondary reference plane was based on a peripheral location along the RPE/BM complex, 1500 µm external to the NCO centroid (Fortune et al., 2009). The depth of the NCO centroid relative to the secondary, peripheral reference plane was calculated for each eye (Figure 4-33A). RNFL thickness (RNFLT) was calculated at an eccentricity of 1200 µm from the NCO centroid (Figure 4-33B) as previously described (Fortune et al., 2009). The RNFL volume (RNFLV) represents the volume of RNFL between the eccentricities of 1200 and 1500 µm from the NCO centroid. It is bounded above and below by the ILM and RNFL surfaces, respectively, interpolated across all 40 B-scans, internally by a cylinder with a 1200 µm radius orientated perpendicular to the NCO plane, and externally by a cylinder with a 1500 µm radius oriented perpendicular to the NCO plane (Figure 4-33C). The NCO area was calculated as the area of the best-fitting ellipse determined by the 80 delineated NCO points (section 4.2.3). Likewise the border tissue area was calculated as the area of the ellipse determined by the innermost delineated border tissue point at either side of the neural canal in each of the 40 B-scans (Figure 4-33D). The neuroretinal ‘mean

rim width' was calculated as the shortest distance between the NCO and the ILM (Figure 4-34A) and the neuroretinal rim volume was calculated as the volume anterior to the NCO reference plane, contained by the ILM and a vertical perpendicular projection from the NCO (Figure 4-34B). Most of the parameters described above are reported here as the mean of the 80 samples obtained in each SDOCT volume (such as mean RNFLT, mean rim width, etc.); however, the rim volume and RNFLV parameters are calculated by interpolation of surfaces between adjacent B-scans in each SDCOT volume. The two area measurements (NCO and Border Tissue) represent the area of the best-fitted ellipse as described.

In terms of parameters involving the ALCS delineations, a number of measures were undertaken to account for varying completeness of the delineated surface (primarily because of vessel shadowing) and varying density of ALCS points made on each volume. Firstly, only laminar points from sectors that were 'shared' between all four SDOCT volumes for a given eye were used in the analysis. In other words, the analysis only considered regions of the lamina that were delineated in all four SDOCT volumes. This was achieved as follows: all initially delineated ALCS marks were projected onto the NCO ellipse plane. The ellipse was then converted to unit circle space and the area bound within, containing each of the laminar points, divided into a grid of 100 equal area sectors using concentric rings and radial lines (Figure 4-35). If two or more laminar points were contained within one of these sectors in all four images, then the points contained within that sector were included in the analysis. If fewer than two points were contained in all four images, then the points contained within the sector were excluded from the analysis. Following this point 'filtration' method, the circle space was converted back to the original ellipse configuration.

Secondly, the delineated ALCS points were 'weighted' so that points in the peripheral lamina contributed greater weight to the mean than those in the central portion of the LC. This was done because the points in the peripheral part of the LC represent a 'wider' arc than those toward the centre of the LC (i.e. the area of the ALCS wedge represented by a given point increases with the distance that point is from the center of the LC). The weightings for each delineated point were thus proportional to the distance from the NCO centroid.

Using the “shared” set of weighted ALCS points, prelaminar tissue thickness (PLTT) and ALCS depth were calculated. PLTT was calculated in 3D as the distance between the ALCS and the ILM, measured along the normal to the tangent of the local ALCS. The mean PLTT was calculated for all ‘shared’ ALCS points in each volume. ALCS depth was calculated as the mean distance from the ALCS to the NCO reference plane (ALCS $depth_{NCO}$) and also as the mean distance to the RPE/BM reference plane (ALCS $depth_{BM}$), along the normal to each plane, respectively. Methods for quantifying these three parameters related to the ALCS are illustrated in Figure 4-36.

Statistical Analyses:

The effects of treatment (EG versus control), time and the treatment-time interaction were assessed for each structural parameter using repeated measures analysis of variance (RM-ANOVA) matched for animal (EG eye matched to fellow control eye for each animal). Significant parameter change within individual eyes was identified by establishing a threshold criterion for change based on the coefficient of repeatability (RC) for each parameter (Bland and Altman, 1986). The RC for each parameter was estimated from the two baseline measurements (BL1 and BL2) in each cohort of eyes. As 95% of repeated measurements are expected to be within the range of the RC, any difference from the average baseline to FU1 or FU2 that exceeded the RC was flagged as ‘significant change’ rather than as being within the range of measurement error. The proportion of EG eyes identified as significantly changing could be regarded as ‘positive hit-rate’, a proxy measure of sensitivity. The number of control eyes flagged as changing could be regarded as a measure of false positive rate, and therefore as a proxy measure of specificity. Statistical analyses were performed using either Prism version 4.0 (GraphPad Software, Inc, San Diego, CA) or Excel (Microsoft Corporation, Redmond, WA).

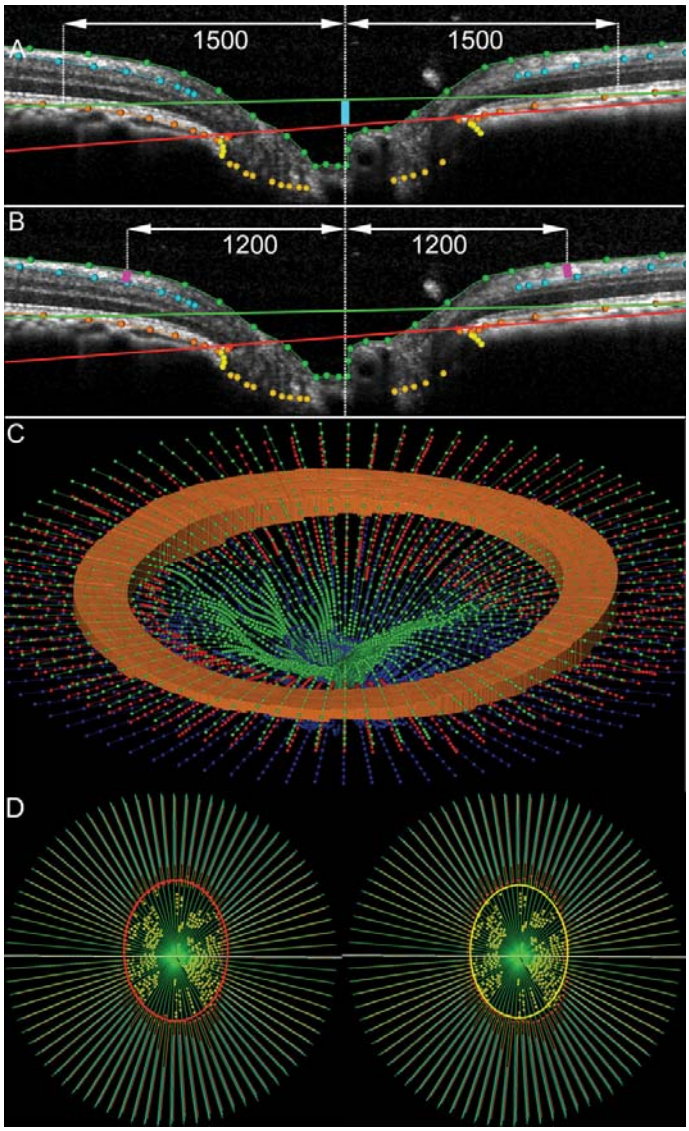

Figure 4-33. Parameterisation of SDOCT volumes. *A:* the primary reference plane (red line) is at the level of NCO. A secondary reference plane is located at BM at 1500 µm from the NCO centroid. NCO depth is measured from the secondary reference plane to the NCO (turquoise line). *B:* RNFLT is measured between ILM and the posterior surface of the RNFL at 1200 µm from the NCO centroid (pink lines). *C:* 3D view to illustrate the RNFLV, shown as an orange cylinder bound by the ILM (green) between 1200 µm and 1500 µm from the NCO centroid and the posterior RNFL (shown in red, in panels A and B in turquoise). *D:* en face view of a fully delineated volume. *Left:* the red ellipse defines NCO area. *Right:* the border tissue area is bound by the yellow ellipse

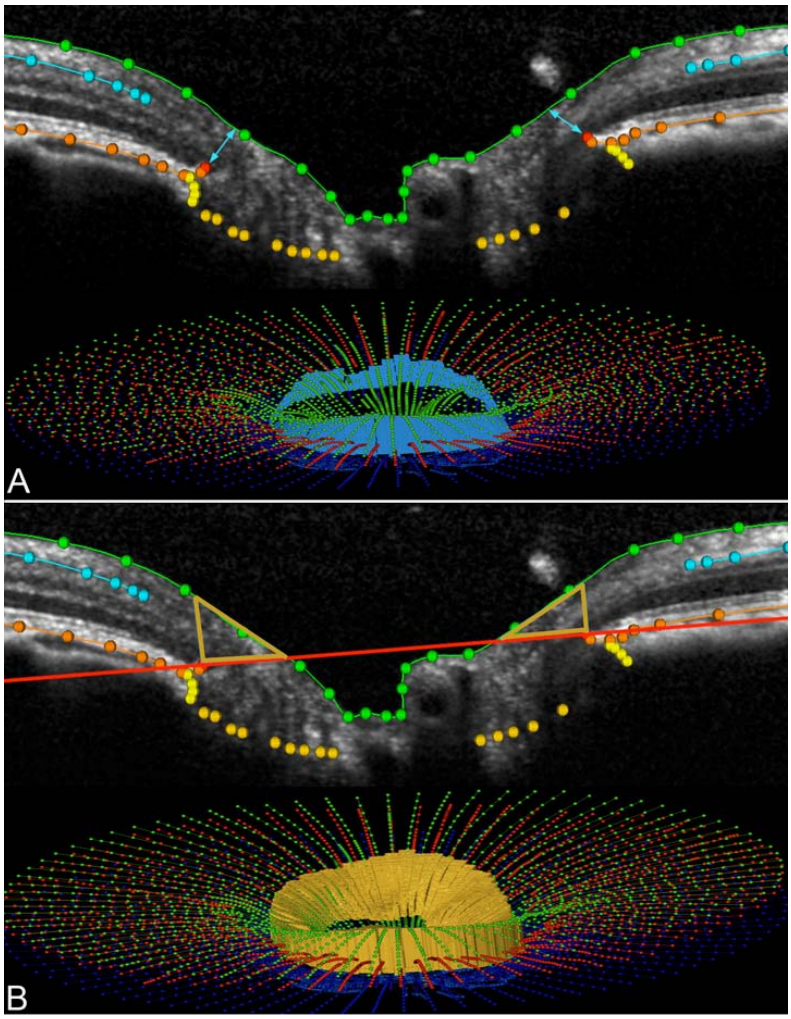

Figure 4-34. Generation of neuroretinal rim parameters in an SDOCT ONH volume. ***A:*** **mean rim 'width' is derived from the minimum distance from NCO to ILM (turquoise arrows in upper B-scan). A 3D representation of mean rim width is shown in a fully delineated volume (turquoise band in lower image).** ***B:*** **mean rim 'volume' is generated from the volume bound between NCO and ILM. This is shown in 2D by gold triangles in a B-scan (upper image) and in 3D (gold) in the lower image**

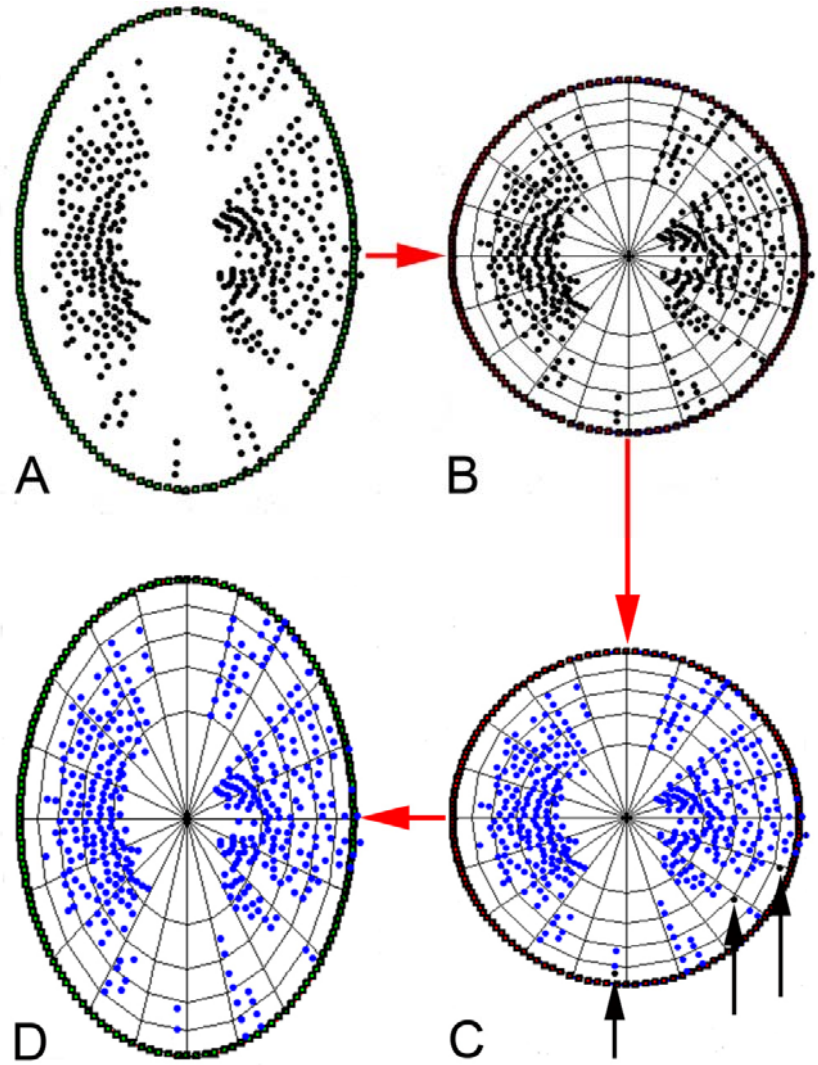

Figure 4-35. Method of ALCS point filtration. *A:* ALCS points (black glyphs) are projected onto the plane of an ellipse best fit to the NCO delineations (green glyphs). *B:* the NCO ellipse is scaled into unit circle space and sub-divided into 100 regions of equal area. *C:* regions where 2 or more ALCS delineated points are present in all 4 volumes in the sequence are maintained for analysis as 'shared regions'. Regions where there are fewer than 2 delineated points (black glyphs, highlighted by black arrows) common to all 4 volumes in the sequence are filtered out of the analysis. *D:* the circle is transformed back to elliptical space, with the shared ALCS points shown

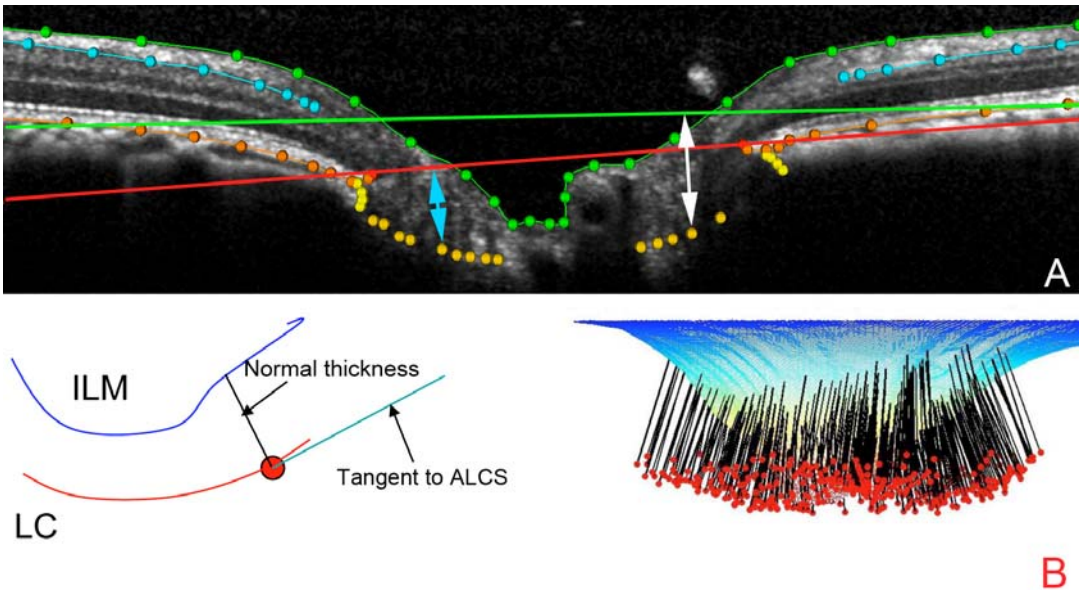

Figure 4-36. Parameters derived from the ALCS delineations. *A:* ALCS depth is the perpendicular distance from the NCO reference plane to the ALCS (ALCS depth$_{NCO}$, turquoise arrow). A secondary ALCS depth is the perpendicular distance from the BM reference plane to the ALCS (ALCS depth$_{BM}$). *B:* PLTT is measured as the normal from the tangent to the ALCS to the ILM *(left)*. PLTT measurement normals are shown for a full 3D volume *(right)*

4.6.4 Results

The mean age of animals was 11 years (range 9 - 19) and the mean length of follow-up after initiation of laser treatments until FU1 was 2.8 months (range 1.2 - 5.8) and until FU2 was 10.7 months (range 7.1 - 14.0). Mean post-laser IOP in the group of EG eyes ranged from 7.1 to 24.6 mmHg at FU1 and from 13.5 to 31.9 mmHg at FU2. Over the same period in the group of control eyes, the mean IOP ranges were 7.2 - 12.6 mmHg (FU1) and 8.9 - 16.0 mmHg (FU2). The peak IOP range in the EG eyes was 11.7 - 32.7 mmHg (FU1) and 23.7 - 61.0 (FU2); for the control eyes the peak IOP range was 10.3 - 17.7 mmHg (FU1) and 15.0 - 22.3 (FU2). The 'cumulative IOP difference' was used to estimate the total post-laser 'IOP insult' sustained by each EG eye as compared with its fellow control eye. For each EG eye, the IOP difference from the fellow control eye was multiplied by the number of days from the last measurement and summed over the

period of post-laser follow-up (IOP difference x days). The cumulative IOP difference ranged from -68.2 to 325.7 mmHg-days at FU1 and from 788.7 to 5755.8 mmHg-days at FU2. The IOP data and demographics of the monkeys included in the study are summarised in Table 4-3.

Subject	Sex	Age /Yrs	Weight /Kg	Time post-laser/ months	Mean IOP EG FU1/FU2	Mean IOP Control FU1/FU2	Peak IOP EG FU1/FU2	Peak IOP Control FU1/FU2	Cumulative IOP Difference FU1/FU2
135	M	11	13.2	1.5/7.3	11/15	10/11	13/40	12/19	42/839
137	M	10	13.0	1.8/7.1	25/32	12/16	30/49	18/22	234/3861
18389	F	19	8.8	2.5/8.3	7/14	7/9	14/39	10/18	54/1698
20377	F	10	5.4	3.6/12.2	11/24	9/11	17/52	13/19	320/5469
20655	F	10	8.4	5.8/14.0	11/13	10/11	17/234	15/15	60/789
21075	M	9	13.1	3.5/12.8	10/26	10/11	12/61	15/15	-68/5756
21152	F	9	7.1	2.2/7.9	22/27	13/11	27/50	14/15	298/4082
21808	F	9	6.5	1.2/13.8	21/21	12/12	33/34	14/17	326/4030
23534	F	11	4.5	3.6/12.9	11/20	11/11	17/36	14/16	20/3611

Table 4-3. Demographics and IOP characteristics (mmHg) of animals

The distribution of parameter values at each time point, for both the group of EG eyes and the group of control eyes, is shown in Figure 4-37. Statistical analysis (RM-ANOVA) identified a significant effect of treatment and a significant time-treatment interaction for the following parameters: ALCS depth$_{NCO}$ (Figure 4-37A), ALCS depth$_{BM}$ (Figure 4-37B), NCO depth (Figure 4-37C), RNFLT (Figure 4-37D), mean rim width (Figure 4-37E), rim volume (Figure 4-37F) and PLTT (Figure 4-37G). When post-hoc testing was applied to these parameters, a significant difference between the group of EG eyes and the group of their fellow control eyes was found at FU2 ($p < 0.001$ for each of the seven parameters). There was no significant effect of treatment nor a treatment-time interaction found for NCO area (Figure 4-37H) or border tissue area (Figure 4-37I). Though the distribution of parameter values for the group of EG eyes suggests that the EG eyes exhibited an increase in ALCS depth$_{NCO}$ (Figure 4-37A), ALCS depth$_{BM}$ (Figure 4-37B) and NCO depth (Figure 4-37C) at FU1, there were no significant differences found by post-hoc testing between EG and control eye groups at FU1. The results of the two intra-eye longitudinal

change analyses described below, however, suggest that the cross-sectional analysis shown in Figure 4-37 is less sensitive for detecting change at this early stage.

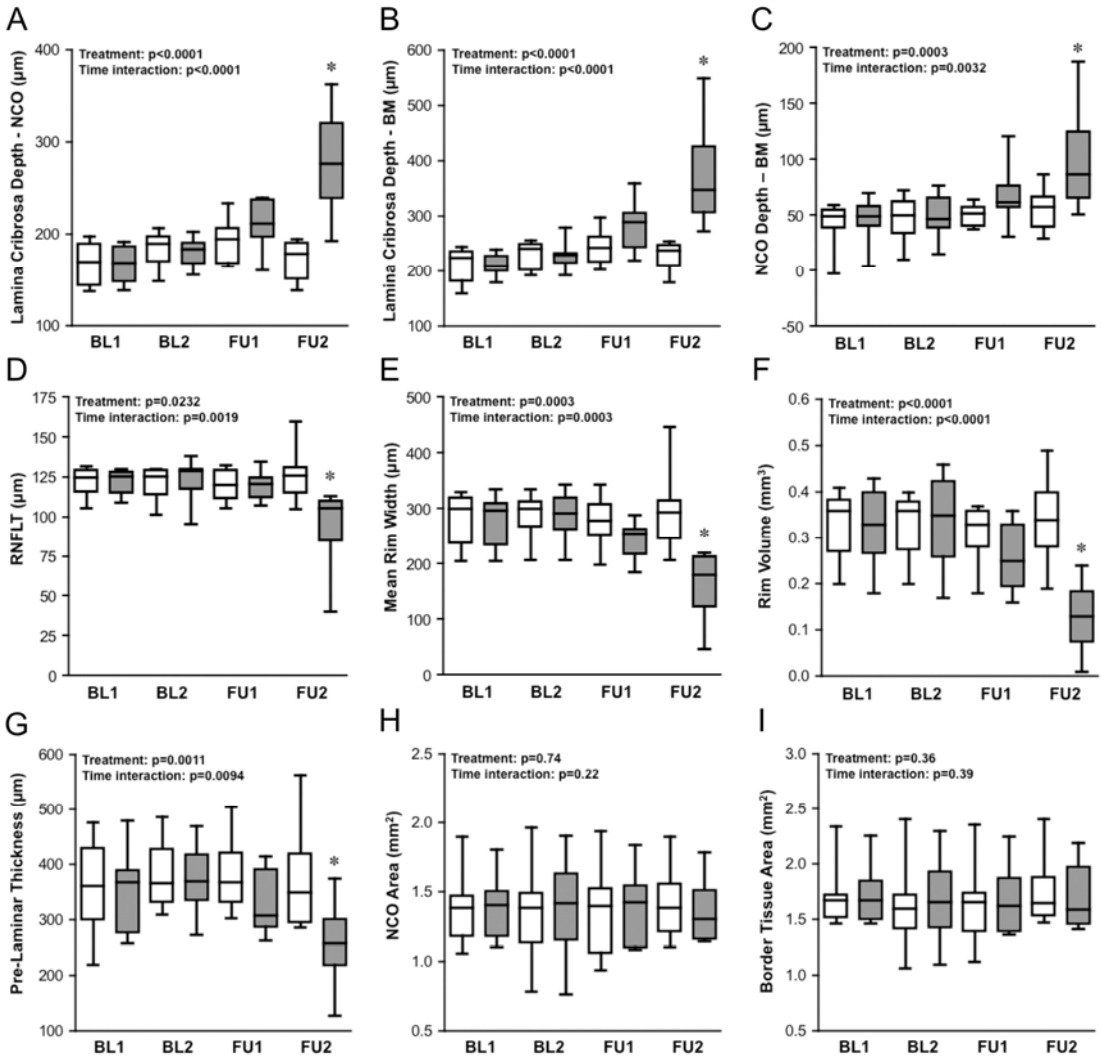

Figure 4-37. Distribution of parameter values at each time point for the EG eyes (filled boxes) and the control eyes (open boxes). Box and whisker plots indicate interquartile range (25th - 75th percentiles), median (hashmark), lower and upper extremes (whiskers). Inset for each panel indicates results of RM-ANOVA with p value for 'treatment' effect (EG versus control) and treatment-time interaction. Asterisk indicates significant difference between EG and control group at a given time point (p<0.001, Bonferroni corrected post hoc t-test)

The percentage change from baseline in the EG eyes is compared with the percentage change in control eyes in Table 4-4 for each of the SDOCT parameters. The values for percentage change were calculated as the difference between the parameter value at the designated follow-up session and the average of the two baseline values (expressed as a percentage). Table 4-4 shows that the magnitude of change was generally greater in EG eyes as compared to control eyes.

	RNFLT	RNFLV	NCO Area	NCO Depth	Border T Area	Rim Width	Rim Volume	PLTT	ALCS $depth_{NCO}$	ALCS $depth_{BM}$
Control FU1	- 1 (5)	-1 (5)	- 1 (9)	6 (18)	- 2 (10)	- 3 (4)	- 4 (8)	3 (9)	10 (14)	11 (13)
EG FU1	-3 (4)	-2 (5)	0 (7)	63 (75)	- 1 (5)	- 13 (10)	- 20 (17)	- 8 (9)	24 (15)	28 (20)
p value	0.2	0.3	0.3	0.01	0.4	0.01	0.01	0.01	0.07	0.06
Control FU2	3 (11)	3 (8)	4 (7)	16 (22)	6 (7)	2 (16)	5 (20)	0 (12)	- 1 (9)	4 (7)
EG FU2	- 23 (22)	-21 (22)	0 (10)	146 (163)	1 (9)	- 40 (26)	- 56 (30)	- 27 (22)	63 (36)	72 (43)
p value	0.02	0.01	0.007	0.01	0.02	0.005	0.001	0.01	0.0005	0.001

Table 4-4. Percentage (standard deviation) difference between the average baseline (BL1 + BL2/2) parameter value and the parameter value at FU1 and FU2 for the group of control and EG eyes. P values listed represent results of paired t-tests comparing the change from average baseline in control eyes versus the change from average baseline in EG eyes (significant differences defined at $p < 0.01$)

In order to evaluate longitudinal changes *within* each group, I compared the raw parameter values for each eye at each follow-up time-point with the average of the two baseline observations for each eye (using paired t-tests and a conservative definition of significance, $p < 0.01$). At FU1, four SDOCT parameters were found to have changed significantly from baseline in the EG eyes: mean rim width ($p = 0.003$, paired t-test corrected for multiple comparisons), mean rim volume ($p = 0.007$), mean ALCS $depth_{NCO}$ ($p = 0.0008$) and mean ALCS $depth_{BM}$ ($p = 0.002$). In EG eyes at FU1, there was no significant change in mean RNFLT ($p = 0.04$) or RNFLV ($p =$

0.13), although both of these parameters declined significantly by FU2 ($p = 0.007$ and $p = 0.009$, respectively). The four parameters identified in EG eyes as having changed significantly at FU1 (mean rim width, rim volume, ALCS $depth_{NCO}$ and ALCS $depth_{BM}$) all continued to significantly change from baseline at FU2 ($p = 0.006$, 0.003, 0.001 and 0.0007, respectively). Mean NCO depth relative to peripheral RPE/BM was also found to significantly increase ($p = 0.002$) and mean PLTT to significantly decrease ($p = 0.009$) in EG eyes at FU2. In the control eye group, none of the SDOCT parameters was found to be significantly different from their average baseline ($p > 0.01$) at either follow-up time-point.

The identification of change within individual eyes was based on the baseline to follow-up difference for the parameter of interest exceeding the RC for that parameter. The number of EG and control eyes identified as having changed significantly at FU1 and FU2 are summarised in Table 4-5.

	RNFL T	RNFL V	NCO Area	NCO Depth	Border T Area	Rim Width	Rim Volume	PLTT	ALCS $depth_{NCO}$	ALCS $depth_{BM}$
Control FU1	1	1	0	1	1	0	0	0	1	2
Estimated Specificity (%)	89	89	100	89	89	100	100	100	89	78
Control FU2	1	1	0	2	0	1	2	1	0	0
Estimated Specificity (%)	89	89	100	78	100	89	78	89	100	100
EG FU1	0	0	0	2	0	5	5	0	6	6
Positive hit rate (%)	0	0	0	22	0	56	56	0	67	67
EG FU2	6	5	0	6	0	8	7	6	7	8
Positive hit rate (%)	67	56	0	67	0	89	78	67	78	89

Table 4-5. Number of control and EG eyes flagged as changing, based on the difference between baseline and follow-up exceeding the RC for that parameter. Estimated specificity = (number of control eyes not changing/total control eyes)*100 Positive hit rate = (number of EG eyes changing/total EG eyes)*100

The highest 'positive hit rate' amongst the EG eyes at FU1 was for ALCS $depth_{NCO}$ and ALCS $depth_{BM}$ (both 67%). However, it should be noted that the 'specificity' at FU1 (based on the number of control eyes flagged as changing) was 89% for ALCS $depth_{NCO}$ and 78% for ALCS $depth_{BM}$. Both of the 'rim' parameters (mean rim width and rim volume) did not flag any control

eyes as changing at FU1 (equivalent to a specificity of 100%), yet had a positive hit rate of 56% in each case. At FU2, ALCS depth$_{NCO}$ and ALCS depth$_{BM}$ had positive hit rates of 78% and 89%, respectively, with no controls flagged as changing (i.e. 'specificity' of 100%); PLTT was flagged as changing in 67% of EG eyes, at FU2, with an estimated specificity of 89%.

An association between the percentage SDOCT parameter change and each method of IOP characterisation (mean IOP, peak IOP and cumulative IOP difference) was observed in the EG eyes at FU2 for each of the parameters. For example, Figure 4-38 shows the percent change from baseline to FU2 versus the mean IOP during follow-up in each eye. For each parameter, the group of EG eyes is shown as filled diamonds and the group of control eyes as open circles. Note that the extent of scatter among the control eyes also serves as an indication of total measurement noise against which significant change can be detected as described above for the longitudinal within-eye analysis. Figure 4-38 shows that there was a significant association between mean IOP and change to FU2 in the following parameters: RNFLT (Figure 4-38A, $p = 0.017$, general estimation equation); mean rim width (Figure 4-38B, $p = 0.002$); rim volume (Figure 4-38C, $p < 0.0001$); ALCS depth$_{NCO}$ (Figure 4-38D, $p = 0.0008$); ALCS depth$_{BM}$ (Figure 4-38E, $p = 0.001$); and PLTT (Figure 4-38F, $p = 0.004$).

In the analysis of the percentage of ALCS area marked, there was no significant effect of treatment (EG versus control; $p = 0.80$, RM-ANOVA), no significant effect of time ($p = 0.47$) and no significant interaction between treatment and time ($p = 0.84$). The percentage of ALCS area marked prior to application of the 'shared area' restriction was 66.6% in control eyes and 66.2% in EG eyes, averaged over all four time-points. Inter-animal differences accounted for 72% of the overall variance in the percentage of ALCS area marked ($p = 0.0005$). Figure 4-39 shows the 'shared' ALCS delineation points (i.e. ALCS points present in all four volumes) projected to the NCO for both eyes of all 9 animals. While the extent of 'missing' areas is variable between animals, in most eyes they directly correspond to the location of the central retinal vasculature. An example of the ILM and ALCS displacements seen in an EG eye is illustrated in Figure 4-40. The changes in this animal represent the approximate midpoint for ONH parameter changes observed in this group of EG eyes at FU2. Note also that these three volumes are aligned in the

z-axis by their NCO centroids, thus the ILM and RPE/ BM surfaces at the more peripheral portions of the follow-up volumes appear to be displaced anteriorly from baseline; if aligned by their peripheral reference planes, the posterior displacement of the ALCS from baseline would appear to be even greater.

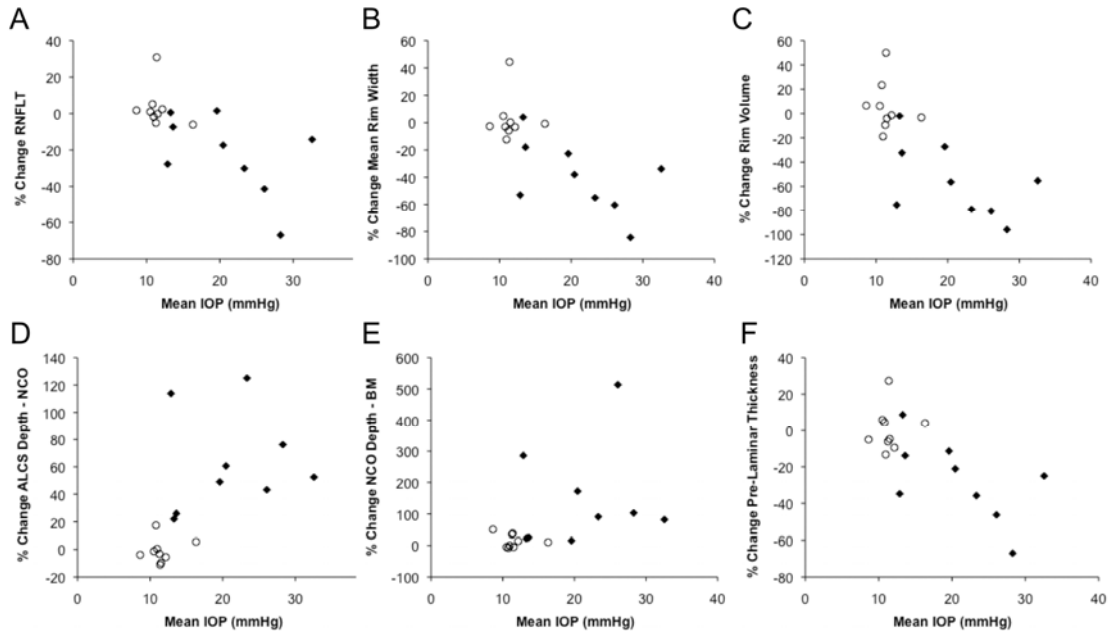

Figure 4-38. The relationship between mean IOP and change in the magnitude of SDOCT parameter (mean baseline value - FU2 value). Closed diamonds = EG eyes, open circles = control eyes

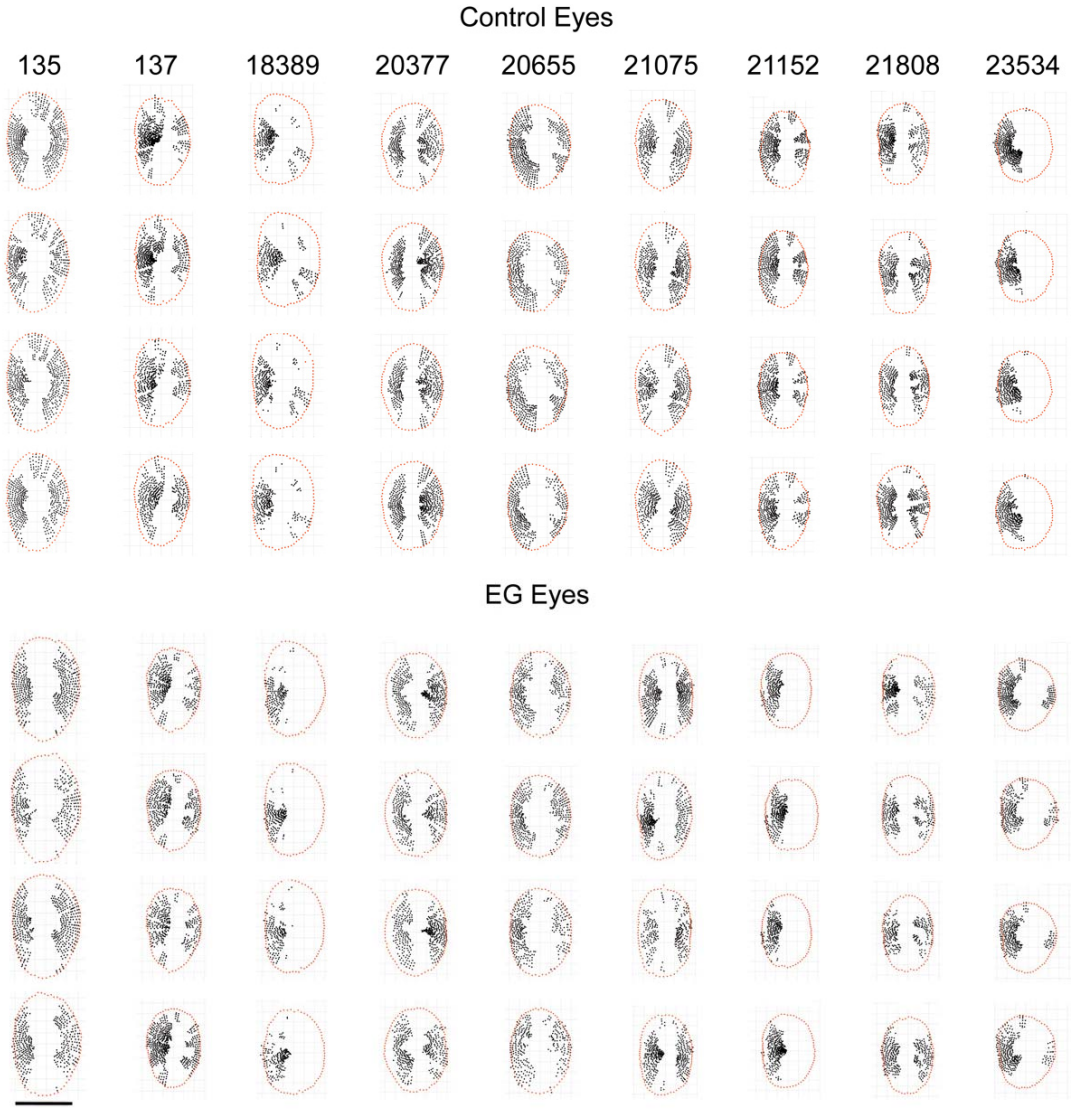

Figure 4-39. Longitudinally shared, SDOCT-detected ALCS points. ALCS points (black points) are projected to the NCO reference plane (red points); all eyes are in the right eye orientation. Calibration bar indicates 1 mm

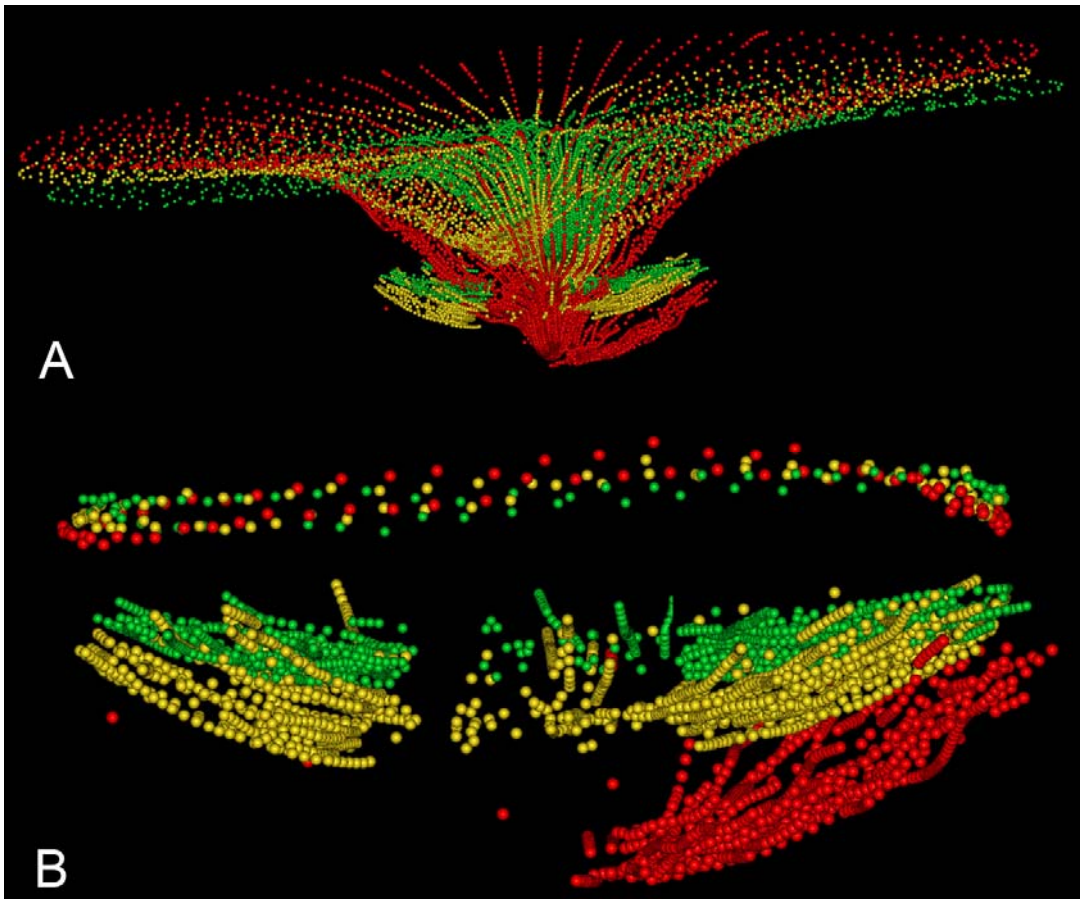

Figure 4-40. ILM and ALCS displacement in an EG eye (18389). *A:* ILM and ALCS delineations are shown, BL1 in green, FU1 in yellow and FU2 in red. *B:* ALCS delineations are magnified, anchored at the level of the NCO (shown above the ALCS delineations)

4.6.5 Discussion

This report is the first to describe the application of longitudinal SDOCT imaging to detect deep structural changes in the glaucomatous ONH. Several deep ONH structural parameters were found to change significantly from baseline in eyes with EG and to remain stable over the same duration in control eyes. The changes were substantial enough at the second follow-up time-point (FU2) to prove to be significantly different even by cross-sectional analysis. Importantly, deep ONH structural changes were also found by longitudinal analysis to be present even at the onset of CSLO-detected ONH surface change. These changes occurred at a stage preceding loss of neural tissue as measured by two parameters, peripapillary RNFLT and RNFLV. Changes in the

neuroretinal rim parameters (rim width and rim volume) were however detectable at the onset of surface height depression. A possible explanation as to why this may occur is that some of the changes occurring at the rim at the earliest time-point may reflect 'conformational' changes in the neural and non-neuronal components of the rim that follow deformation of the underlying and adjacent connective tissues. By contrast, a greater proportion of the changes detected at the more eccentric peripapillary RNFL will likely reflect true loss of axonal tissue, rather than conformational changes in connective tissues. This finding underscores important potential advantages of SDOCT imaging. Specifically, deep ONH changes are detectable at a very early stage (at least in this experimental model of glaucoma), and are distinct from the axonal loss reflected by RNFL thinning. These deep ONH changes underlie the early ONH surface height changes detected by CSLO.

The use of RNFL thickness measurements as captured by TDOCT is generally well established in human glaucoma subjects (Bowd et al., 2000; Deleon-Ortega et al., 2006; Medeiros et al., 2005; Schuman et al., 1995). This is with the caveat, however, that there is a relative paucity of published reports of longitudinal RNFL measurements in human subjects (Medeiros et al., 2009; Wollstein et al., 2005). Whilst I have demonstrated, as expected, that RNFL thinning was detectable at the second follow-up time-point in this experimental model, I was also successful in demonstrating the principal aim of this experiment. Specifically, this was to explore the potential for detecting changes in deep, subsurface ONH structures (at the prelaminar and laminar level) by longitudinal SDOCT imaging. It has recently been suggested, albeit in a cross-sectional study, that SDOCT can detect thinning of the lamina in a series of ocular hypertensive and glaucoma eyes, and that this thinning was correlated with a reduction in visual field mean defect (Inoue et al., 2009). I was unable to replicate this in the current experiment as I could not reliably detect the full thickness of the LC in all images.

The results of this experiment also demonstrated, at least in the sample of EG eyes examined here, that progressive glaucomatous changes include reduction of PLTT, posterior displacement of the ALCS and NCO, and decline of the 'rim' parameters (mean rim width and rim volume). Of note, these deep ONH changes were detectable prior to the onset of peripapillary RNFL thinning

at FU1, at the onset of HRT-detected surface topography depression. Interestingly, a recent study has demonstrated that TCA changes may precede the onset of visual field changes as measured using the Early Manifest Glaucoma Treatment Trial perimetric criteria (Chauhan et al., 2009b). It is likely that surface height changes at the onset detectable by HRT are generated by a combination of changes beneath the ONH surface such as posterior laminar displacement and changes in the shape of the scleral canal and/or posterior eye wall, the latter being inferred from the changes in NCO depth relative to peripheral reference plane. One cannot, therefore, assume that TCA change can isolate either prelaminar changes or laminar displacement alone. Given that surface height depression is specifically designed to detect changes within the nerve head, there is a potential bias against detection of change in the peripapillary RNFL. Given that the structural end-point was based on the HRT, and this device doesn't measure the RNFL directly, it would have been improper to use RNFL as the structural end-point. As OCT (whether TD or SD) has a well-established utility for detecting RNFL changes, any changes in RNFL parameters occurring at the onset of surface height depression should have been detected. In addition to the changes in the PLTT and ALCS, the rim parameters derived from SDOCT volumes proved to be robust and sensitive.

Povazy and colleagues have previously described a method known as 'minimum distance mapping', which identified thinning of the circumpapillary nerve fibre 'band' in glaucomatous eyes (Povazay et al., 2007b). My approach for measuring 'mean rim width' used a very similar technique, although I took my measurements from the NCO. Povazy and colleagues also used the termination of the RPE signal but suggested that this landmark was equivalent to the scleral ring of Elschnig and the termination of the sclera. My examination of the clinical disc margin in 3D histomorphometric reconstructed nerves and in 3D SDOCT ONH volumes (sections 4.3 and 4.4) indicate that this is not the case, with the NCO, border tissue of Elschnig (the correct anatomical landmark for Elschnig's ring) and the anterior scleral canal opening each being detectable as separate structures and each potentially constituting the disc margin, even within the same nerve. SDOCT-detected loss of neuroretinal rim is an important finding as rim loss has a clear relation to what occurs in clinical glaucoma. This feature has been exploited both in HRT classification

systems as well as HRT progression algorithms (Fayers et al., 2007; Strouthidis et al., 2006; Wollstein et al., 1998).

Given the similarity between the experimental optic neuropathy and human glaucomatous optic neuropathy, and the fact that a commercially available imaging device was used, it is reasonable to assume that the findings of this study will be applicable to human patients and are likely to be replicated in studies using human subjects. There are, however, a number of important caveats to take into consideration when trying to translate these findings into clinical practice. Firstly, this experiment was intended as a test of the hypothesis that deep ONH changes could be detected by longitudinal SDOCT imaging. In general a progression algorithm of this type (an 'event' analysis) will need to be more robust in practice, as clinical management decisions may well be based on the observed changes. The most direct way of increasing specificity in a clinical setting would be to perform additional confirmatory tests. However, for the purposes of this experiment, the choice of an event analysis was preferable for detecting parameter 'change' given the limited number of data-points selected. My intention was to evaluate whether detection of 'deep' ONH changes was feasible by SDOCT. Given that the results suggest that this is the case, there is now scope for an expansion of the ONHRL group's longitudinal studies to include additional time-points in the development of a more refined progression algorithm. Indeed, future studies will consider both finer spatial and temporal resolution, such that a larger number of time-points in longitudinal series will be evaluated and sectoral ONH parameters will be analysed. The inclusion of an expanded number of time-points will allow development of a trend analysis, with the advantages of being able to monitor parameter behaviour over time and to generate measures of rate of change. However, development of reliable automated segmentation algorithms will be required to improve clinical implementation of any such detection algorithms.

In a previous report from the ONHRL (Yang et al., 2007a), based on post mortem 3D ONH histomorphometric reconstructions, significant prelaminar tissue thickening was identified at the earliest stages of the experimental neuropathy (at a stage equivalent, but not identical to, FU1 in the current experiment). By contrast, this was not seen in the EG eyes imaged in vivo by SDOCT in this experiment. It is possible that there may be regional changes where prelaminar tissue

thickening is evident at FU1 and masked by prelaminar tissue thinning in other regions of the same ONH. In order to confirm whether or not this finding is present in vivo using longitudinal SDOCT imaging, a more detailed examination (both globally and regionally) of sequential volumes, up to and beyond the detection of HRT surface height depression, will be required. Such an examination is beyond the scope of this experiment, but will be undertaken in the future. It is also possible that the histomorphometric evidence of prelaminar tissue thickening in the previous report was the result of an interaction between the ONH tissues of experimental eyes and the histological processing that did not occur in the contralateral normal eyes, which were processed identically.

The degree of ALCS and ILM displacement observed in this study may well exceed that which might be expected in human subjects, given that the 'peak' IOPs recorded in the EG eyes (range of 23.7 - 61.0 mmHg at FU2) likely exceed those recorded in human ocular hypertensive or treated glaucoma subjects. By stabilising the IOP at 10 mmHg at each imaging session, I took measures to ensure that the structural changes observed by SDOCT were the result of cumulative damage and not secondary to an increased level of IOP at the time of imaging. Indeed, acute IOP elevation has been reported to cause similar changes in the shape of the ONH and peripapillary structures (Fortune et al., 2009). Overall, the mean IOPs for the EG eyes were within the range observed clinically in human glaucoma patients (range of 14.4 - 31.9 mmHg at FU2), but there was clearly a wide variation across tests. Even so, it is interesting to note that at least half of the EG eyes at FU1 (at the onset of HRT surface height depression) had a minimal cumulative IOP insult (i.e. all IOP measurements in some EG eyes had been similar to those recorded in their fellow control eyes up to that follow-up time-point). There was, however, a clear association between parameter changes and magnitude of IOP (whether mean, peak or cumulative insult) in the EG eyes. The IOP characterisation in these animals is limited to approximately weekly measurements, but I have no record of the IOPs between these dates. These issues will be addressed by real time IOP telemetry. I have been involved in a trial of implantable intraocular IOP telemetry devices in a number of normal monkey eyes in collaboration with the OBL but this is beyond the scope of this PhD (Downs et al., 2011).

I have previously suggested that BMO or NCO would serve as an optimal, stable, reference plane in both 3D histomorphometric reconstructions and in 3D SDOCT ONH volumes (section 4.2). I therefore adopted an NCO-based reference plane as the primary reference plane for quantification in this experiment. However, the ONHRL has previously reported evidence that the ONH likely deforms outward relative to the peripheral retina following acute IOP elevations (Yang et al., 2009b). The results of the current study demonstrate posterior movement of the NCO relative to the peripheral BM in the setting of chronic IOP elevation and confirm previous 3D histomorphometric detection of this finding at the earliest stages of the neuropathy (in this study at FU1) (Yang et al., 2009a; Yang et al., 2007b). Peripheral BM is assumed to be relatively stable in the neuropathy.

The above findings do not necessarily preclude the use of the NCO as the basis for an SDOCT reference plane. Firstly, it is reasonable to expect that an NCO reference plane is valid for the quantification of ONH parameters that are bound within the NCO circumference. Although the entire ONH (including the NCO) may move posteriorly (relative to the more peripheral BM) with progressive neuropathy, the structures within the nerve head will still be displaced relative to the NCO. This is demonstrated by the fact that the relative degree of posterior displacement of the ALCS was similar regardless of whether the peripheral BM or NCO reference plane was used. Secondly, the NCO is still required for the generation of the peripheral BM reference plane in my current scheme, as it is anchored to the NCO centroid. The NCO is likely to be a relatively simple target for automatic segmentation algorithms, so it will be a key landmark in the definition of reference planes, whether centrally or peripherally located. Moreover, the NCO area did not change significantly in any of the eyes (EG or control eyes) at any time point, thus the NCO centroid should serve as a relatively stable reference.

A peripheral reference plane will be vital for structures external to the NCO area, such as the peripapillary sclera. I was unable to reliably detect peripapillary sclera in the monkey eyes examined in this study but have noted in preliminary SDOCT examinations of human eyes that the scleral surface may be more easily detected in myopic and glaucomatous human eyes. Expansion of the scleral canal opening has been identified as an important histomorphometric

finding in early EG (Yang et al., 2007b). I therefore fully expect that parameters based on the detection of the peripapillary sclera will become important, which will necessitate the use of a peripheral, NCO-anchored, reference plane. The adoption of a longer wavelength (~1 micrometer) SDOCT imaging source may result in improved detection of deeper ONH structures, including the scleral architecture (Povazay et al., 2007a; Povazay et al., 2007b; Srinivasan et al., 2008). The ONHRL are soon to begin testing of a prototype Spectralis device outfitted with a 1060 nm center-wavelength imaging source; a comparison with existing 870 nm wavelength technology will be pursued as part of the preliminary assessments. An alternative method (enhanced depth imaging - EDI), not used in the current study, which has been reported to improve depth penetration, involves advancing the SDOCT imaging head anteriorly so that the fundus image is inverted (Spaide et al., 2008).

There are a number of issues concerning the detection of the ALCS in the SDOCT volumes examined in this study. It is clear that detection of the ALCS is frequently incomplete, particularly in regions where there is shadowing from the central retinal vasculature. It is unclear whether the observer's ability to detect the anterior lamina was influenced by the thickness of prelaminar tissue. One may hypothesise that the degree of ALCS detection increases as glaucoma progresses, as depth penetration improves with the diminution of the prelaminar tissue. It is equally plausible that the detection of the ALCS may improve because changes in the conformation of laminar architecture and/or its tissue properties as glaucoma progresses may strengthen the reflectance signal. However, the examination of the percentage of ALCS regions marked across the 4 volumes for each of the 9 eyes suggests that a relatively large proportion (~two thirds of the laminar area on average) was detected and reproducibly delineated and that the area of ALCS marked was reliable over time in both control and EG eyes. The rationale for choosing two or more ALCS points in each of the 100 subdivisions to be the 'minimal threshold' for detection across the four images was to balance a desire to limit spurious detection of ALCS (as may occur with a single ALCS point in a region) whilst not being so conservative as to exclude genuine ALCS delineations (by not filtering out regions with greater than two ALCS points). At present, automatic segmentation of the lamina is likely to prove very difficult, as it is so

highly variable. Having meticulously compared serial histological sections of a normal monkey ONH with matched B-scans acquired by SDOCT from the same eye in the preceding experiment (section 4.5), I have been able to establish visual clues which are indicative of the ALCS in an SDOCT volume. I trained the other masked observers to recognise the same features of the ALCS signal (using a different data set). I minimised the impact of inter-observer reproducibility by factoring it into the study design (control eyes) as well as into the progression algorithm used to flag individual eyes as progressing given that any parameter change in any individual eye had to exceed the RC for that parameter.

In summary, I report SDOCT detected ONH changes in longitudinally examined eyes with experimental glaucomatous optic neuropathy. This is the first SDOCT imaging study to report longitudinal changes at the level of prelaminar and laminar tissues. The results of this experiment support the ability of SDOCT imaging to detect ONH structural damage in human subjects with, or at risk of, glaucoma. The PLTT and ALCS height are tangible parameters for human imaging. Further study is required to establish robust, specific progression algorithms and to identify what constitutes clinically important changes in these structures.

4.7 The Effect of Acute IOP on the ONH as Detected by SDOCT

4.7.1 Background

The biomechanical paradigm is based on the premise that IOP acts as a mechanical load resulting in stress and strain of the tissues in and around the ONH, in particular the LC and the peripapillary sclera (Burgoyne et al., 2005). This paradigm postulates that IOP-related biomechanical stresses and/or strains act as key instigators of glaucomatous damage in the ONH. Further, the paradigm proposes that the biomechanical effects of IOP result in changes to the ONH microstructure that underpin susceptibility to vascular insult (Burgoyne et al., 2005). Understanding biomechanical behaviour of the ONH can be aided by application of imaging techniques to monitor ONH 'compliance' while load (IOP) is varied.

To date, the biomechanics of the ONH have only been explored ex vivo, augmented by modelling strategies such as finite element modeling (Downs et al., 2009; Girard et al., 2009; Sigal et al., 2004). This is a computational tool, which enables prediction of how a biological tissue with complex architecture and material properties will respond to different magnitudes of load. This technique is limited by the accuracy of the inputs, specifically knowledge of the geometry and material properties of the tissues examined. With the commercial introduction of high speed, high resolution SDOCT it has become feasible to detect structures deep to the surface of the optic disc cup, including the prelaminar tissue, the LC (as demonstrated in the previous two experiments, sections 4.5 and 4.6) and, in some eyes, the peripapillary sclera (Inoue et al., 2009; Kagemann et al., 2008; Srinivasan et al., 2008; Strouthidis et al., 2010). Compliance testing using SDOCT, if successful, should allow one to test the hypothesis that the surface changes seen with acute elevation of IOP using other imaging modalities (as detailed in section 2.4.3) underpin changes to deeper connective tissues. Such 'deep' in vivo compliance testing may also serve to verify or refute the observations made ex vivo and to further advance computational studies of ONH biomechanics (Roberts et al., 2010; Sigal et al., 2010; Sigal et al., 2011).

In the previous experiment (section 4.6), I described a series of structural parameters derived from 3D SDOCT ONH volumes, which were used to detect longitudinal changes in the neuroretinal rim width and volume, PLTT and ALCS at the earliest stages of a monkey EG model

(Strouthidis et al., 2011). Prior to the current experiment, I collaborated with other colleagues from the ONHRL in a study examining the effect of acute IOP elevation on peripapillary nerve fibre layer thickness as detected by SDOCT (using conventional peripapillary scans) and scanning laser polarimetry in both eyes of five normal rhesus macaques (Fortune et al., 2009). In the current experiment, I apply my strategy for delineation and parameterisation of ONH structure to that acute IOP imaging data-set.

4.7.2 Purpose

The purpose of this experiment was to investigate the effect of acutely elevated IOP upon ONH structures detected in vivo using SDOCT.

4.7.3 Methods

Two young (< 3 years), two young adult (3 - 8 years) and one adult (> 8 years) rhesus macaque monkeys (*Macaca mulatta*) were included in this study (Table 4-6). The mean (range) age of subject animals included was 5.6 (1 - 10) years, the mean (range) weight was 5.0 (2.7 - 7.2) kg. All testing was performed using the conditions of the 'long' compliance test as described in section 3.3.

Imaging:

All ONH imaging was performed using a commercially available SDOCT device (Spectralis, Heidelberg Engineering GmbH, Heidelberg, Germany). 15°, 80 radial B-scan images (768 A-scans per B-scan), centred on the ONH, were acquired from both eyes of 3 animals and 48 radial B-scan images in the other 2 animals. The device's eye tracking facility was turned on during image acquisition to enable B-scan acquisition repetition (n=9) and sweep averaging in real time to reduce speckle noise. For each eye, the scans were not referenced to the 'baseline' image, in order to prevent any 'distortion' of the images that was due to image processing rather than due to acute IOP elevation. However, within each volume the individual B-scans were registered to each other along the z-axis by post hoc processing based on the native Spectralis algorithm for this function.

Testing Protocol:

At the start of the imaging session, IOP in both eyes was adjusted to 10 mmHg and SDOCT scans were acquired after a 30-minute period of stabilisation at this IOP. In 6 eyes of three animals, SDOCT images were also acquired after 10 minutes of IOP stabilisation at 10 mmHg. IOP was then raised to 30 mmHg in both eyes for 30 minutes and then 45 mmHg in both eyes for 60 minutes, after which the SDOCT scans were repeated. SDOCT data were compared between the IOP 45 mmHg condition (60 minutes of IOP 45 mmHg but 90 minutes of total IOP elevation above 10 mmHg) and the baseline 10 mmHg condition at 30 minutes. The scans acquired after 10 minutes at IOP 10 mmHg were matched against those obtained at 30 minutes at IOP 10 mmHg; this served as a control experiment to evaluate inter-scan variability in the absence of any IOP change. Of note, image acquisition during acute IOP elevation to 45 mmHg was unaffected by the presence of corneal oedema which was minimal or negligible throughout the testing procedure.

Subject ID	Age (Years)	Weight (Kg)	SDOCT Scan Pattern	Experimental Protocol
23534	10	4.0	80 radial B-scans	Acute IOP + Control
21808	7	6.0	80 radial B-scans	Acute IOP + Control
21152	8	7.2	80 radial B-scans	Acute IOP + Control
25340	2	5.4	48 radial B-scans	Acute IOP
25904	1	2.7	48 radial B-scans	Acute IOP

Table 4-6. Characteristics of subjects included in the experiment. Alternate B-scans were delineated for the 80 radial B-scan volumes (i.e. 40 B-scans per volume) whereas all B-scans were delineated for the 48 radial B-scan patterns

Delineation and Parameterisation of SDOCT Volumes:

The method for delineating structures within each SDOCT volume using Multiview was identical to that described in previous experiments (sections 4.2, 4.4 and 4.6). Three observers (including myself), masked to each IOP condition, manually delineated pertinent features within alternating B-scans of the 80 radial B-scan volumes (i.e. 40 B-scans per 80 radial B-scan volume, 6 eyes of 3 animals) and in every B-scan of the 48 radial B-scan volumes (4 eyes of 2 animals). In each

case, the first delineated B-scan was at the vertical, 0° location, and delineation proceeded in a clockwise fashion through each of the successive B-scans. The features delineated were as per the preceding experiment (section 4.6); ILM, RNFL, posterior surface of the RPE/BM complex, NCO, border tissue and the ALCS. Examples of each of these delineation categories can be found by referring back to Figure 4-32.

The following parameters were generated, as described in section 4.6: NCO depth, RNFLT, RNFLV, NCO area, neuroretinal 'mean rim width' and neuroretinal 'rim volume' (Strouthidis et al., 2011). All parameters generated are global and thus generated as mean values derived from the 40 or 48 B-scans delineated in each SDOCT volume. The exceptions to this are volume measurements (RNFLV and rim volume), which are calculated by interpolation of surfaces between adjacent B-scans in each SDOCT volume, and NCO area, which is derived from the area of a best-fitting ellipse (Strouthidis et al., 2011).

In the previous experiment (section 4.6), I advocated using regions of ALCS delineation that were common or shared to each of the volumes for a particular eye in order to restrict the number of 'spurious' delineations, in a process called 'point filtration' (Figure 4-35) (Strouthidis et al., 2011). For the current experiment, there were considerably fewer scans available for each eye (two) compared to the previous study (four) and therefore point filtration would likely have resulted in loss of potentially useful data. Hence I elected to include all delineated ALCS points for each volume. Furthermore, it was demonstrated in the preceding experiment (section 4.6) that, at least in terms of EG, there appears to be no effect of either time or treatment (EG) upon the area of ALCS detectable by SDOCT (Strouthidis et al., 2011). Using 'weighted' ALCS points, PLTT and ALCS depth were calculated. ALCS depth was relative to the NCO reference plane (ALCS $depth_{NCO}$) and to the peripheral RPE/BM reference plane (ALCS $depth_{BM}$). Methods for generating all SDOCT parameters can be reviewed by referring back to Figures 4-33, 4-34 and 4-36.

Statistical Analyses:

All differences between the SDOCT parameters at the two different IOP conditions (IOP 45 mmHg after 60 minutes versus IOP 10 mmHg after 30 minutes for the acute IOP elevation

experiment and IOP 10 mmHg after 30 minutes versus IOP 10 mmHg after 10 minutes for the control IOP experiment) were calculated. All differences (n = 10) between the two IOP conditions were assessed using generalised estimating equations in order to account for correlation between the two eyes of each animal. In order to correct for multiple comparisons (Yan, 2002), I established a cut-off of $p < 0.005$ (based on the fact that I am examining approximately n = 10 SDOCT parameters; 0.05/10 = 0.005; thus using a conservative correction essentially identical to a Bonferroni correction to maintain a family-wise Type-I error rate near 0.05). All statistical analyses were performed using either Prism (version 4.0, GraphPad Software, Inc, San Diego, CA), Excel (Microsoft Corporation, Redmond, WA) or R (R Foundation for Statistical Computing, Vienna, Austria).

4.7.4 Results

Significant structural parameter changes ($p < 0.005$) between IOP 10 mmHg/30 minutes and IOP 45 mmHg/60 minutes (Table 4-7) were observed for neuroretinal rim measurements (RW and RV, both decreasing), RNFLV (decreasing) PLTT (decreasing), ALCS $depth_{BM.}$(increasing) and NCO depth (increasing). There were no significant changes in structural parameters generated from the volumes evaluated in the 'control' experiment (IOP 10 mmHg/10 minutes compared to IOP 10 mmHg/30 minutes - Table 4-8). Table 4-9 shows the change in each parameter for each eye compared between IOP 10 mmHg/30 minutes and IOP 45 mmHg/60 minutes. Table 4-10 shows the change in each parameter for each of the 6 eyes included in the control experiment. A marked decrease in rim width (expressed as % of baseline value, % standard deviation; -11%, 2%), rim volume (-15%, 5%) and PLTT (-12%, 5%) were observed as well as considerable increases in NCO depth (65%, 25%) and ALCS $depth_{BM}$ (20%, 8%). The amount of change observed in RNFLT, RNFLV, NCO area with elevated IOP was in each case negligible, amounting to a mean of 2% or less in either direction, which was equivalent to what had been observed for those parameters in the control experiment. Although a higher percentage change was detected for ALCS $depth_{NCO}$ with IOP elevation (5%, 6%), this change was within the inter-scan variability observed in the control experiment (-1%, 8%).

Parameter	Condition (10 eyes total)		Comparison
	10/30	45/60	p-value
RNFLT (µm)	122 (3.5)	120 (4.1)	0.0230
RNFLV (mm^3)	0.28 (0.09)	0.28 (0.09)	0.0001
RW (µm)	**282 (39.2)**	**252 (34.3)**	**< 0.0001**
RV (mm^3)	**0.30 (0.06)**	**0.26 (0.05)**	**< 0.0001**
NCO Depth (µm)	**60 (15.0)**	**98 (24.7)**	**< 0.0001**
NCO Area (mm^2)	1.25 (0.19)	1.25 (0.22)	1.0000
ALCS $depth_{NCO}$ (µm)	179 (28.4)	189 (37.0)	0.0190
ALCS $depth_{BM}$ (µm)	**241 (29.1)**	**290 (44.0)**	**< 0.0001**
PLTT (µm)	**371 (76.9)**	**324 (58.3)**	**< 0.0001**

Table 4-7. Mean (standard deviation) of parameters generated in the acute IOP experimental protocol. 10/30 condition refers to parameters derived from an image acquisition after 30 minutes at IOP 10 mmHg; 45/60 condition refers to parameters derived from an image acquisition after 60 minutes at IOP 45 mmHg. The pair-wise comparisons have been performed using generalised estimating equations, p < 0.005. Significant parameters are highlighted in bold

Parameter	Condition (6 eyes total)		Comparison
	10/10	10/30	p-value
RNFLT (µm)	121 (3.7)	123 (4.1)	0.0410
RNFLV (mm^3)	0.28 (0.01)	0.29 (0.01)	0.0000
RW (µm)	304 (32.0)	304 (31.3)	0.4800
RV (mm^3)	0.32 (0.06)	0.32 (0.06)	0.0460
NCO Depth (µm)	56 (9.3)	57 (10.5)	0.0920
NCO Area (mm^2)	1.11 (0.04)	1.12 (0.03)	0.0250
ALCS $depth_{NCO}$ (µm)	171 (28.8)	168 (22.8)	0.2300
ALCS $depth_{BM}$ (µm)	229 (37.7)	228 (30.0)	0.7800
PLTT (µm)	416 (76.5)	414 (68.4)	0.6700

Table 4-8. Mean (standard deviation) of parameters generated in the control experimental protocol. 10/10 condition refers to parameters derived from an image acquisition after 10 minutes at IOP 10 mmHg; 10/30 condition refers to parameters derived from an image acquisition after 30 minutes at IOP 10 mmHg. The pair-wise comparisons have been performed using generalised estimating equations, p < 0.005

ID	Eye	RNFLT	RNFLV	RW	RV	NCO depth	NCO area	ALCS $depth_{NCO}$	ALCS $depth_{BM}$	PLTT
		µm	mm^3	µm	mm^3	µm	mm^2	µm	µm	µm
21152	OD	-2	0.00	-33	-0.05	53	-0.02	-7	45	-61
21152	OS	-4	-0.01	-33	-0.04	51	-0.01	8	57	-46
21808	OD	-1	0.00	-34	-0.07	68	-0.02	40	111	-93
21808	OS	-1	-0.01	-37	-0.08	41	-0.04	5	50	-74
23534	OD	0	0.00	-38	-0.05	31	-0.02	0	32	-46
23534	OS	-3	-0.01	-36	-0.05	31	0.00	9	41	-52
25340	OD	1	0.00	-23	-0.03	20	0.02	6	26	-23
25340	OS	1	0.00	-22	-0.03	19	0.03	21	40	-42
25904	OD	-5	-0.01	-20	-0.04	33	0.03	11	40	-8
25904	OS	-4	-0.01	-25	-0.03	35	0.03	7	42	-24
Mean		-2	-0.004	-30	-0.05	38	0.00	10	48	-47
SD		2	0.005	7	0.02	15	0.02	13	24	25

Table 4-9. Changes in each parameter value for individual eyes when increasing IOP from 10 mmHg/30 minutes to 45 mmHg/60 minutes

ID	Eye	RNFLT	RNFLV	RW	RV	NCO depth	NCO area	ALCS $depth_{NCO}$	ALCS $depth_{BM}$	PLTT
		µm	mm^3	µm	mm^3	µm	mm^2	µm	µm	µm
21152	OD	4	0	1	0	0	0	1	2	-10
21152	OS	6	0	3	0	0	0	-13	-14	-3
21808	OD	1	0	3	0	5	0	-17	-13	5
21808	OS	2	0	1	0	1	0	19	21	-15
23534	OD	1	0	-5	0	7	0	1	9	5
23534	OS	2	0	1	0	-2	0	-9	-11	10
Mean		3	0	1	0	2	0	-3	-1	-1
SD		1.9	0.0	2.9	0.0	3.4	0.0	13.1	14.3	9.8

Table 4-10. Changes in each parameter value for individual eyes during the control experiment when acquiring images at IOP 10 mmHg/10 minutes and at IOP 10 mmHg/30 minutes

Figure 4-41 illustrates the relationship between the change in NCO depth and the change in PLTT (left panel) and the change in rim volume (right panel) for the 10 acute IOP elevation eyes and the 6 'control' experiment eyes. In both cases, there was a clear association between the change in each parameter and the magnitude of NCO depth change (R^2 = 0.49 for change in

PLTT, R^2 = 0.41 for change in rim volume for the 10 eyes with acute IOP elevation). Images obtained from the eye with the most profound changes associated with acute elevation of IOP (right eye of 21808) are shown in Figure 4-42. The delineated structures at 10 mmHg/30 minutes (panel A) and at IOP 45 mmHg/60 minutes (panel B) are overlaid using the NCO reference plane (panel C) and using the secondary peripheral BM reference plane (panel D). An obvious posterior movement of the ILM is seen using the NCO reference plane, whereas the posterior movement of the ALCS is clearly present but less striking. When the secondary reference plane is utilised, the posterior movement of both the ILM and the ALCS is increased and posterior movement of BM is also seen. When examining individual eye change, only two eyes demonstrated a substantial increase in ALCS depth relative to NCO (40 µm observed for 21808 OD, as illustrated in Figure 4-42, and 21 µm observed for 25340 OS). In both cases, the increase in ALCS $depth_{NCO}$ exceeded the maximal change observed for that parameter in the control group (19 µm).

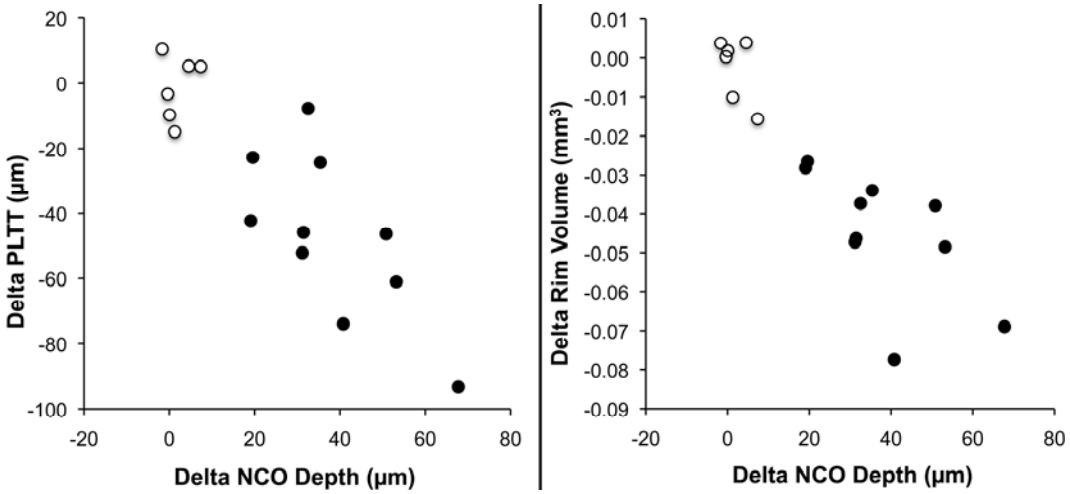

Figure 4-41. Scatter plots demonstrating the relationship between the change in NCO depth relative to a peripheral BM reference plane (x axes) and the change in PLTT (left plot) and rim volume (right plot). Open circles = control experiment eyes, filled circles = acute IOP elevation eyes

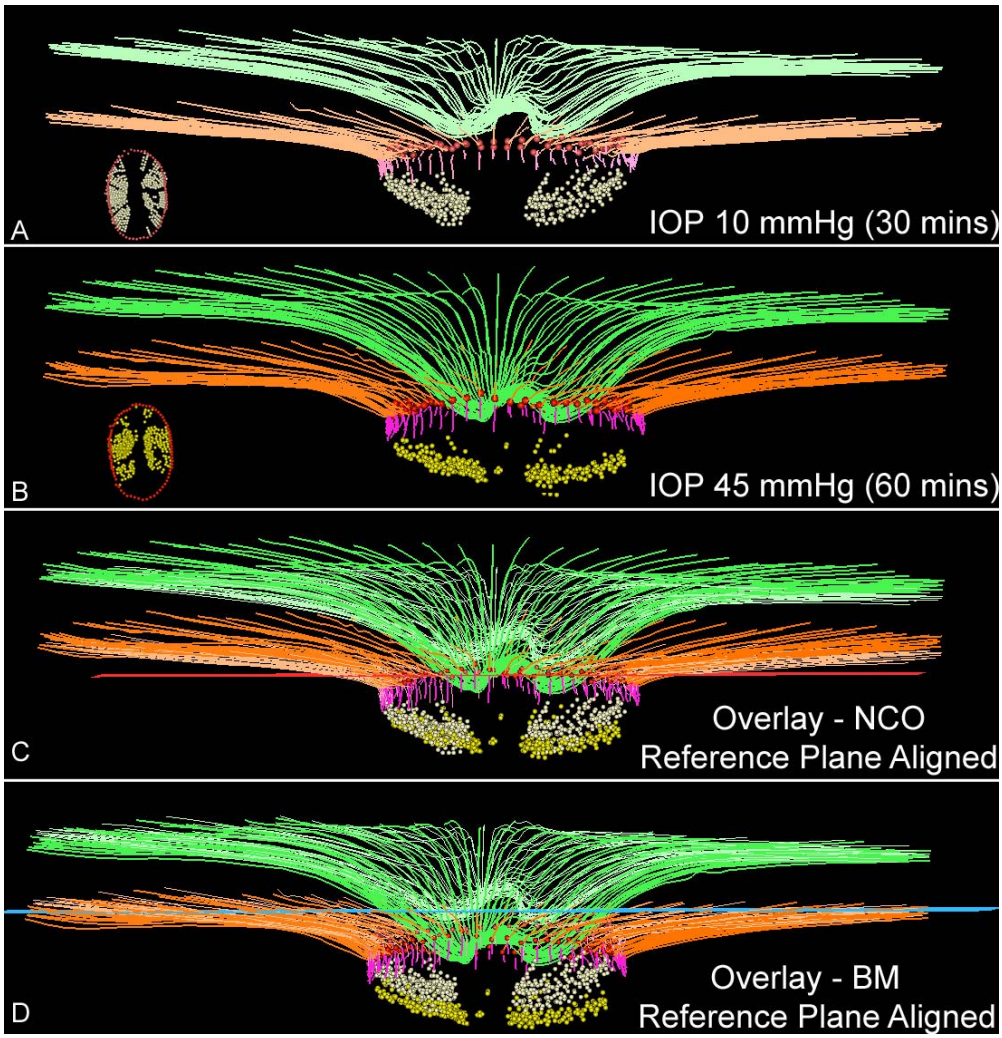

Figure 4-42. Example (animal 21808) of SDOCT changes observed with acute IOP elevation. *A:* 10 mmHg sustained for 30 minutes. *B:* 45 mmHg after 60 minutes. Inlays in A and B show en face view of delineated NCO and ALCS points. *C:* delineated SDOCT volumes have been overlaid, anchored to the NCO reference plane (red horizontal line). *D:* anchored to peripheral BM reference (horizontal turquoise line). Posterior movement of ALCS is present in C; this movement increases in D, along with movement of BM. No adjustments to z-axis magnification have been made to these images. Structures shown are: ILM (green), BM (orange), NCO (red points), border tissue (pink) and ALCS (yellow points). In order to differentiate the structures in the overlaid images, the colours at 10 mmHg/30 minutes have been washed-out

4.7.5 Discussion

The principal findings of this study may be summarised as follows: acute IOP elevation in the normal monkey eye resulted in significant reductions in neuroretinal rim parameters (rim width and rim volume), PLTT and significant increases in the depth of the neural canal opening (NCO depth) and the depth of the ALCS relative to peripheral BM (ALCS $depth_{BM}$). An increase in ALCS depth relative to the NCO (ALCS $depth_{NCO}$) was detectable in some eyes.

This study has expanded upon previous work from the ONHRL, firstly using digitised photographs (Burgoyne et al., 1995b), and subsequently using CSLO images (Heickell et al., 2001). These studies identified that acute elevation of IOP results in reversible deformation of the normal ONH surface. The current experiment has capitalised upon SDOCT's ability to capture structures deep to the ONH surface thereby indicating the underlying mechanism behind surface compliance changes.

Overall, changes in ALCS depth are detectable but appear to be greater when considered relative to peripheral BM rather than to the NCO. This observation may be linked to the finding that significant posterior movement of the NCO relative to peripheral BM was also observed. In previous work from the ONHRL, where compliance testing in normal monkey eyes using CSLO images was reported (Heickell et al., 2001), increasing the scan angle from 15º to 20º was found to be often associated with an increase in surface compliance. This phenomenon was interpreted as reflecting involvement of the peripapillary sclera in the posterior deformation associated with acute IOP elevation. Given that SDOCT was unable to capture the scleral canal opening or peripapillary sclera, we cannot be certain of the precise anatomical changes underpinning these findings.

Two eyes (21808 OD and 25340 OS) also demonstrated a substantial increase in ALCS $depth_{NCO}$, suggesting that in some eyes deformation of the ALCS is not solely driven by changes to peripapillary structures. It is not immediately apparent why these eyes should have behaved differently. One hypothesis regarding ONH compliance is that age plays a role, with 'young' eyes expected to demonstrate increased compliance as compared to 'aged' eyes. In the case of 21808, the animal was a young adult and clearly demonstrated increased compliance as

compared to the single adult (23534, aged 10 years) included in the study, but also compared to the two young animals aged less than 3. Indeed there does not appear to be any clear age-related trend, with similar ALCS depth change occurring in both the young and the adult eyes, although this is with the caveat that only 10 eyes are available for comparison. I hypothesise that the response of the load-bearing connective tissues of the ONH (LC and peripapillary sclera) in response to acute IOP elevation will vary from subject to subject and perhaps between individual eyes in the same subject (as observed in this experiment) due to variability in the material properties (themselves influenced by age, and geometric properties) of the tissues under force.

Agoumi and colleagues found that significant prelaminar tissue 'displacement' but not laminar displacement was detectable by SDOCT in vivo in 36 human subjects (including glaucoma subjects, age matched controls and young controls) in whom IOP was transiently elevated using an ophthalmodynamometer (Agoumi et al., 2011). The apparent similarity in results to the current experiment occurred despite some important methodological differences. Firstly, as this experiment was performed in non-human primates, IOP elevation was accurately and sustainably titrated by manometric control; whereas using an ophthalmodynamometer achieved an average estimated IOP increase of 10 mmHg, which was only sustained for the duration of the imaging session (approximately two minutes). Furthermore, I generated parameters using 40 or 48 radial B-scans; in the human study only the best 4 matching radial B-scans from a 12 radial B-scan pattern were used. Despite these important methodological differences, the close similarity in findings between these two studies and another recent study in the rat (Fortune et al., 2011), suggests that the changes observed with acute IOP elevation are consistent and likely to be generalisable. Agoumi and coworkers only used one reference plane, based on a line connecting BMO points (equivalent to our primary NCO-based reference plane), so did not look for changes in laminar depth relative to the periphery, unlike this experiment.

Interestingly, a single NCO-based reference plane was also used in a recent report of ex vivo SDOCT compliance testing using porcine eyes (Fatehee et al., 2011). In contrast to both the current experiment and the SDOCT study performed in vivo in human eyes (Agoumi et al., 2011), prelaminar tissue and LC cross sectional areas within a central B-scan both significantly

decreased with incremental IOP elevation. Furthermore, a multivariate regression indicated that the IOP-dependent increase in the size of the cup could mostly be explained by changes in the position and cross sectional area of the LC. My results suggest that in most cases, increases in cup (although not directly measured) are mostly driven by a reduction in PLTT and by posterior displacement of the NCO (perhaps indirectly reflecting deformation of the peripapillary sclera). It is possible that a proportion of the posterior laminar displacement noted ex vivo in porcine eyes may have been driven by posterior displacement of the NCO/peripapillary scleral deformation which might have been detected had a peripheral reference plane also been adopted, as in the current experiment. As the lamina is more anteriorly placed within the pig's ONH as compared to the human or monkey, more of the thickness of the lamina could be captured, although it should be noted that the measurements were in two dimensions only and were not necessarily comparable to those of the current study. The apparent reduction in laminar area, which is independent of reference plane, suggests that laminar deformation plays a major role in ONH compliance in the pig's eye. The apparent increased laminar deformation seen in the pig eye as compared to the monkey eye may simply reflect the aforementioned differences in measurement. Accepting this major caveat, it is possible that the lamina is highly compliant in the pig eye or indeed that the observed changes might be a consequence of 'stiffer' peripapillary sclera in the pig eye. This latter hypothesis might have been confirmed if significant scleral canal expansion was detectable in the monkey but not the pig eye (Bellezza et al., 2003a), had it been possible to detect the deeper scleral tissues in either animal by SDOCT. Fortunately, this is likely to be possible with 1000 nm wavesource imaging and/or EDI (either at 870 nm or 1000 nm).

The dynamic interaction between LC and sclera is central to the understanding of ONH biomechanics. Capture of the deeper scleral tissues represents a major hurdle as in vivo measurements of scleral canal expansion will be needed to effectively refine and validate finite element models of ONH biomechanics (Sigal and Ethier, 2009; Sigal et al., 2005a).

Agoumi and colleagues assumed that thinning of the prelaminar tissue was a consequence of compression of the ILM and the prelaminar tissue (Agoumi et al., 2011). Numerical models, however, have suggested that acute increases in IOP would result in thinning of the prelaminar

tissues due to lateral displacement, without compression (Sigal et al., 2009a). The volume of prelaminar tissue may therefore remain unchanged with acutely elevated IOP and the apparent 'thinning' or compression simply reflects a redistribution of the prelaminar tissues. These changes may also be influenced by conformational alterations in adjacent structures, such as the peripapillary sclera, which was not directly measurable by SDOCT in this study. It is likely that the increased depth penetration afforded by EDI and/or 1000 nm wave source SDOCT may allow improved visualisation of the most posterior recesses of the neural canal. If an expansion of the deeper canal is detectable then it is feasible that the resulting increased 'volume' space may allow for prelaminar and rim tissue redistribution.

This study supports the use of SDOCT to detect in vivo changes in ONH parameters following acute elevation in IOP. There is therefore potential to use this technology to characterise in vivo biomechanics of the ONH in both monkeys and human eyes for the first time and to further inform and validate numerical models. Such acute IOP ONH 'compliance' testing may be of important clinical relevance, as it will help differentiate 'permanent' structural changes (assumed to be due to tissue loss, or remodelling) from reversible changes. If in vivo ONH biomechanical behaviour can be linked to distinct patterns of functional damage then this opens up the possibility of SDOCT-assisted compliance testing becoming a component of future risk profiling in patients with, or at risk of, glaucoma.

5. SECTION V:

CONCLUSIONS

5.1 Summary

The major conclusions from this body of research may be summarised as follows:

1. SDOCT has been shown to be capable of detecting structures deep to the surface of the cup within the monkey ONH. Specifically, my work has shown - by comparison primarily with conventional histology but also with 3D histomorphometric reconstructions and clinical disc photographs (in my examination of disc margin anatomy) - that SDOCT reliably detects the prelaminar tissue and prelaminar glial columns, RPE/BM complex and its termination within the neural canal (NCO/BMO), the border tissue of Elschnig and the anterior-most aspects of the LC. To a variable degree, SDOCT may detect more posterior aspects of the LC, the peripapillary scleral surface and the anterior scleral canal opening in some eyes. However these targets were not visualised consistently enough to be able to generate meaningful quantitative parameters.

2. In a detailed examination of the structural basis of the clinically perceived optic disc margin, I demonstrated the complex and variable 3D architecture of this construct. In the monkey eye, the disc margin may comprise the termination of BM (BMO), the border tissue itself, the termination of border tissue or the anterior scleral canal opening. A major defining characteristic is the orientation of border tissue, which may be internally oblique, externally oblique, vertical or horizontal and these varieties may all co-exist within the same eye. This variability in border tissue orientation has not previously been noted.

3. Perhaps the key finding in this PhD and the one that I expect will have the greatest translational impact is the demonstration that SDOCT scanning can detect longitudinal changes to ‘deep’ ONH structures in an experimental model of glaucoma. At the time of writing, longitudinal assessment of structural change in glaucoma has focused on loss of RNFL, loss in neuroretinal rim/increase in cup and changes in surface height. My research has demonstrated that SDOCT is not only capable of detecting each of these ‘conventional’ measures but can also identify thinning of the prelaminar tissue and posterior displacement of the anterior lamina. How these changes impact upon visual function was beyond the scope of this research, but it is

interesting to note that they could be detected before the onset of RNFL loss as measured by SDOCT. It is possible, therefore, that SDOCT-detected changes in laminar position, orientation and thickness might be the earliest clinical findings of IOP-related distress, as has been suggested from 3D histomorphometric reconstructions of monkey EG eyes (Yang et al., 2007b).

4. In terms of generating SDOCT ONH parameters, it is essential that a relatively stable, easily identified landmark structure is used as the basis for the reference plane. In this PhD, I have demonstrated that the NCO is one such reference plane 'source structure'. However, I did find that NCO moved posteriorly relative to peripheral BM both following chronic and acute IOP elevation. I presented most of my findings relative both to a reference plane located at the NCO itself and to a secondary reference plane located at peripheral BM but anchored at a set distance from the centre of the NCO ellipse. I worked on the assumption that the NCO reference plane might be acceptable to follow parameters 'within' the ONH (whereby all structures might move 'with' the NCO), whereas the peripheral reference plane would be more appropriate to follow structures outside of the ONH, such as those that might theoretically relate to the peripapillary sclera. In practice, however, I think the degree of observed posterior NCO displacement can be so profound that a peripheral reference plane will probably be the basis for parameterisation of longitudinal human glaucoma SDOCT images.

5. In the final investigation, I performed SDOCT imaging of the ONH in normal monkey eyes undergoing acute manipulations in IOP. The results indicate that acute IOP elevation resulted in prelaminar tissue thinning, posterior displacement of NCO and posterior displacement of ALCS relative to peripheral BM. In a small number of eyes there was significant posterior displacement of ALCS relative to NCO. This study has demonstrated the effectiveness of SDOCT during 'compliance' experiments. Whilst the results are of interest, it is perhaps too early to say how effectively SDOCT compliance testing might increase our understanding of glaucoma pathophysiology or indeed how it might help to validate or improve numerical models of ONH biomechanics.

5.2 Impact

This body of work represents the first detailed exploration of SDOCT imaging of the monkey ONH. Having established that the NCO is a potentially useful landmark for defining a reference plane, a number of groups have subsequently followed this approach in humans and in other species (Agoumi et al., 2011; Fatehee et al., 2011). If posterior NCO displacement is found to occur in human eyes with acute and/or chronic IOP elevation, then it will be essential that a peripheral reference plane should also be investigated.

One of the major disadvantages of my method for identifying the NCO (and indeed all other SDOCT landmarks) is that it relied upon a labour-intensive manual delineation process. Obviously, an automated segmentation algorithm capable of reliably detecting the NCO is an essential next step. The OCT image processing group led by Abramoff and Garvin in Iowa has already presented an algorithm that successfully identifies the NCO in Cirrus SDOCT images (Hu et al., 2010). A PhD student from their group, Zhigong Hu, subsequently applied this algorithm to my Spectralis SDOCT images, and its performance compared favourably to my original NCO delineations, although this work has yet to be published. Robust automated NCO delineation will undoubtedly lead on to the development of standardised automated 3D ONH parameters in the future; attempts at automatically detecting ALCS are already underway in multiple laboratories.

The true impact of my work in clinical disc margin anatomy was unlikely to be appreciated until the same investigations have been undertaken in a larger number of human subjects. After my departure from the ONHRL, Professor Burgoyne began a collaboration with the group from Dalhousie, Halifax, to investigate disc margin anatomy in glaucomatous and normal human subjects (Reis et al., 2011). This study, just accepted for publication, confirms that the different border tissue orientations I observed in the monkey eye are all present in humans. In most discs, more than one border tissue orientation is present although internally oblique border tissue (with BM overhang) is the predominant form. Externally oblique border tissue is far less prevalent but is relatively more common in glaucoma eyes, particularly in the temporal and inferior regions of the disc. It would appear that the anatomy of the human disc margin is far more complex than that of the monkey. Although in some eyes BMO or the termination of border tissue corresponded to the

disc margin (as in the monkey), the clinical disc margin most frequently corresponded to a region of BM external to its termination. The implication is that Bruch's membrane overhang is not detectable ophthalmoscopically in humans. It is possible that the presence of patchy pigment or some other different optical properties of the monkey BM may account for the consistent visibility of BM overhang in monkey eyes. My work in the monkey and this subsequent work in human eyes will both have important implications for clinical imaging in glaucoma as well as the way in which neuroretinal rim is assessed during ophthalmoscopy.

With the advent of SDOCT imaging in ophthalmic practice, there has been the expected 'deluge' of clinical glaucoma imaging studies. Most of these have focused on RNFL imaging, comparisons with TDOCT, with other imaging modalities and between different SDOCT devices. Whilst I was undertaking this research in the monkey, investigators in other laboratories (specifically in Kyoto, Seoul, Pittsburgh and Halifax) began to concurrently and independently investigate SDOCT imaging of the LC in human eyes. To most observers, myself included, the high intensity signal seen in SDOCT B-scans below the surface of the cup was assumed to correspond to the LC. Indeed, one group reported SDOCT measurements of LC thickness and their correlations to visual field mean deviation in glaucoma eyes (Inoue et al., 2009), despite a lack of any validation that the target signal corresponded to the LC. My comparison between in vivo SDOCT B-scans and post mortem histology sections from a normal monkey represents the first real 'proof' of what structures within the ONH can be detected by SDOCT. I believe a benchmark has now been set whereby any assertion that 'full' laminar thickness may be measured by SDOCT (something that I was unable to demonstrate in the monkey eye) ought to be validated by further comparison to conventional histology.

It is perhaps too early to have identified any tangible impact yet from my longitudinal imaging study. It will take a number of years for sufficient longitudinal deep ONH SDOCT imaging data to be accrued in glaucoma subjects. The potential impact, though, is immense. My work clearly demonstrates that changes to the prelaminar thickness and anterior laminar position can be detected by SDOCT in the monkey model of glaucoma. Monitoring of these parameters will hopefully prove to be of value in human subjects, although their relationship to visual function

remains speculative. The ONHRL are collaborating with other clinicians and scientists at Devers, led by Dr Demirel, in the continuation of a well-established glaucoma longitudinal study (now renamed the 'Portland Progression Project'). In this study, ocular hypertensive, glaucoma and control subjects are undergoing regular deep ONH SDOCT imaging, in addition to a battery of conventional imaging and psychophysical tests. It is hoped that this study might be the first to validate the utility of deep ONH SDOCT in the follow-up of patients with, or at risk of, glaucoma. The application of SDOCT imaging to acute IOP ONH compliance testing is likely to have a major impact upon our ability to measure ONH biomechanics for the first time in vivo. Unfortunately there is a major hurdle that needs to be overcome before this becomes a reality, which is the inability of current SDOCT strategies to capture peripapillary sclera convincingly or reliably. The interplay between peripapillary sclera and the LC is so fundamental to the determination of how an individual ONH responds to IOP that measurements pertaining only to LC will remain inadequate until measurements such as peripapillary scleral thickness and scleral canal opening dimensions can be made in vivo. I believe that such targets are tantalisingly close and might even be achieved using existing SDOCT technology such as enhanced depth imaging (now incorporated into the Spectralis acquisition module) or image compensation (Girard et al., 2011). Once peripapillary scleral imaging has been validated, I expect SDOCT compliance testing will become the key tool in the measurement of ONH biomechanics.

5.3 Future Investigations

The future work inspired by this PhD can be divided into investigations that will be undertaken by the group at the ONHRL and investigations that I aim to undertake in the UK. The reason for this distinction is the fact that Professor Burgoyne and his colleagues continue to use the monkey model of glaucoma, something that I will not have access to in the UK. I, on the other hand, have returned to clinical practice in the UK and hopefully will be in a position to translate some of the methods and concepts described in this thesis into glaucoma management. I continue to provide input into the ongoing work of the ONHRL and hope that this collaboration continues to be fruitful.

Investigations either underway or planned at the ONHRL are as follows:

1. An assessment of whether EDI can improve the visibility and repeatability of both anterior and posterior surfaces of the LC as compared to standard SDOCT imaging in normal and EG monkey eyes imaged at 10 mmHg. This study has recently been completed and confirms that EDI does improve both visualisation of the lamina and its reproducibility.

2. Longitudinal analysis of SDOCT images in monkey eyes with unilateral EG sacrificed either at the achievement of a structural end-point (HRT-detected surface height depression) or at the achievement of a functional end-point (using multifocal electroretinography). This study is an addition to Professor Burgoyne's main R1 grant in which the specific aim is to identify histomorphometric differences between the ONHs in either group. Furthermore, as each leg of this study has been conducted in 4 young and 4 old monkeys, it is hoped that any age-related differences might also be exposed.

3. Assessment of a custom-built Spectralis device outfitted with a 1000 nm light-source. The ONHRL have recently received such a device from Heidelberg Engineering. An exhaustive assessment of this device's deep imaging capabilities is already underway and this will include direct comparisons with serial histology as per the investigation in this thesis, as well as direct comparisons to 870 nm Spectralis imaging. I understand that serial longitudinal imaging using the newer device, in addition to the standard 870 nm device, has also begun in animals with unilateral EG.

4. Acute compliance testing in monkey eyes will be expanded to include animals of differing age (young versus old) and differing stages of glaucoma damage (early versus moderate versus severe EG). The addition of EDI and perhaps 1000 nm SDOCT imaging may glean sufficient data (including peripapillary scleral parameters) to allow full characterisation of ONH biomechanics.

My personal research plan is as follows:

1. SDOCT compliance testing in POAG and NTG subjects. I have begun a study, in collaboration with Dr Girard (a bioengineer), in which 10 unstable POAG (high IOP) eyes and 10 unstable NTG (low IOP) eyes are imaged before and after trabeculectomy surgery. I speculate that IOP-lowering by trabeculectomy should be sufficient to allow detection of anterior displacement of the LC. Two new methods have been developed for this project. Firstly, Dr Girard, myself and Dr Mari (an ultrasound engineer) have developed a method to 'compensate' SDOCT images by removing vessel shadows and improve contrast (Girard et al., 2011). This new method allows for a post hoc improvement in the visualisation of the full thickness and width of the LC. The second method, as yet unpublished, is a 'tracking' algorithm that enables the detection of strain in ONH surfaces without the need for manual delineation. It is hoped that this study will demonstrate that SDOCT imaging can be used to measure ONH biomechanics in vivo.

2. Dr Girard and I have recently received funding to investigate in vivo measurement of corneal biomechanics in humans. Spectralis SDOCT imaging is capable of imaging the full thickness of the cornea in high resolution, just with the use of an additional lens. We now have ethical approval to image 5 ocular hypertensive, 5 POAG, 5 NTG and 10 normal subjects before and after IOP elevation using an ophthalmodynamometer. Our intention is to capture both corneal deformations and ONH deformations (imaging both structures separately before and after IOP elevation). We hope to firstly confirm that corneal biomechanics may be measured in vivo by SDOCT and then try to correlate corneal with ONH biomechanics (as measured using methods developed in the previous proposed experiment). I will also carry out visual field testing in all subjects and will therefore be able to assess whether there is any relationship between visual function, corneal and ONH biomechanics in this small cohort.

3. If our initial pilot investigations into in vivo ONH biomechanical testing (and indeed corneal biomechanical testing) prove to be successful, my long-term aim will be to apply longitudinal deep ONH SDOCT imaging to a large cohort of subjects at risk of progressive

glaucoma. I will also aim to perform baseline SDOCT compliance testing (i.e. imaging during a manipulation of IOP prior to the instigation of treatment) in each subject. My hope is that such a study will enable the role of LC-based measurements and of ONH biomechanics in clinical glaucoma practice to be fully understood and realised. It is possible that baseline measurements of ONH biomechanical behaviour may indicate predisposition to future visual damage. Whilst such an eventuality shows promise for 'risk-profiling' in glaucoma, demonstration of how ONH biomechanics may influence susceptibility to glaucoma may open up the possibility of new treatment modalities that might target modification of biomechanical behaviour.

6. SECTION VI:

REFERENCES

Abbott C. J., McBrien N. A., Grunert U., Pianta M. J. (2009) Relationship of the optical coherence tomography signal to underlying retinal histology in the tree shrew (Tupaia belangeri). *Invest Ophthalmol Vis Sci,* 50, 414-423.

Agoumi Y., Sharpe G. P., Hutchison D. M., Nicolela M. T., Artes P. H., Chauhan B. C. (2011) Laminar and prelaminar tissue displacement during intraocular pressure elevation in glaucoma patients and healthy controls. *Ophthalmology,* 118, 52-59.

Ahn J. K., Park K. H. (2002) Morphometric change analysis of the optic nerve head in unilateral disk hemorrhage cases. *Am J Ophthalmol,* 134, 920-922.

Airaksinen P. J., Mustonen E., Alanko H. I. (1981) Optic disc haemorrhages precede retinal nerve fibre layer defects in ocular hypertension. *Acta Ophthalmol (Copenh),* 59, 627-641.

Airaksinen P. J., Tuulonen A. (1984) Early glaucoma changes in patients with and without an optic disc haemorrhage. *Acta Ophthalmol (Copenh),* 62, 197-202.

Airaksinen P. J., Tuulonen A., Alanko H. I. (1992) Rate and pattern of neuroretinal rim area decrease in ocular hypertension and glaucoma. *Arch Ophthalmol,* 110, 206-210.

Albon J., Karwatowski W. S., Avery N., Easty D. L., Duance V. C. (1995) Changes in the collagenous matrix of the aging human lamina cribrosa. *Br J Ophthalmol,* 79, 368-375.

Albon J., Karwatowski W. S., Easty D. L., Sims T. J., Duance V. C. (2000a) Age related changes in the non-collagenous components of the extracellular matrix of the human lamina cribrosa. *Br J Ophthalmol,* 84, 311-317.

Albon J., Purslow P. P., Karwatowski W. S., Easty D. L. (2000b) Age related compliance of the lamina cribrosa in human eyes. *Br J Ophthalmol,* 84, 318-323.

Alencar L. M., Zangwill L. M., Weinreb R. N., Bowd C., Vizzeri G., Sample P. A., Susanna R., Jr., Medeiros F. A. (2010) Agreement for detecting glaucoma progression with the GDx guided progression analysis, automated perimetry, and optic disc photography. *Ophthalmology,* 117, 462-470.

Altangerel U., Bayer A., Henderer J. D., Katz L. J., Steinmann W. C., Spaeth G. L. (2005) Knowledge of chronology of optic disc stereophotographs influences the determination of glaucomatous change. *Ophthalmology,* 112, 40-43.

Anderson D. R. (1969) Ultrastructure of human and monkey lamina cribrosa and optic nerve head. *Arch Ophthalmol,* 82, 800-814.

Anderson D. R., Braverman S. (1976) Reevaluation of the optic disk vasculature. *Am J Ophthalmol,* 82, 165-174.

Anderson D. R., Hendrickson A. (1974) Effect of intraocular pressure on rapid axoplasmic transport in monkey optic nerve. *Invest Ophthalmol Vis Sci,* 13, 771-783.

Anderson D. R., Hoyt W. F. (1969) Ultrastructure of intraorbital portion of human and monkey optic nerve. *Arch Ophthalmol,* 82, 506-530.

Anderson M. G., Smith R. S., Hawes N. L., Zabaleta A., Chang B., Wiggs J. L., John S. W. (2002) Mutations in genes encoding melanosomal proteins cause pigmentary glaucoma in DBA/2J mice. *Nat Genet,* 30, 81-85.

Anger E. M., Unterhuber A., Hermann B., Sattmann H., Schubert C., Morgan J. E., Cowey A., Ahnelt P. K., Drexler W. (2004) Ultrahigh resolution optical coherence tomography of the monkey fovea. Identification of retinal sublayers by correlation with semithin histology sections. *Exp Eye Res,* 78, 1117-1125.

Anton A., Andrada M. T., Mujica V., Calle M. A., Portela J., Mayo A. (2004) Prevalence of primary open-angle glaucoma in a Spanish population: the Segovia study. *J Glaucoma,* 13, 371-376.

Armaly M. F. (1964) Aqueous Outflow Facility in Monkeys and the Effect of Topical Corticoids. *Invest Ophthalmol,* 3, 534-538.

Armaly M. F. (1965a) On the Distribution of Applanation Pressure. I. Statistical Features and the Effect of Age, Sex, and Family History of Glaucoma. *Arch Ophthalmol,* 73, 11-18.

Armaly M. F. (1965b) Statistical Attributes of the Steroid Hypertensive Response in the Clinically Normal Eye. I. The Demonstration of Three Levels of Response. *Invest Ophthalmol,* 4, 187-197.

Artal P., Guirao A., Berrio E., Williams D. R. (2001) Compensation of corneal aberrations by the internal optics in the human eye. *J Vis,* 1, 1-8.

Artes P. H., Chauhan B. C. (2005) Longitudinal changes in the visual field and optic disc in glaucoma. *Prog Retin Eye Res,* 24, 333-354.

Azuara-Blanco A., Katz L. J., Spaeth G. L., Vernon S. A., Spencer F., Lanzl I. M. (2003) Clinical agreement among glaucoma experts in the detection of glaucomatous changes of the optic disk using simultaneous stereoscopic photographs. *Am J Ophthalmol,* 136, 949-950.

Bakalash S., Shlomo G. B., Aloni E., Shaked I., Wheeler L., Ofri R., Schwartz M. (2005) T-cell-based vaccination for morphological and functional neuroprotection in a rat model of chronically elevated intraocular pressure. *J Mol Med (Berl),* 83, 904-916.

Balazsi A. G., Rootman J., Drance S. M., Schulzer M., Douglas G. R. (1984) The effect of age on the nerve fiber population of the human optic nerve. *Am J Ophthalmol,* 97, 760-766.

Bankes J. L., Perkins E. S., Tsolakis S., Wright J. E. (1968) Bedford glaucoma survey. *Br Med J,* 1, 791-796.

Barkana Y., Harizman N., Gerber Y., Liebmann J. M., Ritch R. (2006) Measurements of optic disk size with HRT II, Stratus OCT, and funduscopy are not interchangeable. *Am J Ophthalmol,* 142, 375-380.

Becker B. (1965) Intraocular Pressure Response to Topical Corticosteroids. *Invest Ophthalmol,* 4, 198-205.

Bellezza A. J., Hart R. T., Burgoyne C. F. (2000) The optic nerve head as a biomechanical structure: initial finite element modeling. *Invest Ophthalmol Vis Sci,* 41, 2991-3000.

Bellezza A. J., Rintalan C. J., Thompson H. W., Downs J. C., Hart R. T., Burgoyne C. F. (2003a) Anterior scleral canal geometry in pressurised (IOP 10) and non-pressurised (IOP 0) normal monkey eyes. *Br J Ophthalmol,* 87, 1284-1290.

Bellezza A. J., Rintalan C. J., Thompson H. W., Downs J. C., Hart R. T., Burgoyne C. F. (2003b) Deformation of the lamina cribrosa and anterior scleral canal wall in early experimental glaucoma. *Invest Ophthalmol Vis Sci,* 44, 623-637.

Bengtsson B. (1976) The variation and covariation of cup and disc diameters. *Acta Ophthalmol (Copenh),* 54, 804-818.

Bengtsson B. (1980) The alteration and asymmetry of cup and disc diameters. *Acta Ophthalmol (Copenh),* 58, 726-732.

Bengtsson B., Krakau C. E. (1977) Some essential optical features of the Zeiss fundus camera. *Acta Ophthalmol (Copenh),* 55, 123-131.

Bengtsson B., Krakau C. E. (1992) Correction of optic disc measurements on fundus photographs. *Graefes Arch Clin Exp Ophthalmol,* 230, 24-28.

Bhandari A., Fontana L., Fitzke F. W., Hitchings R. A. (1997) Quantitative analysis of the lamina cribrosa in vivo using a scanning laser opthalmoscope. *Curr Eye Res,* 16, 1-8.

Bjerrum J. (1889) Om en tilföjelse til den saedvanlige synfeltsundersökelse samt om synsfeltet ved glaukom. *Nord Ophthalmol Tskr (Copenhagen),* 2, 141-185.

Bland J. M., Altman D. G. (1986) Statistical methods for assessing agreement between two methods of clinical measurement. *Lancet,* 1, 307-310.

Blumenthal E. Z., Parikh R. S., Pe'er J., Naik M., Kaliner E., Cohen M. J., Prabakaran S., Kogan M., Thomas R. (2007) Retinal nerve fibre layer imaging compared with histological measurements in a human eye. *Eye*.

Boland M. V., Zhang L., Broman A. T., Jampel H. D., Quigley H. A. (2008) Comparison of optic nerve head topography and visual field in eyes with open-angle and angle-closure glaucoma. *Ophthalmology,* 115, 239-245 e232.

Bonomi L., Marchini G., Marraffa M., Bernardi P., De Franco I., Perfetti S., Varotto A., Tenna V. (1998) Prevalence of glaucoma and intraocular pressure distribution in a defined population. The Egna-Neumarkt Study. *Ophthalmology,* 105, 209-215.

Bowd C., Weinreb R. N., Williams J. M., Zangwill L. M. (2000) The retinal nerve fiber layer thickness in ocular hypertensive, normal, and glaucomatous eyes with optical coherence tomography. *Arch Ophthalmol,* 118, 22-26.

Brandt J. D. (2007) Central corneal thickness--tonometry artifact, or something more? *Ophthalmology,* 114, 1963-1964.

Britton R. J., Drance S. M., Schulzer M., Douglas G. R., Mawson D. K. (1987) The area of the neuroretinal rim of the optic nerve in normal eyes. *Am J Ophthalmol,* 103, 497-504.

Broadway D. C., Nicolela M. T., Drance S. M. (1999) Optic disk appearances in primary open-angle glaucoma. *Surv Ophthalmol,* 43 Suppl 1, S223-243.

Bron A. J., Tripathi R. C., Tripathi B. J. 1997 *Wolff's anatomy of the eye and orbit.* Eighth ed. London: Chapman and Hall Medical

Brown D. J., Morishige N., Neekhra A., Minckler D. S., Jester J. V. (2007) Application of second harmonic imaging microscopy to assess structural changes in optic nerve head structure ex vivo. *J Biomed Opt,* 12, 024029.

Buckingham B. P., Inman D. M., Lambert W., Oglesby E., Calkins D. J., Steele M. R., Vetter M. L., Marsh-Armstrong N., Horner P. J. (2008) Progressive ganglion cell degeneration precedes neuronal loss in a mouse model of glaucoma. *J Neurosci,* 28, 2735-2744.

Budenz D. L., Anderson D. R., Varma R., Schuman J., Cantor L., Savell J., Greenfield D. S., Patella V. M., Quigley H. A., Tielsch J. (2007) Determinants of normal retinal nerve fiber layer thickness measured by Stratus OCT. *Ophthalmology,* 114, 1046-1052.

Budenz D. L., Chang R. T., Huang X., Knighton R. W., Tielsch J. M. (2005) Reproducibility of retinal nerve fiber thickness measurements using the stratus OCT in normal and glaucomatous eyes. *Invest Ophthalmol Vis Sci,* 46, 2440-2443.

Budenz D. L., Fredette M. J., Feuer W. J., Anderson D. R. (2008) Reproducibility of peripapillary retinal nerve fiber thickness measurements with stratus OCT in glaucomatous eyes. *Ophthalmology,* 115, 661-666 e664.

Buhrmann R. R., Quigley H. A., Barron Y., West S. K., Oliva M. S., Mmbaga B. B. (2000) Prevalence of glaucoma in a rural East African population. *Invest Ophthalmol Vis Sci,* 41, 40-48.

Burgoyne C. F., Downs J. C. (2008) Premise and Prediction – How Optic Nerve Head Biomechanics Underlies the Susceptibility and Clinical Behavior of the Aged Optic Nerve Head. *J Glaucoma,* 17, 318-328.

Burgoyne C. F., Downs J. C., Bellezza A. J., Hart R. T. (2004) Three-dimensional reconstruction of normal and early glaucoma monkey optic nerve head connective tissues. *Invest Ophthalmol Vis Sci,* 45, 4388-4399.

Burgoyne C. F., Downs J. C., Bellezza A. J., Suh J. K., Hart R. T. (2005) The optic nerve head as a biomechanical structure: a new paradigm for understanding the role of IOP-related stress and

strain in the pathophysiology of glaucomatous optic nerve head damage. *Prog Retin Eye Res,* 24, 39-73.

Burgoyne C. F., Morrison J. C. (2001) The Anatomy and Pathophysiology of the Optic Nerve Head in Glaucoma. *J Glaucoma,* 10, S16-S18.

Burgoyne C. F., Quigley H. A., Thompson H. W., Vitale S., Varma R. (1995a) Early changes in optic disc compliance and surface position in experimental glaucoma. *Ophthalmology,* 102, 1800-1809.

Burgoyne C. F., Quigley H. A., Thompson H. W., Vitale S., Varma R. (1995b) Measurement of optic disc compliance by digitized image analysis in the normal monkey eye. *Ophthalmology,* 102, 1790-1799.

Burgoyne C. F., Varma R., Quigley H. A., Vitale S., Pease M. E., Lenane P. L. (1994) Global and regional detection of induced optic disc change by digitized image analysis. *Arch Ophthalmol,* 112, 261-268.

Burk R. O. W., Vihanninjoki K., Bartke T., Tuulonen A., Airaksinen P. J., Volcker H.-E., Konig J. M. (2000) Development of the standard reference plan for the Heidelberg retina tomograph. *Graefes Arch Clin Exp Ophthalmol,* 238, 375-384.

Burke D. (1968) A modification for the combined staining of cells and fibers in the nervous system. *Am J Med Technol,* 34, 667-670.

Burns S. A., Tumbar R., Elsner A. E., Ferguson D., Hammer D. X. (2007) Large-field-of-view, modular, stabilized, adaptive-optics-based scanning laser ophthalmoscope. *J Opt Soc Am A Opt Image Sci Vis,* 24, 1313-1326.

Caprioli J. (1994) Clinical evaluation of the optic nerve in glaucoma. *Trans Am Ophthalmol Soc,* 92, 589-641.

Caprioli J., Miller J. M. (1987) Optic disc rim area is related to disc size in normal subjects. *Arch Ophthalmol,* 105, 1683-1685.

Caprioli J., Spaeth G. L. (1985) Comparison of the optic nerve head in high- and low-tension glaucoma. *Arch Ophthalmol,* 103, 1145-1149.

Carel R. S., Korczyn A. D., Rock M., Goya I. (1984) Association between ocular pressure and certain health parameters. *Ophthalmology,* 91, 311-314.

Carpel E. F., Engstrom P. F. (1981) The normal cup-disk ratio. *Am J Ophthalmol,* 91, 588-597.

Carpineto P., Ciancaglini M., Aharrh-Gnama A., Cirone D., Mastropasqua L. (2005) Custom measurement of retinal nerve fiber layer thickness using STRATUS OCT in normal eyes. *Eur J Ophthalmol,* 15, 360-366.

Cartwright M. J., Anderson D. R. (1988) Correlation of asymmetric damage with asymmetric intraocular pressure in normal-tension glaucoma (low-tension glaucoma). *Arch Ophthalmol,* 106, 898-900.

Cense B., Chen T. C., Park B. H., Pierce M. C., de Boer J. F. (2004a) In vivo birefringence and thickness measurements of the human retinal nerve fiber layer using polarization-sensitive optical coherence tomography. *J Biomed Opt,* 9, 121-125.

Cense B., Chen T. C., Park B. H., Pierce M. C., de Boer J. F. (2004b) Thickness and birefringence of healthy retinal nerve fiber layer tissue measured with polarization-sensitive optical coherence tomography. *Invest Ophthalmol Vis Sci,* 45, 2606-2612.

Chang R. T., Knight O. J., Feuer W. J., Budenz D. L. (2009) Sensitivity and specificity of time-domain versus spectral-domain optical coherence tomography in diagnosing early to moderate glaucoma. *Ophthalmology,* 116, 2294-2299.

Chauhan B. C., Blanchard J. W., Hamilton D. C., LeBlanc R. P. (2000) Technique for detecting serial topographic changes in the optic disc and peripapillary retina using scanning laser tomography. *Invest Ophthalmol Vis Sci,* 41, 775-782.

Chauhan B. C., Hutchison D. M., Artes P. H., Caprioli J., Jonas J. B., LeBlanc R. P., Nicolela M. T. (2009a) Optic disc progression in glaucoma: comparison of confocal scanning laser tomography to optic disc photographs in a prospective study. *Invest Ophthalmol Vis Sci,* 50, 1682-1691.

Chauhan B. C., Nicolela M. T., Artes P. H. (2009b) Incidence and rates of visual field progression after longitudinally measured optic disc change in glaucoma. *Ophthalmology,* 116, 2110-2118.

Chauhan D. S., Marshall J. (1999) The interpretation of optical coherence tomography images of the retina. *Invest Ophthalmol Vis Sci,* 40, 2332-2342.

Chen E., Gedda U., Landau I. (2001) Thinning of the papillomacular bundle in the glaucomatous eye and its influence on the reference plane of the Heidelberg retinal tomography. *J Glaucoma,* 10, 386-389.

Chen T. C., Cense B., Miller J. W., Rubin P. A., Deschler D. G., Gragoudas E. S., de Boer J. F. (2006) Histologic correlation of in vivo optical coherence tomography images of the human retina. *Am J Ophthalmol,* 141, 1165-1168.

Chihara E., Chihara K. (1994) Covariation of optic disc measurements and ocular parameters in the healthy eye. *Graefes Arch Clin Exp Ophthalmol,* 232, 265-271.

Cho J. W., Sung K. R., Hong J. T., Um T. W., Kang S. Y., Kook M. S. (2011) Detection of glaucoma by spectral domain-scanning laser ophthalmoscopy/optical coherence tomography (SD-SLO/OCT) and time domain optical coherence tomography. *J Glaucoma,* 20, 15-20.

Choma M., Sarunic M., Yang C., Izatt J. (2003) Sensitivity advantage of swept source and Fourier domain optical coherence tomography. *Opt Express,* 11, 2183-2189.

Choma M. A., Hsu K., Izatt J. A. (2005) Swept source optical coherence tomography using an all-fiber 1300-nm ring laser source. *J Biomed Opt,* 10, 44009.

CNTGS. (1998) Comparison of glaucomatous progression between untreated patients with normal-tension glaucoma and patients with therapeutically reduced intraocular pressures. Collaborative Normal-Tension Glaucoma Study Group. *Am J Ophthalmol,* 126, 487-497.

Coffey M., Reidy A., Wormald R. P. L., Wu J. X., Wright L. A., Courtney P. (1993) Prevalence of glaucoma in the west of Ireland. *Br J Ophthalmol,* 77, 17-21.

Coleman A. L., Quigley H. A., Vitale S., Dunkelberger G. (1991) Displacement of the optic nerve head by acute changes in intraocular pressure in monkey eyes. *Ophthalmology,* 98, 35-40.

Colton T., Ederer F. (1980) The distribution of intraocular pressures in the general population. *Surv Ophthalmol,* 25, 123-129.

Congdon N. G., Broman A. T., Bandeen-Roche K., Grover D., Quigley H. A. (2006) Central corneal thickness and corneal hysteresis associated with glaucoma damage. *Am J Ophthalmol,* 141, 868-875.

Coops A., Henson D. B., Kwartz A. J., Artes P. H. (2006) Automated analysis of heidelberg retina tomograph optic disc images by glaucoma probability score. *Invest Ophthalmol Vis Sci,* 47, 5348-5355.

Correnti A. J., Wollstein G., Price L. L., Schuman J. S. (2003) Comparison of optic nerve head assessment with a digital stereoscopic camera (discam), scanning laser ophthalmoscopy, and stereophotography. *Ophthalmology,* 110, 1499-1505.

Crichton A., Drance S. M., Douglas G. R., Schulzer M. (1989) Unequal intraocular pressure and its relation to asymmetric visual field defects in low-tension glaucoma. *Ophthalmology,* 96, 1312-1314.

Curcio C. A., Allen K. A. (1990) Topography of ganglion cells in human retina. *J Comp Neurol,* 300, 5-25.

Dandona L., Quigley H. A., Brown A. E., Enger C. (1990) Quantitative regional structure of the normal human lamina cribrosa. A racial comparison. *Arch Ophthalmol,* 108, 393-398.

David R., Zangwill L. M., Tessler Z., Yassur Y. (1985) The correlation between intraocular pressure and refractive status. *Arch Ophthalmol,* 103, 1812-1815.

de Boer J. F., Cense B., Park B. H., Pierce M. C., Tearney G. J., Bouma B. E. (2003) Improved signal-to-noise ratio in spectral-domain compared with time-domain optical coherence tomography. *Opt Lett,* 28, 2067-2069.

de Boer J. F., Milner T. E., van Gemert M. J., Nelson J. S. (1997) Two-dimensional birefringence imaging in biological tissue by polarization-sensitive optical coherence tomography. *Opt Lett,* 22, 934-936.

de Bruin D. M., Burnes D. L., Loewenstein J., Chen Y., Chang S., Chen T. C., Esmaili D. D., de Boer J. F. (2008) In vivo three-dimensional imaging of neovascular age-related macular degeneration using optical frequency domain imaging at 1050 nm. *Invest Ophthalmol Vis Sci,* 49, 4545-4552.

De Moraes C. G., Juthani V. J., Liebmann J. M., Teng C. C., Tello C., Susanna R., Jr., Ritch R. (2011) Risk factors for visual field progression in treated glaucoma. *Arch Ophthalmol,* 129, 562-568.

De Moraes C. G., Prata T. S., Liebmann C. A., Tello C., Ritch R., Liebmann J. M. (2009) Spatially consistent, localized visual field loss before and after disc hemorrhage. *Invest Ophthalmol Vis Sci,* 50, 4727-4733.

DeLeon Ortega J. E., Sakata L. M., Kakati B., McGwin G., Jr., Monheit B. E., Arthur S. N., Girkin C. A. (2007) Effect of glaucomatous damage on repeatability of confocal scanning laser ophthalmoscope, scanning laser polarimetry, and optical coherence tomography. *Invest Ophthalmol Vis Sci,* 48, 1156-1163.

Deleon-Ortega J. E., Arthur S. N., McGwin G., Jr., Xie A., Monheit B. E., Girkin C. A. (2006) Discrimination between glaucomatous and nonglaucomatous eyes using quantitative imaging devices and subjective optic nerve head assessment. *Invest Ophthalmol Vis Sci,* 47, 3374-3380.

Dielemans I., Vingerling J. R., Wolfs R. C., Hofman A., Grobbee D. E., de Jong P. T. (1994) The prevalence of primary open-angle glaucoma in a population-based study in The Netherlands. The Rotterdam Study. *Ophthalmology,* 101, 1851-1855.

Dongqi H., Zeqin R. (1999) A biomathematical model for pressure-dependent lamina cribrosa behavior. *J Biomech,* 32, 579-584.

Donnelly W. J., 3rd, Roorda A. (2003) Optimal pupil size in the human eye for axial resolution. *J Opt Soc Am A Opt Image Sci Vis,* 20, 2010-2015.

Douglas G. R., Drance S. M., Schulzer M. (1975) The visual field and nerve head in angle-closure glaucoma. A comparison of the effects of acute and chronic angle closure. *Arch Ophthalmol,* 93, 409-411.

Downs J. C., Blidner R. A., Bellezza A. J., Thompson H. W., Hart R. T., Burgoyne C. F. (2002) Peripapillary scleral thickness in perfusion-fixed normal monkey eyes. *Invest Ophthalmol Vis Sci,* 43, 2229-2235.

Downs J. C., Burgoyne C. F., Seigfreid W. P., Reynaud J. F., Strouthidis N. G., Sallee V. (2011) 24-Hour IOP Telemetry in the Non-human Primate: Implant System Performance and Initial Characterization of IOP At Multiple Timescales. *Invest Ophthalmol Vis Sci*.

Downs J. C., Ensor M. E., Bellezza A. J., Thompson H. W., Hart R. T., Burgoyne C. F. (2001) Posterior Scleral Thickness in Perfusion-Fixed Normal and Early-Glaucoma Monkey Eyes. *Invest Ophthalmol Vis Sci,* 42, 3202-3208.

Downs J. C., Roberts M. D., Burgoyne C. F. (2008) Mechanical environment of the optic nerve head in glaucoma. *Optom Vis Sci,* 85, 425-435.

Downs J. C., Roberts M. D., Burgoyne C. F., Hart R. T. (2009) Multiscale finite element modeling of the lamina cribrosa microarchitecture in the eye. *Conf Proc IEEE Eng Med Biol Soc,* 2009, 4277-4280.

Downs J. C., Yang H., Girkin C., Sakata L., Bellezza A. J., Thompson H., Burgoyne C. F. (2007) Three Dimensional Histomorphometry of the Normal and Early Glaucomatous Monkey Optic Nerve Head: Neural Canal and Subarachnoid Space Architecture. *Invest Ophthalmol Vis Sci,* 48, 3195-3208.

Drance S. M., Fairclough M., Butler D. M., Kottler M. S. (1977) The importance of disc hemorrhage in the prognosis of chronic open angle glaucoma. *Arch Ophthalmol,* 95, 226-228.

Dreher A. W., Tso P. C., Weinreb R. N. (1991) Reproducibility of topographic measurements of the normal and glaucomatous optic nerve head with the laser tomographic scanner. *Am J Ophthalmol,* 111, 221-229.

Drexler W., Fujimoto J. G. (2008) State-of-the-art retinal optical coherence tomography. *Prog Retin Eye Res,* 27, 45-88.

Drexler W., Morgner U., Ghanta R. K., Kartner F. X., Schuman J. S., Fujimoto J. G. (2001) Ultrahigh-resolution ophthalmic optical coherence tomography. *Nat Med,* 7, 502-507.

Edwards M. E., Good T. A. (2001) Use of a Mathematical Model to Estimate Stress and Strain During Elevated Pressure Induced Lamina Cribrosa Deformation. *Curr Eye Res,* 23, 215-225.

Ehlers N. (1970) On corneal thickness and intraocular pressure. II. A clinical study on the thickness of the corneal stroma in glaucomatous eyes. *Acta Ophthalmol (Copenh),* 48, 1107-1112.

Emery J. M., Landis D., Paton D., Boniuk M., Craig J. M. (1974) The lamina cribrosa in normal and glaucomatous human eyes. *Trans Am Acad Ophthalmol Otolaryngol,* 78, OP290-297.

Ernest J. T., Potts A. M. (1968) Pathophysiology of the distal portion of the optic nerve. I. Tissue pressure relationships. *Am J Ophthalmol,* 66, 373-380.

Ethier C. R., Johnson M., Ruberti J. (2004) Ocular biomechanics and biotransport. *Annu Rev Biomed Eng,* 6, 249-273.

Fantes F. E., Anderson D. R. (1989) Clinical histologic correlation of human peripapillary anatomy. *Ophthalmology,* 96, 20-25.

Fatehee N., Yu P. K., Morgan W. H., Cringle S. J., Yu D. Y. (2011) The impact of acutely elevated intraocular pressure on the porcine optic nerve head. *Invest Ophthalmol Vis Sci,* 52, 6192-6198.

Fayers T., Strouthidis N. G., Garway-Heath D. F. (2007) Monitoring glaucomatous progression using a novel Heidelberg Retina Tomograph event analysis. *Ophthalmology,* 114, 1973-1980.

Fechtner R. D., Weinreb R. N. (1994) Mechanisms of optic nerve damage in primary open angle glaucoma. *Surv Ophthalmol,* 39, 23-42.

Fercher A. F. (2010) Optical coherence tomography - development, principles, applications. *Z Med Phys,* 20, 251-276.

Fercher A. F., Hitzenberger C. K., Camp G., El-Zaiat S. Y. (1995) Measurement of intraocular distances by backscattering spectral interferometry. *Optics Communications,* 117, 43-48.

Fercher A. F., Mengedoht K., Werner W. (1988) Eye-length measurement by interferometry with partially coherent light. *Opt Lett,* 13, 186-188.

Fernandez E., Drexler W. (2005) Influence of ocular chromatic aberration and pupil size on transverse resolution in ophthalmic adaptive optics optical coherence tomography. *Opt Express,* 13, 8184-8197.

Ferreras A., Pajarin A. B., Polo V., Larrosa J. M., Pablo L. E., Honrubia F. M. (2007) Diagnostic Ability of Heidelberg Retina Tomograph 3 Classifications Glaucoma Probability Score versus Moorfields Regression Analysis. *Ophthalmology,* 114, 1981-1987.

Fingert J. H., Clark A. F., Craig J. E., Alward W. L., Snibson G. R., McLaughlin M., Tuttle L., Mackey D. A., Sheffield V. C., Stone E. M. (2001) Evaluation of the myocilin (MYOC) glaucoma gene in monkey and human steroid-induced ocular hypertension. *Invest Ophthalmol Vis Sci,* 42, 145-152.

Fitzke F. W., Masters B. R. (1993) Three-dimensional visualization of confocal sections of in vivo human fundus and optic nerve. *Curr Eye Res,* 12, 1015-1018.

Flammer J., Pache M., Resink T. (2001) Vasospasm, its role in the pathogenesis of diseases with particular reference to the eye. *Prog Retin Eye Res,* 20, 319-349.

Fontana L., Bhandari A., Fitzke F. W., Hitchings R. A. (1998a) In vivo morphometry of the lamina cribrosa and its relation to visual field loss in glaucoma. *Curr Eye Res,* 17, 363-369.

Fontana L., Poinoosawmy D., Bunce C. V., O'Brien C., Hitchings R. A. (1998b) Pulsatile ocular blood flow investigation in asymmetric normal tension glaucoma and normal subjects. *Br J Ophthalmol,* 82, 731-736.

Ford B. A., Artes P. H., McCormick T. A., Nicolela M. T., LeBlanc R. P., Chauhan B. C. (2003) Comparison of data analysis tools for detection of glaucoma with the Heidelberg Retina Tomograph. *Ophthalmology,* 110, 1145-1150.

Fortune B., Choe T. E., Reynaud J., Hardin C., Cull G. A., Burgoyne C. F., Wang L. (2011) Deformation of the Rodent Optic Nerve Head and Peripapillary Structures during Acute Intraocular Pressure Elevation. *Invest Ophthalmol Vis Sci,* 52, 6651-6661.

Fortune B., Yang H., Strouthidis N. G., Cull G. A., Grimm J. L., Downs J. C., Burgoyne C. F. (2009) The effect of acute intraocular pressure elevation on peripapillary retinal thickness, retinal nerve fiber layer thickness, and retardance. *Invest Ophthalmol Vis Sci,* 50, 4719-4726.

Foster P. J., Buhrmann R., Quigley H. A., Johnson G. J. (2002) The definition and classification of glaucoma in prevalence surveys. *Br J Ophthalmol,* 86, 238-242.

Franceschetti A., Bock R. H. (1950) Megalopapilla; a new congenital anomaly. *Am J Ophthalmol,* 33, 227-235, illust.

Frishman L. J., Saszik S., Harwerth R. S., Viswanathan S., Li Y., Smith E. L., 3rd, Robson J. G., Barnes G. (2000) Effects of experimental glaucoma in macaques on the multifocal ERG. Multifocal ERG in laser-induced glaucoma. *Doc Ophthalmol,* 100, 231-251.

Frishman L. J., Shen F. F., Du L., Robson J. G., Harwerth R. S., Smith E. L., Carter-Dawson L., Crawford M. L. (1996) The scotopic electroretinogram of macaque after retinal ganglion cell loss from experimental glaucoma. *Invest Ophthalmol Vis Sci,* 37, 125-141.

Fujimoto J. G., De Silvestri S., Ippen E. P., Puliafito C. A., Margolis R., Oseroff A. (1986) Femtosecond optical ranging in biological systems. *Opt Lett,* 11, 150.

Funk J., Dieringer T., Grehn F. (1989) Correlation between neuroretinal rim area and age in normal subjects. *Graefes Arch Clin Exp Ophthalmol,* 227, 544-548.

Gaasterland D., Kupfer C. (1974) Experimental glaucoma in the rhesus monkey. *Invest Ophthalmol,* 13, 455-457.

Gaasterland D., Tanishima T., Kuwabara T. (1978) Axoplasmic flow during chronic experimental glaucoma. 1. Light and electron microscopic studies of the monkey optic nerve head during development of glaucomatous cupping. *Invest Ophthalmol Vis Sci,* 17, 838-846.

Gabriele M. L., Ishikawa H., Wollstein G., Bilonick R. A., Townsend K. A., Kagemann L., Wojtkowski M., Srinivasan V. J., Fujimoto J. G., Duker J. S., Schuman J. S. (2008) Optical coherence tomography scan circle location and mean retinal nerve fiber layer measurement variability. *Invest Ophthalmol Vis Sci,* 49, 2315-2321.

Gabriele M. L., Wollstein G., Ishikawa H., Kagemann L., Xu J., Folio L. S., Schuman J. S. (2011) Optical coherence tomography: history, current status, and laboratory work. *Invest Ophthalmol Vis Sci,* 52, 2425-2436.

Garas A., Vargha P., Hollo G. (2010) Reproducibility of retinal nerve fiber layer and macular thickness measurement with the RTVue-100 optical coherence tomograph. *Ophthalmology,* 117, 738-746.

Garcia-Valenzuela E., Shareef S., Walsh J., Sharma S. C. (1995) Programmed cell death of retinal ganglion cells during experimental glaucoma. *Exp Eye Res,* 61, 33-44.

Garway-Heath D. F., Ruben S. T., Viswanathan A., Hitchings R. A. (1998a) Vertical cup/disc ratio in relation to optic disc size: its value in the assessment of the glaucoma suspect. *Br J Ophthalmol,* 82, 1118-1124.

Garway-Heath D. F., Rudnicka A. R., Lowe T., Foster P. J., Fitzke F. W., Hitchings R. A. (1998b) Measurement of optic disc size: equivalence of methods to correct for ocular magnification. *Br J Ophthalmol,* 82, 643-649.

Garway-Heath D. F., Wollstein G., Hitchings R. A. (1997) Aging changes of the optic nerve head in relation to open angle glaucoma. *Br J Ophthalmol,* 81, 840-845.

Geijssen H. C., Greve E. L. (1987) The spectrum of primary open angle glaucoma. I: Senile sclerotic glaucoma versus high tension glaucoma. *Ophthalmic Surg,* 18, 207-213.

Girard M. J., Downs J. C., Bottlang M., Burgoyne C. F., Suh J. K. (2009) Peripapillary and posterior scleral mechanics--part II: experimental and inverse finite element characterization. *J Biomech Eng,* 131, 051012.

Girard M. J., Strouthidis N. G., Ethier C. R., Mari J. M. (2011) Shadow removal and contrast enhancement in optical coherence tomography images of the human optic nerve head. *Invest Ophthalmol Vis Sci*.

Girkin C. A. Principles of confocal scanning laser ophthalmoscopy for the clinician. In: Fingeret M., Flanagan J. G., Liebmann J. (eds), *The essential HRT primer.* San Ramon, California: Jocoto Advertising, Inc.; 2005:2-7.

Gloesmann M., Hermann B., Schubert C., Sattmann H., Ahnelt P. K., Drexler W. (2003) Histologic correlation of pig retina radial stratification with ultrahigh-resolution optical coherence tomography. *Invest Ophthalmol Vis Sci,* 44, 1696-1703.

Gonzalez-Garcia A. O., Vizzeri G., Bowd C., Medeiros F. A., Zangwill L. M., Weinreb R. N. (2009) Reproducibility of RTVue retinal nerve fiber layer thickness and optic disc measurements and agreement with Stratus optical coherence tomography measurements. *Am J Ophthalmol,* 147, 1067-1074, 1074 e1061.

Gordon M. O., Beiser J. A., Brandt J. D., Heuer D. K., Higginbotham E. J., Johnson C. A., Keltner J. L., Miller J. P., Parrish R. K., 2nd, Wilson M. R., Kass M. A. (2002) The Ocular Hypertension Treatment Study: baseline factors that predict the onset of primary open-angle glaucoma. *Arch Ophthalmol,* 120, 714-720; discussion 829-730.

Gordon M. O., Torri V., Miglior S., Beiser J. A., Floriani I., Miller J. P., Gao F., Adamsons I., Poli D., D'Agostino R. B., Kass M. A. (2007) Validated prediction model for the development of primary open-angle glaucoma in individuals with ocular hypertension. *Ophthalmology,* 114, 10-19.

Graham S. L., Drance S. M. (1999) Nocturnal hypotension: role in glaucoma progression. *Surv Ophthalmol,* 43 Suppl 1, S10-16.

Graham S. L., Drance S. M., Wijsman K., Douglas G. R., Mikelberg F. S. (1995) Ambulatory blood pressure monitoring in glaucoma. The nocturnal dip. *Ophthalmology,* 102, 61-69.

Grainger J., Hutchinson R. The Costs of Blindness - An Analysis of the Costs of Visual Impairment and Blindness in the United Kingdom. The Guide Dogs for the Blind Association; 2003.

Greaney M. J., Hoffman D. C., Garway-Heath D. F., Nakla M., Coleman A. L., Caprioli J. (2002) Comparison of optic nerve imaging methods to distinguish normal eyes from those with glaucoma. *Invest Ophthalmol Vis Sci,* 43, 140-145.

Greene P. R. (1985) Closed-form ametropic pressure-volume and ocular rigidity solutions. *Am J Optom Physiol Opt,* 62, 870-878.

Grodum K., Heijl A., Bengtsson B. (2005) Risk of glaucoma in ocular hypertension with and without pseudoexfoliation. *Ophthalmology,* 112, 386-390.

Gross R. L., Ji J., Chang P., Pennesi M. E., Yang Z., Zhang J., Wu S. M. (2003) A mouse model of elevated intraocular pressure: retina and optic nerve findings. *Trans Am Ophthalmol Soc,* 101, 163-169; discussion 169-171.

Hare W., Ton H., Woldemussie E., Ruiz G., Feldmann B., Wijono M. (1999) Electrophysiological and histological measures of retinal injury in chronic ocular hypertensive monkeys. *Eur J Ophthalmol,* 9 Suppl 1, S30-33.

Hare W., WoldeMussie E., Lai R., Ton H., Ruiz G., Feldmann B., Wijono M., Chun T., Wheeler L. (2001) Efficacy and safety of memantine, an NMDA-type open-channel blocker, for reduction of retinal injury associated with experimental glaucoma in rat and monkey. *Surv Ophthalmol,* 45 Suppl 3, S284-289; discussion S295-286.

Harwerth R. S., Carter-Dawson L., Shen F., Smith E. L., Crawford M. L. (1999) Ganglion cell losses underlying visual field defects from experimental glaucoma. *Invest Ophthalmol Vis Sci,* 40, 2242-2250.

Harwerth R. S., Crawford M. L., Frishman L. J., Viswanathan S., Smith E. L., 3rd, Carter-Dawson L. (2002) Visual field defects and neural losses from experimental glaucoma. *Prog Retin Eye Res,* 21, 91-125.

Harwerth R. S., Smith E. L., DeSantis L. (1997) Experimental glaucoma: perimetric field defects and intraocular pressure. *J Glaucoma,* 6, 390-401.

Hayreh S. S. (1975) Segmental nature of the choroidal vasculature. *Br J Ophthalmol,* 59, 631-648.

Hayreh S. S. Structure and blood supply of the optic nerve. In: Heilmann K., Richardson K. T. (eds), *Glaucoma: conceptions of a disease.* Stuttgart: Thieme; 1978:104-137.

Hayreh S. S. (2001) The blood supply of the optic nerve head and the evaluation of it - myth and reality. *Prog Retin Eye Res,* 20, 563-593.

Hayreh S. S., Podhajsky P., Zimmerman M. B. (1999) Role of nocturnal arterial hypotension in optic nerve head ischemic disorders. *Ophthalmologica,* 213, 76-96.

Hayreh S. S., Zimmerman M. B., Podhajsky P., Alward W. L. (1994) Nocturnal arterial hypotension and its role in optic nerve head and ocular ischemic disorders. *Am J Ophthalmol,* 117, 603-624.

Healey P. R., Mitchell P., Smith W., Wang J. J. (1998) Optic disc hemorrhages in a population with and without signs of glaucoma. *Ophthalmology,* 105, 216-223.

Hee M. R., Izatt J. A., Swanson E. A., Huang D., Schuman J. S., Lin C. P., Puliafito C. A., Fujimoto J. G. (1995) Optical coherence tomography of the human retina. *Arch Ophthalmol,* 113, 325-332.

Heickell A. G., Bellezza A. J., Thompson H. W., Burgoyne C. F. (2001) Optic disc surface compliance testing using confocal scanning laser tomography in the normal monkey eye. *J Glaucoma,* 10, 369-382.

Heidelberg Engineering. 2006 *Operating manual for the Heidelberg Retina Tomograph III*. Heidelberg: Heidelberg Engineering

Heidelberg Engineering. 2007 *Spectralis Operating Instructions*. Version 001 ed. Heidelberg, Germany

Heijl A., Leske M. C., Bengtsson B., Hyman L., Hussein M. (2002) Reduction of intraocular pressure and glaucoma progression: results from the Early Manifest Glaucoma Trial. *Arch Ophthalmol,* 120, 1268-1279.

Hermann B., Fernandez E. J., Unterhuber A., Sattmann H., Fercher A. F., Drexler W., Prieto P. M., Artal P. (2004) Adaptive-optics ultrahigh-resolution optical coherence tomography. *Opt Lett,* 29, 2142-2144.

Hernandez M. R. (2000) The optic nerve head in glaucoma: role of astrocytes in tissue. *Prog Retin Eye Res,* 19, 297-321.

Hernandez M. R., Andrzejewska W. M., Neufeld A. H. (1990) Changes in the extracellular matrix of the human optic nerve head in primary open-angle glaucoma. *Am J Ophthalmol,* 109, 180-188.

Hernandez M. R., Luo X. X., Andrzejewska W., Neufeld A. H. (1989) Age-related changes in the extracellular matrix of the human optic nerve head. *Am J Ophthalmol,* 107, 476-484.

Hernandez M. R., Luo X. X., Igoe F., Neufeld A. H. (1987) Extracellular matrix of the human lamina cribrosa. *Am J Ophthalmol,* 104, 567-576.

Herndon L. W., Weizer J. S., Stinnett S. S. (2004) Central corneal thickness as a risk factor for advanced glaucoma damage. *Arch Ophthalmol,* 122, 17-21.

Higginbotham L., Shafranov G., Shields M. B. (2007) Gray optic disc crescent: influence of ethnicity in a glaucoma population. *J Glaucoma,* 16, 572-576.

Hitchings R. A., Spaeth G. L. (1976) The optic disc in glaucoma. I: Classification. *Br J Ophthalmol,* 60, 778-785.

Hitchings R. A., Spaeth G. L. (1977) Fluorescein angiography in chronic simple and low-tension glaucoma. *Br J Ophthalmol,* 61, 126-132.

Hogan M. J., Alvarado J. A., Weddell J. E. Chapter 10 - Optic Nerve (Histology of the Human Eye). *Histology of the Human Eye.* Philadelphia: WB Saunders Co.; 1971:523-606.

Hong S., Kim C. Y., Seong G. J., Hong Y. J. (2007) Central corneal thickness and visual field progression in patients with chronic primary angle-closure glaucoma with low intraocular pressure. *Am J Ophthalmol,* 143, 362-363.

Hood D. C., Frishman L. J., Viswanathan S., Robson J. G., Ahmed J. (1999) Evidence for a ganglion cell contribution to the primate electroretinogram (ERG): effects of TTX on the multifocal ERG in macaque. *Vis Neurosci,* 16, 411-416.

Hougaard J. L., Ostenfeld C., Heijl A., Bengtsson B. (2006) Modelling the normal retinal nerve fibre layer thickness as measured by Stratus optical coherence tomography. *Graefes Arch Clin Exp Ophthalmol*.

How A. C., Tan G. S., Chan Y. H., Wong T. T., Seah S. K., Foster P. J., Aung T. (2009) Population prevalence of tilted and torted optic discs among an adult Chinese population in Singapore: the Tanjong Pagar Study. *Arch Ophthalmol,* 127, 894-899.

Hoyt W. F. (1976) Fundoscopic changes in the retinal nerve-fibre layer in chronic and acute optic neuropathies. *Trans Ophthalmol Soc U K,* 96, 368-371.

Hoyt W. F., Frisen L., Newman N. M. (1973) Fundoscopy of nerve fiber layer defects in glaucoma. *Invest Ophthalmol Vis Sci,* 12, 814-829.

Hoyt W. F., Luis O. (1962) Visual fiber anatomy in the infrageniculate pathway of the primate. *Arch Ophthalmol,* 68, 94-106.

Hoyt W. F., Newman N. M. (1972) The earliest observable defect in glaucoma? *Lancet,* 1, 692-693.

Hu Z., Abramoff M. D., Kwon Y. H., Lee K., Garvin M. K. (2010) Automated segmentation of neural canal opening and optic cup in 3D spectral optical coherence tomography volumes of the optic nerve head. *Invest Ophth Vis Sci,* 51, 5708-5717.

Huang D., Swanson E. A., Lin C. P., Schuman J. S., Stinson W. G., Chang W., Hee M. R., Flotte T., Gregory K., Puliafito C. A., et al. (1991) Optical coherence tomography. *Science,* 254, 1178-1181.

Iester M., Mikelberg F. S., Drance S. M. (1997) The effect of optic disc size on diagnostic precision with the Heidelberg retina tomograph. *Ophthalmology,* 104, 545-548.

Iliev M. E., Meyenberg A., Garweg J. G. (2006) Morphometric assessment of normal, suspect and glaucomatous optic discs with Stratus OCT and HRT II. *Eye,* 20, 1288-1299.

Inoue R., Hangai M., Kotera Y., Nakanishi H., Mori S., Morishita S., Yoshimura N. (2009) Three-dimensional high-speed optical coherence tomography imaging of lamina cribrosa in glaucoma. *Ophthalmology,* 116, 214-222.

Ishida K., Yamamoto T., Sugiyama K., Kitazawa Y. (2000) Disk hemorrhage is a significantly negative prognostic factor in normal-tension glaucoma. *Am J Ophthalmol,* 129, 707-714.

Jaffe G. J., Caprioli J. (2004) Optical coherence tomography to detect and manage retinal disease and glaucoma. *Am J Ophthalmol,* 137, 156-169.

Jakobs T. C., Libby R. T., Ben Y., John S. W., Masland R. H. (2005) Retinal ganglion cell degeneration is topological but not cell type specific in DBA/2J mice. *J Cell Biol,* 171, 313-325.

Jampel H. D., Friedman D., Quigley H., Vitale S., Miller R., Knezevich F., Ding Y. (2009) Agreement among glaucoma specialists in assessing progressive disc changes from photographs in open-angle glaucoma patients. *Am J Ophthalmol,* 147, 39-44 e31.

Janssen P., Naskar R., Moore S., Thanos S., Thiel H. J. (1996) Evidence for glaucoma-induced horizontal cell alterations in the human retina. *Ger J Ophthalmol,* 5, 378-385.

Jay J. L., Murdoch J. R. (1993) The rate of visual field loss in untreated primary open angle glaucoma. *Br J Ophthalmol,* 77, 176-178.

Jeoung J. W., Park K. H. (2010) Comparison of Cirrus OCT and Stratus OCT on the ability to detect localized retinal nerve fiber layer defects in preperimetric glaucoma. *Invest Ophthalmol Vis Sci,* 51, 938-945.

Johnson M. A., Drum B. A., Quigley H. A., Sanchez R. M., Dunkelberger G. R. (1989) Pattern-evoked potentials and optic nerve fiber loss in monocular laser- induced glaucoma. *Invest Ophthalmol Vis Sci,* 30, 897-907.

Jonas J. B. (2005) Clinical implications of peripapillary atrophy in glaucoma. *Curr Opin Ophthalmol,* 16, 84-88.

Jonas J. B., Airaksinen P. J., Robert Y. (1988a) Definitionsentwurf der intra- und parapapillären Parameter für die Biomorphometrie des Nervus opticus. . *Klin Monatsbl Augenheilkd,* 192, 621.

Jonas J. B., Budde W. M. (2000) Diagnosis and pathogenesis of glaucomatous optic neuropathy: morphological aspects. *Prog Retin Eye Res,* 19, 1-40.

Jonas J. B., Fernandez M. C., Naumann G. O. (1992a) Glaucomatous parapapillary atrophy. Occurrence and correlations. *Arch Ophthalmol,* 110, 214-222.

Jonas J. B., Fernandez M. C., Sturmer J. (1993) Pattern of glaucomatous neuroretinal rim loss. *Ophthalmology,* 100, 63-68.

Jonas J. B., Gusek G. C., Guggenmoos Holzmann I., Naumann G. O. (1988b) Variability of the real dimensions of normal human optic discs. *Graefes Arch Clin Exp Ophthalmol,* 226, 332-336.

Jonas J. B., Gusek G. C., Guggenmoos-Holzmann I., Naumann G. O. (1988c) Size of the optic nerve scleral canal and comparison with intravital determination of optic disc dimensions. *Graefes Arch Clin Exp Ophthalmol,* 226, 213-215.

Jonas J. B., Gusek G. C., Naumann G. O. (1988d) Optic disc, cup and neuroretinal rim size, configuration and correlations in normal eyes. . *Invest Ophthalmol Vis Sci,* 29, 1151-1158.

Jonas J. B., Gusek G. C., Naumann G. O. (1988e) Optic disk morphometry in high myopia. *Graefes Arch Clin Exp Ophthalmol,* 226, 587-590.

Jonas J. B., Hayreh S. S. (2000) Ophthalmoscopic appearance of the normal optic nerve head in rhesus monkeys. *Invest Ophthalmol Vis Sci,* 41, 2978-2983.

Jonas J. B., Mardin C. Y., Schlotzer Schrehardt U., Naumann G. O. (1991) Morphometry of the human lamina cribrosa surface. *Invest Ophthalmol Vis Sci,* 32, 401-405.

Jonas J. B., Martus P., Horn F. K., Junemann A., Korth M., Budde W. M. (2004) Predictive factors of the optic nerve head for development or progression of glaucomatous visual field loss. *Invest Ophthalmol Vis Sci,* 45, 2613-2618.

Jonas J. B., Naumann G. O. (1989) Parapapillary retinal vessel diameter in normal and glaucoma eyes. II. Correlations. *Invest Ophthalmol Vis Sci,* 30, 1604-1611.

Jonas J. B., Schmidt A. M., Muller-Bergh J. A., Schlotzer-Schrehardt U. M., Naumann G. O. (1992b) Human optic nerve fiber count and optic disc size. *Invest Ophthalmol Vis Sci,* 33, 2012-2018.

Jonas J. B., Stroux A., Velten I., Juenemann A., Martus P., Budde W. M. (2005) Central corneal thickness correlated with glaucoma damage and rate of progression. *Invest Ophthalmol Vis Sci,* 46, 1269-1274.

Jonas J. B., Thomas R., George R., Berenshtein E., Muliyil J. (2003) Optic disc morphology in south India: the Vellore Eye Study. *Br J Ophthalmol,* 87, 189-196.

Jonas J. B., Xu L. (1994) Optic disk hemorrhages in glaucoma. *Am J Ophthalmol,* 118, 1-8.

Kagemann L., Ishikawa H., Wollstein G., Brennen P. M., Townsend K. A., Gabriele M. L., Schuman J. S. (2008) Ultrahigh-resolution spectral domain optical coherence tomography imaging of the lamina cribrosa. *Ophthalmic Surg Lasers Imaging,* 39, S126-131.

Kahn H. A., Leibowitz H. M., Ganley J. P., Kini M. M., Colton T., Nickerson R. S., Dawber T. R. (1977) The Framingham Eye Study. I. Outline and major prevalence findings. *Am J Epidemiol,* 106, 17-32.

Kass M. A., Heuer D. K., Higginbotham E. J., Johnson C. A., Keltner J. L., Miller J. P., Parrish R. K., 2nd, Wilson M. R., Gordon M. O. (2002) The Ocular Hypertension Treatment Study: a randomized trial determines that topical ocular hypotensive medication delays or prevents the onset of primary open-angle glaucoma. *Arch Ophthalmol,* 120, 701-713; discussion 829-730.

Kaufman P. L., Barany E. H. (1976) Residual pilocarpine effects on outflow facility after ciliary muscle disinsertion in the synomolgus monkey. *Invest Ophthalmol,* 15, 558-561.

Kaufman P. L., Lutjen-Drecoll E., Hubbard W. C., Erickson K. A. (1994) Obstruction of aqueous humor outflow by cross-linked polyacrylamide microgels in bovine, monkey, and human eyes. *Ophthalmology,* 101, 1672-1679.

Kerr J., Nelson P., O'Brien C. (1998) A comparison of ocular blood flow in untreated primary open-angle glaucoma and ocular hypertension. *Am J Ophthalmol,* 126, 42-51.

Kerr J., Nelson P., O'Brien C. (2003) Pulsatile ocular blood flow in primary open-angle glaucoma and ocular hypertension. *Am J Ophthalmol,* 136, 1106-1113.

Kim J. S., Ishikawa H., Gabriele M. L., Wollstein G., Bilonick R. A., Kagemann L., Fujimoto J. G., Schuman J. S. (2010) Retinal nerve fiber layer thickness measurement comparability between time domain optical coherence tomography (OCT) and spectral domain OCT. *Invest Ophthalmol Vis Sci,* 51, 896-902.

Kim J. S., Ishikawa H., Sung K. R., Xu J., Wollstein G., Bilonick R. A., Gabriele M. L., Kagemann L., Duker J. S., Fujimoto J. G., Schuman J. S. (2009) Retinal nerve fibre layer thickness measurement reproducibility improved with spectral domain optical coherence tomography. *Br J Ophthalmol,* 93, 1057-1063.

Kirsch R. E., Anderson D. R. (1973) Clinical recognition of glaucomatous cupping. *Am J Ophthalmol,* 75, 442-454.

Klein B. E., Klein R., Lee K. E., Hoyer C. J. (2006) Does the intraocular pressure effect on optic disc cupping differ by age? *Trans Am Ophthalmol Soc,* 104, 143-148.

Klein B. E., Klein R., Linton K. L. (1992) Intraocular pressure in an American community. The Beaver Dam Eye Study. *Invest Ophthalmol Vis Sci,* 33, 2224-2228.

Knight O. J., Chang R. T., Feuer W. J., Budenz D. L. (2009) Comparison of retinal nerve fiber layer measurements using time domain and spectral domain optical coherent tomography. *Ophthalmology,* 116, 1271-1277.

Ko M. L., Hu D. N., Ritch R., Sharma S. C. (2000) The combined effect of brain-derived neurotrophic factor and a free radical scavenger in experimental glaucoma. *Invest Ophthalmol Vis Sci,* 41, 2967-2971.

Kotera Y., Yasuno Y., Hangai M., Inoue R., Matika S., Nakanishi H., Yamanari M., Yoshimura N. (2008) Comparison of Spectral Domain Optical Coherence Tomography and Color Photographic Imaging of the Optic Nerve Head in Glaucoma Management. *Ophthalmic Surg Lasers Imaging,* 39, S62-S70.

Kourkoutas D., Buys Y. M., Flanagan J. G., Hatch W. V., Balian C., Trope G. E. (2007) Comparison of glaucoma progression evaluated with Heidelberg retina tomograph II versus optic nerve head stereophotographs. *Can J Ophthalmol,* 42, 82-88.

Laemmer R., Schroeder S., Martus P., Viestenz A., Mardin C. Y. (2007) Quantification of neuroretinal rim loss using digital planimetry in long-term follow-up of normals and patients with ocular hypertension. *J Glaucoma,* 16, 430-436.

Lee E. C., de Boer J. F., Mujat M., Lim H., Yun S. H. (2006) In vivo optical frequency domain imaging of human retina and choroid. *Opt Express,* 14, 4403-4411.

Leighton D. A., Tomlinson A. (1973) Ocular tension and axial length of the eyeball in open-angle glaucoma and low tension glaucoma. *Br J Ophthalmol,* 57, 499-502.

Leitgeb R., Hitzenberger C., Fercher A. (2003) Performance of fourier domain vs. time domain optical coherence tomography. *Opt Express,* 11, 889-894.

Leitgeb R., Wojtkowski M., Kowalczyk A., Hitzenberger C. K., Sticker M., Fercher A. F. (2000) Spectral measurement of absorption by spectroscopic frequency-domain optical coherence tomography. *Opt Lett,* 25, 820-822.

Lesk M. R., Hafez A. S., Descovich D. (2006) Relationship between central corneal thickness and changes of optic nerve head topography and blood flow after intraocular pressure reduction in open-angle glaucoma and ocular hypertension. *Arch Ophthalmol,* 124, 1568-1572.

Leske M. C. (2007) Open-angle glaucoma -- an epidemiologic overview. *Ophthalmic Epidemiol,* 14, 166-172.

Leske M. C., Connell A. M., Schachat A. P., Hyman L. (1994) The Barbados Eye Study. Prevalence of open angle glaucoma. *Arch Ophthalmol,* 112, 821-829.

Leske M. C., Connell A. M., Wu S. Y., Nemesure B., Li X., Schachat A., Hennis A. (2001) Incidence of open-angle glaucoma: the Barbados Eye Studies. The Barbados Eye Studies Group. *Arch Ophthalmol,* 119, 89-95.

Leske M. C., Heijl A., Hussein M., Bengtsson B., Hyman L., Komaroff E. (2003) Factors for glaucoma progression and the effect of treatment: the early manifest glaucoma trial. *Arch Ophthalmol,* 121, 48-56.

Leske M. C., Heijl A., Hyman L., Bengtsson B., Dong L., Yang Z. (2007) Predictors of long-term progression in the early manifest glaucoma trial. *Ophthalmology,* 114, 1965-1972.

Lessell S., Kuwabara T. (1969) Experimental alpha-chymotrypsin glaucoma. *Arch Ophthalmol,* 81, 853-864.

Leung C. K., Chan W. M., Hui Y. L., Yung W. H., Woo J., Tsang M. K., Tse K. K. (2005) Analysis of retinal nerve fiber layer and optic nerve head in glaucoma with different reference plane offsets, using optical coherence tomography. *Invest Ophthalmol Vis Sci,* 46, 891-899.

Leung C. K., Cheng A. C. K., Chong K. K. L., Leung K. S., Mohamed S., Lau C. S. L., Cheung C. Y. L., Chu G. C.-h., Lai R. Y. K., Pang C. C. P., Lam D. S. C. (2007) Optic Disc Measurements in Myopia with Optical Coherence Tomography and Confocal Scanning Laser Ophthalmoscopy. *Invest Ophthalmol Vis Sci,* 48, 3178-3183.

Leung C. K., Cheung C. Y., Weinreb R. N., Qiu K., Liu S., Li H., Xu G., Fan N., Pang C. P., Tse K. K., Lam D. S. (2010) Evaluation of retinal nerve fiber layer progression in glaucoma: a study on optical coherence tomography guided progression analysis. *Invest Ophthalmol Vis Sci,* 51, 217-222.

Leung C. K., Cheung C. Y., Weinreb R. N., Qiu Q., Liu S., Li H., Xu G., Fan N., Huang L., Pang C. P., Lam D. S. (2009) Retinal nerve fiber layer imaging with spectral-domain optical coherence tomography: a variability and diagnostic performance study. *Ophthalmology,* 116, 1257-1263.

Levy N. S., Crapps E. E. (1984) Displacement of optic nerve head in response to short-term intraocular pressure elevation in human eyes. *Arch Ophthalmol,* 102, 782-786.

Li J., Herndon L. W., Asrani S. G., Stinnett S., Allingham R. R. (2004) Clinical comparison of the Proview eye pressure monitor with the Goldmann applanation tonometer and the Tonopen. *Arch Ophthalmol,* 122, 1117-1121.

Lieberman M. F., Maumenee A. E., Green W. R. (1976) Histologic studies of the vasculature of the anterior optic nerve. *Am J Ophthalmol,* 82, 405-423.

Lim H., Mujat M., Kerbage C., Lee E. C., Chen Y., Chen T. C., de Boer J. F. (2006) High-speed imaging of human retina in vivo with swept-source optical coherence tomography. *Opt Express,* 14, 12902-12908.

Littmann H. (1982) [Determination of the real size of an object on the fundus of the living eye]. *Klin Monatsbl Augenheilkd,* 180, 286-289.

Littmann H. (1988) [Determining the true size of an object on the fundus of the living eye]. *Klin Monatsbl Augenheilkd,* 192, 66-67.

Mabuchi F., Lindsey J. D., Aihara M., Mackey M. R., Weinreb R. N. (2004) Optic nerve damage in mice with a targeted type I collagen mutation. *Invest Ophthalmol Vis Sci,* 45, 1841-1845.

Mainster M. A., Timberlake G. T., Webb R. H., Hughes G. W. (1982) Scanning laser ophthalmoscopy. Clinical applications. *Ophthalmology,* 89, 852-857.

Manassakorn A., Ishikawa H., Kim J. S., Wollstein G., Bilonick R. A., Kagemann L., Gabriele M. L., Sung K. R., Mumcuoglu T., Duker J. S., Fujimoto J. G., Schuman J. S. (2008) Comparison of optic disc margin identified by color disc photography and high-speed ultrahigh-resolution optical coherence tomography. *Arch Ophthalmol,* 126, 58-64.

Marshall J., Hamilton A. M., Bird A. C. (1975) Histopathology of ruby and argon laser lesions in monkey and human retina. A comparative study. *Br J Ophthalmol,* 59, 610-630.

Mason R. P., Kosoko O., Wilson M. R., Martone J. F., Cowan C. L., Jr., Gear J. C., Ross-Degnan D. (1989) National survey of the prevalence and risk factors of glaucoma in St. Lucia, West Indies. Part I. Prevalence findings. *Ophthalmology,* 96, 1363-1368.

Mastropasqua L., Lobefalo L., Mancini A., Ciancaglini M., Palma S. (1992) Prevalence of myopia in open angle glaucoma. *Eur J Ophthalmol,* 2, 33-35.

May C. A., Lutjen-Drecoll E. (2002) Morphology of the murine optic nerve. *Invest Ophthalmol Vis Sci,* 43, 2206-2212.

Medeiros F. A., Zangwill L. M., Alencar L. M., Bowd C., Sample P. A., Susanna R., Jr., Weinreb R. N. (2009) Detection of glaucoma progression with stratus OCT retinal nerve fiber layer, optic nerve head, and macular thickness measurements. *Invest Ophthalmol Vis Sci,* 50, 5741-5748.

Medeiros F. A., Zangwill L. M., Bowd C., Vessani R. M., Susanna R., Jr., Weinreb R. N. (2005) Evaluation of retinal nerve fiber layer, optic nerve head, and macular thickness measurements for glaucoma detection using optical coherence tomography. *Am J Ophthalmol,* 139, 44-55.

Medeiros F. A., Zangwill L. M., Bowd C., Weinreb R. N. (2004) Comparison of the GDx VCC scanning laser polarimeter, HRT II confocal scanning laser ophthalmoscope, and stratus OCT optical coherence tomograph for the detection of glaucoma. *Arch Ophthalmol,* 122, 827-837.

Michelson A. A., Morley E. W. (1887) On the Relative Motion of the Earth and the Luminiferous Ether. *Amer J Science,* 22, 333-345.

Michelson G., Langhans M. J., Groh M. J. (1996) Perfusion of the juxtapapillary retina and the neuroretinal rim area in primary open angle glaucoma. *J Glaucoma,* 5, 91-98.

Miglior S., Guareschi M., Albe E., Gomarasca S., Vavassori M., Orzalesi N. (2003) Detection of glaucomatous visual field changes using the Moorfields regression analysis of the Heidelberg retina tomograph. *Am J Ophthalmol,* 136, 26-33.

Miglior S., Pfeiffer N., Torri V., Zeyen T., Cunha-Vaz J., Adamsons I. (2007) Predictive factors for open-angle glaucoma among patients with ocular hypertension in the European Glaucoma Prevention Study. *Ophthalmology,* 114, 3-9.

Miglior S., Rossetti L., Lonati C., Orzalesi N. (1998) Scanning laser ophthalmoscopy of the optic disc at the level of the lamina cribrosa. *Curr Eye Res,* 17, 453-461.

Mikelberg F. S., Drance S. M., Schulzer M., Yidegiligne H. M., Weis M. M. (1989) The normal human optic nerve. Axon count and axon diameter distribution. *Ophthalmology,* 96, 1325-1328.

Miller D. T., Qu J., Jonnal R. S., Thorn K. Coherence grating and adaptive optics in the eye. *Proc SPIE*; 2003:65-72.

Minckler D. S. (1986) Correlations between anatomic features and axonal transport in primate optic nerve head. *Trans Am Ophthalmol Soc,* 84, 429-452.

Minckler D. S., Bunt A. H., Johanson G. W. (1977) Orthograde and retrograde axoplasmic transport during acute ocular hypertension in the monkey. *Invest Ophthalmol Vis Sci,* 16, 426-441.

Minckler D. S., McLean I. W., Tso M. O. (1976) Distribution of axonal and glial elements in the rhesus optic nerve head studied by electron microscopy. *Am J Ophthalmol,* 82, 179-187.

Mitchell P., Hourihan F., Sandbach J., Wang J. J. (1999) The Relationship Between Glaucoma and Myopia. *Ophthalmology,* 106, 2010-2015.

Mitchell P., Smith W., Attebo K., Healey P. R. (1996) Prevalence of open-angle glaucoma in Australia. The Blue Mountains Eye Study. *Ophthalmology,* 103, 1661-1669.

Moreno M. C., Marcos H. J., Oscar Croxatto J., Sande P. H., Campanelli J., Jaliffa C. O., Benozzi J., Rosenstein R. E. (2005) A new experimental model of glaucoma in rats through intracameral injections of hyaluronic acid. *Exp Eye Res,* 81, 71-80.

Moreno-Montanes J., Olmo N., Alvarez A., Garcia N., Zarranz-Ventura J. (2010) Cirrus high-definition optical coherence tomography compared with Stratus optical coherence tomography in glaucoma diagnosis. *Invest Ophthalmol Vis Sci,* 51, 335-343.

Morgan J. E., Jeffery G., Foss A. J. (1998) Axon deviation in the human lamina cribrosa. *Br J Ophthalmol,* 82, 680-683.

Morgan J. E., Uchida H., Caprioli J. (2000) Retinal ganglion cell death in experimental glaucoma. *Br J Ophthalmol,* 84, 303-310.

Morgan-Davies J., Taylor N., Hill A. R., Aspinall P., O'Brien C. J., Azuara-Blanco A. (2004) Three dimensional analysis of the lamina cribrosa in glaucoma. *Br J Ophthalmol,* 88, 1299-1304.

Morrison J. C. (2006) Integrins in the optic nerve head: potential roles in glaucomatous optic neuropathy (an American Ophthalmological Society thesis). *Trans Am Ophthalmol Soc,* 104, 453-477.

Morrison J. C., Cork L. C., Dunkelberger G. R., Brown A., Quigley H. A. (1990a) Aging changes of the rhesus monkey optic nerve. *Invest Ophthalmol Vis Sci,* 31, 1623-1627.

Morrison J. C., Dorman-Pease M. E., Dunkelberger G. R., Quigley H. A. (1990b) Optic nerve head extracellular matrix in primary optic atrophy and experimental glaucoma. *Arch Ophthalmol,* 108, 1020-1024.

Morrison J. C., Jerdan J. A., Dorman M. E., Quigley H. A. (1989a) Structural proteins of the neonatal and adult lamina cribrosa. *Arch Ophthalmol,* 107, 1220-1224.

Morrison J. C., L'Hernault N. L., Jerdan J. A., Quigley H. A. (1989b) Ultrastructural location of extracellular matrix components in the optic nerve head. *Arch Ophthalmol,* 107, 123-129.

Morrison J. C., Moore C. G., Deppmeier L. M., Gold B. G., Meshul C. K., Johnson E. C. (1997) A rat model of chronic pressure-induced optic nerve damage. *Exp Eye Res,* 64, 85-96.

Moya F. J., Brigatti L., Caprioli J. (1999) Effect of aging on optic nerve appearance: a longitudinal study. *Br J Ophthalmol,* 83, 567-572.

Mukesh B. N., McCarty C. A., Rait J. L., Taylor H. R. (2002) Five-year incidence of open-angle glaucoma: the visual impairment project. *Ophthalmology,* 109, 1047-1051.

Mwanza J. C., Chang R. T., Budenz D. L., Durbin M. K., Gendy M. G., Shi W., Feuer W. J. (2010) Reproducibility of peripapillary retinal nerve fiber layer thickness and optic nerve head parameters measured with cirrus HD-OCT in glaucomatous eyes. *Invest Ophthalmol Vis Sci,* 51, 5724-5730.

Nakatani Y., Higashide T., Ohkubo S., Takeda H., Sugiyama K. (2011) Evaluation of macular thickness and peripapillary retinal nerve fiber layer thickness for detection of early glaucoma using spectral domain optical coherence tomography. *J Glaucoma,* 20, 252-259.

Nakazawa T., Nakazawa C., Matsubara A., Noda K., Hisatomi T., She H., Michaud N., Hafezi-Moghadam A., Miller J. W., Benowitz L. I. (2006) Tumor necrosis factor-alpha mediates oligodendrocyte death and delayed retinal ganglion cell loss in a mouse model of glaucoma. *J Neurosci,* 26, 12633-12641.

Nassif N., Cense B., Park B. H., Yun S. H., Chen T. C., Bouma B. E., Tearney G. J., de Boer J. F. (2004) In vivo human retinal imaging by ultrahigh-speed spectral domain optical coherence tomography. *Opt Lett,* 29, 480-482.

Neubauer A. S., Krieglstein T. R., Chryssafis C., Thiel M., Kampik A. (2006) Comparison of optical coherence tomography and fundus photography for measuring the optic disc size. *Ophthalmic Physiol Opt,* 26, 13-18.

NICE. http://www.nice.org.uk/Guidance/CG85. 2009.

Nicolela M. T., Drance S. M. (1996) Various glaucomatous optic nerve appearances: clinical correlations. *Ophthalmology,* 103, 640-649.

Nicolela M. T., Hnik P., Drance S. M. (1996a) Scanning laser Doppler flowmeter study of retinal and optic disk blood flow in glaucomatous patients. *American Journal of Ophthalmology,* 122, 775-783.

Nicolela M. T., McCormick T. A., Drance S. M., Ferrier S. N., LeBlanc R. P., Chauhan B. C. (2003) Visual field and optic disc progression in patients with different types of optic disc damage: a longitudinal prospective study. *Ophthalmology,* 110, 2178-2184.

Nicolela M. T., Soares A. S., Carrillo M. M., Chauhan B. C., LeBlanc R. P., Artes P. H. (2006) Effect of moderate intraocular pressure changes on topographic measurements with confocal scanning laser tomography in patients with glaucoma. *Arch Ophthalmol,* 124, 633-640.

Nicolela M. T., Walman B. E., Buckley A. R., Drance S. M. (1996b) Various glaucomatous optic nerve appearances. A color Doppler imaging study of retrobulbar circulation. *Ophthalmology,* 103, 1670-1679.

Nork T. M., Ver Hoeve J. N., Poulsen G. L., Nickells R. W., Davis M. D., Weber A. J., Vaegan, Sarks S. H., Lemley H. L., Millecchia L. L. (2000) Swelling and loss of photoreceptors in chronic human and experimental glaucomas. *Arch Ophthalmol,* 118, 235-245.

Ogden T. E., Duggan J., Danley K., Wilcox M., Minckler D. S. (1988) Morphometry of nerve fiber bundle pores in the optic nerve head of the human. *Exp Eye Res,* 46, 559-568.

Olver J. M., Spalton D. J., McCartney A. C. (1990) Microvascular study of the retrolaminar optic nerve in man: the possible significance in anterior ischaemic optic neuropathy. *Eye,* 4 (Pt 1), 7-24.

Olver J. M., Spalton D. J., McCartney A. C. (1994) Quantitative morphology of human retrolaminar optic nerve vasculature. *Invest Ophthalmol Vis Sci,* 35, 3858-3866.

Onda E., Cioffi G. A., Bacon D. R., Van Buskirk E. M. (1995) Microvasculature of the human optic nerve. *Am J Ophthalmol,* 120, 92-102.

Orgul S., Flammer J. (1994) Interocular visual-field and intraocular-pressure asymmetries in normal-tension-glaucoma. *Eur J Ophthalmol,* 4, 199-201.

Oyama T., Abe H., Ushiki T. (2006) The connective tissue and glial framework in the optic nerve head of the normal human eye: light and scanning electron microscopic studies. *Arch Histol Cytol,* 69, 341-356.

Panda S., Jonas J. B. (1992) Decreased photoreceptor count in human eyes with secondary angle- closure glaucoma. *Invest Ophthalmol Vis Sci,* 33, 2532-2536.

Parikh R. S., Parikh S. R., Sekhar G. C., Prabakaran S., Babu J. G., Thomas R. (2007) Normal age-related decay of retinal nerve fiber layer thickness. *Ophthalmology,* 114, 921-926.

Park K. H., Caprioli J. (2002) Development of a novel reference plane for the Heidelberg retina tomograph with optical coherence tomography measurements. *J Glaucoma,* 11, 385-391.

Park S. B., Sung K. R., Kang S. Y., Kim K. R., Kook M. S. (2009) Comparison of glaucoma diagnostic Capabilities of Cirrus HD and Stratus optical coherence tomography. *Arch Ophthalmol,* 127, 1603-1609.

Parrish R. K., Schiffman J. C., Feuer W. J., Anderson D. R., Budenz D. L., Wells-Albornoz M. C., Vandenbroucke R., Kass M. A., Gordon M. O. (2005) Test-retest reproducibility of optic disk deterioration detected from stereophotographs by masked graders. *Am J Ophthalmol,* 140, 762-764.

Paunescu L. A., Schuman J. S., Price L. L., Stark P. C., Beaton S., Ishikawa H., Wollstein G., Fujimoto J. G. (2004) Reproducibility of nerve fiber thickness, macular thickness, and optic nerve head measurements using StratusOCT. *Invest Ophthalmol Vis Sci,* 45, 1716-1724.

Pederson J. E., Anderson D. R. (1980) The mode of progressive disc cupping in ocular hypertension and glaucoma. *Arch Ophthalmol,* 98, 490-495.

Perkins E. S., Phelps C. D. (1982) Open angle glaucoma, ocular hypertension, low tension glaucoma and refraction. *Arch Ophthalmol,* 100, 1464-1467.

Pfeiffer N., Torri V., Miglior S., Zeyen T., Adamsons I., Cunha-Vaz J. (2007) Central corneal thickness in the European Glaucoma Prevention Study. *Ophthalmology,* 114, 454-459.

Poli A., Strouthidis N. G., Ho T. A., Garway-Heath D. F. (2008) Analysis of HRT images: comparison of reference planes. *Invest Ophthalmol Vis Sci,* 49, 3970-3975.

Portney G. L. (1976) Photogrammetric analysis of the three-dimensional geometry of normal and glaucomatous optic cups. *Tr Am Acad Ophth & Otol,* 81, 239-246.

Potsaid B., Gorczynska I., Srinivasan V. J., Chen Y., Jiang J., Cable A., Fujimoto J. G. (2008) Ultrahigh speed spectral / Fourier domain OCT ophthalmic imaging at 70,000 to 312,500 axial scans per second. *Opt Express,* 16, 15149-15169.

Povazay B., Bizheva K., Hermann B., Unterhuber A., Sattmann H., Fercher A., Drexler W., Schubert C., Ahnelt P., Mei M., Holzwarth R., Wadsworth W., Knight J., Russell P. S. J. (2003) Enhanced visualization of choroidal vessels using ultrahigh resolution ophthalmic OCT at 1050 nm. *Opt Express,* 11, 1980-1986.

Povazay B., Hermann B., Unterhuber A., Hofer B., Sattmann H., Zeiler F., Morgan J. E., Falkner-Radler C., Glittenberg C., Blinder S., Drexler W. (2007a) Three-dimensional optical coherence tomography at 1050 nm versus 800 nm in retinal pathologies: enhanced performance and choroidal penetration in cataract patients. *J Biomed Opt,* 12, 041211.

Povazay B., Hofer B., Hermann B., Unterhuber A., Morgan J. E., Glittenberg C., Binder S., Drexler W. (2007b) Minimum distance mapping using three-dimensional optical coherence tomography for glaucoma diagnosis. *J Biomed Opt,* 12, 041204.

Qiao-Grider Y., Hung L. F., Kee C. S., Ramamirtham R., Smith E. L., 3rd. (2007a) A comparison of refractive development between two subspecies of infant rhesus monkeys (Macaca mulatta). *Vision Res,* 47, 1668-1681.

Qiao-Grider Y., Hung L. F., Kee C. S., Ramamirtham R., Smith E. L., 3rd. (2007b) Normal ocular development in young rhesus monkeys (Macaca mulatta). *Vision Res,* 47, 1424-1444.

Quigley H., Anderson D. R. (1976) The dynamics and location of axonal transport blockade by acute intraocular pressure elevation in primate optic nerve. *Invest Ophthalmol Vis Sci,* 15, 606-616.

Quigley H. A. (1986) Examination of the retinal nerve fiber layer in the recognition of early glaucoma damage. *Trans Am Ophthalmol Soc,* 84, 920-966.

Quigley H. A. Overview and introduction to session on connective tissue of the optic nerve in glaucoma. Chapter 2. In: Drance S. M., Anderson, D.R. (ed), *Optic Nerve in Glaucoma.* Amsterdam/New York: Kugler Publications; 1995:15-36.

Quigley H. A. (1998) Selectivity in glaucoma injury. *Arch Ophthalmol,* 116, 396-398.

Quigley H. A. (2011) Glaucoma. *Lancet,* 377, 1367-1377.

Quigley H. A., Addicks E. M. (1981) Regional differences in the structure of the lamina cribrosa and their relation to glaucomatous optic nerve damage. *Arch Ophthalmol,* 99, 137-143.

Quigley H. A., Addicks E. M., Green W. R. (1982) Optic nerve damage in human glaucoma. III. Quantitative correlation of nerve fiber loss and visual field defect in glaucoma, ischemic neuropathy, papilledema, and toxic neuropathy. *Arch Ophthalmol,* 100, 135-146.

Quigley H. A., Addicks E. M., Green W. R., Maumenee A. E. (1981) Optic nerve damage in human glaucoma. II. The site of injury and susceptibility to damage. *Arch Ophthalmol,* 99, 635-649.

Quigley H. A., Anderson D. R. (1977) Distribution of axonal transport blockade by acute intraocular pressure elevation in the primate optic nerve head. *Invest Ophthalmol Vis Sci,* 16, 640-644.

Quigley H. A., Broman A. T. (2006) The number of people with glaucoma worldwide in 2010 and 2020. *Br J Ophthalmol,* 90, 262-267.

Quigley H. A., Brown A., Dorman Pease M. E. (1991a) Alterations in elastin of the optic nerve head in human and experimental glaucoma. *Br J Ophthalmol,* 75, 552-557.

Quigley H. A., Brown A. E., Morrison J. D., Drance S. M. (1990) The size and shape of the optic disc in normal human eyes. *Arch Ophthalmol,* 108, 51-57.

Quigley H. A., Dorman Pease M. E., Brown A. E. (1991b) Quantitative study of collagen and elastin of the optic nerve head and sclera in human and experimental monkey glaucoma. *Curr Eye Res,* 10, 877-888.

Quigley H. A., Green W. R. (1979) The histology of human glaucoma cupping and optic nerve damage: clinicopathologic correlation in 21 eyes. *Ophthalmology,* 86, 1803-1830.

Quigley H. A., Hohman R. M., Addicks E. M., Massof R. W., Green W. R. (1983) Morphologic changes in the lamina cribrosa correlated with neural loss in open-angle glaucoma. *Am J Ophthalmol,* 95, 673-691.

Quigley H. A., McKinnon S. J., Zack D. J., Pease M. E., Kerrigan-Baumrind L. A., Kerrigan D. F., Mitchell R. S. (2000) Retrograde axonal transport of BDNF in retinal ganglion cells is blocked by acute IOP elevation in rats. *Invest Ophthalmol Vis Sci,* 41, 3460-3466.

Quigley H. A., Nickells R. W., Kerrigan L. A., Pease M. E., Thibault D. J., Zack D. J. (1995) Retinal ganglion cell death in experimental glaucoma and after axotomy occurs by apoptosis. *Invest Ophthalmol Vis Sci,* 36, 774-786.

Quigley H. A., Pease M. E. (1996) Change in the optic disc and nerve fiber layer estimated with the glaucoma-scope in monkey eyes. *J Glaucoma,* 5, 106-116.

Quigley H. A., Sanchez R. M., Dunkelberger G. R., L'Hernault N. L., Baginski T. A. (1987) Chronic glaucoma selectively damages large optic nerve fibers. *Invest Ophthalmol Vis Sci,* 28, 913-920.

Quigley H. A., Sommer A. (1987) How to use nerve fiber layer examination in the management of glaucoma. *Trans Am Ophthalmol Soc,* 85, 254-272.

Racette L., Wilson M. R., Zangwill L. M., Weinreb R. N., Sample P. A. (2003) Primary open-angle glaucoma in blacks: a review. *Surv Ophthalmol,* 48, 295-313.

Radius R. L. (1981) Regional specificity in anatomy at the lamina cribrosa. *Arch Ophthalmol,* 99, 478-480.

Radius R. L., Gonzales M. (1981) Anatomy of the lamina cribrosa in human eyes. *Arch Ophthalmol,* 99, 2159-2162.

Ramrattan R. S., Wolfs R. C., Jonas J. B., Hofman A., de Jong P. T. (1999) Determinants of optic disc characteristics in a general population: The Rotterdam Study. *Ophthalmology,* 106, 1588-1596.

Rankin S. J. A., Walman B. E., Buckley A. R., Drance S. M. (1995) Color doppler imaging and spectral analysis of the optic nerve vasculature in glaucoma. *Am J Ophthalmol,* 119, 685-693.

Rasker M. T., van den Enden A., Bakker D., Hoyng P. F. (1997) Deterioration of visual fields in patients with glaucoma with and without optic disc hemorrhages. *Arch Ophthalmol,* 115, 1257-1262.

Rauhut D., Rohen J. W. (1972) Electron Microscopic study of the trabecular meshwork in alphachymotrypsin glaucoma. *Albrecht Von Graefes Arch Klin Exp Ophthalmol,* 184, 29-41.

Read R. M., Spaeth G. L. (1974) The practical clinical appraisal of the optic disc in glaucoma: the natural history of cup progression and some specific disc-field correlations. *Trans Am Acad Ophthalmol Otolaryngol,* 78, OP255-274.

Reis A. S., Sharpe G. P., Yang H., Nicolela M. T., Burgoyne C. F., Chauhan B. C. (2011) Optic disc margin anatomy in glaucoma patients and normal controls with spectral domain optical coherence tomography. *Ophthalmology (in press)*.

Repka M. X., Quigley H. A. (1989) The effect of age on normal human optic nerve fiber number and diameter. *Ophthalmology,* 96, 26-32.

Reus N. J., Lemij H. G., Garway-Heath D. F., Airaksinen P. J., Anton A., Bron A. M., Faschinger C., Hollo G., Iester M., Jonas J. B., Mistlberger A., Topouzis F., Zeyen T. G. (2010) Clinical assessment of stereoscopic optic disc photographs for glaucoma: the European Optic Disc Assessment Trial. *Ophthalmology,* 117, 717-723.

Ridley H. (1950) Television in ophthalmology. *XVI Concilium Ophthalmologicum Brittania Acta,* 2, 1397-1404.

Ritch R., Shields M. B., Krupin T. 1989 *The Glaucomas Vol 1*. Second ed. St. Louis, Missouri: Mosby

Roberts M. D., Grau V., Grimm J., Reynaud J., Bellezza A. J., Burgoyne C. F., Downs J. C. (2009) Remodeling of the connective tissue microarchitecture of the lamina cribrosa in early experimental glaucoma. *Invest Ophthalmol Vis Sci,* 50, 681-690.

Roberts M. D., Liang Y., Sigal I. A., Grimm J., Reynaud J., Bellezza A., Burgoyne C. F., Downs J. C. (2010) Correlation between local stress and strain and lamina cribrosa connective tissue volume fraction in normal monkey eyes. *Invest Ophthalmol Vis Sci,* 51, 295-307.

Rockwood E. J., Anderson D. R. (1988) Acquired peripapillary changes and progression in glaucoma. *Graefes Arch Clin Exp Ophthalmol,* 226, 510-515.

Rotchford A. P., Johnson G. J. (2002) Glaucoma in Zulus: a population-based cross-sectional survey in a rural district in South Africa. *Arch Ophthalmol,* 120, 471-478.

Rotchford A. P., Kirwan J. F., Muller M. A., Johnson G. J., Roux P. (2003) Temba glaucoma study: a population-based cross-sectional survey in urban South Africa. *Ophthalmology,* 110, 376-382.

Ruggeri M., Wehbe H., Jiao S., Gregori G., Jockovich M. E., Hackam A., Duan Y., Puliafito C. A. (2007) In vivo three-dimensional high-resolution imaging of rodent retina with spectral-domain optical coherence tomography. *Invest Ophthalmol Vis Sci,* 48, 1808-1814.

Sakamoto A., Hangai M., Yoshimura N. (2008) Spectral-domain optical coherence tomography with multiple B-scan averaging for enhanced imaging of retinal diseases. *Ophthalmology,* 115, 1071-1078 e1077.

Sandell J. H., Peters A. (2001) Effects of age on nerve fibers in the rhesus monkey optic nerve. *J Comp Neurol,* 429, 541-553.

Sandell J. H., Peters A. (2002) Effects of age on the glial cells in the rhesus monkey optic nerve. *J Comp Neurol,* 445, 13-28.

Sander E. A., Downs J. C., Hart R. T., Burgoyne C. F., Nauman E. A. (2006) A cellular solid model of the lamina cribrosa: mechanical dependence on morphology. *J Biomech Eng,* 128, 879-889.

Savini G., Barboni P., Carbonelli M., Zanini M. (2007) The effect of scan diameter on retinal nerve fiber layer thickness measurement using stratus optic coherence tomography. *Arch Ophthalmol,* 125, 901-905.

Savini G., Carbonelli M., Parisi V., Barboni P. (2010) Effect of pupil dilation on retinal nerve fibre layer thickness measurements and their repeatability with Cirrus HD-OCT. *Eye (Lond),* 24, 1503-1508.

Schmidt K. G., von Ruckmann A., Pillunat L. E. (1998) Topical carbonic anhydrase inhibition increases ocular pulse amplitude in high tension primary open angle glaucoma. *Br J Ophthalmol,* 82, 758-762.

Schuman J. S. (2008) Spectral domain optical coherence tomography for glaucoma (an AOS thesis). *Trans Am Ophthalmol Soc,* 106, 426-458.

Schuman J. S., Hee M. R., Puliafito C. A., Wong C., Pedut-Kloizman T., Lin C. P., Hertzmark E., Izatt J. A., Swanson E. A., Fujimoto J. G. (1995) Quantification of nerve fiber layer thickness in normal and glaucomatous eyes using optical coherence tomography. *Arch Ophthalmol,* 113, 586-596.

Schuman J. S., Wollstein G., Farra T., Hertzmark E., Aydin A., Fujimoto J. G., Paunescu L. A. (2003) Comparison of optic nerve head measurements obtained by optical coherence tomography and confocal scanning laser ophthalmoscopy. *Am J Ophthalmol,* 135, 504-512.

Schwartz B., Rieser J. C., Fishbein S. L. (1977) Fluorescein angiographic defects of the optic disc in glaucoma. *Arch Ophthalmol,* 95, 1961-1974.

Seddon J. M., Schwartz B., Flowerdew G. (1983) Case control study of ocular hypertension. *Arch Ophthalmol,* 101, 891-894.

See J. L., Nicolela M. T., Chauhan B. C. (2009) Rates of neuroretinal rim and peripapillary atrophy area change: a comparative study of glaucoma patients and normal controls. *Ophthalmology,* 116, 840-847.

Sehi M., Grewal D. S., Sheets C. W., Greenfield D. S. (2009) Diagnostic ability of Fourier-domain vs time-domain optical coherence tomography for glaucoma detection. *Am J Ophthalmol,* 148, 597-605.

Senatorov V., Malyukova I., Fariss R., Wawrousek E. F., Swaminathan S., Sharan S. K., Tomarev S. (2006) Expression of mutated mouse myocilin induces open-angle glaucoma in transgenic mice. *J Neurosci,* 26, 11903-11914.

Seong M., Sung K. R., Choi E. H., Kang S. Y., Cho J. W., Um T. W., Kim Y. J., Park S. B., Hong H. E., Kook M. S. (2010) Macular and peripapillary retinal nerve fiber layer measurements by spectral domain optical coherence tomography in normal-tension glaucoma. *Invest Ophthalmol Vis Sci,* 51, 1446-1452.

Shareef S. R., Garcia-Valenzuela E., Salierno A., Walsh J., Sharma S. C. (1995) Chronic ocular hypertension following episcleral venous occlusion in. *Exp Eye Res,* 61, 379-382.

Shields M. B. (1980) Gray crescent in the optic nerve head. *Am J Ophthalmol,* 89, 238-244.

Shimmyo M., Ross A. J., Moy A., Mostafavi R. (2003) Intraocular pressure, Goldmann applanation tension, corneal thickness, and corneal curvature in Caucasians, Asians, Hispanics, and African Americans. *Am J Ophthalmol,* 136, 603-613.

Siegner S. W., Netland P. A. (1996) Optic disc hemorrhages and progression of glaucoma. *Ophthalmology,* 103, 1014-1024.

Sigal I. A., Ethier C. R. (2009) Biomechanics of the optic nerve head. *Exp Eye Res,* 88, 799-807.

Sigal I. A., Flanagan J. G., Ethier C. R. (2005a) Factors influencing optic nerve head biomechanics. *Invest Ophthalmol Vis Sci,* 46, 4189-4199.

Sigal I. A., Flanagan J. G., Tertinegg I., Ethier C. R. (2004) Finite element modeling of optic nerve head biomechanics. *Invest Ophthalmol Vis Sci,* 45, 4378-4387.

Sigal I. A., Flanagan J. G., Tertinegg I., Ethier C. R. (2005b) Reconstruction of human optic nerve heads for finite element modeling. *Technol Health Care,* 13, 313-329.

Sigal I. A., Flanagan J. G., Tertinegg I., Ethier C. R. (2007) Predicted extension, compression and shearing of optic nerve head tissues. *Exp Eye Res,* 85, 312-322.

Sigal I. A., Flanagan J. G., Tertinegg I., Ethier C. R. (2009a) Modeling individual-specific human optic nerve head biomechanics. Part I: IOP-induced deformations and influence of geometry. *Biomech Model Mechanobiol,* 8, 85-98.

Sigal I. A., Flanagan J. G., Tertinegg I., Ethier C. R. (2009b) Modeling individual-specific human optic nerve head biomechanics. Part II: influence of material properties. *Biomech Model Mechanobiol,* 8, 99-109.

Sigal I. A., Flanagan J. G., Tertinegg I., Ethier C. R. (2010) 3D morphometry of the human optic nerve head. *Exp Eye Res,* 90, 70-80.

Sigal I. A., Yang H., Roberts M. D., Burgoyne C. F., Downs J. C. (2011) IOP-induced lamina cribrosa displacement and scleral canal expansion: an analysis of factor interactions using parameterized eye-specific models. *Invest Ophthalmol Vis Sci,* 52, 1896-1907.

Silver D. M., Farrell R. A., Langham M. E., O'Brien V., Schilder P. (1989) Estimation of pulsatile ocular blood flow from intraocular pressure. *Acta Ophthalmol Suppl,* 191, 25-29.

Silver D. M., Geyer O. (2000) Pressure-volume relation for the living human eye. *Curr Eye Res,* 20, 115-120.

Sommer A., Miller N. R., Pollack I., Maumenee A. E., George T. (1977) The nerve fiber layer in the diagnosis of glaucoma. *Arch Ophthalmol,* 95, 2149-2156.

Sommer A., Pollack I., Maumenee A. E. (1979a) Optic disc parameters and onset of glaucomatous field loss. I. Methods and progressive changes in disc morphology. *Arch Ophthalmol,* 97, 1444-1448.

Sommer A., Pollack I., Maumenee A. E. (1979b) Optic disc parameters and onset of glaucomatous field loss. II. Static screening criteria. *Arch Ophthalmol,* 97, 1449-1454.

Sommer A., Tielsch J. M., Katz J., Quigley H. A., Gottsch J. D., Javitt J., Singh K. (1991) Relationship between intraocular pressure and primary open angle glaucoma among white and black Americans. The Baltimore Eye Survey. *Arch Ophthalmol,* 109, 1090-1095.

Sonnsjo B., Dokmo Y., Krakau T. (2002) Disc haemorrhages, precursors of open angle glaucoma. *Prog Retin Eye Res,* 21, 35-56.

Spaeth G. L. (1994) A new classification of glaucoma including focal glaucoma. *Surv Ophthalmol,* 38 Suppl, S9-17.

Spaeth G. L., Hitchings R. A., Sivalingam E. (1976) The optic disc in glaucoma: pathogenetic correlation of five patterns of cupping in chronic open-angle glaucoma. *Trans Sect Ophthalmol Am Acad Ophthalmol Otolaryngol,* 81, 217-223.

Spaide R. F., Koizumi H., Pozzoni M. C. (2008) Enhanced depth imaging spectral-domain optical coherence tomography. *Am J Ophthalmol,* 146, 496-500.

Sponsel W. E. (1989) Tonometry in question: can visual screening tests play a more decisive role in glaucoma diagnosis and management? *Surv Ophthalmol,* 33 Suppl, 291-300.

Srinivasan V. J., Adler D. C., Chen Y., Gorczynska I., Huber R., Duker J. S., Schuman J. S., Fujimoto J. G. (2008) Ultrahigh-speed optical coherence tomography for three-dimensional and en face imaging of the retina and optic nerve head. *Invest Ophthalmol Vis Sci,* 49, 5103-5110.

Srinivasan V. J., Huber R., Gorczynska I., Fujimoto J. G., Jiang J. Y., Reisen P., Cable A. E. (2007) High-speed, high-resolution optical coherence tomography retinal imaging with a frequency-swept laser at 850 nm. *Opt Lett,* 32, 361-363.

Strouthidis N. G., Fortune B., Yang H., Sigal I. A., Burgoyne C. F. (2011) Longitudinal change detected by spectral domain optical coherence tomography in the optic nerve head and peripapillary retina in experimental glaucoma. *Invest Ophthalmol Vis Sci,* 52, 1206-1219.

Strouthidis N. G., Gardiner S. K., Sinapis C., Burgoyne C. F., Garway-Heath D. F. (2009a) The spatial pattern of neuroretinal rim loss in ocular hypertension. *Invest Ophthalmol Vis Sci,* 50, 3737-3742.

Strouthidis N. G., Grimm J., Williams G. A., Cull G. A., Wilson D. J., Burgoyne C. F. (2010) A comparison of optic nerve head morphology viewed by spectral domain optical coherence tomography and by serial histology. *Invest Ophthalmol Vis Sci,* 51, 1464-1474.

Strouthidis N. G., Scott A., Peter N. M., Garway-Heath D. F. (2006) Optic disc and visual field progression in ocular hypertensive subjects: detection rates, specificity, and agreement. *Invest Ophthalmol Vis Sci,* 47, 2904-2910.

Strouthidis N. G., White E. T., Owen V. M., Ho T. A., Garway-Heath D. F. (2005a) Improving the repeatability of Heidelberg retina tomograph and Heidelberg retina tomograph II rim area measurements. *Br J Ophthalmol,* 89, 1433-1437.

Strouthidis N. G., White E. T., Owen V. M., Ho T. A., Hammond C. J., Garway-Heath D. F. (2005b) Factors affecting the test-retest variability of Heidelberg retina tomograph and Heidelberg retina tomograph II measurements. *Br J Ophthalmol,* 89, 1427-1432.

Strouthidis N. G., Yang H., Downs J. C., Burgoyne C. F. (2009b) Comparison of Clinical and Three-Dimensional Histomorphometric Optic Disc Margin Anatomy. *Invest Ophthalmol Vis Sci,* 50, 2165-2174.

Strouthidis N. G., Yang H., Fortune B., Downs J. C., Burgoyne C. F. (2009c) Detection of Optic Nerve Head Neural Canal Opening within Histomorphometric and Spectral Domain Optical Coherence Tomography Data Sets. *Invest Ophthalmol Vis Sci,* 50, 214-223.

Sugiyama K., Tomita G., Kitazawa Y., Onda E., Shinohara H., Park K. H. (1997) The associations of optic disc hemorrhage with retinal nerve fiber layer defect and peripapillary atrophy in normal-tension glaucoma. *Ophthalmology,* 104, 1926-1933.

Sugiyama K., Uchida H., Tomita G., Sato Y., Iwase A., Kitazawa Y. (1999) Localized wedge-shaped defects of retinal nerve fiber layer and disc hemorrhage in glaucoma. *Ophthalmology,* 106, 1762-1767.

Sung K. R., Kim D. Y., Park S. B., Kook M. S. (2009) Comparison of retinal nerve fiber layer thickness measured by Cirrus HD and Stratus optical coherence tomography. *Ophthalmology,* 116, 1264-1270, 1270 e1261.

Swindale N. V., Stjepanovic G., Chin A., Mikelberg F. S. (2000) Automated analysis of normal and glaucomatous optic nerve head topography images. *Invest Ophthalmol Vis Sci,* 41, 1730-1742.

Tan J. C., Garway-Heath D. F., Fitzke F. W., Hitchings R. A. (2003a) Reasons for rim area variability in scanning laser tomography. *Invest Ophthalmol Vis Sci,* 44, 1126-1131.

Tan J. C., Garway-Heath D. F., Hitchings R. A. (2003b) Variability across the optic nerve head in scanning laser tomography. *Br J Ophthalmol,* 87, 557-559.

Tan J. C., Hitchings R. A. (2003) Reference plane definition and reproducibility in optic nerve head images. *Invest Ophthalmol Vis Sci,* 44, 1132-1137.

Tan O., Chopra V., Lu A. T., Schuman J. S., Ishikawa H., Varma R., Huang D. (2009) Detection of Macular Ganglion Cell Loss in Glaucoma by Fourier-Domain Optical Coherence Tomography. *Ophthalmology*.

Tezel G., Hernandez M. R., Wax M. B. (2001) In vitro evaluation of reactive astrocyte migration, a component of tissue remodeling in glaucomatous optic nerve head. *Glia,* 34, 178-189.

Tezel G., Kolker A. E., Kass M. A., Wax M. B., Gordon M., Siegmund K. D. (1997a) Parapapillary chorioretinal atrophy in patients with ocular hypertension. I. An evaluation as a predictive factor for the development of glaucomatous damage. *Arch Ophthalmol,* 115, 1503-1508.

Tezel G., Kolker A. E., Wax M. B., Kass M. A., Gordon M., Siegmund K. D. (1997b) Parapapillary chorioretinal atrophy in patients with ocular hypertension. II. An evaluation of progressive changes. *Arch Ophthalmol,* 115, 1509-1514.

Thorleifsson G., Magnusson K. P., Sulem P., Walters G. B., Gudbjartsson D. F., Stefansson H., Jonsson T., Jonasdottir A., Stefansdottir G., Masson G., Hardarson G. A., Petursson H., Arnarsson A., Motallebipour M., Wallerman O., Wadelius C., Gulcher J. R., Thorsteinsdottir U., Kong A., Jonasson F., Stefansson K. (2007) Common sequence variants in the LOXL1 gene confer susceptibility to exfoliation glaucoma. *Science,* 317, 1397-1400.

Tielsch J. M., Sommer A., Katz J., Royall R. M., Quigley H. A., Javitt J. (1991) Racial variations in the prevalence of primary open-angle glaucoma. The Baltimore Eye Survey. *Jama,* 266, 369-374.

Tong L., Chan Y. H., Gazzard G., Loon S. C., Fong A., Selvaraj P., Healey P. R., Tan D., Wong T. Y., Saw S. M. (2007) Heidelberg retinal tomography of optic disc and nerve fiber layer in singapore children: variations with disc tilt and refractive error. *Invest Ophthalmol Vis Sci,* 48, 4939-4944.

Toth C. A., Birngruber R., Boppart S. A., Hee M. R., Fujimoto J. G., DiCarlo C. D., Swanson E. A., Cain C. P., Narayan D. G., Noojin G. D., Roach W. P. (1997a) Argon laser retinal lesions evaluated in vivo by optical coherence tomography. *Am J Ophthalmol,* 123, 188-198.

Toth C. A., Narayan D. G., Boppart S. A., Hee M. R., Fujimoto J. G., Birngruber R., Cain C. P., DiCarlo C. D., Roach W. P. (1997b) A comparison of retinal morphology viewed by optical coherence tomography and by light microscopy. *Arch Ophthalmol,* 115, 1425-1428.

Trew D. R., Smith S. E. (1991) Postural studies in pulsatile ocular blood flow: II. Chronic open angle glaucoma. *Br J Ophthalmol,* 75, 71-75.

Tsai C. S., Ritch R., Shin D. H., Wan J. Y., Chi T. (1992) Age-related decline of disc rim area in visually normal subjects. *Ophthalmology,* 99, 29-35.

Tuulonen A., Airaksinen P. J. (1991) Initial Glaucomatous Optic Disk and Retinal Nerve Fiber Layer Abnormalities and Their Progression. *Am J Ophthalmol,* III, 485-490.

Uchida H., Ugurlu S., Caprioli J. (1998) Increasing peripapillary atrophy is associated with progressive glaucoma. *Ophthalmology,* 105, 1541-1545.

Ueda J., Sawaguchi S., Hanyu T., Yaoeda K., Fukuchi T., Abe H., Ozawa H. (1998) Experimental glaucoma model in the rat induced by laser trabecular photocoagulation after an intracameral injection of India ink. *Jpn J Ophthalmol,* 42, 337-344.

Urcola J. H., Hernandez M., Vecino E. (2006) Three experimental glaucoma models in rats: comparison of the effects of intraocular pressure elevation on retinal ganglion cell size and death. *Exp Eye Res,* 83, 429-437.

Varela H. J., Hernandez M. R. (1997) Astrocyte responses in human optic nerve head with primary open-angle glaucoma. *J Glaucoma,* 6, 303-313.

Varma R., Tielsch J. M., Quigley H. A., Hilton S. C., Katz J., Spaeth G. L., Sommer A. (1994) Race-, age-, gender-, and refractive error-related differences in the normal optic disc. *Arch Ophthalmol,* 112, 1068-1076.

Viswanathan S., Frishman L. J., Robson J. G. (2000) The Uniform Field and Pattern ERG in Macaques with Experimental Glaucoma: Removal of Spiking Activity. *Invest Ophthalmol Vis Sci,* 41, 2797-2810.

Viswanathan S., Frishman L. J., Robson J. G., Harwerth R. S., Smith E. L. (1999) The photopic negative response of the macaque electroretinogram: reduction by experimental glaucoma. *Invest Ophthalmol Vis Sci,* 40, 1124-1136.

Vizzeri G., Weinreb R. N., Gonzalez-Garcia A. O., Bowd C., Medeiros F. A., Sample P. A., Zangwill L. M. (2009a) Agreement between spectral-domain and time-domain OCT for measuring RNFL thickness. *Br J Ophthalmol,* 93, 775-781.

Vizzeri G., Weinreb R. N., Martinez de la Casa J. M., Alencar L. M., Bowd C., Balasubramanian M., Medeiros F. A., Sample P., Zangwill L. M. (2009b) Clinicians agreement in establishing glaucomatous progression using the Heidelberg retina tomograph. *Ophthalmology,* 116, 14-24.

von Graefe A. (1857) Uber die iridktomie bei glaukom and uber den glaukomatosen prozess. *Albrecht Von Graefes Arch Ophthalmol,* 3, 456-650.

Vongphanit J., Mitchell P., Wang J. J. (2002) Population prevalence of tilted optic disks and the relationship of this sign to refractive error. *Am J Ophthalmol,* 133, 679-685.

Wakitani Y., Sasoh M., Sugimoto M., Ito Y., Ido M., Uji Y. (2003) Macular thickness measurements in healthy subjects with different axial lengths using optical coherence tomography. *Retina,* 23, 177-182.

Wang R. F., Schumer R. A., Serle J. B., Podos S. M. (1998) A comparison of argon laser and diode laser photocoagulation of the trabecular meshwork to produce the glaucoma monkey model. *J Glaucoma,* 7, 45-49.

Wang Y., Nelson J., Chen Z., Reiser B., Chuck R., Windeler R. (2003) Optimal wavelength for ultrahigh-resolution optical coherence tomography. *Opt Express,* 11, 1411-1417.

Watkins R. J., Broadway D. C. (2005) Intraobserver and interobserver reliability indices for drawing scanning laser ophthalmoscope optic disc contour lines with and without the aid of optic disc photographs. *J Glaucoma,* 14, 351-357.

Webb R. H., Hughes G. W. (1981) Scanning laser ophthalmoscope. *IEEE Trans Biomed Eng,* 28, 488-492.

Webb R. H., Hughes G. W., Pomerantzeff O. (1980) Flying spot TV ophthalmoscope. *Appl Opt,* 19, 2991-2997.

Weber A. J., Kaufman P. L., Hubbard W. C. (1998) Morphology of single ganglion cells in the glaucomatous primate retina. *Invest Ophthalmol Vis Sci,* 39, 2304-2320.

Weber A. J., Zelenak D. (2001) Experimental glaucoma in the primate induced by latex microspheres. *J Neurosci Methods,* 111, 39-48.

Weinreb R. N., Lusky M., Bartsch D. U., Morsman D. (1993) Effect of repetitive imaging on topographic measurements of the optic nerve head. *Arch Ophthalmol,* 111, 636-638.

Weinreb R. N., Toris C. B., Gabelt B. T., Lindsey J. D., Kaufman P. L. (2002) Effects of prostaglandins on the aqueous humor outflow pathways. *Surv Ophthalmol,* 47 Suppl 1, S53-64.

Wiggs J. L. (2007) Genetic etiologies of glaucoma. *Arch Ophthalmol,* 125, 30-37.

Williams Z. Y., Schuman J. S., Gamell L., Nemi A., Hertzmark E., Fujimoto J. G., Mattox C., Simpson J., Wollstein G. (2002) Optical coherence tomography measurement of nerve fiber layer thickness and the likelihood of a visual field defect. *Am J Ophthalmol,* 134, 538-546.

Wilson M. R., Hertzmark E., Walker A. M., Childs-Shaw K., Epstein D. L. (1987) A case-control study of risk factors in open angle glaucoma. *Arch Ophthalmol,* 105, 1066-1071.

Wojtkowski M., Leitgeb R., Kowalczyk A., Bajraszewski T., Fercher A. F. (2002) In vivo human retinal imaging by Fourier domain optical coherence tomography. *J Biomed Opt,* 7, 457-463.

Wojtkowski M., Srinivasan V., Fujimoto J. G., Ko T., Schuman J. S., Kowalczyk A., Duker J. S. (2005) Three-dimensional retinal imaging with high-speed ultrahigh-resolution optical coherence tomography. *Ophthalmology,* 112, 1734-1746.

Wolfs R. C., Klaver C. C., Ramrattan R. S., van Duijn C. M., Hofman A., de Jong P. T. (1998) Genetic risk of primary open-angle glaucoma. Population-based familial aggregation study. *Arch Ophthalmol,* 116, 1640-1645.

Wollstein G., Garway-Heath D. F., Hitchings R. A. (1998) Identification of early glaucoma cases with the scanning laser ophthalmoscope. *Ophthalmology,* 105, 1557-1563.

Wollstein G., Schuman J. S., Price L. L., Aydin A., Stark P. C., Hertzmark E., Lai E., Ishikawa H., Mattox C., Fujimoto J. G., Paunescu L. A. (2005) Optical coherence tomography longitudinal evaluation of retinal nerve fiber layer thickness in glaucoma. *Arch Ophthalmol,* 123, 464-470.

Wong T. Y., Klein B. E., Klein R., Knudtson M., Lee K. E. (2003) Refractive errors, intraocular pressure, and glaucoma in a white population. *Ophthalmology,* 110, 211-217.

Wu S. Y., Leske M. C. (1997) Associations with intraocular pressure in the Barbados Eye Study. *Arch Ophthalmol,* 115, 1572-1576.

Xu L., Wang Y., Yang H., Zhang L., Jonas J. B. (2007) Size of the neuroretinal rim and optic cup and their correlations with ocular and general parameters in adult Chinese: the Beijing eye study. *Br J Ophthalmol,* 91, 1616-1619.

Yamanari M., Lim Y., Makita S., Yasuno Y. (2009) Visualization of phase retardation of deep posterior eye by polarization-sensitive swept-source optical coherence tomography with 1-microm probe. *Opt Express,* 17, 12385-12396.

Yamazaki S., Inoue Y., Yoshikawa K. (1996) Peripapillary fluorescein angiographic findings in primary open angle glaucoma. *Br J Ophthalmol,* 80, 812-817.

Yan D. B., Coloma F. M., Metheetrairut A., Trope G. E., Heathcote J. G., Ethier C. R. (1994) Deformation of the lamina cribrosa by elevated intraocular pressure. *Br J Ophthalmol,* 78, 643-648.

Yan J. (2002) geepack: Yet Another Package for Generalized Estimating Equations. *R-News,* 2/3, 12-14.

Yang H., Downs J. C., Bellezza A. J., Thompson H., Burgoyne C. F. (2007a) 3-D Histomorphometry of the Normal and Early Glaucomatous Monkey Optic Nerve Head: Prelaminar Neural Tissues and Cupping. *Invest Ophthalmol Vis Sci,* 48, 5068-5084.

Yang H., Downs J. C., Burgoyne C. F. (2009a) Physiologic intereye differences in monkey optic nerve head architecture and their relation to changes in early experimental glaucoma. *Invest Ophthalmol Vis Sci,* 50, 224-234.

Yang H., Downs J. C., Girkin C., Sakata L., Bellezza A., Thompson H., Burgoyne C. F. (2007b) 3-D Histomorphometry of the Normal and Early Glaucomatous Monkey Optic Nerve Head: Lamina Cribrosa and Peripapillary Scleral Position and Thickness. *Invest Ophthalmol Vis Sci,* 48, 4597-4607.

Yang H., Downs J. C., Sigal I. A., Roberts M. D., Thompson H., Burgoyne C. F. (2009b) Deformation of the normal monkey optic nerve head connective tissue after acute IOP elevation within 3-D histomorphometric reconstructions. *Invest Ophthalmol Vis Sci,* 50, 5785-5799.

Yang H., Thompson H., Roberts M. D., Sigal I. A., Downs J. C., Burgoyne C. F. (2011) Deformation of the early glaucomatous monkey optic nerve head connective tissue after acute IOP elevation in 3-D histomorphometric reconstructions. *Invest Ophthalmol Vis Sci,* 52, 345-363.

Yaqoob Z., Wu J., Yang C. (2005) Spectral domain optical coherence tomography: a better OCT imaging strategy. *Biotechniques,* 39, S6-13.

Yasuno Y., Hong Y., Makita S., Yamanari M., Akiba M., Miura M., Yatagai T. (2007) In vivo high-contrast imaging of deep posterior eye by 1-microm swept source optical coherence tomography and scattering optical coherence angiography. *Opt Express,* 15, 6121-6139.

You Q. S., Xu L., Jonas J. B. (2008) Tilted optic discs: The Beijing Eye Study. *Eye (Lond),* 22, 728-729.

Yucel Y. H., Kalichman M. W., Mizisin A. P., Powell H. C., Weinreb R. N. (1999) Histomorphometric analysis of optic nerve changes in experimental glaucoma. *J Glaucoma,* 8, 38-45.

Yucel Y. H., Zhang Q., Gupta N., Kaufman P. L., Weinreb R. N. (2000) Loss of neurons in magnocellular and parvocellular layers of the lateral geniculate nucleus in glaucoma. *Arch Ophthalmol,* 118, 378-384.

Yucel Y. H., Zhang Q., Weinreb R. N., Kaufman P. L., Gupta N. (2001) Atrophy of relay neurons in magno- and parvocellular layers in the lateral geniculate nucleus in experimental glaucoma. *Invest Ophthalmol Vis Sci,* 42, 3216-3222.

Yucel Y. H., Zhang Q., Weinreb R. N., Kaufman P. L., Gupta N. (2003) Effects of retinal ganglion cell loss on magno-, parvo-, koniocellular pathways in the lateral geniculate nucleus and visual cortex in glaucoma. *Prog Retin Eye Res,* 22, 465-481.

Zangwill L., Irak I., Berry C. C., Garden V., de Souza Lima M., Weinreb R. N. (1997) Effect of cataract and pupil size on image quality with confocal scanning laser ophthalmoscopy. *Arch Ophthalmol,* 115, 983-990.

Zangwill L. M., Bowd C., Berry C. C., Williams J., Blumenthal E. Z., Sanchez-Galeana C. A., Vasile C., Weinreb R. N. (2001) Discriminating between normal and glaucomatous eyes using the Heidelberg Retina Tomograph, GDx Nerve Fiber Analyzer, and Optical Coherence Tomograph. *Arch Ophthalmol,* 119, 985-993.

Zangwill L. M., Jain S., Racette L., Ernstrom K. B., Bowd C., Medeiros F. A., Sample P. A., Weinreb R. N. (2007) The effect of disc size and severity of disease on the diagnostic accuracy of the Heidelberg Retina Tomograph Glaucoma Probability Score. *Invest Ophthalmol Vis Sci,* 48, 2653-2660.

Zawadzki R. J., Choi S. S., Fuller A. R., Evans J. W., Hamann B., Werner J. S. (2009) Cellular resolution volumetric in vivo retinal imaging with adaptive optics-optical coherence tomography. *Opt Express,* 17, 4084-4094.

Zawadzki R. J., Choi S. S., Jones S. M., Oliver S. S., Werner J. S. (2007) Adaptive optics-optical coherence tomography: optimizing visualization of microscopic retinal structures in three dimensions. *J Opt Soc Am A Opt Image Sci Vis,* 24, 1373-1383.

Zeimer R., Asrani S., Zou S., Quigley H., Jampel H. (1998) Quantitative detection of glaucomatous damage at the posterior pole by retinal thickness mapping. A pilot study. *Ophthalmology,* 105, 224-231.

Zeimer R., Shahidi M., Mori M., Zou S., Asrani S. (1996) A new method for rapid mapping of the retinal thickness at the posterior pole. *Invest Ophthalmol Vis Sci,* 37, 1994-2001.

Zeimer R. C., Ogura Y. (1989) The relation between glaucomatous damage and optic nerve head mechanical compliance. *Arch Ophthalmol,* 107, 1232-1234.

Zeyen T., Miglior S., Pfeiffer N., Cunha-Vaz J., Adamsons I. (2003) Reproducibility of evaluation of optic disc change for glaucoma with stereo optic disc photographs. *Ophthalmology,* 110, 340-344.

Zhang J., Rao B., Chen Z. (2005a) Swept source based fourier domain functional optical coherence tomography. *Conf Proc IEEE Eng Med Biol Soc,* 7, 7230-7233.

Zhang Y., Rha J., Jonnal R., Miller D. (2005b) Adaptive optics parallel spectral domain optical coherence tomography for imaging the living retina. *Opt Express,* 13, 4792-4811.

Zhou Y., Grinchuk O., Tomarev S. I. (2008) Transgenic mice expressing the Tyr437His mutant of human myocilin protein develop glaucoma. *Invest Ophthalmol Vis Sci,* 49, 1932-1939.

Zimmerman L. E., De Venecia G., Hamasaki D. I. (1967) Pathology of the optic nerve in experimental acute glaucoma. *Invest Ophthalmol Vis Sci,* 6, 109-125.

Zinser G. Heidelberg retina tomograph; the system. *Optic nerve head and retinal nerve fibre analysis.* Savona: Editrice Dogma; 2005:59-61.